UNIVERSITÀ DEGLI STUDI DI TRIESTE
e
UNIVERSITÀ CA' FOSCARI DI VENEZIA

XXXII CICLO DEL DOTTORATO DI RICERCA IN

_____CHIMICA_____

PO FRIULI VENEZIA GIULIA - FONDO SOCIALE EUROPEO 2014/2020

Synthesis of Nitrogen Doped Carbon Nanodots and their Applications as Functional Materials

Settore scientifico-disciplinare: **CHIM/06**

DOTTORANDO
MICHELE CACIOPPO

COORDINATORE
PROF. BARBARA MILANI

SUPERVISORE DI TESI
PROF. MAURIZIO PRATO

CO-SUPERVISORI DI TESI
DOTT.SSA FRANCESCA ARCUDI
DOTT. LUKA ĐORĐEVIĆ

ANNO ACCADEMICO 2018/2019

“There are two possible outcomes: if the result confirms the hypothesis, then you've made a measurement. If the result is contrary to the hypothesis, then you've made a discovery.”

Enrico Fermi

Acknowledgements

To my supervisor Prof. Maurizio Prato for having given me the great chance of working in a so advanced scientific environment. Your interest, passion and ability on teaching and divulgate science represented for me a source of inspiration during the PhD course. Thanks for your availability on facing all the problems, obstacles and the projects we worked on. I considered this a great chance to improve my working independence, a thing that, in my opinion, a student needs for the improvement of his skills. Your behavior is synonym of great humanity, humility and experience, typical of a high-level leader that acts as mentor of the younger scientific minds.

To my co-supervisors Francesca Arcudi and Luka Đorđević for the formative, friendly and professional collaboration during these three years. Thanks for having believed in me sharing your knowledge, encouraging and supporting me through this intense PhD course. I consider both of you a model to follow because of your high-professional working style and for the passion that you exhibit every day for science. You are the best that a PhD student can desire for a successful, fruitful and individual scientific growth.

To Francesco Amato my dear friend and colleague for being close on sharing with me the good and the bad, for being comprehensive and helpful, for being like a brother with me during these intense years.

To all the Prato group and to all the other colleagues of the chemistry department of University of Trieste and Ca Foscari for all the significant time spend together inside and outside the lab.

To all the collaborators I had the opportunity to work with.

To Prof. Dr. Wolfgang Parak and Dr. Neus Feliu for hosting me during a great research period in Hamburg and to all the colleagues and friends met there.

A big thanks to mamma, papà and my two brothers Alessandra and Manfredi, no words can explain how much I feel lucky to have a so strong and wonderful family, thanks for being with me and for me every single day.

To all my friends of ever: Vito, Giacomo, Valerio, Elena, Omar, Marco, Silvia, Alessandro P., Alessandro M., Roberto, Vita, Mario, Emanuela, Alessio, Carla, Nino, Marco, Marisa, Paolo, my two bands gli eSKA Viva and Skabrosi, Vincenzo, Francesco C., Gabriella, Manfredi, Giuseppe, Sara.

A very special thanks is for you Caterina, there are so many things I would like to say, but there is one thing that is worth telling you: thank you simply because you became part of my life.

Table of Contents

Abbreviations

0D	Zero Dimensional
a	Amphiphilic
AFM	Atomic Force Microscopy
Arg	L-arginine
ATP	Adenosine Triphosphate
BDA	1,4-butanediamine
BODIPY	difluoro-boron-dipyrromethene
BPEI	Branched Polyethyleneimine
Br_2NDA	2,6-Dibromonaphthalene-1,4:5,8-Tetracarboxylic Dianhydride
CDs	Carbon Dots
CHDA	Cyclohexane Diamine
CLSM	Confocal Laserc Scanning Microscopy
CNDs	Carbon Nanodots
CNTs	Carbon Nanotubes
CPDs	Carbon Polymer Dots
CPL	Circularly Polarized Luminescence
CQDs	Carbon Quantum Dots
CRR	Carbon Dioxide Reduction Reaction
D-A	Electron Donor-Acceptor
DEA	Diethylamine
DFT	Density Functional Theory
DHP	1,4-dihydro-2,6-dimethylpyridine-3,5-dicarboxylate
DNA	Deoxyribonucleic Acid
DSSCs	Dye Sensitized Solar Cells
ECD	Electronic Circular Dichroism
ECL	Electrochemiluminescence
EDA	Ethylene diamine
EDC	1-Ethyl-3-(3-dimethylaminopropyl)carbodiimide
FC	Flow Cytometry
FDCD	Fluorescence Detection of Circular Dichroism
FT-IR	Fourier Transform Infrared Spectroscopy
GC	Glassy Carbon
GQDs	Graphene Quantum Dots
H_2TSPP^{4-}	meso-tetrakis(4-sulfonatophenyl)porphyrin
hb	Hydrophobic
HER	Hydrogen Evolution Reaction
hp	Hydrophilic
HSA	Human Serum Albumin
i.m.	Intramuscular
i.v.	Intravenous
LEDs	Light Emitting Diodes
MW	Microwave
MWCNTs	Multi-Walled Carbon Nanotubes
NCs	Silicon Nanocrystals
Nd:YAG	Neodymium-Doped Yttrium Aluminum Garnet
NDA	Naphthalene dianhydride
NDI	Naphthalene Diimide
NIR	Near-Infrared

Abbreviations

NMR	Nuclear Magnetic Resonance
NPs	Chiral Nanoparticles
ORR	Oxygen Reduction Reaction
PBS	Phosphate Buffered Saline
PCE	Power Conversion Efficiency
Pcs	Phthalocyanines
PDI	Perylenediimide
PEG	Polyethylene Glycol
PET	Photoinduced Electron Transfer
PL	Photoluminescence
QDs	Metal-Based Semiconductor Suantum Dots
QY	Quantum Iield
RLS	Resonance Light Scattering
RPMI	Roswell Park Memorial Institute 1640 Cell Medium
$Ru(bpy)_3^{2+}$	ruthenium(II)tris(2,2'-bipyridyl)
s.c.	Subcutaneous
SEC	Size Exclusion Chromatography
SWCNTs	Single-Walled Carbon Nanotubes
TEA	Triethylamine
TEM	Transmission Electron Microscopy
TPrA	Tri-n-propylamine
TTF	Tetrathiafulvalene
UV	Ultraviolet
VCD	Vibrational Circular Spectroscopy
XPS	X-Ray Photoelectron Spectroscopy
ZnP	Zinc Tetraarylporphyrin
ZnPc	Zinc Phthalocyanine

Abstract

Carbon dots (CDs) are the latest member to join the large family of carbon-based nanomaterials and represent the central topic of this dissertation. This nanomaterial consists on quasi-spherical 0D nanoparticles with rich redox chemistry, wide light absorption and emission and high chemical and photo-stability. These favorable properties have increased the interest of the scientific community toward preparation and application of these nanoparticles in many applicative areas, ranging from biological to energy related applications.

Chapter 1 provides a general overview of the state of the art of CDs. The structures and the relative properties of the four CDs typologies are discussed: graphene quantum dots (GQDs), carbon quantum dots (CQDs), carbon nanodots (CNDs) and carbon polymer dots (CPDs). In the second section, the synthetic approaches (bottom-up and top-down methods) for the synthesis of CDs are described, with particular emphasis on the strategies focused on the engineering of the properties of CDs. In the final section, the most common applications of CDs are reported.

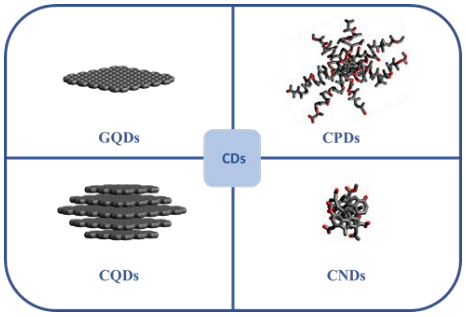

Chapter 2 shows that chiral carbon carbon nanodots (sCNDs) can be readily prepared using hydrothermal microwave-assisted synthesis. These nanoparticles, with size around 3 nm, are highly soluble in water and display mirror-image profile both in the UV–Vis and in the infrared regions, as detected by electronic and vibrational circular dichroism, respectively. We proposed the presence of a chiral shell that is originated by cyclohexanediamine moieties incorporated on the dots. The proposed synthetic strategy opens up exciting opportunities for developing a variety of chiral nanodots. As representative examples, we report the preparation of CNDs with different absorption and emission properties by using different core precursor or doping molecules. This simple (and effective) synthetic methodology inspires us towards

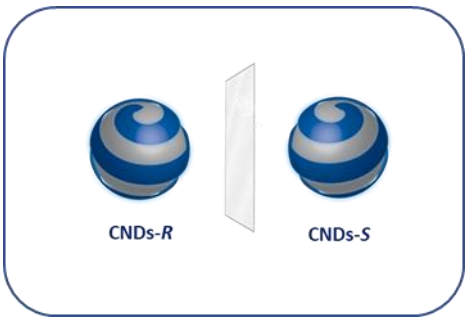

exciting opportunities, such as the use of these nanoparticles as templates for the formation of chiral chromophoric (porphyrin) assemblies in water. Finally, the effects that the chiral surface of CDs has on protein and cells is discussed.

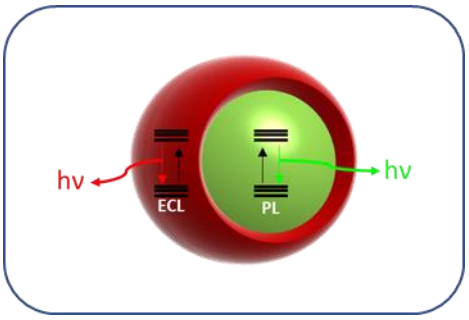

C*hapter 3* reports the design, synthesis and characterization of CNDs doped with BODIPY dyes (BCNDs) showing the versatility of a multicomponent hydrothermal synthesis for preparing materials with predictable optical properties. Experimental evidences suggest that the BODIPY has been successfully incorporated in the nanodots through a carboxylic moiety on the meso-phenyl ring that likely reacts with the amines of Arg and EDA. The BCNDs are highly water soluble, possess amino groups on the surface that are amenable for further functionalization and present the typical green fluorescence emission of the BODIPY. The photoluminescence quantum yield (PLQY) of the dye affects the PLQY of the resulting nanoparticles demonstrating that structural modifications of the BODIPY precursor lead to nanodots with enhanced fluorescence emission. In addition, in the quest for novel ECL emitters, able to emit across a palette of colors and to be easily modified for bioconjugation reaction, we studied the ECL properties of these nanoparticles. Our findings show that BCNDs are good ECL emission that can be mainly modulated through post-synthetic surface modification, and the dye is likely incorporated in the core of the nanodots. The rational brought forward in this work could be extended for preparing multicolored CNDs by using different BODIPY precursors.

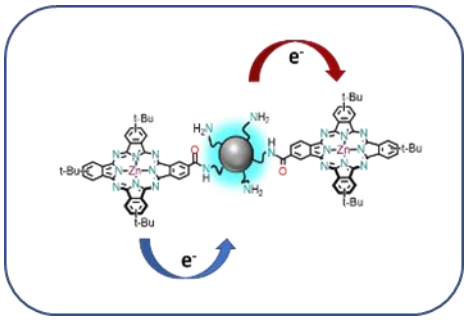

Chapter 4 focuses on the use of nitrogen doped CNDs (NCNDs) as building blocks for the preparation of donor-acceptor covalent hybrids with zinc phthalocyanines (ZnPc). The amino groups from the NCNDs and the carboxylic acid from a ZnPc are combined through a carbodiimide coupling protocol. The study show the presence of two (or

more) units of ZnPcs per nanoparticle and an in-depth photophysical investigation reveals the donor-acceptor properties of the hybrid materials.

Riassunto

I *carbon dots* (CDs) sono i nanomateriali a base di carbonio di piú recente scoperta e rappresentano l'argomento centrale di questa tesi. Questo nanomateriale è costituito da nanoparticelle 0D quasi sferiche con interessanti proprietà redox, ampio spettro di assorbimento ed emissione, e elevata stabilità chimica e fotochimica. Queste attraenti proprietà hanno fatto crescere l'interesse della comunità scientifica verso la preparazione e l'uso di queste nanoparticelle in molte aree applicative, dalle bio-applicazioni a utilizzi in campo energetico.

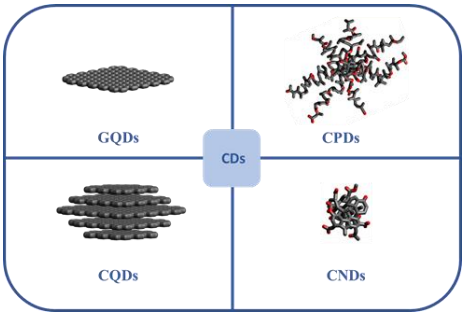

Il *capitolo 1* offre una panoramica generale dello stato dell'arte dei CDs. Sono discusse le strutture e proprietà delle quattro tipologie esistenti: *graphene quantum dots* (GQD), *carbon quantum dots* (CQD), *carbon nanodots* (CND) e *carbon polymer dots* (CPD). Alla classificazione dei CDs segue una trattazione degli approcci sintetici più comuni (metodi *bottom-up* e *top-down*) impiegati per la loro produzione e facendo risaltare, in particolare, le strategie utili all'ottenimento di materiali con specifiche proprietà ottiche ed elettroniche, come l'emissione di fluorescenza e il potenziale redox. Infine, una trattazione generale sulle applicazioni più comuni dei CDs descrive i principali vantaggi derivanti dall'uso di queste nanoparticelle in ambiti che spaziano dalla biologia all'optoelettronica.

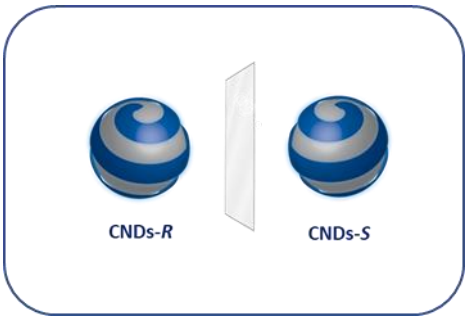

Il *Capitolo 2* dimostra che CNDs chirali (sCND) possono essere prontamente preparati usando una sintesi multicomponente assistita da microonde. Queste nanoparticelle, con una dimensione di circa 3 nm, sono altamente solubili in acqua e mostrano dicroismo circolare speculare sia nella regione dell'ultravioletto-visibile che in quella infrarossa dello spettro elettromagnetico. Tali proprietà vengono studiate rispettivamente da analisi in dicroismo circolare elettronico e vibrazionale. Abbiamo proposto la presenza di una *shell* chirale derivante dalla presenza di unità

strutturali di cicloesandiammine nella struttura della nanoparticella. La strategia sintesica proposta offre interessanti opportunità per lo sviluppo di diverse nanoparticelle di carbonio chirali. Come esempi rappresentativi, abbiamo riportato la preparazione di CNDs con diverse proprietà di assorbimento e fluorescenza attraverso l'impiego di diversi precursori responsabili della formazione del *core* o di molecole dopanti. Questa semplice (ed efficace) metodologia ci ha ispirato nell'esplorare nuove opportunità applicative, ad esempio l'impiego di queste nanoparticelle come templati per la formazione di aggregati cromoforici (porfirinici) chirali in acqua. Infine, vengono discussi gli effetti della superficie chirale dei CDs su proteine e cellule.

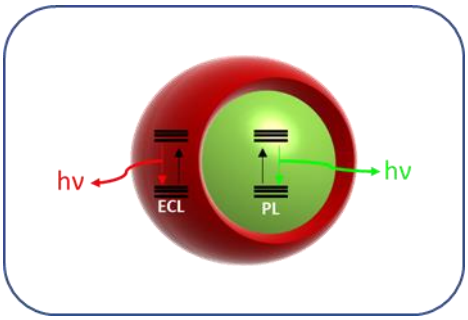

Il *capitolo 3* riporta la progettazione, la sintesi e la caratterizzazione dei CNDs dopati con fluorofori BODIPY (BCNDs). L'approccio sintetico riportato consiste in una sintesi idrotermica multicomponente che è risultata versatile per la preparazione di materiali con proprietà ottiche specifiche. Le evidenze sperimentali, emerse dallo studio, hanno suggerito che le molecole di fluoroforo sono state incorporate con successo nella struttura delle nanoparticelle attraverso la possibile reazione del gruppo carbossilico del BODIPY con le ammine di arginina ed etilen diammina. I BCNDs ottenuti sono risultati altamente solubili in acqua, possiedono gruppi amminici superficiali che possono essere ulteriormente funzionalizzati, e presentano la tipica emissione di fluorescenza verde del BODIPY. Studi fotofisici hanno rivelato che la resa quantica di fotoluminescenza (PLQY) del BODIPY influenza la PLQY delle nanoparticelle risultanti. Questo dato ha dimostrato che la modifica strutturale del BODIPY risulta nella produzione di nanoparticelle con una migliore emissione di fluorescenza. Inoltre, considerato il crescente interesse verso la produzione di nuovi emettitori per elettrochemiluminescenza (ECL), aventi emissioni variabili dello spettro del visibile e in grado di essere facilmente modificabili, abbiamo studiato anche le proprietà ECL di queste nanoparticelle. I BCNDs hanno mostrato una buona emissione di ECL che può essere modulata principalmente attraverso la modifica della superficie via post-funzionalizzazione,

suggerendo che il fluoroforo è probabilmente incorporato nel nucleo della nanoparticella. Il metodo proposto in questo lavoro potrebbe essere esteso per preparare CNDs con tunabile luminescenza usando diversi BODIPY come precursori.

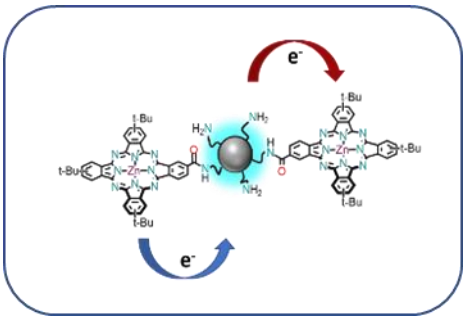

Il *capitolo 4* si concentra sull'uso di CNDs dopati con azoto (NCNDs) come elementi costitutivi per la preparazione di ibridi covalenti donatore-accettore di con zinco ftalocianine (ZnPc). I gruppi amminici degli NCNDs sono stati fatti reagire con gli acidi carbossilici di un derivato di ZnPc tramite un protocollo di accoppiamento con carbodiimide. Lo studio dimostra la presenza di due (o più) unità di ZnPc per nanoparticella e le indagini fotofisico hanno dimostrato le proprietà donatore-accettore del materiale ibrido.

1 Carbon-based Dots

1.1 Classification and properties of carbon-based dots

Carbon-based dots (CDs) are the latest discovered members of the large family of carbon nanomaterials and consist of 0D nanoparticles made of carbon, hydrogen and oxygen. CDs were accidentally observed during the analysis of purification of carbon nanotubes (CNTs) in 2004.[1] Subsequent to their discovery, this nanomaterial received more and more interest because of its intriguing properties. Among these, their fascinating luminescence stands out and qualifies CDs as next-generation luminescent material.[2] These nanoparticles present different structures and, consequently, different properties. The vast variability in their structures, as well as the large variety of possible starting materials and synthetic methods, complicated their nomenclature and subsequent classification. This problem was firstly discussed by Valcarel and coworkers proposing a nomenclature for the three main types of CDs: graphene quantum dots (GQDs), carbon quantum dots (CQDs) and carbon nanodots (CNDs).[3] In this classification, the main differences were principally focused on the structure and quantum confinement. GQDs and CQDs, differing from CNDs, possess extended π-conjugated carbon structures and (but not always proved) quantum size effect. Although GQDs and CQDs present similar properties, their structures present some differences. GQDs are composed of single graphene discs, while CQDs are graphitic quasi-spherical nanoparticles. CNDs, on the other hand, show a different structure having a core composed of a mix of amorphous and graphitic domains made of sp^3 and sp^2 atoms, respectively, and do not show quantum confinement effect. The CD fluorescence emission is strongly dependent on the level of π-conjugation in GQDs and CQDs, while it is mainly originating from molecular-like structures in CNDs. Although the structural classification worked toward elucidating inconsistencies in CD classification, it revealed to be unsatisfactory. For example, GQDs are indeed individual graphene discoidal sheets, but their edges contain structural defects such as oxygen-containing functional groups. On the contrary, CQDs and CNDs are quasi-spherical

nanoparticles, but can consist of different mixtures of sp^2 and sp^3 carbons, as well as different amounts of oxygen functional groups (-COOH, CHO, -OH). Similarly to CQDs, CNDs present various organic functional groups on the surface, but also possess an amorphous carbon core that contains higher amounts of oxygen. These observations brought Reiner and coworkers to redefine the nomenclature of these nanoparticles.[4] By considering the main structural features of the nanoparticle, they defined CDs as graphitic, *g*-CDs, or amorphous, *a*-CDs. Moreover, considering also the surface polarity of these nanoparticles, Naccache and coworkers identified CDs as hydrophobic (hb-CDs), hydrophilic (hp-CDs) and amphiphilic (a-CDs).[5] In addition to these categories, in the last years a novel class of CDs was identified on particles exhibiting polymeric features. These are called carbonized polymer dots (CPDs) and result from the partial carbonization of polymeric precursors.[6] In particular, these nanoparticles show a carbonized core surrounded by polymeric chains that contain multiple functional groups.[7–14] Therefore, CDs can be categorized in four main typologies (**Figure 1.1**): GQDs, CQDs, CNDs and CPDs. Each of these types could be better identified if also the surface polarity is indicated before the name (as suggested by Naccache and coworkers).

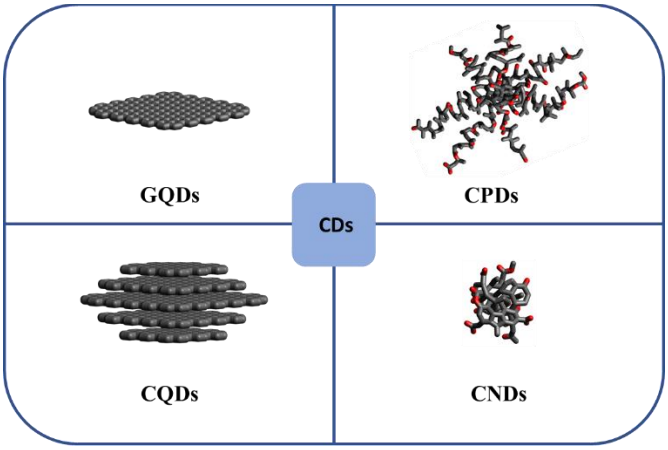

Figure 1.1 Schematic representation of the four typologies of CDs: quantum sized GQDs and CQDs (red); amorphous CNDs and CPDs (blue).

Moreover, the presence of heteroatoms, other than oxygen, also should be specified. These doping elements are introduced to tune or enhance specific CDs properties.[15] Dopants could be metal[16] or non-metal[17] atoms and are usually introduced during the carbonization process using appropriate precursors. To improve the systematic nomenclature of CDs, the information about the presence of doping elements

should be also included by adding the symbols of the dopant before the typology. This could be made writing in alphabetical order the metallic atoms followed by the non-metallic ones. For metals, also the oxidation state of the atom is mentioned into brackets. As an example, iron (III) and sulfur co-doped carbon nanodots soluble in water are identified as hp-Fe(III)S-CNDs.

Even though of the structural diversity, the CDs classes presents similar features such as water solubility, generally low toxicity/biocompatibility, light absorption/emission and photoinduced charge separation. In light of these properties, ever since their discovery, CDs have been considered a valuable alternative to metal-based quantum-dots (QDs).[3]

CDs are generally easily dispersible in water or polar solvents thanks to the presence of many oxygen functional groups on the surface.[18] The hydrophilicity and easy dispersibility in polar media, just after their synthesis, is one of the main properties that attracted the interest of these nanoparticles for biological applications (see **Section 1.4**).[19] However, different examples report that hydrophobic CDs could be produced from the partial carbonization of hydrophobic precursors.[20–23] Moreover the surface modification of these nanoparticles have been revealed very useful for the tuning of the solubility (see **Section 1.3.3**).[24]

The low cytotoxicity of CDs has determined the success of their use in biological applications (see **Section 1.4.1**).[19] The small size, the high water solubility, bio-compatibility are the main features that make these nanoparticles good candidates for theragnostic uses.[25] Generally, at concentrations lower than 500 $\mu g\ mL^{-1}$, these nanoparticles result no toxic and their clearance is not affected by inflammation and immunoresponse.[26–32]

The four typologies of CDs present, despite the different structures, similar light-absorption properties.[33–35] The light absorption spectrum generally presents a stronger absorption band in the UV that tails to the visible. This absorption is ascribed to the $\pi \rightarrow \pi^*$ electronic transitions of the aromatic conjugated moieties and the $n \rightarrow \pi^*$ arising from the absorption of the functionalities containing oxygen and doping heteroatoms. Notably the doping effect could be responsible for changing the shape of the curve, resulting in stronger absorptions in different regions of the

visible (see **Section 1.3.1**).[36] Generally CDs are highly structurally stable nanomaterials upon light irradiation.[37] For this reason, and thanks to their fascinating photoluminescence, CDs have been employed in optoelectronics for different applications (see **Section 1.4**).

The photoluminescence presents mechanisms that are strictly related to the structural features of the nanoparticle.[38] More specifically, the structure should be considered as a core/shell system. Then, depending on the arrangement of the atoms composing the structure, there are different mechanisms of excitation and relaxation resulting in light emission. In particular, GQDs and CQDs present a crystalline and π-conjugated carbon structure with few surface functional groups. On the contrary, CNDs and CPDs have an amorphous carbon core containing and being surrounded by multiple emissive functional groups. In the case of GQDs and CQDs, generally quantum confinement contributes to the photoluminescence as well as surface effects. This is due to the discrete energy levels of the conduction and valence band that arises from the π-conjugated system and the size affects the band gap.[39] The general observed trend is a blue shifted emission for smaller nanoparticles (high energy band gap) and redshift for bigger particles (low energy band gap).[40,41] On the contrary, CNDs and CPDs exhibit a molecule-like photoluminescence that arises from the multiple emissive sites in the structure.[42,43] These emissive centers could be produced during the synthetic process *via* oxidation of the surface or partial graphitization of the core. Multiple chromophores could be produced possessing different excitation energies that generally result in the excitation-dependent emission of the nanoparticle. These were identified based on the oxidation degree of the surface and the presence of surface functional groups.[44–46] The former typology of emissive sites is strongly dependent on the oxygen content, resulting generally in a red shifted emission at higher oxidation degree. The surface defects originating from the oxidation are responsible for the trapping of excitons and the radiation due to the recombination of these. In the latter typology, the surface states are correlated to the specific surface functional groups. In this case groups containing for example C=O or C=N are considered responsible of the fluorescence emission. For this reason, each functional group could generate different fluorophores on the nanoparticle surface. Consequently, by the design of

the typology of the structure it is possible to forecast some photoluminescence properties (see **Section 1.3**). In the case of GQDs and CQDs, after the formation of the core, the growth of the particle is essential to tune the emission range. CNDs and CPDs could be instead designed by the rational introduction of molecular-like chromophores.

The photoinduced charge separation in CDs, related to the light interaction properties, has made these nanoparticle advantageous nanomaterials for applications in opto-electronics and photocatalysis (see **Section 1.4.2**).[47] In particular, CDs showed to be good electron donors and acceptors upon light irradiation. This is possible due to the generation of electrons and holes that could interact with other electron accepting or donating molecules or materials.[48–51] The mechanism of generation of these photoinduced electron accepting/donating species strongly depends, similarly to the optical properties, to the peculiar nanoparticle electronic structure. For example, in GQDs and CQDs the bandgap of excitation and the electron transfer properties are affected by quantum size effects and, therefore, these could be tuned by controlling the size. Differently from these, CNDs and CPDs present electron donating and accepting features that depends on interactions between the aromatic π-conjugated system and the structural defects of the amorphous domains. Moreover, the introduction of doping atoms or selected surface functional groups in CDs would result in the modification of the electronic structure. Depending on these features, the nanoparticle could assume a more electron donating or accepting behavior (see **Section 1.3**).[52–59]

Despite all these advantageous properties, one of the main problems of this nanomaterial resides in the low rationalization of structural control.[60] However, looking at the extensive literature produced till today, it emerges that the structure could be, at least in part, tuned by the choice of the precursors and the synthetic strategy.[4,47] To give a general overview about these methods we will firstly discuss in the following sections the main synthetic approaches for CDs production (**Section 1.2**). Subsequently we will analyze more in detail the different methods to engineer these nanoparticles in order to tune the final properties (**Section 1.3**). Finally, we will highlight the main applications of these nanoparticles in function of their properties (**Section 1.4**).

1.2 Top-down and bottom-up synthetic methods

Over the past few years, a variety of synthetic methods for CDs production have been explored. Based on the typology of precursor, the CDs synthetic methods can be generally classified into two main categories, namely, top-down (see **Section 1.2.1**) and bottom-up (see **Section 1.2.2**). While the former route involves the breaking down of larger carbon structures, in the latter CDs are formed from small molecular precursors (**Figure 1.2**).

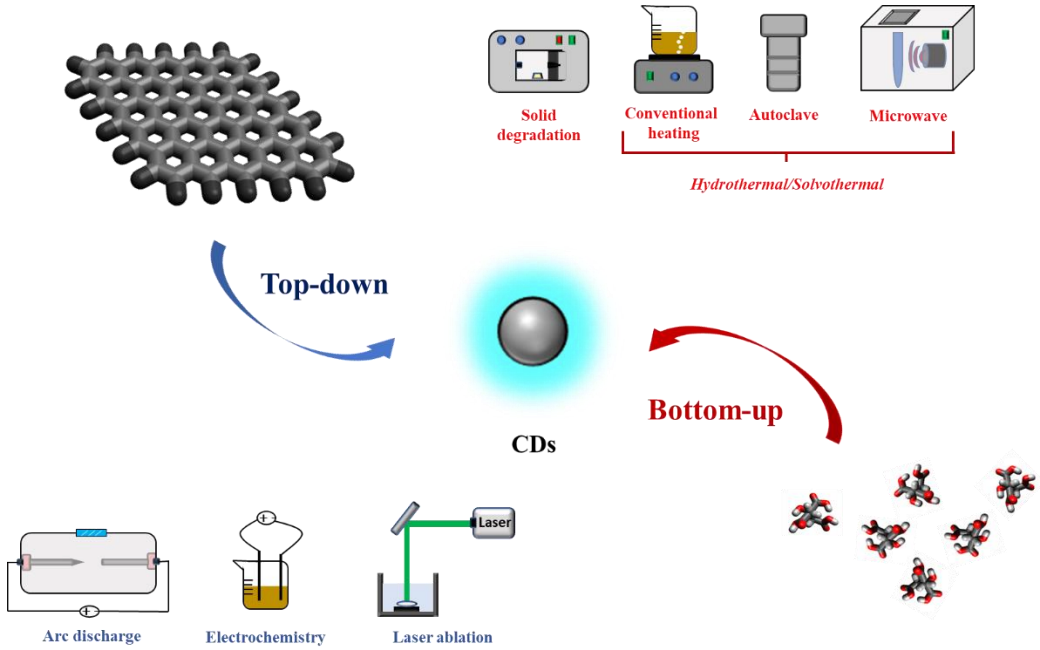

Figure 1.2 Schematic representation of the top-down and bottom-up synthetic approaches for CDs synthesis.

1.2.1 Top-down Approaches

Top-down methods mainly consist of arc-discharge, laser ablation, electrochemical and sonochemical methods using starting materials such as graphite powder or multi-walled carbon nanotubes (MWCNTs). Arc discharge consists on generating an arc discharge on two electrodes that are fixed at close distance in a chamber and in presence of inert gas. The electrodes used are generally made of graphite representing the carbon source. In the case of CDs production, small amounts of water vapor are introduced to promote the formation of oxidized groups in the structure. Laser ablation, on the other hand, is an effective synthetic methodology

that consists on abrading a solid carbon source by irradiation with a mix of laser wavelengths. Through irradiation, small carbonized fragments of carbon nanoparticles are produced and can be subsequently isolated from the bulk carbonaceous material.

Carbon nanoparticles can be also produced by using electrochemical methods, which are based on the oxidation and degradation of graphite electrodes, by applying an external voltage. Alternatively, CDs can be produced by sonochemical treatment of graphite or graphene in solution. Ultrasound waves in solution induce a rapid change of pressure that results in the formation of cavitation bubbles.[61] The vapor filled bubbles collapse, generating high temperatures and pressures and a shock wave in the local region. This process oxidizes and degrades metals and also carbon-based bulk materials producing CDs from graphitic or graphene surfaces.

In 2004, hp-N-CNDs were discovered as fluorescent fragments, during an electrophoretic purification of SWCNTs.[1] Arc-discharged soot was oxidized with nitric acid and then extracted with basic water. The presence of three class of materials was surprisingly observed during the purification process of the as-obtained suspension through gel electrophoresis. In addition to the expected nanotubes, identified by a slow-moving dark band, and another fast-moving fluorescent band was detected. The fluorescent material was found to be a mixture of nanoparticles composed by carbon, hydrogen, oxygen and nitrogen atoms. This product was then separated into three fractions having different emission colors under UV light.

The first electrochemical preparation of blue luminescent CDs was reported by Ding and coworkers in 2007.[62] Blue-luminescent spherical-shaped hp-CQDs, with narrow size distribution of 2.8 ± 0.5 nm, were obtained through the electrochemical cleavage of MWCNTs grown on a carbon paper and by applying cycling potentials ranging from −2.0 to +2.0 V. The electrochemical treatment of graphene oxide has been also used to produce green emissive hp-GQDs.[63] Graphene oxide was used as electrode, with Pt and Ag/AgCl wires as counter and reference electrodes respectively, in a 0.1 M phosphate buffer solution. By applying cycling potentials

of ±3.0 V, with scan rates of 0.5 V s^{-1}, green emissive hp-GQDs of sizes between 3 and 5 nm were obtained.

Sun and coworkers reported the first synthesis of CDs using the laser ablation of carbon bulk materials.[64,65] The method consisted of a laser treatment on a carbon target, using a Nd:YAG laser at 1064 nm and a frequency of 10 Hz. The process involves harsh experimental conditions, reaching 900 °C and 75 kPa, and water and argon as gas carriers during the procedure. After purification, the as-obtained hp-CNDs showed a good water solubility, but no fluorescence emission has been detected. The latter has been improved though the surface passivation of these particles by using organic polymers such as polyethylene glycol (PEG) as coating layer. This was the first demonstration of enhancing fluorescence emission through the passivation of the surface emissive traps.

The use of a sonochemical treatment as top-down method for the preparation of CDs was first reported by Lee and coworkers.[66] hp-GQDs showing a bright blue emission have been produced by sonicating a dispersion of graphene oxide in concentrated sulfuric and nitric acids for 12 hours. The acids were then removed as exhaust gases *via* a calcination step and the mixture was purified by microfiltration and dialysis using water as solvent.

The processes described above represent the main top-down approaches employed for the preparation of CDs. Despite the effectiveness in producing CDs, which usually possess a graphitic core structure, these methods require harsh synthetic conditions and suffer of low yields, due to the large formation of carbonaceous aggregates and intense post-synthetic purification. These disadvantages can be overcome with the use of bottom-up approaches that are discussed in the next section.

1.2.2 Bottom-Up Approaches

Bottom-up syntheses provide more accessible and cost-effective processes than top-down methods. CDs are synthetized by using small molecular or polymeric precursors and the generally accepted formation mechanism consists of three steps:

(1) reactions of the precursors, such as condensation reactions; (2) formation of a polymer-like intermediates; (3) carbonization, which also includes aromatization reactions, to give the final nanoparticle.[38] In a representative work Liu and coworkers studied the formation mechanism of hp-NS-CQDs obtained by thermal treatment of L-cysteine and ammonia.[67] The synthetic process involved the decomposition of the cysteine, the formation of polymer like structures. After aggregation, these structures went toward carbonization, forming a crystalline doped core typical of CQDs. Zang and coworkers obtained similar results obtaining hp-Gd(III)N-CQDs from citric acid, ethylene diamine (EDA) and $GdCl_3$.[68] More specifically, it appeared that citric acid reacts with EDA forming a polymer-like structure, which formed small nuclei after carbonization. These nuclei growth forming particles bearing surface functional groups able to complex the Gd(III) ions.

In summary, from these examples emerges how the thermal decomposition of solid (thermolysis), or thermal treatment of dissolved precursors promotes the formation of small nuclei that can grow at different sizes. In the former high temperatures induce the degradation of the solid precursors, followed by the formation of the nanoparticles. In the case of solvothermal or hydrothermal treatment of the precursors, partially or totally solubilized, conventional heating or thermic processes in autoclave or through microwave irradiation (MW) are the most common synthetic methods. Conventional heating refers to the use of reaction temperatures below, or close to, the boiling point of solvents. The thermal process in autoclave allows working at higher temperatures than the boiling points, by reaching higher pressures inside the reactor, which generally consists on a sealed Teflon vessel. Microwave-assisted solvothermal processes hold the advantage of fast and homogeneous heating.[5] Microwave is absorbed in solution when the frequency of radiation is in resonance with the rotational frequency of the solvent molecules or solutes. The absorption of the radiation results on the excitation to higher rotational states that release heating after relaxation. Domestic microwave oven has been widely used for the preparation of CDs, but the use of a microwave reactor allows a better control and modulation of the reaction parameters such as temperature, pressure, time and power. The latter synthetic methodology ensures a

more reproducible synthesis and represents one of the commonly used synthetic techniques for the preparation of CDs. Representative examples of these bottom-up approaches are reported below.

Reisner and coworkers successfully obtained CDs through the thermal decomposition of solid precursors.[69,70] Blue emissive hp-CQDs were obtained by the thermal treatment of citric acid in furnace at 180 °C for 40 h. Nanoparticles with an average size of 6.8 nm were obtained after a treatment with aqueous NaOH to deprotonate the surface carboxylic acids. A similar synthetic process was used to obtain hp-N-CQDs from L-aspartic acid through the graphitization of the solid precursor at 320 °C for 100 hours. The obtained nanoparticles showed an average size of 3.6 nm, together with nitrogen doping resulting in pyrrolic and pyridinic moieties.

A representative example of CDs synthesis by conventional heating was reported by Li and coworkers.[71] In this work, sucrose was heated in oleic acid at 215 °C for 5 minutes under magnetic stirring and a nitrogen atmosphere. The solid product was then purified by extraction with hexane and dialyzed in water, giving hp-CNDs. This thermal process was also used for the production of dots from a gel by Hu and coworkers.[72] A gel was first produced by reacting citric acid in presence of polyethyleneimine (BPEI) *via* a hydrothermal process at 200 °C. The thermal process was then repeated after the addition of water, obtaining hp-N-CQDs.

A representative example of hydrothermal process in autoclave to produce co-doped CDs was reported by Yu and coworkers.[73] hp-NS-CQDs were produced by heating a water solution of citric acid and cysteine at 200 °C for 3 h. The nanoparticles showed height with sizes of *ca.* 2 nm and strong fluorescence emission in the blue region. The preparation of CDs in autoclave has been also reported using organic solvents.[74] hp-N-CQDs were produced by heating a mixture of CCl_4 and EDA at 200 °C for different times. The first precursor is both solvent and carbon source, while the second is a nitrogen doping source. It was demonstrated that the doping level can be tuned with the varying the content of nitrogen precursor. The hydrothermal method was also employed for the preparation of CPDs. In this context Yang and coworkers used polyacrylic acid and

EDA to synthetize hp-N-CPDs in autoclave.[11] The process consisted on heating a water solution of the two precursors at 200 °C for 8 h and the resulting nanoparticles showed strong blue luminescence in solution and a stable phosphorescence emission in the solid state.

Microwave methods emerged as powerful synthetic routes for CDs. They ensure high energy efficiency, which often results in a higher yield and shorter reaction time and therefore could lead to important advancement in large-scale production of high-quality nanomaterials. The use of water as a solvent in microwave-assisted organic syntheses has also risen significantly because of the interest in ecofriendly processes in Green Chemistry. As a result of this effectiveness, MW-assisted synthesis has been explored by several research groups, including ours.[75,76] One of the first synthesis of CDs using a MW-assisted process was reported by Qu and coworkers in one of the pioneering studies of CDs formation.[77] hp-CNDs,. highly soluble in water and with an excitation dependent emission, were successfully by heating glycerol in a phosphate buffer solution (at pH 7.4) at 750 W for 14 minutes, in a domestic MW oven. Our group reported a procedure in 2016, which uses a two-component approach, together with a fast microwave-assisted hydrothermal synthesis, to produce doped CDs in only three minutes.[75,78] More specifically, strong blue luminescent hp-N-CNDs were obtained by using L-arginine (Arg) and EDA as carbon and nitrogen precursors. A detailed structural characterization through an NMR study on ^{13}C-enriched NCNDs revealed that while the aromatic core, the aliphatic and the carbonyl region mainly originate from Arg, EDA mostly contribute to the typical region of aliphatic carbon atoms connected to heteroatoms. We expanded this original procedure to tailor the properties of CDs to exhibit different fluorescence or tune their bandgap (see **Section 1.3**).[75,76] This synthetic approach lays the foundation for preparation of the nanomaterials reported in this dissertation.

1.3 Engineered carbon-based dots

CDs could be engineered for the extending (or enhancing) of targeted properties, in order to optimize their use in different applications (see **Section 1.4**). The three main routes to modify these nanoparticles are the pre-synthetic design, the doping and surface passivation/functionalization. Each of these methods focuses on the modification of the structure *via* different routes. The pre-synthetic design exploits the use of selected precursors and conditions in order to provide certain reactions that lead to one typology of CDs (see **Section 1.3.1**). The doping and surface passivation are especially useful for enhancing the optical properties *via* the modification of the chemical structure and the introduction of specific emissive surface functional groups (see **Section 1.3.2**). Surface passivation is useful for the functionalization of such nanoparticles with other molecules or materials, in order to obtain hybrids of specific interest (see **Section 1.3.3**).

1.3.1 Pre-synthetic design

The pre-synthetic design of carbon dots has emerged as a useful tool to prepare CDs with expected structural features by choosing specific precursors. This approach emerged from the knowledge and rationalization acquired during the decade of studies on these nanoparticles. Generally, the specific synthetic approach, together with the nature of the precursor, determines the final structure.

Top-down routes use large sp^2-rich precursors, such as graphite or nanotubes, that are broken by powerful methods. The use of arc-discharge, laser ablation or electrochemical treatment on these materials gives aromatic and π-conjugated cores that exhibit quantum size effect. Therefore the most obtained particles by these methods are essentially GQDs and CQDs.[79,80] Bottom-up methods, on the other hand, allow the use of less energies and milder conditions on molecular or polymeric precursors. These generally lead to obtain more amorphous cores or partially carbonized particles, resulting in CNDs and CPDs.[6,43,81] These could be considered as general synthetic guidelines to obtain preferentially one of the four structures. However, each of these structures controls the above-mentioned

properties by different mechanisms. For this reason, each property could be tuned considering the peculiar structural properties of the particle.

In GQDs and CQDs the core is mainly responsible for the electronic structure of the whole particle. This is due to the extended π-conjugated structure that is subjected to quantum size effect. For example, as introduced in Section **1.4**, under 10 nm, obtaining larger π-structures results in a red shift of the fluorescence emission.[2] Moreover, the introduction of oxidation defects or heteroatoms is helpful for tuning the QY of emission and modifying the redox properties of the nanoparticles.[47]

Because of their amorphous structures, the design of CNDs and CPDs has been more difficult to achieve and the preferential method to obtain such nanoparticles is the bottom-up. Due to the large variety of molecular and polymeric precursors many structures could be obtained. These could exhibit very different properties, making their design difficult.

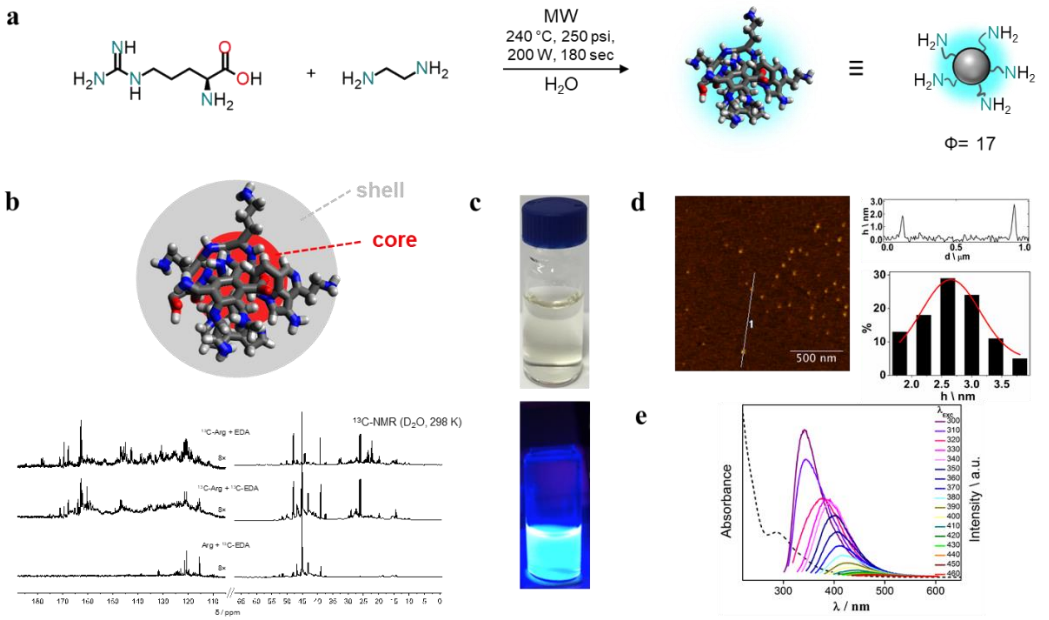

Figure 1.3 Synthesis and characterization of hp-N-CNDs: (**a**) scheme of the synthetic process, (**b**) scheme of the core/shell structure and ^{13}C-NMR experiments, (**c**) hp-N-CNDs aqueous solution irradiated under daylight (top) and 365 nm UV light (bottom), (**d**) atomic force microscopy image of hp-N-CNDs (left), height profile (top right) and height size distribution histogram (bottom right), (**e**) superimposed UV-Vis absorption and fluorescence emission of hp-N-CNDs in water. Adapted from reference [78].

In our research group we have approached these issues by exploring not only the synthetic parameters, but also by trying to rationalize the use of specific precursors.

In this context, the aim of the first CNDs prepared in our lab[75,78] was to control the synthetic process in order to obtain nitrogen-doped carbon nanodots (hp-N-CNDs). In particular, by controlling the synthetic process, using a microwave assisted hydrothermal process and N-rich precursors (EDA and Arg), hp-N-CNDs were successfully obtained with the desired/designed doping (**Figure 1.3a**).

The nanoparticles were subsequently purified by a multistep protocol that was conceived for the production of the material in high purity.[75,78] After the hydrothermal process, the nanoparticles were purified firstly by microfiltration and then by dialysis. The former purification resulted quite important for the removal of minute amount of raw carbonaceous material (> 100 nm). The latter was important for the purification from smaller sized molecular and polymeric side-products. The mixture from the hydrothermal process, on the other hand, could be purified by size exclusion chromatography (SEC) that revealed to be a useful technique also for the separation of materials reported in this thesis. A high fluorescence emission, compared to the commonly reported CNDs at that time, was possible thanks to the nitrogen doping (**Figure 1.3e**). Moreover, the control of the synthetic parameters by using a microwave reactor allowed to obtain a narrow size distribution of the nanoparticles (**Figure 1.3d**). This work represented the basis useful for the conception and design of new series of CNDs structures. This was possible also because the role of the two precursors, towards the final structure, was achieved through one- and bi-dimensional NMR studies. In particular, Arg was shown to act as the core precursor, while the EDA mainly contributes to the formation of the surface (**Figure 1.3b**).

Based on this work, we started to design and conceive new carbon nanodots in our lab.[76] Notable examples include the electrochemically tunable CNDs[59] or the white emitting CNDs.[33] These materials were rationally designed by modifying the Arg/EDA synthetic protocol, by introducing selected precursors in the reaction mixture. For tuning the electrochemistry of CNDs, the introduction of quinones, together with Arg and EDA, was key (**Figure 1.4**).[59] In the former, molecules such as benzoquinone, naphthoquinone and anthraquinone derivatives were reacted with the two basic precursors to obtain hp-N-CNDs with different redox potentials. The obtained dots showed interesting electrochemistry with modified redox potentials

when compared to the CDs prepared only from Arg/EDA. Moreover, these materials showed an interesting activity in photo-driven electron transfers. This ability was studied using such nanoparticles as photocatalysis in a model reaction, namely the photoreduction of methyl viologen.

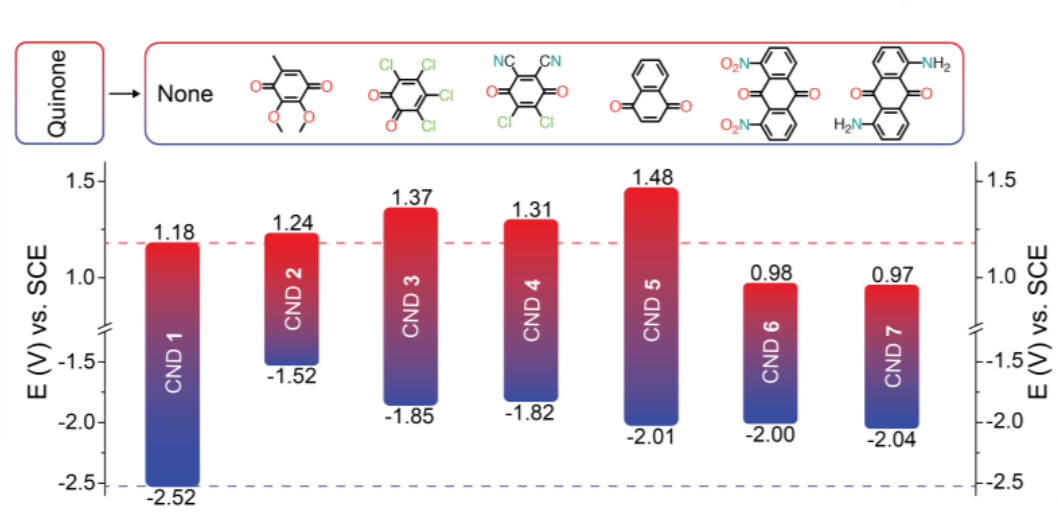

Figure 1.4 Redox potentials of quinone doped CNDs. Adapted from reference [59].

The use of the naphthalene diimide chemistry resulted interesting for the tailoring of the absorption/emission properties of CNDs (**Figure 1.5**).[33] hp-N-CNDs were obtained by adding, to the Arg/EDA reaction mixture, dibromonaphthalene dianhydride (Br_2NDA) and naphthalene dianhydride (NDA). After an accurate screening of the molar ratios of the four precursors, nanoparticles with blue, orange and white emission were successfully obtained. These results opened the possibility to tune the CNDs properties by inserting selected organic groups in the structure. This could be made by designing the nanoparticle starting from an accurate choice of the molecular precursors. These should be chosen considering their reactivity during the thermal process. Only by this way it is possible to expect the formation of a polymer like structure, bearing selected functional groups, that undergoes carbonization forming the dot (as discussed in **Section 1.2.2**). It is noteworthy to point out that that the desired functionalities should be stable the properties retained under the synthetic conditions.

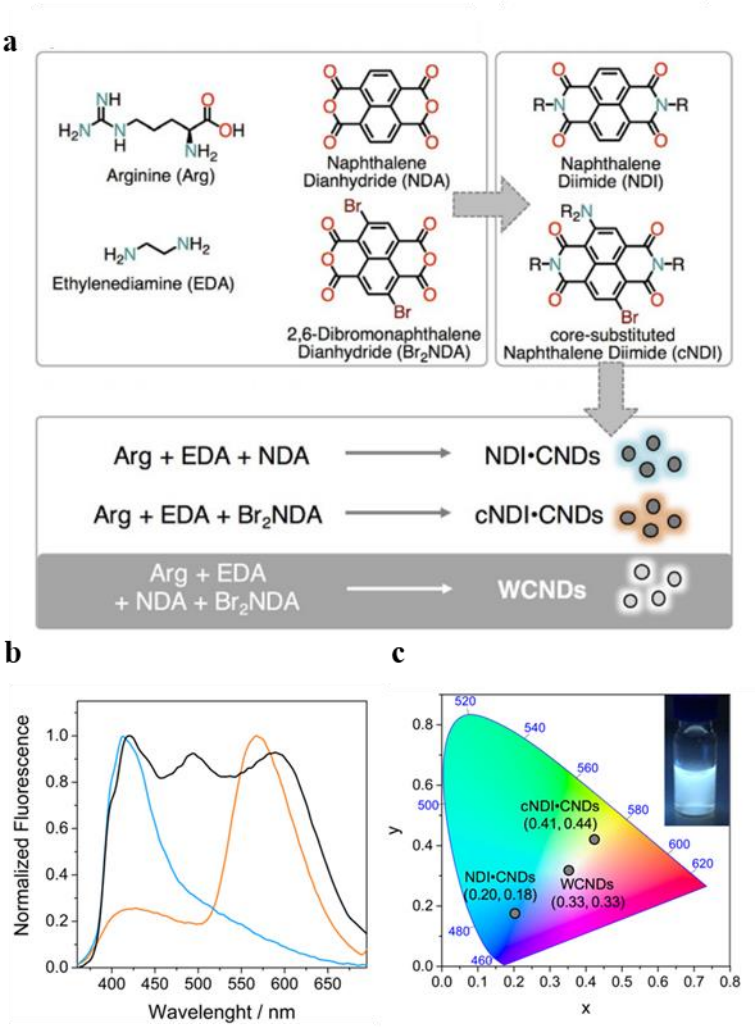

Figure 1.5 (**a**) Organic precursors and MW-assisted synthesis used to produce NDI-doped hp-N-CNDs with tunable emission (NDI·CNDs, cNDI·CNDs and WCNDs); (**b**) Normalized emission spectra of blue emissive (NDI·CNDs, blue line), orange emissive (cNDI·CNDs, orange line) and white emissive (WCNDs, black line) hp-N-CNDs; (**c**) 1931 CIE chromaticity diagram showing coordinates of the produced hp-N-CNDs, the inset shows a solution of white emissive hp-N-CNDs in water exposed to UV light (365 nm). Adapted from reference [33].

1.3.2 Doping and surface passivation

Doping and surface passivation are two common methods to modify the structure and therefore the properties of CDs. In the former case, these modifications are especially responsible for tuning the fluorescence emission and the redox properties. The increase of fluorescence quantum yield and the modification of emission range are the two most researched photophysical properties. The former

process consists on the introduction of heteroatoms, metals and non-metals, resulting generally in the modification of the chemical and electronic structure.[15–17,46] The latter approach involves the surface passivation with selected functional groups for the tailoring of the emissive properties.[46] Besides these, the modification of the redox properties is generally related to the electronic structure variation. This confers electron-donor or -acceptor behavior to the final nanoparticles, when interfaced with other materials. The main effects of these modifications affect not only the photophysical/redox properties, but also the solubility/dispersibility and reactivity of the nanoparticles.

Depending on the typology of structure, heteroatom doping can act in different ways. In GQDs and CQDs it results in the substitution of the oxygen or carbon atoms with the doping elements. This results in the modification of the aromatic conjugated core and edge sites.[82] On the other hand, doping of amorphous CNDs and CPDs consists in the introduction of new functional groups in the structure.[33,59] As seen in the previous section, the use of nitrogen containing precursors, such as EDA, is responsible for the introduction of amino moieties and nitrogen containing chromophores (NDI).[76,78] The resulting hp-N-CNDs showed new photo-physical properties (enhanced quantum yield of emission), or a tuned emission (presence of chromophores such as naphthalene diimides). In the case of quantum sized nanoparticles, Stolarczyk and coworkers reported an interesting study elucidating the structural role of nitrogen doping in CQDs,[83] with study focused on the nitrogen positioning in the structure. The particles consisted on hp-N-CQDs, obtained by a hydrothermal process from citric acid and polyethyleneimine (BPEI). The doping was varied by modifying the ratio of BPEI with respect to citric acid. The subsequent structural characterization determined that, at lower concentrations, the nitrogen doping affected especially the core. On the contrary, increasing the concentration of the polymer in the reaction mixture resulted in the modification of the aromatic edge sites of the particle. The former process modified the fluorescence emission resulting in an enhanced quantum yield, while the latter led to the improvement of the electron transfer properties.

Besides nitrogen and other non-metals, in the last years the use of metal atoms as dopants has attracted attention.[16] This interest was principally due to the

advantageous enhancing of the optical properties and catalytic activity. A very common strategy to introduce metals in the carbonaceous dot structure has been the use of metal salts or hydroxides. Such precursors can be directly reacted with organic precursors that can act as ligands for the metal sequestration in the final carbon structure. An interesting example in this context was reported by Zeng and coworkers. that successfully doped CQDs with copper (**Figure 1.6**).[56] hp-Cu(II)N-CQDs were synthetized *via* calcination of a copper EDTA complex, Na_2[Cu(EDTA)]. The structural characterization showed the presence of Cu atoms in the carbon scaffold. As compared to the bare CQDs obtained using only the organic precursor, these nanoparticles exhibited enhanced light harvesting that inspired their use as photocatalysts for the photooxidation of 1,4-dihydro-2,6-dimethylpyridine-3,5-dicarboxylate (DHP) in aqueous solution.

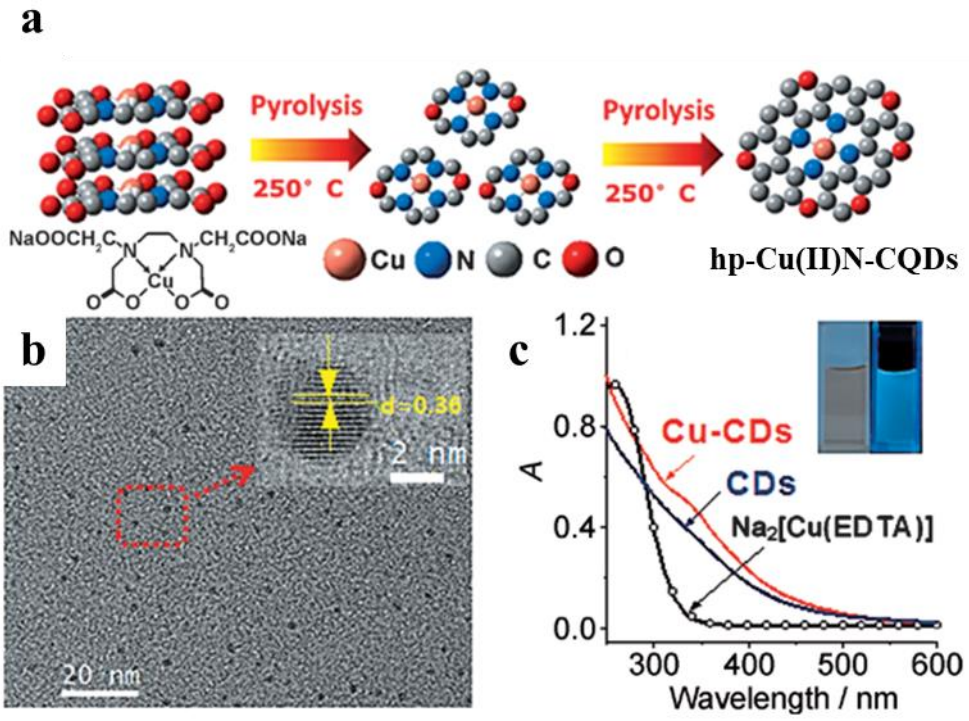

Figure 1.6 (**a**) Schematic representation of the synthetic process to obtain hp-Cu(II)N-CQDs; (**b**) TEM and HR-TEM (inset) images of hp-Cu(II)N-CQDs; (**c**) Absorption spectra of hp-Cu(II)N-CQDs, hp-CQDs and Na_2[Cu(EDTA)] precursors (inset image: photographs showing hp-Cu(II)N-CQDs in daylight, left, and under UV-light (365 nm, right). Adapted from reference [56].

Literature gives many examples of surface passivation that uses synthetic and post-synthetic routes to passivate the nanoparticle surface with selected functional groups.[46,84] For example, and as discussed above, EDA in a multi-component synthesis was reported to act mainly as passivating agent. This precursor acted not only as dopant, but also as surface passivation agent during the synthesis obtaining, multiple amine groups on the CNDs surface.[75,78] Similarly to the use of EDA, Liu and coworkers used other amines that acted both as doping and passivating agents.[85] hp-N-CNDs were obtained by MW assisted hydrothermal carbonization of citric acid in presence of EDA, diethylamine (DEA), triethylamine (TEA) or 1,4-butanediamine (BDA). The use of different amines and by varying the concentrations and reaction times resulted in different magnitudes of passivation/doping and subsequently in altered photoluminescence intensities.

The post-synthetic routes provide the surface functionalization *via* reaction with organic molecules or polymers. Chua and coworkers reported an interesting approach to modify the edge hydroxy groups of GQDs (obtained from fullerenes) for the modification of the emissive properties.[86] These functional groups were converted in trifluoroacetate groups (*via* esterification with trifluoroacetic anhydride) or were modified in hydroxamic acid/oximes groups (using hydroxylamine as reactant). The former modification resulted in a blue-shift of the GQDs fluorescence emission maximum, while the latter induced a red-shift. Another interesting work was reported by Yan and coworkers who engineered GQDs edges for the tuning of the bandgap structure for photocatalytic applications.[87] The post-synthetic process consisted on condensation reactions between the edge GQDs carbonyl groups and the amino groups of different aromatic molecules, such as *o*-phenylenediamine, 2,3-diaminonaphthalene and 1,8-diaminonaphtalene.

Besides the passivation with small molecular reagents, Sun and coworkers reported the use of polymeric passivation agents for the improvement of the CQDs photoluminescence.[64] Oligomeric polymers, such as PEG (molecular weight 1500 Da) were used to decorate the nanoparticle surface resulting in the stabilization of the surface emissive functional groups and the enhancement of the fluorescence emission.

1.3.3 Surface functionalization

The surface functionalization is a commonly used to synthetize CDs-based hybrids. Literature gives many examples reporting the covalent or non-covalent functionalization of CDs surfaces with molecules of interest.[36] By this way, nanohybrids could be designed for application in areas like sensing, bioapplications, optoelectronics, photo- and electro-catalysis or electrochemiluminescence. In all of these applications CDs are designed to interact and cooperate with these molecules for different purposes. For example, the covalent attachment of hydrophobic molecules could result in an increased solubility thanks to the hydrophilic CDs. Besides the solubility, the attachment of electro- or photo-active building blocks could result interesting because of the intramolecular interaction with the electronic and optical properties of the nanoparticle.

In our group, we performed the covalent functionalization of CDs for many purposes. Post-functionalization was mainly performed for preparation of CDs-based hybrids that could work as carriers of drugs or bioactive molecules in a biological system.[88] We reported an example of this by engineering hp-N-CNDs based hybrids for the delivery of Paclitaxel, an anticancer drug, in *in vitro* cancer models.[89] This molecule was covalently attached to hp-N-CNDs *via* a carbodiimide coupling between its carboxyl group and the surface amino groups of the nanodots. The hydrophobic drug was observed to have a better delivery in different cell lines, thanks to the hybridization with the dot that worked as vector. On the other hand, for the modification of electro- and photo-active properties, our group reported two examples of surface functionalization *via* the abovementioned covalent reaction. For example, hp-N-CNDs were hybridized with ruthenium(II)tris(2,2'-bipyridyl) ($Ru(bpy)_3^{2+}$) or tetrarylporphyrin in order to obtain nanomaterials that could find applications as electrochemiluminescent platform (**Figure 1.7**) and as light harvesters exploiting photoinduced electron transfer.[48,75,90]

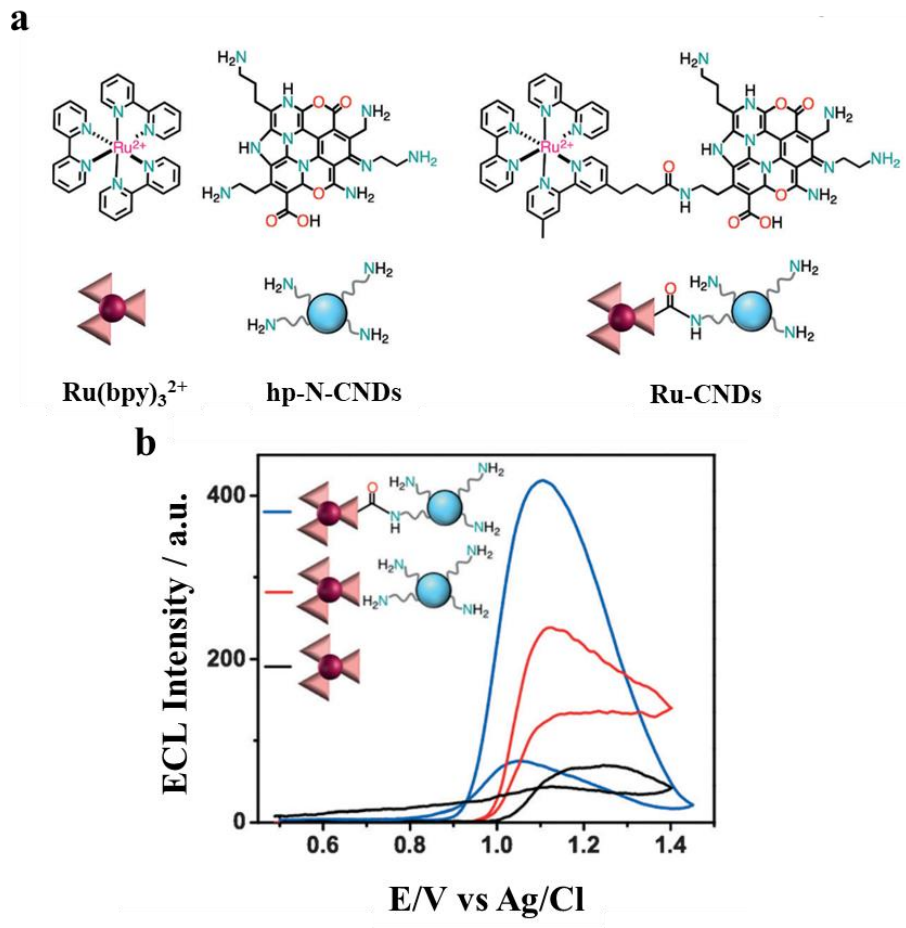

Figure 1.7 (**a**) Schematic representation and chemical structures of tris(2,2'-bipyridine)ruthenium(II) ($Ru(bpy)_3^{2+}$), hp-N-CNDs and the covalent hybrid $Ru(bpy)_3^{2+}$-hp-N-CNDs (Ru-CNDs); (**b**) ECL intensity during a potential scan of 0.1 mM PBS solution (pH 7.4) of $Ru(bpy)_3^{2+}$ (black line), upon addition of 0.1 mg mL^{-1} of hp-N-CNDs (red line) and of Ru-NCNDs (blue line) with a concentration of ruthenium complex of 0.1 mM. Scan rate 0.05 Vs^{-1}. GC electrode (d=3mm), potential referred to Ag/AgCl (KCl sat.) at room temperature, with a platinum wire as counter electrode. Adapted from reference [90].

1.4 Applications of carbon-based dots

As partially discussed in the previous sections, CDs are believed to be potentially highly competitive luminescent and semiconductors materials in many application areas. Besides their fluorescence emission, the very low toxicity and the ease of synthesis from many precursors have encouraged and inspired their uses. CDs have shown to be promising materials in many fields, ranging from biological[19] to energy related applications.[47] In particular, their use as new type of biocompatible carbon-based nanomaterial in biomedical applications has been the most studied so far (see Section **1.4.1**), but also uses in optoelectronics and energy devices are rapidly attracting attention (see Section **1.4.2**). The following sections will give a general overview of the main uses of CDs in these large applicative areas. Moreover, we will show how the concepts of CDs engineering discussed before (Section **1.3**) could result useful for the production of nanoparticles for specific uses.

1.4.1 Bioapplications

Since their discovery, CDs were explored in bioapplications owing to their low cytotoxicity at moderated concentrations (<500 μg mL^{-1}) and ease to be degraded or removed by the excretory system.[26,91–93] In addition, the fluorescence emission made apparent their use in bioimaging and biosensing.[94–99] Moreover their small size, high surface area and hydrophilicity resulted advantageous for the use as drug-delivery, cancer targeting and antibiotic systems.[89,100–104] The tunable surface chemistry of such nanoparticles could be exploited for interaction with biomolecules, for the tuning enzyme activity, cell-membrane permeability and gene expression.[37,105–110]

An example of CDs used for bioimaging is reported by Dekaliuk and coworkers.[99] In this work, hp-N-CNDs with violet and blue emission were obtained respectively from β-alanine and citric acid/urea mixture. These nanoparticles were successfully employed for imaging both living and apoptotic cells. CDs were successfully used for investigations based on both fluorescence confocal microscopy and flow cytometry.

In a representative work, Chen and coworkers reported the biodistribution, clearance and tumor uptake of CDs (**Figure 1.8**).[91] PEG passivated hp-CQDs were conjugated to a near-infrared (NIR) dye and a positron-emission tomography (PET) isotope ^{64}Cu in order to locate the nanoparticles in the body of a mouse. From this work emerged that carbon dots possess a good stability in an *in vivo* system and exhibit a fast renal clearance. In addition, the tumor targeting tests showed a homogeneous prolonged uptake of the tumor *via* three different injection routes ("i.v." intravenous, "s.c." subcutaneous and "i.m." intramuscular). These results revealed that these nanoparticles represent a good alternative to other commercialized systems for bioimaging and targeting.

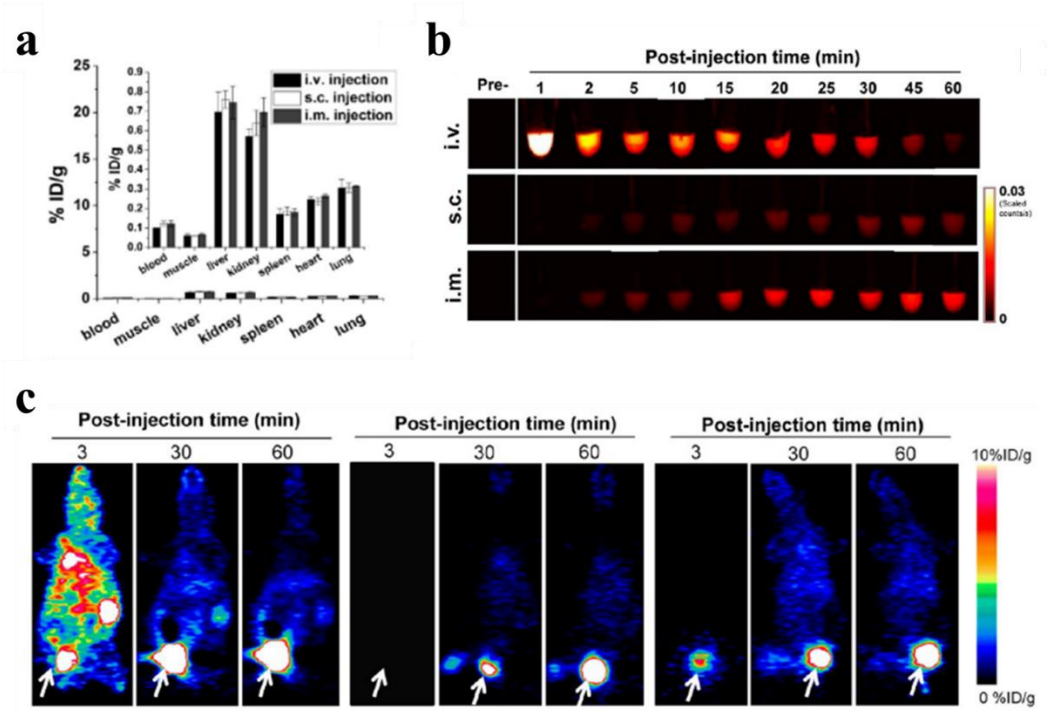

Figure 1.8 (**a**) Quantification of the biodistribution of ^{64}Cu labeled hp-CQDs via three injection routes at 24 hours after injection timepoints; (**b**) NIR detection of NIR dye labeled hp-CQDs in vein blood samples (5 µL) at indicated time points (collected into Eppendorf tubes) containing 5 µL of heparin solution; (**c**) Representative images of dynamic PET imaging of hp-CQDs labeled with ^{64}Cu and injected *via* three routes: i.v. (left); s.c. (middle); i.m. (right). Adapted from reference [91].

In the large area of theragnostic uses, besides the multiple applications of CDs as drug delivery systems, as seen for example in section **1.3.3**, the use of CDs for antibiosis has also been largely investigated. An interesting work reported by Qu and coworkers demonstrated that ,depending on the surface charge CDs could be

toxic for selected cells.[103] The study focused on *E. Coli* cultures exposed to three differently charged nanoparticles: positive, negative and uncharged. The study revealed that only uncharged dots do not induce the cell death. In the other two cases the apoptotic program is activated in the cells inducing DNA fragmentation, chromosomal condensation and loss of structural integrity.

A remarkable example of the use of CDs surface interaction with biological structures in dependence of functional groups was recently reported by Kang and coworkers.[107] In this work emerged that, besides the surface charge, the nature of the surface functional groups could affect the permeability of the cell membrane. Three typologies of hp-CQDs were used bearing respectively hydroxyl/carboxyl, amino and PEG surface moieties. Testing the cell membrane permeability of HeLa cells toward the uptake of these nanoparticles revealed that the amino covered CQDs exhibited the better uptake. These findings further support the fact that CDs surface functionalization or passivation could be crucial for the enhancement of cellular uptake.

1.4.2 Energy-related applications

Thanks to their light absorption and photoluminescence ranges, CDs have been mostly studied as catalytic centers or as photosensitizers for various applicartions. Examples of photocatalyzed reactions have been the water splitting, the H_2 evolution (HER), the CO_2 and O_2 reduction (CRR and ORR), the degradation of organic molecules and the organic syntheses.[111–119] Besides the catalytic applications, the optical properties of CDs together with their semiconductor properties and resistance to photobleaching have inspired many groups to apply these nanoparticles in photovoltaics and energy storage.[63,120–133] In addition to these applications, photoluminescent CDs represent a good ecofriendly and low-cost alternative starting materials for the production of light emitting diodes.[34,134–138] All these applications exploit the photoinduced electron transfer (PET) or attitude to charge separation in CDs. In the case of photocatalysis this process could directly catalyze the reaction. In addition, if coupled to another catalyst, this property could be used to co-catalyze or sensitize the material resulting in an enhancement of the

whole activity. In photovoltaics, the PET exhibited by CDs have been exploited for light harvesting purposes enhancing the range of absorption and transferring energy thanks to the semiconductor property. This property is also exploited in LED application. Thanks to the semiconductor behavior CDs could exhibit electrogenerated luminescence also in the solid state. This could be possible if the nanoparticles in the solid state are well separated in order to avoid self-quenching processes.

In a representative work Teng and coworkers reported the use of hp-N-GQDs as efficient photocatalysts for water splitting reaction.[111] The use of these nanoparticles was believed suitable for this application because of the p- and n-type conductive band present in the structure. In fact, thanks to the nitrogen doping these nanoparticles possessed excitation energies that could match the requisites for water splitting. According to the proposed mechanism each nanoparticle works as nanodiode in which the cathode is composed by N doped regions, with a n-type domain, while the anode consists on the O-grafted regions with a p-type domain. The former was believed responsible of the O_2 production, while the latter was recognized as the center of H^+ reduction to H_2. Besides the use as single catalytic center, CDs properties were also used to sensitize and optimize existing catalysts. Reisner and coworkers reported a notable example of this use.[69] The enhancement of the catalytic activity of a Ni based molecular catalyst *via* photosensitization with hp-CQDs was reported. In optimized condition the dots showed competitive activity under sun light irradiation respect to other metal-based photosensitizers. Moreover, the good photostability after 24 hours showed that these nanoparticles result advantageous if one considers also the low environmental impact.

A representative example of CDs use in photocatalysis for organic synthesis was reported by Kang and coworkers.[118] In this work NIR emissive hp-CQDs were successfully employed for the photo-driven conversion of benzyl alcohol into benzaldehyde. The interesting results showed conversion efficiencies of 92% and selectivity of 100%. The proposed mechanism was ascribed to the NIR induced electron transfer responsible for converting the H_2O_2 in $OH^{\bullet}$, the latter being the active oxygen species responsible for alcohol conversion in aldehyde.

Qu and coworkers reported an interesting use of CDs as dyes for the sensitization of photovoltaic cells (**Figure 1.9**).[63] In this work hp-GQDs resulted to enhance the power conversion efficiency (PCE) working as sensitizing dye in solar cells (DSSCs). n- and p-type domains in hp-GQDs were useful for enhancing the charge transfer after the light absorption. This resulted in a photoinduced electric current of 1.28%, compared to other organic photovoltaic cells functionalized with graphene. Moreover, the use of hp-GQDs revealed to be advantageous thanks to the easier introduction of the particles in the organic photoactive polymer.

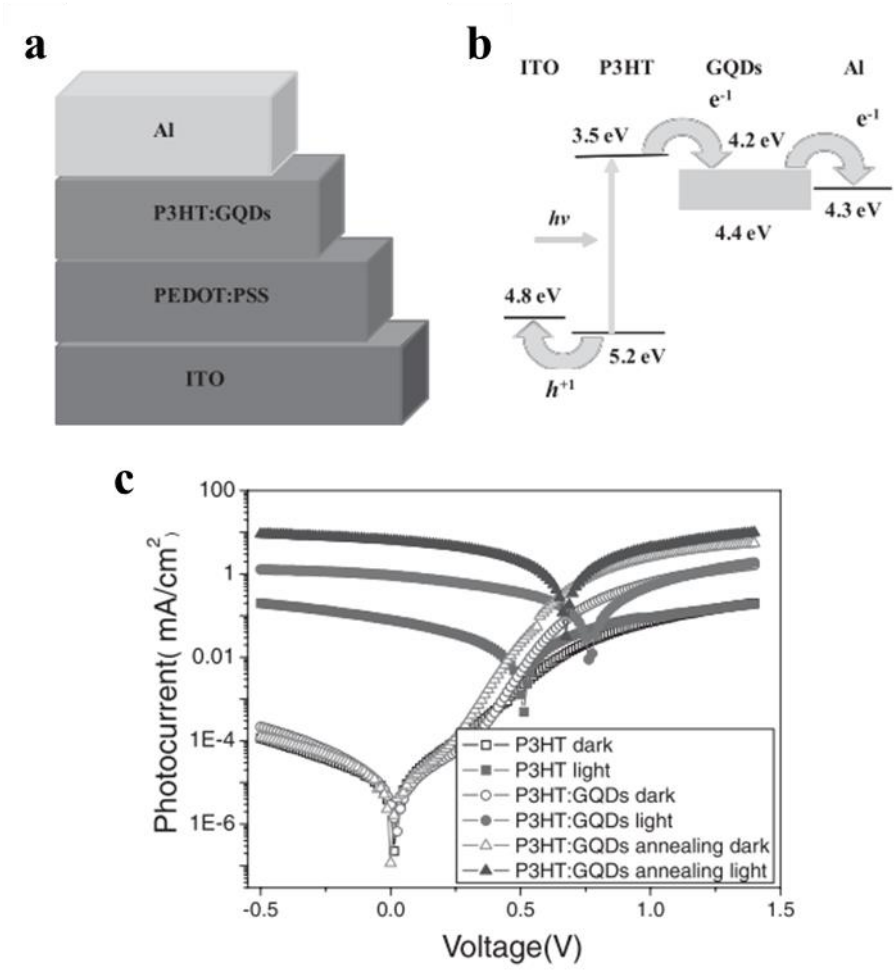

Figure 1.9 Schemes of the hp-GQDs sensitized photovoltaic cell (**a**) and the relative energy band diagrams (**b**). ITO (anode) = indium tin oxide, PEDOT:PSS = poly(3,4-ethylenedioxythiophene) polystyrene sulfonate, P3HT = poly(3-hexylthiophene), Al (cathode) = aluminum. (**c**) Current–voltage (mA cm^{-2} vs V) characteristic curves for the photovoltaic cell in presence or absence of hp-GQDs and after annealing at 140 ° C for 10 min (single log scale). In presence of hp-GQDs the photovoltaic cell produces higher photocurrents at the same experimental conditions. Adapted from reference [63].

Fan and coworkers reported a first relevant result on the use of CDs for lithium and sodium ion batteries.[139] hp-GQDs were used to coat a VO_2 electrode of a battery *via* an electrophoresis deposition, resulting on a homogeneous coverage of the material. The energy storage studies conducted on this system revealed that GQDs served not only as covering/protecting agent of VO_2 but resulted to enhance also the ion storage. The former action was useful to avoid the corrosion and agglomeration of the electrode, while the latter was possible thanks to the accumulation of ions in the interstitial π-layers of the nanoparticles. Finally, the obtained materials showed excellent high capacity retentions for lithium (98%) and sodium (88%) batteries that were retained for at least 1500 cycles.

Finally a representative and interesting example about CDs employment in LEDs application was reported by Chen and coworkers.[134] In this work hp-CQDs of blue, orange and white fluorescence emission were dispersed in a silicone matrix and applied after a thermal treatment on a InGaN LED chip to obtain a luminescent phosphor based device. The produced LEDs showed an emissive component at 370 nm from the inorganic chip and a visible component from 450 to 770 nm ascribable to the CDs embed in the solid matrix.

1.5 References

(1) Xu, X.; Ray, R.; Gu, Y.; Ploehn, H. J.; Gearheart, L.; Raker, K.; Scrivens, W. A. Electrophoretic Analysis and Purification of Fluorescent Single-Walled Carbon Nanotube Fragments. *J. Am. Chem. Soc.* **2004**, *126* (40), 12736–12737.

(2) Yan, F.; Sun, Z.; Zhang, H.; Sun, X.; Jiang, Y.; Bai, Z. The Fluorescence Mechanism of Carbon Dots, and Methods for Tuning Their Emission Color: A Review. *Microchim. Acta* **2019**, *186* (8).

(3) Cayuela, A.; Soriano, M. L.; Carrillo-Carrión, C.; Valcárcel, M. Semiconductor and Carbon-Based Fluorescent Nanodots: The Need for Consistency. *Chem. Commun.* **2016**, *52* (7), 1311–1326.

(4) Hutton, G. A. M. M.; Martindale, B. C. M. M.; Reisner, E. Carbon Dots as Photosensitisers for Solar-Driven Catalysis. *Chem. Soc. Rev.* **2017**, *46* (20), 6111–6123.

(5) de Medeiros, T. V.; Manioudakis, J.; Noun, F.; Macairan, J.-R.; Victoria, F.; Naccache, R. Microwave-Assisted Synthesis of Carbon Dots and Their Applications. *J. Mater. Chem. C* **2019**, *7*, 7175–7195.

(6) Xia, C.; Zhu, S.; Feng, T.; Yang, M.; Yang, B. Evolution and Synthesis of Carbon Dots : From Carbon Dots to Carbonized Polymer Dots. *Adv. Sci.* **2019**, *1901316*.

(7) Zhu, S.; Meng, Q.; Wang, L.; Zhang, J.; Song, Y.; Jin, H.; Zhang, K.; Sun, H.; Wang, H.; Yang, B. Highly Photoluminescent Carbon Dots for Multicolor Patterning , Sensors , and Bioimaging. *Angew. Chem. Int. Ed.* **2013**, *52*, 3953–3957.

(8) Liu, J. J.; Li, D.; Zhang, K.; Yang, M.; Sun, H.; Yang, B. One-Step Hydrothermal Synthesis of Nitrogen-Doped Conjugated Carbonized Polymer Dots with 31% Efficient Red Emission for In Vivo Imaging. *Small* **2018**, *14* (15), 1–10.

(9) Xia, C.; Tao, S.; Zhu, S.; Song, Y.; Feng, T.; Zeng, Q.; Liu, J.; Yang, B. Hydrothermal Addition Polymerization for Ultrahigh-Yield Carbonized Polymer Dots with Room Temperature Phosphorescence via Nanocomposite. *Chem.: Eur. J.* **2018**, *24* (44), 11303–11308.

(10) Song, Y.; Zhu, S.; Zhang, S.; Fu, Y.; Wang, L.; Zhao, X.; Yang, B. Investigation from Chemical Structure to Photoluminescent Mechanism: A Type of Carbon Dots from the Pyrolysis of Citric Acid and an Amine. *J. Mater. Chem. C* **2015**, *3* (23), 5976–5984.

(11) Tao, S.; Lu, S.; Geng, Y.; Zhu, S.; Redfern, S. A. T.; Song, Y.; Feng, T.; Xu, W.; Yang, B.; Materials, T. P.; et al. Design of Metal-Free Polymer Carbon Dots: A New Class of Room-Temperature Phosphorescent Materials. *Angew. Chem. Int. Ed.* **2018**, *57* (9), 2393–2398.

(12) Zhu, S.; Wang, L.; Zhou, N.; Zhao, X.; Song, Y.; Maharjan, S.; Zhang, J.; Lu, L.; Wang, H.; Yang, B. The Crosslink Enhanced Emission (CEE) in Non-Conjugated Polymer Dots: From the Photoluminescence Mechanism to the Cellular Uptake Mechanism and Internalization. *Chem. Commun.* **2014**, *50* (89), 13845–13848.

(13) Zhu, S.; Zhang, J.; Wang, L.; Song, Y.; Zhang, G.; Wang, H.; Yang, B. A General Route to Make Non-Conjugated Linear Polymers Luminescent. *Chem. Commun.* **2012**, *48*, 10889–10891.

(14) Lu, S.; Sui, L.; Liu, J.; Zhu, S.; Chen, A.; Jin, M.; Yang, B. Near-Infrared Photoluminescent Polymer–Carbon Nanodots with Two-Photon Fluorescence. *Adv. Mater.* **2017**, *29* (15), 1–6.

(15) Kandasamy, G. Recent Advancements in Doped/Co-Doped Carbon Quantum Dots for Multi-Potential Applications. *C* **2019**, *5* (2), 24.

(16) Lin, L.; Luo, Y.; Tsai, P.; Wang, J.; Chen, X. Metal Ions Doped Carbon Quantum Dots: Synthesis, Physicochemical Properties, and Their Applications. *Trends Anal. Chem.* **2018**, *103*, 87–101.

(17) Li, F.; Yang, D.; Xu, H. Non-Metal-Heteroatom-Doped Carbon Dots: Synthesis and Properties. *Chem.: Eur. J.* **2019**, *25* (5), 1165–1176.

(18) Bourlinos, A. B.; Stassinopoulos, A.; Anglos, D.; Zboril, R.; Georgakilas, V.; Giannelis, E. P. Photoluminescent Carbogenic Dots. *Chem. Mater.* **2008**, *20* (14), 4539–4541.

(19) Jaleel, J. A.; Pramod, K. Artful and Multifaceted Applications of Carbon Dot in Biomedicine. *J. Control. Release* **2018**, *269* (November 2017), 302–321.

(20) Mitra, S.; Chandra, S.; Kundu, T.; Banerjee, R.; Pramanik, P.; Goswami, A. Rapid Microwave Synthesis of Fluorescent Hydrophobic Carbon Dots. *RSC Adv.* **2012**, *2* (32), 12129.

(21) Yan, L.; Yang, Y.; Ma, C. Q.; Liu, X.; Wang, H.; Xu, B. Synthesis of Carbon Quantum Dots by Chemical Vapor Deposition Approach for Use in Polymer Solar Cell as the Electrode Buffer Layer. *Carbon* **2016**, *109*, 598–607.

(22) Yang, H.; Liu, Y.; Guo, Z.; Lei, B.; Zhuang, J.; Zhang, X.; Liu, Z.; Hu, C. Hydrophobic Carbon Dots with Blue Dispersed Emission and Red Aggregation-Induced Emission. *Nat. Commun.* **2019**, *10* (1), 1789.

(23) Prikhozhdenko, E. S.; Bratashov, D. N.; Mitrofanova, A. N.; Sapelkin, A. V.; Yashchenok, A. M.; Sukhorukov, G. B.; Goryacheva, I. Y. Solvothermal Synthesis of Hydrophobic Carbon Dots in Reversed Micelles. *J. Nanoparticle Res.* **2018**, *20*, 234–254.

(24) Yan, F.; Jiang, Y.; Sun, X.; Bai, Z.; Zhang, Y.; Zhou, X. Surface Modification and Chemical Functionalization of Carbon Dots: A Review. *Microchimica Acta*. Microchimica Acta 2018.

(25) Huang, X.; Zhang, F.; Zhu, L.; Choi, K. Y.; Guo, N.; Guo, J.; Tackett, K.; Anilkumar, P.; Liu, G.; Quan, Q.; et al. Effect of Injection Routes on the Tumor Uptake of Carbon Dots. *ACS Nano* **2013**, No. 7, 5684–5693.

(26) Nurunnabi, M.; Khatun, Z.; Huh, K. M.; Park, S. Y.; Lee, D. Y.; Cho, K. J.; Lee, Y. K. In Vivo Biodistribution and Toxicology of Carboxylated Graphene Quantum Dots. *ACS Nano* **2013**, *7* (8), 6858–6867.

(27) Ding, C.; Zhu, A.; Tian, Y. Functional Surface Engineering of C-Dots for Fluorescent Biosensing and in Vivo Bioimaging. *Acc. Chem. Res.* **2014**, *47* (1), 20–30.

(28) Yang, S.-T.; Cao, L.; Luo, P. G.; Lu, F.; Wang, X.; Wang, H.; Meziani, M. J.; Liu, Y.; Qi, G.; Sun, Y.-P. Carbon Dots for Optical Imaging in Vivo. *J. Am. Chem. Soc.* **2009**, *131* (32), 11308–11309.

(29) Luo, P. G.; Yang, F.; Yang, S.-T.; Sonkar, S. K.; Yang, L.; Broglie, J. J.; Liu, Y.; Sun, Y.-P. Carbon-Based Quantum Dots for Fluorescence Imaging of Cells and Tissues. *RSC Adv.* **2014**, *4* (21), 10791.

(30) Du, J.; Xu, N.; Fan, J.; Sun, W.; Peng, X. Carbon Dots for In Vivo Bioimaging and Theranostics. *Small* **2019**, *15*, 1805087.

(31) Roy, P.; Periasamy, A. P.; Lin, C.-Y.; Her, G.-M.; Chiu, W.-J.; Li, C.-L.; Shu, C.-L.; Huang, C.-C.; Liang, C.-T.; Changa, H.-T. Photoluminescent Graphene Quantum Dots for in Vivo Imaging of Apoptotic Cells. *Nanoscale* **2015**, *7*, 2504–2510.

(32) Wang, K.; Gao, Z.; Gao, G.; Wo, Y.; Wang, Y.; Shen, G.; Cui, D. Systematic Safety Evaluation on Photoluminescent Carbon Dots. *Nanoscale Res. Lett.* **2013**, *8* (1), 1–9.

(33) Arcudi, F.; Đorđević, L.; Prato, M.; Arcudi, F.; Dordevic, L. Rationally Designed Carbon NanoDots En Route to Pure White-Light Emission. *Angew. Chem. Int. Ed.* **2017**, *56* (15), 4170–4173.

(34) Miao, X.; Qu, D.; Yang, D.; Nie, B.; Zhao, Y.; Fan, H.; Sun, Z. Synthesis of Carbon Dots with Multiple Color Emission by Controlled Graphitization and Surface Functionalization. *Adv. Mater.* **2018**, *30* (1), 1704740.

(35) Tepliakov, N. V.; Kundelev, E. V.; Khavlyuk, P. D.; Xiong, Y.; Leonov, M. Y.; Zhu, W.; Baranov, A. V.; Fedorov, A. V.; Rogach, A. L.; Rukhlenko, I. D. Sp2–Sp3-Hybridized Atomic Domains Determine Optical Features of Carbon Dots. *ACS Nano* **2019**, acsnano.9b05444.

(36) Park, Y.; Yoo, J.; Lim, B.; Kwon, W.; Rhee, S.-W. Improving the Functionality of Carbon Nanodots: Doping and Surface Functionalization. *J. Mater. Chem. A* **2016**, *4*, 11582–11603.

(37) Hutton, G. A. M.; Reuillard, B.; Martindale, B. C. M. M.; Caputo, C. A.; Lockwood, C. W. J. J.; Butt, J. N.; Reisner, E. Carbon Dots as Versatile Photosensitizers for Solar-Driven Catalysis with Redox Enzymes. *J. Am. Chem. Soc.* **2016**, *138* (51), 16722–16730.

(38) Liu, M. L.; Chen, B. Bin; Li, C. M.; Huang, C. Z. Carbon Dots: Synthesis, Formation Mechanism, Fluorescence Origin and Sensing Applications. *Green Chem.* **2019**, *21* (3), 449–471.

(39) Wang, X.; Feng, Y.; Dong, P.; Huang, J. A Mini Review on Carbon Quantum Dots: Preparation, Properties, and Electrocatalytic Application. *Front. Chem.* **2019**, *7* (October), 1–9.

(40) Zhang, F.; Liu, F.; Wang, C.; Xin, X.; Liu, J.; Guo, S.; Zhang, J. Effect of Lateral Size of Graphene Quantum Dots on Their Properties and Application. *ACS Appl. Mater. Interfaces* **2016**, *8* (3), 2104–2110.

(41) Molaei, M. J. A Review on Nanostructured Carbon Quantum Dots and Their Applications in Biotechnology, Sensors, and Chemiluminescence. *Talanta* **2019**, *196*, 456–478.

(42) Strauss, V.; Margraf, J. T.; Dolle, C.; Butz, B.; Nacken, T. J.; Walter, J.; Bauer, W.; Peukert, W.; Spiecker, E.; Clark, T.; et al. Carbon Nanodots: Toward a Comprehensive Understanding of Their Photoluminescence. *J. Am. Chem. Soc.* **2014**, *136* (49), 17308–17316.

(43) Sciortino, A.; Cannizzo, A.; Messina, F. Carbon Nanodots: A Review—From the Current Understanding of the Fundamental Photophysics to the Full Control of the Optical Response. *C* **2018**, *4* (4), 67.

(44) Ding, H.; Yu, S. B.; Wei, J. S.; Xiong, H. M. Full-Color Light-Emitting Carbon Dots with a Surface-State -Controlled Luminescence Mechanism. *ACS Nano* **2016**, *10* (1), 484–491.

(45) Hola, K.; Bourlinos, A. B.; Kozak, O.; Berka, K.; Siskova, K. M.; Havrdova, M.; Tucek, J.; Safarova, K.; Otyepka, M.; Giannelis, E. P.; et al. Photoluminescence Effects of Graphitic Core Size and Surface Functional Groups in Carbon Dots: COO- Induced Red-Shift Emission. *Carbon* **2014**, *70*, 279–286.

(46) Li, L.; Dong, T. Photoluminescence Tuning in Carbon Dots: Surface Passivation or/and Functionalization, Heteroatom Doping. *J. Mater. Chem. C* **2018**, *6* (30), 7944–7970.

(47) Hu, C.; Li, M.; Qiu, J.; Sun, Y. P. Design and Fabrication of Carbon Dots for Energy Conversion and Storage. *Chem. Soc. Rev.* **2019**, *48* (8), 2315–2337.

(48) Prato, M.; Arcudi, F.; Strauss, V.; Cadranel, A.; Guldi, D. M.; Dordevic, L.; Dordević, L.; Cadranel, A.; Guldi, D. M.; Prato, M.; et al. Porphyrin Antennas on Carbon Nanodots: Excited State Energy and Electron Transduction. *Angew. Chem. Int. Ed.* **2017**, *56* (40), 12097–12101.

(49) Han, M.; Zhu, S.; Lu, S.; Song, Y.; Feng, T.; Tao, S.; Liu, J.; Yang, B. Recent Progress on the Photocatalysis of Carbon Dots: Classification, Mechanism and Applications. *Nano Today*. Elsevier Ltd 2018, pp 201–218.

(50) Yu, H.; Shi, R.; Zhao, Y.; Waterhouse, G. I. N.; Wu, L. Z.; Tung, C. H.; Zhang, T. Smart Utilization of Carbon Dots in Semiconductor Photocatalysis. *Adv. Mater.* **2016**, *28* (43), 9454–9477.

(51) Cadranel, A.; Margraf, J. T.; Strauss, V.; Clark, T.; Guldi, D. M. Carbon Nanodots for Charge-Transfer Processes. *Acc. Chem. Res.* **2019**, *52* (4), 955–963.

(52) Wibmer, L.; Lourenço, L. M. O.; Roth, A.; Katsukis, G.; Neves, M. G. P. M. S.; Cavaleiro, J. A. S.; Tomé, J. P. C.; Torres, T.; Guldi, D. M. Decorating Graphene Nanosheets with Electron Accepting Pyridyl-Phthalocyanines. *Nanoscale* **2015**, *7* (13), 5674–5682.

(53) Liua, S.; Zhaoa, N.; Cheng, Z.; Liu, H. Amino-Functionalized Green Fluorescent Carbon Dots as Surface Energy Transfer Biosensors for Hyaluronidase. *Nanoscale* **2008**, *26* (5).

(54) Chu, K.; Lee, S. L.; Chang, C.; Liu, L. Recent Progress of Carbon Dot Precursors and Photocatalysis Applications. *Polymers (Basel).* **2019**, *11*, 689.

(55) Long, R.; Casanova, D.; Fang, W. H.; Prezhdo, O. V. Donor-Acceptor Interaction Determines the Mechanism of Photoinduced Electron Injection from Graphene Quantum Dots into TiO2: π-Stacking Supersedes Covalent Bonding. *J. Am. Chem. Soc.* **2017**, *139* (7), 2619–2629.

(56) Wu, W.; Zhan, L.; Fan, W.; Song, J.; Li, X.; Li, Z.; Wang, R.; Zhang, J.; Zheng, J.; Wu, M.; et al. Cu-N Dopants Boost Electron Transfer and Photooxidation Reactions of Carbon Dots. *Angew. Chem. Int. Ed.* **2015**, *54* (22), 6540–6544.

(57) Bera, K.; Sau, A.; Mondal, P.; Mukherjee, R.; Mookherjee, D.; Metya, A.; Kundu, A. K.; Mandal, D.; Satpati, B.; Chakrabarti, O.; et al. Metamorphosis of Ruthenium-Doped Carbon Dots: In Search of the Origin of Photoluminescence and Beyond. *Chem. Mater.* **2016**, *28* (20), 7404–7413.

(58) Zhang, R.; Adsetts, J. R.; Nie, Y.; Sun, X.; Ding, Z. Electrochemiluminescence of Nitrogen- and Sulfur-Doped Graphene Quantum Dots. *Carbon* **2018**, *129*, 45–53.

(59) Rigodanza, F.; Dordević, L.; Arcudi, F.; Prato, M.; Francesco, R.; Luka, Đ.; Francesca, A.;

Maurizio, P.; Rigodanza, F.; Đorđević, L.; et al. Customizing the Electrochemical Properties of Carbon Nanodots with Quinones in Bottom-Up Syntheses. *Angew. Chem. Int. Ed.* **2018**, *57* (18), 5062–5067.

(60) Yao, B.; Huang, H.; Liu, Y.; Kang, Z. Carbon Dots: A Small Conundrum. *Trends Chem.* **2019**, *1* (2), 235–246.

(61) Suslick, K. S. Sonochemistry. *Science* **1990**, *247* (4949), 1439–1445.

(62) Zhou, J.; Booker, C.; Li, R.; Zhou, X.; Sham, T. K.; Sun, X.; Ding, Z. An Electrochemical Avenue to Blue Luminescent Nanocrystals from Multiwalled Carbon Nanotubes (MWCNTs). *J. Am. Chem. Soc.* **2007**, *129* (4), 744–745.

(63) Li, Y.; Hu, Y.; Zhao, Y.; Shi, G.; Deng, L.; Hou, Y.; Qu, L.; Zhou, J.; Booker, C.; Li, R.; et al. An Electrochemical Avenue to Green-Luminescent Graphene Quantum Dots as Potential Electron-Acceptors for Photovoltaics. *Adv. Mater.* **2011**, *23* (6), 776–780.

(64) Sun, Y.; Zhou, B.; Lin, Y.; Wang, W.; Fernando, K. A. S.; Pathak, P.; Meziani, M. J.; Harruff, B. A.; Wang, X.; Wang, H.; et al. Quantum-Sized Carbon Dots for Bright and Colorful Photoluminescence. *J. Am. Chem. Soc.* **2006**, *128*, 7756–7757.

(65) Cao, L.; Wang, X.; Meziani, M. J.; Lu, F.; Wang, H.; Luo, P. G.; Harruff, B. a; Veca, L. M.; Murray, D.; Xie, S.; et al. Carbon Dots for Multiphoton Bioimaging. *J. Am. Chem. Soc.* **2007**, *129*, 11318–11319.

(66) Zhuo, S.; Shao, M.; Lee, S. T.; Tan, D.; Zhou, S.; Qiu, J. Upconversion and Downconversion Fluorescent Graphene Quantum Dots: Ultrasonic Preparation and Photocatalysis. *ACS Nano* **2012**, *6* (2), 1059–1064.

(67) Song, Z.; Quan, F.; Xu, Y.; Liu, M.; Cui, L.; Liu, J. Multifunctional N,S Co-Doped Carbon Quantum Dots with PH- and Thermo-Dependent Switchable Fluorescent Properties and Highly Selective Detection of Glutathione. *Carbon* **2016**, *104*, 169–178.

(68) Xu, Y.; Jia, X. H.; Yin, X. B.; He, X. W.; Zhang, Y. K. Carbon Quantum Dot Stabilized Gadolinium Nanoprobe Prepared via a One-Pot Hydrothermal Approach for Magnetic Resonance and Fluorescence Dual-Modality Bioimaging. *Anal. Chem.* **2014**, *86* (24), 12122–12129.

(69) Martindale, B. C. M.; Hutton, G. A. M.; Caputo, C. A.; Reisner, E. Solar Hydrogen Production Using Carbon Quantum Dots and a Molecular Nickel Catalyst. *J. Am. Chem. Soc.* **2015**, *137* (18), 6018–6025.

(70) Martindale, B. C. M. M.; Hutton, G. A. M. M.; Caputo, C. A.; Prantl, S.; Godin, R.; Durrant, J. R.; Reisner, E. Enhancing Light Absorption and Charge Transfer Efficiency in Carbon Dots through Graphitization and Core Nitrogen Doping. *Angew. Chem. Int. Ed.* **2017**, *56* (23), 6459–6463.

(71) Chen, B.; Li, F.; Weng, W.; Guo, H.; Zhang, X.; Chen, Y.; Huang, T.; Hong, X.; You, S.; Lin, Y.; et al. Large Scale Synthesis of Photoluminescent Carbon Nanodots and Their Application for Bioimaging. *Nanoscale* **2013**, *5* (5), 1967–1971.

(72) Hu, S.; Trinchi, A.; Atkin, P.; Cole, I. Tunable Photoluminescence across the Entire Visible Spectrum from Carbon Dots Excited by White Light. *Angew. Chem. Int. Ed.* **2015**, *54* (10), 2970–2974.

(73) Dong, Y.; Pang, H.; Yang, H. Bin; Guo, C.; Shao, J.; Chi, Y.; Li, C. M.; Yu, T. Carbon-Based Dots Co-Doped with Nitrogen and Sulfur for High Quantum Yield and Excitation-Independent Emission. *Angew. Chem. Int. Ed.* **2013**, *52* (30), 7800–7804.

(74) Qian, Z.; Ma, J.; Shan, X.; Feng, H.; Shao, L. Highly Luminescent N-Doped Carbon Quantum Dots as an Effective Multifunctional Fluorescence Sensing Platform. *Chem.: Eur. J.* **2014**, *20*, 2254–2263.

(75) Đorđević, L.; Arcudi, F.; Prato, M. Preparation, Functionalization and Characterization of Engineered Carbon Nanodots. *Nat. Protoc.* **2019**, *14* (10), In press.

(76) Arcudi, F.; Đorđević, L.; Prato, M. Design, Synthesis, and Functionalization Strategies of Tailored Carbon Nanodots. *Acc. Chem. Res.* **2019**, *52* (8), 2070–2079.

(77) Wang, X.; Qu, K.; Xu, B.; Ren, J.; Qu, X. Microwave Assisted One-Step Green Synthesis of Cell-Permeable Multicolor Photoluminescent Carbon Dots without Surface Passivation Reagents. *J.*

Mater. Chem. **2011**, *21* (8), 2445–2450.

(78) Arcudi, F.; Dordevic, L.; Prato, M.; Arcudi, F.; Dordevic, L.; Arcudi, F. Synthesis, Separation, and Characterization of Small and Highly Fluorescent Nitrogen-Doped Carbon Nanodots. *Angew. Chem. Int. Ed.* **2016**, *55* (6), 2107–2112.

(79) Yan, Y.; Gong, J.; Chen, J.; Zeng, Z.; Huang, W.; Pu, K.; Liu, J.; Chen, P. Recent Advances on Graphene Quantum Dots: From Chemistry and Physics to Applications. *Adv. Mater.* **2019**, *31* (21), 1–22.

(80) Molaei, M. J. Carbon Quantum Dots and Their Biomedical and Therapeutic Applications: A Review. *RSC Adv.* **2019**, *9* (12), 6460–6481.

(81) Kasouni, A.; Chatzimitakos, T.; Stalikas, C. Bioimaging Applications of Carbon Nanodots: A Review. *C* **2019**, *5* (2), 19.

(82) Messina, F.; Sciortino, L.; Popescu, R.; Venezia, A. M.; Sciortino, A.; Buscarino, G.; Agnello, S.; Schneider, R.; Gerthsen, D.; Cannas, M.; et al. Fluorescent Nitrogen-Rich Carbon Nanodots with an Unexpected β-C 3 N 4 Nanocrystalline Structure. *J. Mater. Chem. C* **2016**, *4* (13), 2598–2605.

(83) Bhattacharyya, S.; Ehrat, F.; Urban, P.; Teves, R.; Wyrwich, R.; Döblinger, M.; Feldmann, J.; Urban, A. S.; Stolarczyk, J. K. Effect of Nitrogen Atom Positioning on the Trade-off between Emissive and Photocatalytic Properties of Carbon Dots. *Nat. Commun.* **2017**, *8* (1), 1401.

(84) Liu, W.; Li, C.; Ren, Y.; Sun, X.; Pan, W.; Li, Y.; Wang, J.; Wang, W. Carbon Dots: Surface Engineering and Applications. *J. Mater. Chem. B* **2016**, *4* (35), 5772–5788.

(85) Zhai, X.; Zhang, P.; Liu, C.; Bai, T.; Li, W.; Dai, L.; Liu, W. Highly Luminescent Carbon Nanodots by Microwave-Assisted Pyrolysis. *Chem. Commun.* **2012**, *48* (64), 7955–7957.

(86) Chua, C. K.; Sofer, Z.; Šimek, P.; Jankovský, O.; Klímová, K.; Bakardjieva, S.; Hrdličková Kučková, Š.; Pumera, M. Synthesis of Strongly Fluorescent Graphene Quantum Dots by Cage-Opening Buckminsterfullerene. *ACS Nano* **2015**, *9* (3), 2548–2555.

(87) Yan, Y.; Chen, J.; Li, N.; Tian, J.; Li, K.; Jiang, J.; Liu, J.; Tian, Q.; Chen, P. Systematic Bandgap Engineering of Graphene Quantum Dots and Applications for Photocatalytic Water Splitting and CO2 Reduction. *ACS Nano* **2018**, *12* (4), 3523–3532.

(88) Yi, C.; Pan, Y.; Fang, Y. Surface Engineering of Carbon Nanodots (C-Dots) for Biomedical Applications. In *Novel Nanomaterials for Biomedical, Environmental and Energy Applications*; Elsevier Inc., 2019; pp 137–188.

(89) Gomez, I. J.; ARNAIZ, B.; Cacioppo, M.; Arcudi, F.; Prato, M. Nitrogen-Doped Carbon Nanodots for Bioimaging and Delivery of Paclitaxel. *J. Mater. Chem. B* **2018**, *6* (35), 5540–5548.

(90) Carrara, S.; Arcudi, F.; Prato, M.; Cola, L. De; De Cola, L. Amine-Rich Nitrogen-Doped Carbon NanoDots as Platform for Self-Enhancing Electrochemiluminescence. *Angew. Chem. Int. Ed.* **2017**, 4757–4761.

(91) Huang, X.; Zhang, F.; Zhu, L.; Choi, K. Y.; Guo, N.; Guo, J.; Tackett, K.; Anilkumar, P.; Liu, G.; Quan, Q.; et al. Effect of Injection Routes on the Biodistribution, Clearance, and Tumor Uptake of Carbon Dots. *ACS Nano* **2013**, *7* (7), 5684–5693.

(92) Havrdova, M.; Hola, K.; Skopalik, J.; Tomankova, K.; Petr, M.; Cepe, K.; Polakova, K.; Tucek, J.; Bourlinos, A. B.; Zboril, R. Toxicity of Carbon Dots-Effect of Surface Functionalization on the Cell Viability, Reactive Oxygen Species Generation and Cell Cycle. *Carbon* **2016**, *99*, 238–248.

(93) Parvin, N.; Mandal, T. K. Synthesis of a Highly Fluorescence Nitrogen-Doped Carbon Quantum Dots Bioimaging Probe and Its in Vivo Clearance and Printing Applications. *RSC Adv.* **2016**, *6* (22), 18134–18140.

(94) Lan, M.; Zhao, S.; Zhang, Z.; Yan, L.; Guo, L.; Niu, G.; Zhang, J.; Zhao, J.; Zhang, H.; Wang, P.; et al. Two-Photon-Excited near-Infrared Emissive Carbon Dots as Multifunctional Agents for Fluorescence Imaging and Photothermal Therapy. *Nano Res.* **2017**, *10* (9), 3113–3123.

(95) Zhu, A.; Qu, Q.; Shao, X.; Kong, B.; Tian, Y. Carbon-Dot-Based Dual-Emission Nanohybrid Produces a Ratiometric Fluorescent Sensor for in Vivo Imaging of Cellular Copper Ions. *Angew. Chem. Int. Ed.* **2012**, *51* (29), 7185–7189.

(96) Zhu, X.; Zhao, T.; Nie, Z.; Miao, Z.; Liu, Y.; Yao, S. Nitrogen-Doped Carbon Nanoparticle Modulated Turn-on Fluorescent Probes for Histidine Detection and Its Imaging in Living Cells. *Nanoscale* **2016**, *8* (4), 2205–2211.

(97) Campuzano, S.; Paloma, Y.; Pingarron, M. Carbon Dots and Graphene Quantum Dots in Electrochemical Biosensing. *Nanomaterials* **2019**, *9*, 634.

(98) Boakye-Yiadom, K. O.; Kesse, S.; Opoku-Damoah, Y.; Filli, M. S.; Aquib, M.; Joelle, M. M. B.; Farooq, M. A.; Mavlyanova, R.; Raza, F.; Bavi, R.; et al. Carbon Dots: Applications in Bioimaging and Theranostics. *Int. J. Pharm.* **2019**, *564*, 308–317.

(99) Dekaliuk, M.; Pyrshev, K.; Demchenko, A. Visualization and Detection of Live and Apoptotic Cells with Fluorescent Carbon Nanoparticles. *J. Nanobiotechnology* **2015**, *13* (1), 1–8.

(100) Jung, Y. K.; Shin, E.; Kim, B.-S. Cell Nucleus-Targeting Zwitterionic Carbon Dots. *Sci. Rep.* **2015**, *5*, 18807.

(101) Zheng, M.; Liu, S.; Li, J.; Qu, D.; Zhao, H.; Guan, X.; Hu, X.; Xie, Z.; Jing, X.; Sun, Z. Integrating Oxaliplatin with Highly Luminescent Carbon Dots: An Unprecedented Theranostic Agent for Personalized Medicine. *Adv. Mater.* **2014**, *26* (21), 3554–3560.

(102) Li, J.; Yang, S.; Deng, Y.; Chai, P.; Yang, Y.; He, X.; Xie, X.; Kang, Z.; Ding, G.; Zhou, H.; et al. Emancipating Target-Functionalized Carbon Dots from Autophagy Vesicles for a Novel Visualized Tumor Therapy. *Adv. Funct. Mater.* **2018**, *28* (30), 1–9.

(103) Bing, W.; Sun, H.; Yan, Z.; Ren, J.; Qu, X. Programmed Bacteria Death Induced by Carbon Dots with Different Surface Charge. *Small* **2016**, *12* (34), 4713–4718.

(104) Mishra, V.; Patil, A.; Thakur, S.; Kesharwani, P. Carbon Dots: Emerging Theranostic Nanoarchitectures. *Drug Discovery Today*. Elsevier Ltd 2018, pp 1219–1232.

(105) Zhang, M.; Wang, H.; Wang, B.; Ma, Y.; Huang, H.; Liu, Y.; Shao, M.; Yao, B.; Kang, Z. Maltase Decorated by Chiral Carbon Dots with Inhibited Enzyme Activity for Glucose Level Control. *Small* **2019**, *1901512*, 1–7.

(106) Hu, L.; Li, H.; Liu, C.; Song, Y.; Zhang, M.; Huang, H.; Liu, Y.; Kang, Z. Chiral Evolution of Carbon Dots and the Tuning of Laccase Activity. *Nanoscale* **2018**, *10*, 2333–2340.

(107) Kong, W.; Liu, J.; Liu, R.; Li, H.; Liu, Y.; Huang, H.; Li, K.; Liu, J.; Lee, S. T.; Kang, Z. Quantitative and Real-Time Effects of Carbon Quantum Dots on Single Living HeLa Cell Membrane Permeability. *Nanoscale* **2014**, *6* (10), 5116–5120.

(108) Wang, H. J.; He, X.; Luo, T. Y.; Zhang, J.; Liu, Y. H.; Yu, X. Q. Amphiphilic Carbon Dots as Versatile Vectors for Nucleic Acid and Drug Delivery. *Nanoscale* **2017**, *9* (18), 5935–5947.

(109) He, X.; Chen, P.; Zhang, J.; Luo, T. Y.; Wang, H. J.; Liu, Y. H.; Yu, X. Q. Cationic Polymer-Derived Carbon Dots for Enhanced Gene Delivery and Cell Imaging. *Biomater. Sci.* **2019**, *7* (5), 1940–1948.

(110) Hu, L.; Sun, Y.; Li, S.; Wang, X.; Hu, K.; Wang, L.; Liang, X. J.; Wu, Y. Multifunctional Carbon Dots with High Quantum Yield for Imaging and Gene Delivery. *Carbon* **2014**, *67*, 508–513.

(111) Yeh, T. F.; Teng, C. Y.; Chen, S. J.; Teng, H. Nitrogen-Doped Graphene Oxide Quantum Dots as Photocatalysts for Overall Water-Splitting under Visible Light Illumination. *Adv. Mater.* **2014**, *26* (20), 3297–3303.

(112) Liu, J.; Liu, Y.; Liu, N.; Han, Y.; Zhang, X.; Huang, H.; Lifshitz, Y.; Lee, S. T.; Zhong, J.; Kang, Z. Metal-Free Efficient Photocatalyst for Stable Visible Water Splitting via a Two-Electron Pathway. *Science* **2015**, *347* (6225), 970–974.

(113) Zhang, P.; Wang, T.; Chang, X.; Zhang, L.; Gong, J. Synergistic Cocatalytic Effect of Carbon Nanodots and Co3O4 Nanoclusters for the Photoelectrochemical Water Oxidation on Hematite. *Angew. Chem. Int. Ed.* **2016**, *55* (19), 5851–5855.

(114) Zhu, C.; Liu, C.; Zhou, Y.; Fu, Y.; Guo, S.; Li, H.; Zhao, S.; Huang, H.; Liu, Y.; Kang, Z. Carbon Dots Enhance the Stability of CdS for Visible-Light-Driven Overall Water Splitting. *Appl. Catal. B Environ.* **2017**, *216*, 114–121.

(115) Zhang, X.; Wang, F.; Huang, H.; Li, H.; Han, X.; Liu, Y.; Kang, Z. Carbon Quantum Dot Sensitized

TiO2 Nanotube Arrays for Photoelectrochemical Hydrogen Generation under Visible Light. *Nanoscale* **2013**, *5* (6), 2274–2278.

(116) Cao, L.; Sahu, S.; Anilkumar, P.; Bunker, C. E.; Xu, J.; Fernando, K. A. S.; Wang, P.; Guliants, E. A.; Tackett, K. N.; Sun, Y. P. Carbon Nanoparticles as Visible-Light Photocatalysts for Efficient CO 2 Conversion and Beyond. *J. Am. Chem. Soc.* **2011**, *133* (13), 4754–4757.

(117) Qu, D.; Zheng, M.; Du, P.; Zhou, Y.; Zhang, L.; Li, D.; Tan, H.; Zhao, Z.; Xie, Z.; Sun, Z. Highly Luminescent S, N Co-Doped Graphene Quantum Dots with Broad Visible Absorption Bands for Visible Light Photocatalyst. *Nanoscale* **2013**, *5*, 12272–12277.

(118) Li, H.; Liu, R.; Lian, S.; Liu, Y.; Huang, H.; Kang, Z. Near-Infrared Light Controlled Photocatalytic Activity of Carbon Quantum Dots for Highly Selective Oxidation Reaction. *Nanoscale* **2013**, *5* (8), 3289–3297.

(119) Liu, R.; Huang, H.; Li, H.; Liu, Y.; Zhong, J.; Li, Y.; Zhang, S.; Kang, Z.; Accepted, J. Metal Nanoparticle / Carbon Quantum Dot Composite as Photocatalyst for High Efficiency Cyclohexane Oxidation. *Acs Catal.* **2014**, *4*, 328–336.

(120) Gao, P.; Ding, K.; Wang, Y.; Ruan, K.; Diao, S.; Zhang, Q.; Sun, B.; Jie, J. Crystalline Si/Graphene Quantum Dots Heterojunction Solar Cells. *J. Phys. Chem. C* **2014**, *118* (10), 5164–5171.

(121) Qing, M.; Meng, Y.; Wang, Y.; Li, X.; Zhou, C.; Liang, Y.; Zhang, Z.; Liu, Q.; Guo, Y.; Xiao, D. Building Nanoparticle-Stacking MoO2-CDs via in-Situ Carbon Dots Reduction as High-Performance Anode Material for Lithium Ion and Sodium Ion Batteries. *Electrochim. Acta* **2019**, *319*, 740–752.

(122) Feng, H.; Xie, P.; Xue, S.; Li, L.; Hou, X.; Liu, Z.; Wu, D.; Wang, L.; Chu, P. K. Synthesis of Three-Dimensional Porous Reduced Graphene Oxide Hydrogel/Carbon Dots for High-Performance Supercapacitor. *J. Electroanal. Chem.* **2018**, *808* (December 2017), 321–328.

(123) Li, Q.; Cheng, H.; Wu, X.; Wang, C. F.; Wu, G.; Chen, S. Enriched Carbon Dots/Graphene Microfibers towards High-Performance Micro-Supercapacitors. *J. Mater. Chem. A* **2018**, *6* (29), 14112–14119.

(124) Li, X.; Rui, M.; Song, J.; Shen, Z.; Zeng, H. Carbon and Graphene Quantum Dots for Optoelectronic and Energy Devices: A Review. *Adv. Funct. Mater.* **2015**, *25* (31), 4929–4947.

(125) Mitra, I.; Paul, S.; Bardhan, M.; Das, S.; Saha, M.; Saha, A.; Ganguly, T. Effects of Carbon Quantum Dots (CQD) on the Energy Storage Capacity of a Novel Synthesized Short-Chain Dyad. *Chem. Phys. Lett.* **2019**, *726* (April), 1–6.

(126) Xie, C.; Nie, B.; Zeng, L.; Liang, F. X.; Wang, M. Z.; Luo, L.; Feng, M.; Yu, Y.; Wu, C. Y.; Wu, Y.; et al. Core-Shell Heterojunction of Silicon Nanowire Arrays and Carbon Quantum Dots for Photovoltaic Devices and Self-Driven Photodetectors. *ACS Nano* **2014**, *8* (4), 4015–4022.

(127) Tian, B.; Zheng, X.; Kempa, T. J.; Fang, Y.; Yu, N.; Yu, G.; Huang, J.; Lieber, C. M. Coaxial Silicon Nanowires as Solar Cells and Nanoelectronic Power Sources. *Nature* **2007**, *449* (October), 71018.

(128) Liu, T.; Yu, K.; Gao, L.; Chen, H.; Wang, N.; Hao, L.; Li, T.; He, H.; Guo, Z. A Graphene Quantum Dot Decorated SrRuO3 Mesoporous Film as an Efficient Counter Electrode for High-Performance Dye-Sensitized Solar Cells. *J. Mater. Chem. A* **2017**, *5* (34), 17848–17855.

(129) Zhu, Z.; Ma, J.; Wang, Z.; Mu, C.; Fan, Z.; Du, L.; Bai, Y.; Fan, L.; Yan, H.; Phillips, D. L.; et al. Efficiency Enhancement of Perovskite Solar Cells through Fast Electron Extraction: The Role of Graphene Quantum Dots. *J. Am. Chem. Soc.* **2014**, *136* (10), 3760–3763.

(130) Li, H.; Shi, W.; Huang, W.; Yao, E. P.; Han, J.; Chen, Z.; Liu, S.; Shen, Y.; Wang, M.; Yang, Y. Carbon Quantum Dots/TiOx Electron Transport Layer Boosts Efficiency of Planar Heterojunction Perovskite Solar Cells to 19%. *Nano Lett.* **2017**, *17* (4), 2328–2335.

(131) Duan, J.; Zhao, Y.; He, B.; Tang, Q.; Material, E. S.; This, M. C. A.; Society, T. R. High-Purity Inorganic Perovskite Films for Solar Cells with 9.72 % Efficiency. *Angew. Chem. Int. Ed.* **2018**, *57* (14), 3787–3791.

(132) Novoselov, K. S.; Geim, A. K.; Morozov, S. V.; Jiang, D.; Zhang, Y.; Dubonos, S. V.; Grigorieva, I. V.; Firsov, A. A. Electric Field Effect in Atomically Thin Carbon Films Supplementary. *Science*

2004, *5* (1), 1–12.

(133) Balogun, M. S.; Luo, Y.; Lyu, F.; Wang, F.; Yang, H.; Li, H.; Liang, C.; Huang, M.; Huang, Y.; Tong, Y. X. Carbon Quantum Dot Surface-Engineered VO2 Interwoven Nanowires: A Flexible Cathode Material for Lithium and Sodium Ion Batteries. *ACS Appl. Mater. Interfaces* **2016**, *8* (15), 9733–9744.

(134) Guo, X.; Wang, C.-F. F.; Yu, Z.-Y. Y.; Chen, L.; Chen, S.; Chen*, S. Facile Access to Versatile Fluorescent Carbon Dots toward Light-Emitting Diodes. *Chem. Commun.* **2012**, *48* (21), 2692–2694.

(135) Chen, Y.; Zheng, M.; Xiao, Y.; Dong, H.; Zhang, H.; Zhuang, J.; Hu, H.; Lei, B.; Liu, Y. A Self-Quenching-Resistant Carbon-Dot Powder with Tunable Solid-State Fluorescence and Construction of Dual-Fluorescence Morphologies for White Light-Emission. *Adv. Mater.* **2016**, *28* (2), 312–318.

(136) Zhou, D.; Li, D.; Jing, P.; Zhai, Y.; Shen, D.; Qu, S.; Rogach, A. L. Conquering Aggregation-Induced Solid-State Luminescence Quenching of Carbon Dots through a Carbon Dots-Triggered Silica Gelation Process. *Chem. Mater.* **2017**, *29* (4), 1779–1787.

(137) Wang, F.; Chen, Y. H.; Liu, C. Y.; Ma, D. G. White Light-Emitting Devices Based on Carbon Dots Electroluminescence. *Chem. Commun.* **2011**, *47* (12), 3502–3504.

(138) Zhang, X. X.; Wang, F.; Huang, H.; Li, H.; Han, X.; Liu, Y.; Kang, Z.; Zhang, Y.; Wang, Y. Y. Y.; Kalytchuk, S.; et al. Color-Switchable Electroluminescence of Carbon Dot Light-Emitting Diodes. *ACS Nano* **2013**, *7* (12), 11234–11241.

(139) Chao, D.; Zhu, C.; Xia, X.; Liu, J.; Zhang, X.; Wang, J.; Liang, P.; Lin, J.; Zhang, H.; Shen, Z. X.; et al. Graphene Quantum Dots Coated VO 2 Arrays for Highly Durable Electrodes for Li and Na Ion Batteries. *Nano Lett.* **2015**, *15* (1), 565–573.

2 Chirality in CNDs

This chapter focuses on the rational design of CNDs, discussed in **Subsection 1.3.2**, aimed at conferring chirality. In particular, it is reported a multi-component microwave-assisted hydrothermal synthesis for preparing chiral hp-N-CNDs (hp-N-cCNDs) and the study of their (chiro)optical properties. Density functional theory (DFT) have been key in understanding the origin of chirality. This approach could be extended for obtaining chiral CNDs with different properties by using different precursors or dopants (S**ubsection 2.1.2** and **Section 2.2**). These nanoparticles have been also used as templates for the formation of chiral chromophoric assemblies in water (**Subsection 2.1.3**).

Finally, the effects that the chiral surface of CNDs has on proteins and cells (**Subsection 2.1.4**) have been studied. This work has been performed during an Erasmus period spent in the research group of *Prof. Dr. Wolfgang J. Parak* (Center for Hybrid Nanostructures, University of Hamburg) with the aid of *Dr. Neus Feliu*, *Ms. Huijie Yan* and *Ms. Ziyao Liu*.

Part of the work presented in this chapter has been published as “Design principles of chiral carbon nanodots help convey chirality from molecular to nanoscale level” in *Nature Communications* **2018**, 9, 1, 3442.

2.1 A bottom-up approach to chiral carbon nanodots

2.1.1 Synthesis and purification

Chiral nanoparticles (NPs) have recently attracted much attention from scientific community because of the various fields of application, which range from asymmetric catalysis to chiral biosensing.[1] Two decades ago, the first inorganic chiral nanoparticles (NPs) were reported, employing stabilizing chiral ligands (glutathione) for gold nanoclusters.[2] While most studies are focused on metal nanoclusters (gold and silver), this approach has been also extended to semiconductor nanocrystals, magnetic NPs and other nanostructures.[1–10] Design of carbon-based chiral NPs has been a challenge because of the complexity of their structure and the absence of a widely accepted theory about the mechanism of their formation. The two main synthetic approaches have been the post-functionalization of achiral carbon dots and the single/multicomponent synthesis starting directly from a chiral precursor. The former was firstly introduced in the same year (2016) by Martin[11] and Kotov[12] who introduced chirality in GQDs by the attaching of chiral moieties to their edges (**Figure 2.1**). Subsequently a similar approach was used for CNDs *via* post-functionalization of achiral nanoparticles obtained from sucrose with aminoacid.[13] The latter methodology was used basically to obtain CQDs from a single chiral precursor or by this in presence of another molecule.[14–22] In all these cases the chirality was introduced by the use of enantiopure amino acids or sugars. Moreover, the conferring of chirality during these synthetic processes is no supported by structural information and is only investigated with circular dichroism similarly to the first methodology. In addition to these aspects, the majority of these synthetic approaches reported incomplete purification procedures. In these cases, after the synthesis, CDs were purified only by dialysis[12,15–20,22] or centrifugation,[14] without a pre-microfiltration step. Recently it was found that by similar purification procedures, the presence of larger or littler byproducts mixed to the dots is more possible and could induce to misleading information.[23,24]

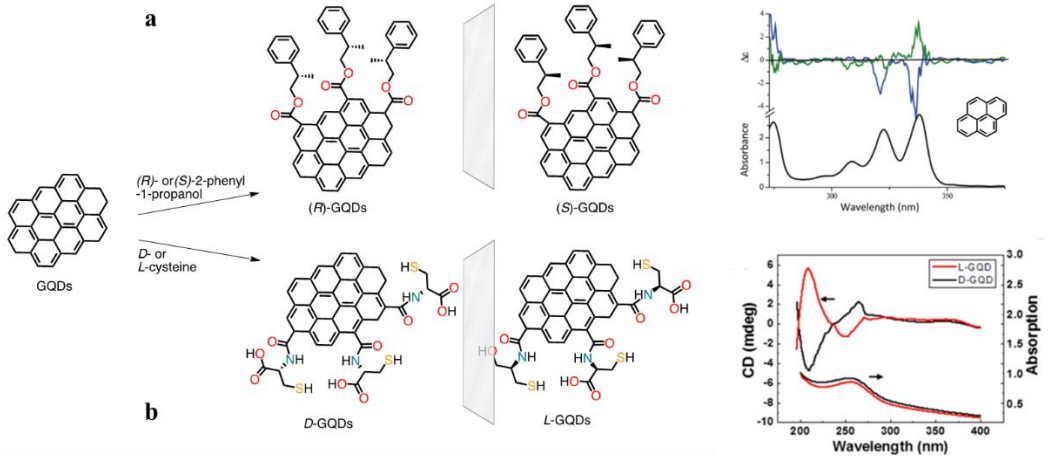

Figure 2.1 Schematic representation of the post functionalization of GQDs to confer chirality *via* the methodologies reported by Martin[11] (**a**) and Kotov[12] (**b**). Adapted from references [11] and [12].

These evidences encouraged us to use our synthesis/purification/characterization protocol to fully combine carbon nanomaterials with chiroptical properties.[25–27] As discussed in **chapter 1**, our group has reported in the last three years a rational approach for the synthesis of pure core/shell hp-N-CNDs by an accurate choice of carbon precursors (Arg, as core precursor and EDA as surface precursor) and a multi-step purification. In the contest of chirality introduction, since we used enantiopure arginine as core precursor, we firstly investigated if the obtained nanoparticles were chiral. However during the hydrothermal microwave-assisted synthesis, as expected, arginine undergoes racemization or consumption, resulting in achiral carbon nanodots (**Figure S2.1**).[28] Then we reasoned that, by appropriate choice of surface precursor, *i.e.* a chiral diamine that retains chirality at high temperatures in water, chiral carbon dots could be prepared. Chiral carbon dots were therefore prepared *via* microwave-assisted hydrothermal synthesis by using arginine, as the core precursor, and (*R*,*R*)- or (*S*,*S*)-1,2-cyclohexanediamine,[29] as the chiral surface precursor.[30] During the process of microwave heating, the solution changed color from transparent to dark brown as a result of the formation of nanodots. Large carbon nanoparticles were removed by micro-filtration and the yellow filtrate was dialyzed against Milli-Q water. The obtained nanodots (hp-N-cCNDs), named hp-N-CNDs-*R* or hp-N-CNDs-*S*, were soluble in water and other common polar organic solvents (**Figure 2.2**).

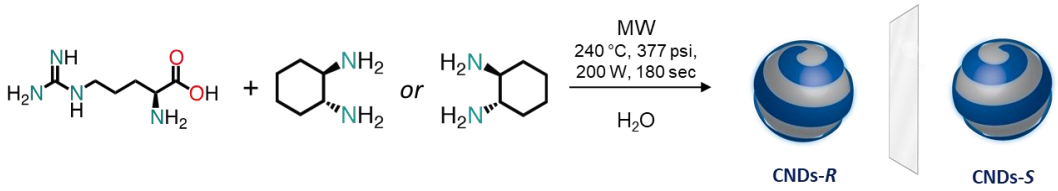

Figure 2.2 Scheme of the hp-N-cCNDs synthesis.[30]

2.1.2 Characterization

Morphological and structural characterization (**Figure 2.3**) was carried out using FT-IR spectroscopy, X-ray photoelectron spectroscopy (XPS) and atomic force microscopy (AFM).

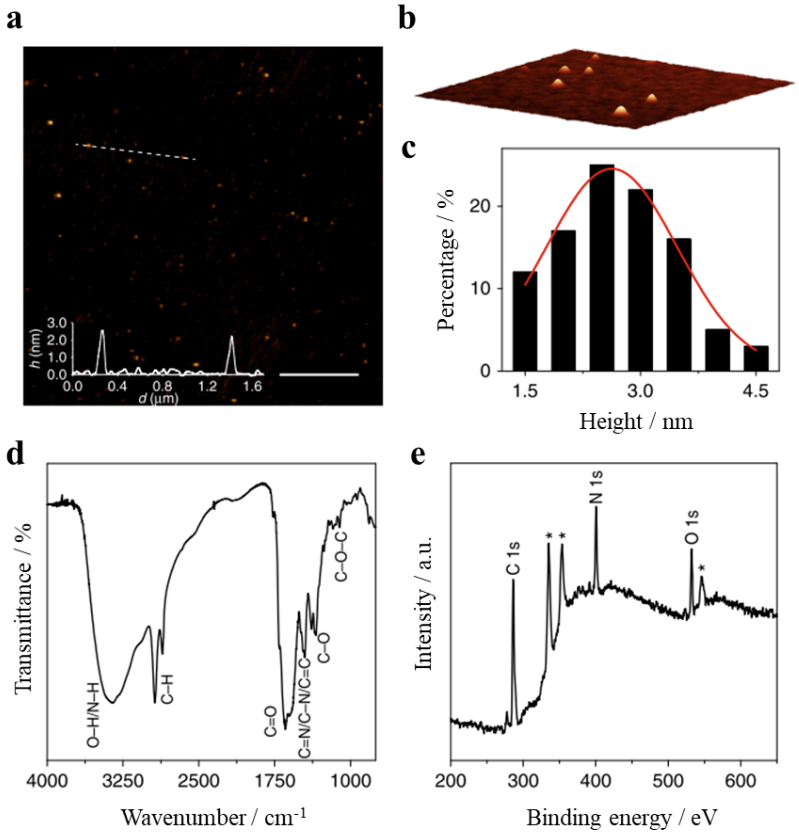

Figure 2.3 Structural and morphological characterization of cCNDs: (**a**) hp-N-CNDs-*R* tapping mode AFM image (4.4 × 4.4 μm), on the bottom left the height profile along the dashed line, on the bottom right the white scale bar (1 μm); (**b**) 3D close-up hp-N-CNDs-*R* AFM image (0.5 × 0.5 μm); (**c**) height sizes distribution histogram and superimposed Gaussian fit; (**d**) FT-IR spectrum (KBr) of hp-N-CNDs-*S*; (**e**) XPS survey spectrum of hp-N-CNDs-*S* showing the C1s, N1s, and O1s.

As expected, the two chiral nanoparticles showed similar results. Moreover, the structure of these particles was found comparable to the achiral ones (hp-N-CNDs),[25] obtained using EDA. The hp-N-cCNDs AFM images show particles with round shape with an average size of 2.64 ± 0.89 nm (**Figure 2.3 a, b, c and Figure S2.2**) comparable with the achiral nanoparticles. The FT-IR spectrum of the -*S* shows different functional groups similar to the ones of the achiral dots (**Figure 2.3 d**). In particular the peaks at 1174 and 1107 cm^{-1} indicate the presence of C-O-C bonds, confirmed by the signals at 1386, 1353 and 1342 cm^{-1} that are representative of C-O bonds. Going to higher wavenumbers, the absorptions at 1646, 1703 and 1766 cm^{-1} indicate the presence of C=O bonds, while the peak at 3350 cm^{-1} reveals the presence of O-H/N-H stretching. Moreover, the signals at 1491, 1470 and 1452 cm^{-1} are indicative of C-N/C=N/C=C bonds stretching. Finally, the absorptions at 2935 and 2859 cm^{-1} are indicative of the C-H stretching. The chemical composition of the particles was investigated by a full-scan of the XPS spectrum on hp-N-CNDs-*R* (**Figure 2.3 e**). The results showed the presence of carbon, nitrogen and oxygen respectively at 286.2 eV (C1s), 400.6 eV (N1s) and 532.3 eV (O1s). These three components were found on a C/N/O percentage ratio of 65.9/23.7/10.4. Moreover the fitting of the mentioned signals revealed chemical bonds similar to the ones showed by the FT-IR data (**Figure 2.4** and **Figure S2.4**). The deconvolution of the C1s peak show the presence of C=C (284.8 eV, 5.1%), C-C/C-H (285.8 eV, 20.2%), C-O/C-N (286.7 eV, 56.8%), C=O/C=N (288.5 eV, 5.7%) and O-C=O (289.6 eV, 12.2%) bonds. By deconvoluting the N1s peak C=N (398.7 eV, 7.1%), NH_2 (399.9 eV, 25.7%), C-N-C (400.9 eV, 52.9%) and N-C_3 (401.9 eV 14.3%) bonds were found. A Kaiser test revealed the presence of 795 μmol g^{-1} of primary amino groups. This result is in accordance with the XPS data and the detected bonds were found similar but with different content if compared to the achiral hp-N-CNDs.

The optical properties were firstly evaluated by UV-Vis absorption (**Figure 2.5a**). Two main peaks were detected at 270 and 330 nm. These are related to the C=C and C=O transition, typically π/n to π*. The electronic circular dichroism (ECD) spectra showed the successful conferring of chirality during the synthetic process (**Figure 2.5b**). The -*R* exhibited negative Cotton effects at 260 and 320 nm that correspond to the UV-Vis absorption. In accordance to the -*R* nanoparticles, hp-N-

CNDs-*S* presented a specular spectrum with two positive Cotton effects in correspondence of the same wavelengths. Moreover, preparing CNDs with different ratios of the two chiral precursors, we showed that the circular dichroism is dependent on the optical purity of the amine in the particle (**Figure S2.5**).

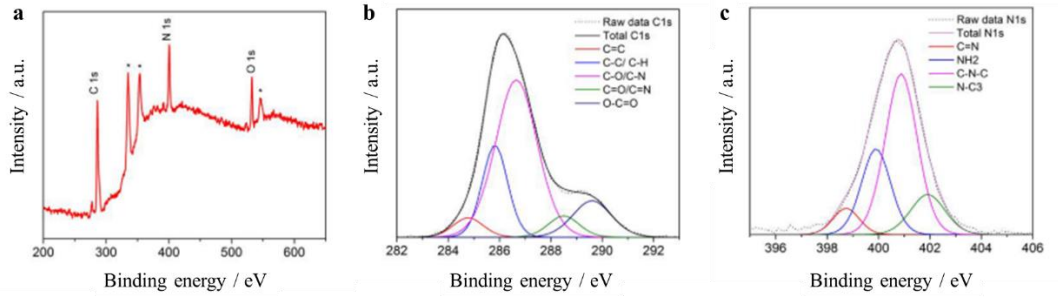

Figure 2.4 XPS analysis of hp-N-CNDs-*S*: (**a**) XPS survey showing the C1s, N1s and O1s (*from substrate Au4d3, Au4d5 and Au4p); (**b**) deconvolution of C1s profile; **c** deconvolution of N1s profile.

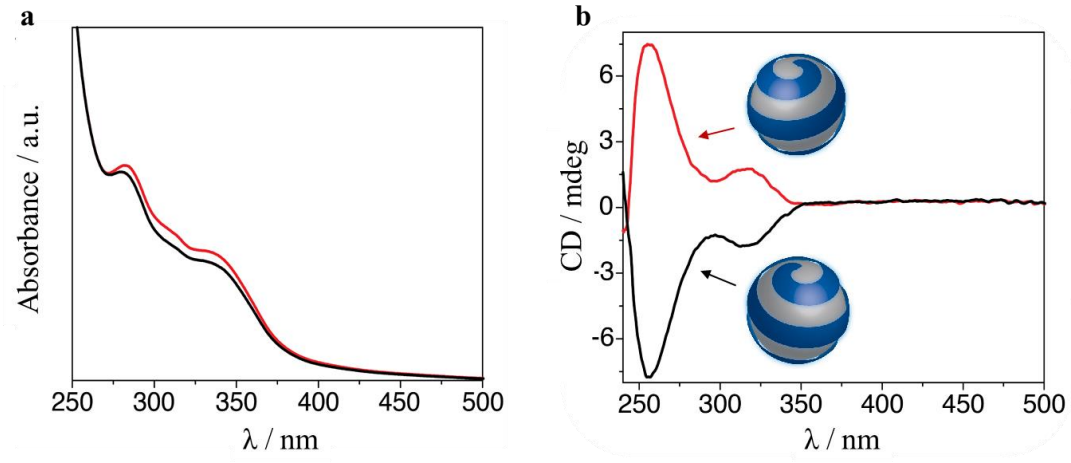

Figure 2.5 Overlayed UV-Vis (**a**) and CD (**b**) spectra of hp-N-CNDs-*S* (red profile) and hp-N-CNDs-*R* (black profile) in water.

The emission properties were analyzed by recording the fluorescence spectrum of the two chiral hp-N-cCNDs (**Figure 2.6a and Figure S2.6**). Both nanoparticles show very similar emission profiles. The fluorescence is excitation dependent, from 320 to 440 nm, with fluorescence that shifts from 419 to 466 nm. The different emissive properties reveal different surface functional groups in the chiral hp-N-cCNDs when compared to the achiral hp-N-CNDs. Indeed, the nanodot surface affects the emission properties since it determines the trapping of excitons under excitation. Light emission was also investigated by determining the quantum yields

and the fluorescence lifetimes. The two nanoparticles showed emission of 20% and average fluorescence lifetimes of 8 ns (double-exponential fit showed a τ_1 short and τ_2 long components respectively at 1.2 and 11 ns, **Figure S2.7**).

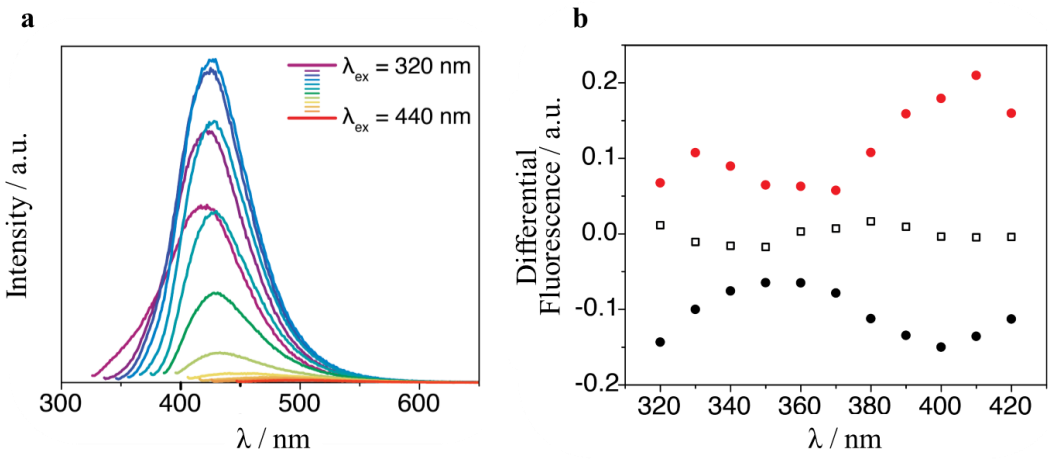

Figure 2.6 (**a**) Fluorescence emission spectra of hp-N-CNDs-*R* exciting from 320 to 440 nm and (**b**) Fluorescence detection of circular dichroism of hp-N-CNDs-*S* (red circles), hp-N-CNDs-*R* (black circles) and fluorescein (empty squares) registered with the experimental set up reported in **Section 2.4.2.**

The chirality of the ground and excited states of CNDs was then probed through the detection of luminescence. The former was analyzed *via* the fluorescence detection of circular dichroism (FDCD). By this technique the sample is excited using circularly polarized light and then the fluorescence emission generated is detected (**Figure 2.6b**). The two nanoparticles showed opposite FDCD spectra if excited at 280 nm and these were in accord to the CD results.

Their opposite sign agrees with the opposite chirality observed in the electronic circular dichroism spectra. This result was not affected by fluorescence polarization effects or by polarized scattering; indeed, the differential fluorescence collected at the symmetric angle ($\theta = -15°$) show the same spectral features (**Figure S2.8**) and the contribution from the elastic scattering of CND was so low (i.e., the measured value of the excess scattered intensity in the visible wavelength range is almost comparable with pure solvent) that the long pass filter rejected it completely. Even placing an analyzer at the magic angle, despite the increased noise, did not change the spectral response. The negligible fluorescence polarization effects in the FDCD spectra can be led back to the long average fluorescence lifetime, which was about 8 ns for both CNDs (**Figure S2.7**). During this time, the small size of CNDs allows

for rotations fast enough to depolarize fluorescence emission (measured steady-state anisotropy = 0.03). Unfortunately, circularly polarized luminescence (CPL) spectra did not show any detectable chiroptical signal and thus no information about the excited state of the dots was obtained.

To better understand the correlation between chirality and light interaction, we looked inside the fluorescence emission. This ranges from 400 nm up to 600 nm and is composed of many bands that are excitation dependent (**Figure 2.6a and Figure S2.6**). This behavior is typically attributed to the multiple dipoles able to interact with light. These are present in the various chromophores of the amorphous structure and could absorb light from UV to visible but emit fluorescence only if excited above 280 nm. For this reason, chirality could be observed only in the UV region of the differential absorption spectrum. At longer wavelengths (going towards the visible) the differential absorption shows small amplitudes and the differential fluorescence signal could be detected.

Chirality was finally studied with vibration circular spectroscopy (VCD), a differential absorption of left and right circularly polarized IR light, which was previously employed in chirally capped metal NPs to obtain structural information.[3] The results showed a mirror image relationship of the two enantiomeric particles spectra (**Figure 2.7a and Figure S2.9**). In particular two stronger bands at 1600 cm^{-1} and at slightly above 1350 cm^{-1} were detected. To better understand which absorbent groups were responsible for these bands VCD spectra on various cyclohexanediamine fragments were simulated (**Figure 2.7b**, see **Section 2.4.2** for gurther details on DFT methods).[31] Density functional theory (DFT) calculation showed that the stronger signal arises from the bending vibrational modes of the CHDA N-H and C-H. The band at 1600 cm-1 could have contribution of the amidic C=O functional groups (**Figure S2.10**). Although these calculations are related to simpler systems, these were able to identify the vibrational absorbers of the strongest signals. Moreover these results remark the theory of the core/shell structure investigated in achiral hp-N-CNDs of our first work.[25] Here the CHDA derived surface amines are also responsible of the chirality of the nanoparticle.

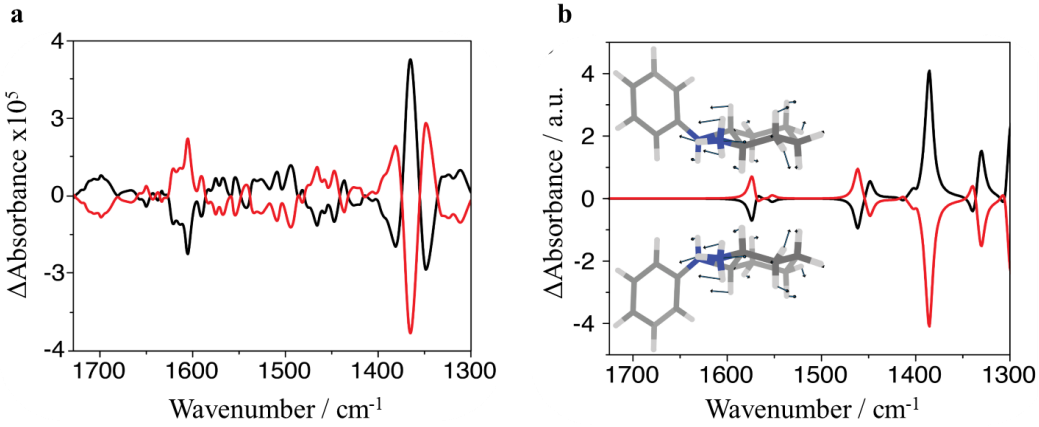

Figure 2.7 Compared experimental (**a**) and simulated (**b**) VCD spectra of hp-N-CNDs-*S* (red line) and hp-N-CNDs-*R* (black line). The experimental spectra were performed at 298 K using water as solvent. The simulated spectra were obtained by a DFT method explained in **Section 2.4.2**. The indicated structure shows the main displacement vectors of the computed chiral fragments.

These structural findings open to the possibility of exploit such nanoparticles in different applications. As representative studies we investigated these nanoparticles as templates in chirality transfer (**Subsection 2.1.3**) and as enantioselective biological interactions in *in vitro* systems (**Subsection 2.1.4**). Compared to other attempts,[14–22] the approach discussed in this work let to obtain chiral nanoparticles by a rational design with proper purification and extensive investigation of chirality. This methodology could be used for the synthesis and characterization of other types of chiral carbon dots. Moreover, by using our multicomponent approach chirality could be conferred by chiral molecules to different core precursors. As representative example, we produced a new typology of chiral nanoparticles using citric acid instead of arginine but keeping CHDAs as chiral precursors. The synthesis produced, again, chiral carbon dots, hp-N-CitCNDs-*R* or -*S*, with mirror-like images at the CD spectra (**Figure S2.11b**). However, the different structure obtained by the use of citric acid exhibited different absorption/emission properties (**Figure S2.11a,c,d**). Therefore, this methodology inspired us to the production of tailored carbon dots for specific needs using analogous rational approaches. In **Section 2.2**, we will use this methodology to give another example of chiral CNDs exploiting the chemistry oh naphthalene dianhydrides as molecular dopants.

2.1.3 Templating supramolecular assemblies

The chiral surface of hp-N-CNDs-*R* and -*S* could be conceptually used as supramolecular template to transfer chirality to other molecules. To prove this hypothesis we focused on their non-covalent interaction with porphyrins that previously were showed to form electron donor-acceptor complexes with CNDs.[32,33] These molecules consists on square planar aromatic structures composed of 18 π electrons. Their high structural stability and excellent optical properties have been wide used for many supramolecular systems.[34–36] In addition, porphyrins could be chemically modified tuning the electronic and optical properties.[37,38] Moreover, the peripheric sites of the molecule could be functionalized with charged functional groups to achieve water-solubility. This typology of porphyrins has been high investigated because of the dual hydrophilic (periphery) and hydrophobic (central π-conjugated) behavior. In particular, this dichotomy is responsible of the tendency of these molecules to aggregate in solution.[39,40] Moreover, the use of molecular templates can tune their aggregation towards specific supramolecular structures.[41] These aggregates don't show ECD, but when the porphyrins bind chiral molecules the resulted aggregates show ECD in correspondence of their absorbance region.[42] To perform the study in presence of chiral hp-N-cCNDs as chirality inducers we focused on the water soluble tetranionic *meso*-tetrakis(4-sulfonatophenyl)porphyrin (H_2TSPP^{4-}). Depending on the level of protonation, the zwitterionic form H_4TSPP^{2-} (pK_a = 4.8) could form face-to-face (H type, λ_{max} = 420 nm) and edge-to-edge (J type, λ_{max} = 490 nm) aggregates.[43–47] These aggregates are generally formed by self-assembly processes that are governed by different thermodynamic and kinetic paths. These are highly influenced by the solvent and the experimental conditions: pH, concentration, ionic strength and so on).[48–50] Moreover, these porphyrins could form chiral aggregates. In particular, H_4TPPS^{2-} could form racemic mixtures that, of course don't show EDC.[51] Even the presence of traces of chiral contaminants could affect the aggregation process and this results on the preferential formation of one of the two enantiomers. Moreover, there are still few studies that deal with the chirality induction on H_4TSPP^{2-} aggregates induced by templating chiral molecules.[50,52] The

study of chirality induction on H_2TSPP^{4-} started by adding the porphyrin to an aqueous solution of hp-N-CNDs-*R* or -*S*, buffered at pH = 9.0 (**Figure 2.8a**).

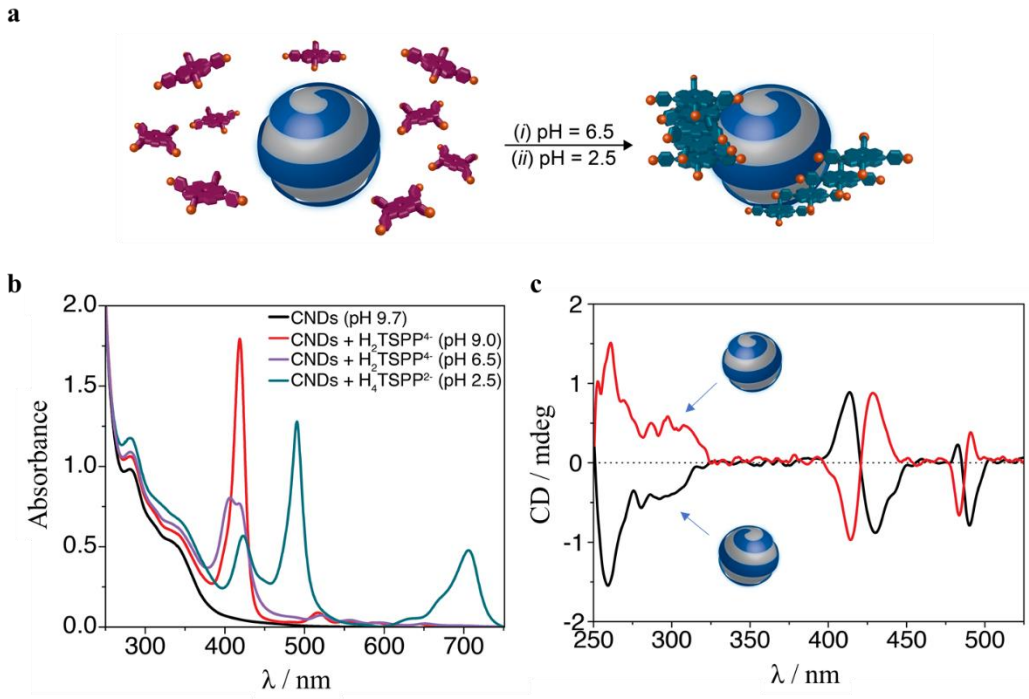

Figure 2.8 Use of hp-N-cCNDs as templates for chiral supramolecular porphyrin aggregates: (**a**) scheme of the hp-N-cCNDs as chiral templates (purple = free non-protonated porphyrins, green = assembled protonated porphyrins); (**b**) UV-Vis spectra of the hp-N-cCNDs (black profile) and hp-N-cCNDs in presence of porphyrin (6 μM) at different pH values; (**c**) ECD spectra of hp-N-CNDs-*R* (red profile) and hp-N-CNDs-*S* (black profile) in presence of porphyrin at pH = 2.5.

Here, the porphyrin in solution showed a low interaction with hp-N-cCNDs due to the hypochromic effect and the slight broadening of the Soret band (H ~35%). By varying the pH, the hp-N-cCNDs surface amines could be protonated, varying the charge and inducing the interaction with the negative charges of the porphyrins. In particular, decreasing the pH to a value of 6.5 H_2TSPP^{4-} absorption spectrum showed a high hypochromic effect (H ~75%) and a splitting of the Soret band (one intense at ~400 nm and the other at ~419 nm). This result is a clear evidence of the presence of electrostatic interaction between hp-N-cCNDs (with more positive charges) and the tetranionic. Lowering the pH value to 2.5, with hydrochloric acid, the protonation of porphyrin (H_4TSPP^{2-}) led to the formation of H- and J-type aggregates (**Figure 2.8b**). These were formed in less than 1 hour and were confirmed by the UV-Vis spectrum. Then, the CD spectra recorded on such

solutions, in presence of CND-*R* or -*S*, showed that the resulted aggregates showed ECD (**Figure 2.8c**). In particular, the band of the hp-N-cCNDs resulted decreased, while ECD opposite porphyrin bands were observed at 420 and 490 nm (aggregate absorption region). We reasoned that the low intensity of the ECD signals of the porphyrin aggregates could be due to the low efficiency of hp-N-cCNDs to transfers chirality since when protonated their EDC band result lowered. Moreover, another aspect is related to the electronic communication of the porphyrins when aggregated that could affect the ECD signal. Further resonance light scattering (RLS) measurements showed the formation of shorter porphyrin aggregates in the presence of hp-N-cCNDs (**Figure S2.12**).

2.1.4 Chirality as driving force in biological interactions: *in vitro* investigation

In vitro studies are key for the evaluation of the behavior of nanoparticles in a biological system.[53] These studies represent the most important model for the evaluation of subsequent *in vivo* applications especially for nanomedicine.[54] In this context, these studies could be divided in two main categories regarding the nanoparticle interactions with biomolecules and cells.[55–58] The former is focused on how the nanoparticle-biomolecule interaction could affect their mobility and stability in a biological system. In particular, the nanoparticle-protein interactions are the most studied ones.[58] Proteins are present in all the biological systems and generally have an important role in mediating the nanoparticle interaction with other biological entities.[59] Interestingly, the presence of a protein-coated surface could affect the nanoparticle behavior compared to the 'naked' nanoparticle. This typology of coating is better known as "protein corona" and it is mediated by different proteins of the extracellular environment and blood. In this context, the main investigated protein is the serum albumin because of its high percentage in the blood serum, its binding versatility and carrier behaviour.[60–62] This protein contains different hydrophilic and hydrophobic pockets that enhance the binding affinities toward a large variety of substrates. Indeed, almost all the types of nanoparticles interact with these proteins when introduced in a biological system. Depending on

the size of the particle, the protein corona could be responsible of a new biological identity for the nanoparticles. These bio-conjugates exhibit increased hydrodynamic sizes, characteristic surface charge and could undergo aggregation mechanisms. These aspects could affect different biological behaviors such as cell interaction and drug delivery.[59,61–70] In the case of CNDs size scale (<10 nm), the protein assumes the function of carrier (**Figure 2.9**).[71]

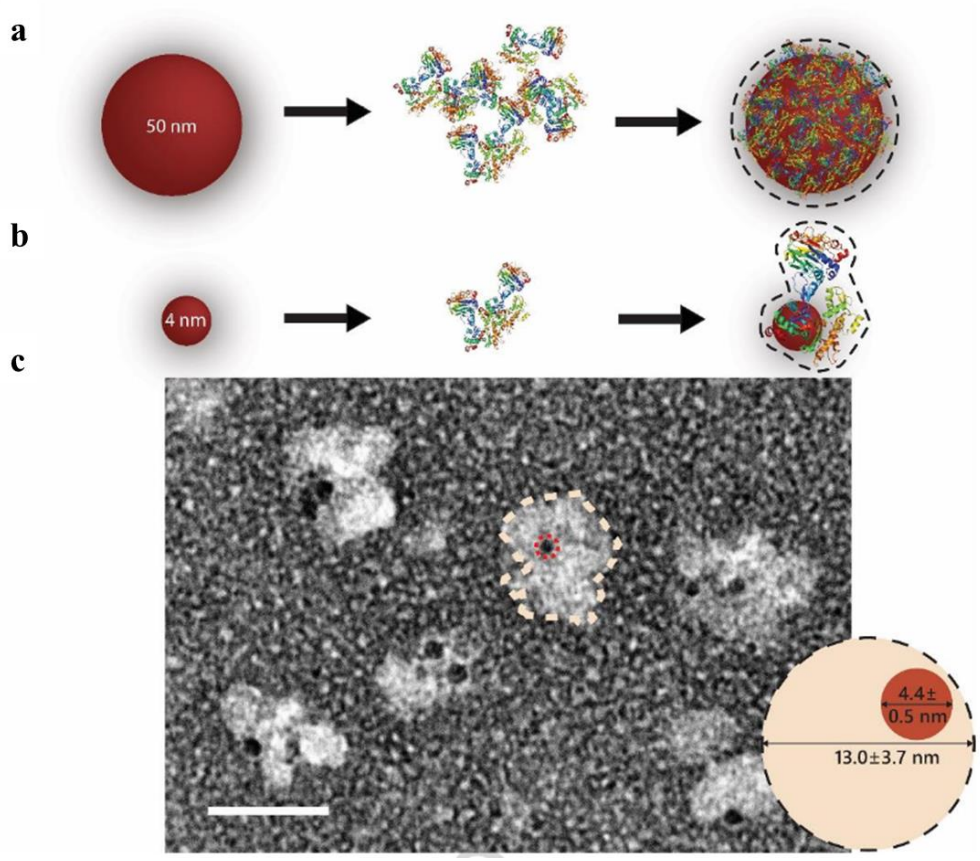

Figure 2.9 Schematic illustration of the nanoparticle interaction with the protein in function of its size (**a**, **b**) and relative TEM image of 4 nm gold nanoparticles complexed with human serum album, scale bar 25 nm (**c**). Adapted from reference [71].

For CNDs, usually the number of proteins adsorbed is lower compared to bigger particles (> 20 nm), causing a less efficient coverage of the surface, and the high curvature of the particle make the interaction weaker compared to larger surfaces.[72–74] These studies show that the lower is the protein binding force and the more is exposed the particle, the more the cellular uptake is favored. The second typology of studies regards the nanoparticle/cell interaction. When nanoparticles reach the

proximity of a cytoplasmatic membrane, they could interact with the cell by activating different uptake mechanisms (**Figure 2.10**).[75]

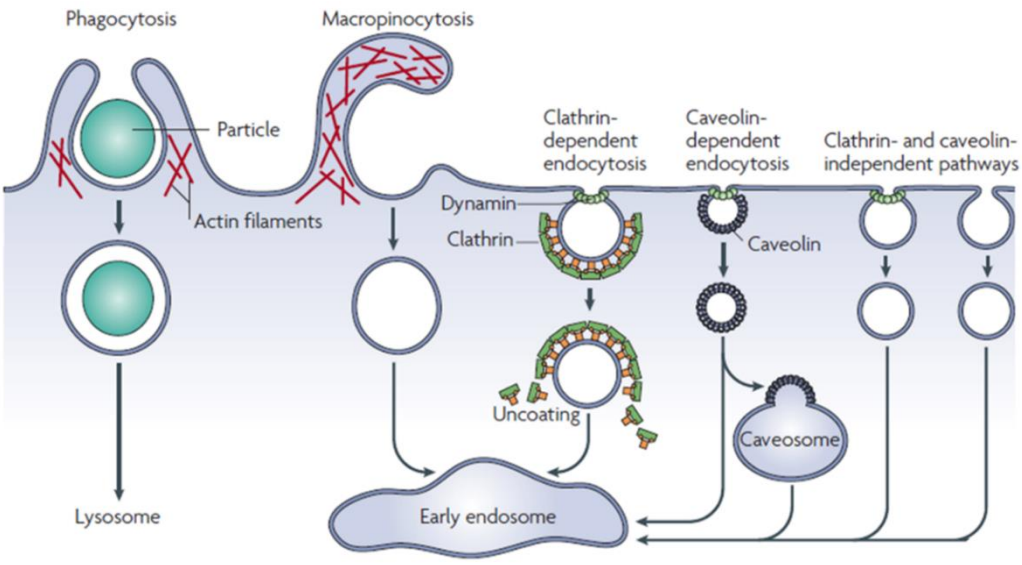

Figure 2.10 Schematic representation of the principal active uptake mechanisms. Adapted from reference [75].

The membrane exchange substances *via* passive and active transport. The passive transport is governed by the difference of concentration inside and outside the cell. Through this mechanism, uncharged hydrophilic and hydrophobic molecules (oxygen, carbon dioxide, water, benzene and so on) freely pass through the membrane moving towards region at lower concentration. Active transport, on the other hand, involves mechanisms that use chemical energy, in form of adenosine triphosphate (ATP), to activate the uptake. The active mechanism occurs for hydrophilic molecules or nanoparticles, polar or charged, and could be divided in phagocytosis and pinocytosis (**Figure 2.10**). The former is mediated by the so known phagocytes that transport inside the cell big hydrophilic molecules, bacteria or cell debris *via* the formation of a phagosome. The phagosome is a membrane vesicle that is formed by cell membrane extensions by incorporating the extracellular material. Generally, nanoparticles bigger than 200 nm are taken by phagocytosis *via* opsonization. The particles surface binds biological macromolecules, called opsonins (immunoglobulins, such as antibodies, and proteins, such as blood serum) *via* non-covalent interactions. Opsonins serve as stealth coatings that interact with the membrane receptors, activating the

phagocytosis by biological signaling. The second active uptake mechanism is activated by all the types of cells for hydrophilic particles with sizes of few nanometers. In this case, the cellular membrane forms a vesicle that incorporates a droplet of extracellular fluid, in which the nanoparticles are present. This process is better known as invagination and could occur by different pathways named: clathrin-mediated endocytosis, caveolate-mediated endocytosis, caveolate- and clathrin-independent endocytosis and macropinocytosis. The first two are activated by membrane proteins, respectively clathrin and caveolin, that contain receptors. Receptors are activated by selected functional groups and mediate the formation of the vesicle that incorporate the extracellular material. Clathrin mediated pathways are activated in presence of nanoparticle surfaces covered of lipids, polylactide acids and derivates and Si-OH groups.[76,77] The third is common in cells that do not have such membrane proteins and is activated by the presence of growth hormones, glycosylphosphatidylinositol, interleukin-2 and folic acid containing protein or particles.[78–80] The fourth occurs when a larger volume of external fluid is incorporated during the formation of the vesicle, called macropinosome. This typology of cell uptake typically occurs in presence of very big extracellular biological objects to be internalized such as dead cells, bacteria, viruses and big nanoparticles (micron sized) that cannot be internalized *via* other mechanisms.[81–84] In summary, depending on the type of cell, nanoparticles could be internalized by activating selected mechanisms in dependence of the size and the surface charge. Despite their small size, carbon dots can be internalized into a cell by different patways.[85–88] Indeed, beside the size, the surface charge and the agglomeration level (also in presence of the protein corona) affect the interaction, the uptake mechanism, the rate of internalization and the cellular retention.[85,88–90]

Considering all the factors that could affect the nanoparticle biological interactions, forecasting and designing the performances generally result very hard.[56,57,91] In addition to particle size and charge, shape and elasticity are the properties that generally need to be considered when studying the behavior of nanoparticles in a biological systems. Since these systems are composed and regulated by different chiral biomolecules (*i.e.* DNA, proteins, sugars and so on), chirality is an important biological property, responsible of many biological processes.[92,93] Interestingly,

chemistry has played an important role in developing enantiomeric molecules, like drugs, that show a relevant biological activity owing to their chirality.[94,95] This is due to the enantioselectivity of the interaction mediated by the chiral biomolecules. For this reasons, chirality showed also high relevance for bio-applications in nanoscience.[96–98] Cells are able to discriminate chiral surfaces and favor one enantiomer compared to the other during their growth. This fascinating effect is due to the chirality of the biomolecules, present in the cells or biological fluids, that are enantioselective in supramolecular interactions.[99–102] This selection is responsible for the activation of different biological processes such as cells surface adhesion, proliferation and growth. These findings promote the development of nanoparticles bearing chiral surfaces in order to study their selectivity in biological interactions.[103] Considerable efforts have been devoted to the study of the interaction of nanoparticle with cells and proteins. The first is useful in understanding cellular uptake, intracellular trafficking and the possible (positive or negative) effect that the chirality of the nanoparticle might have on their cellular toxicity.[104–108] The second, the nanoparticle/protein interaction, focuses on the study of the chirality-dependent stability of the supramolecular interaction and the related effects on the protein structure.[109–112]

These considerations encouraged us to perform the first mechanistic studies of chirality-dependent biological interaction of chiral carbon dots. Because of their low toxicity and high solubility in water, quasi-spherical and hydrophilic CNDs have shown a high versatility for different biological applications.[113] Moreover, taking advantage of the fluorescence emission of these nanoparticles, it is possible to determine their localization in biological environments.[114] All this features have increased the interest in different bio-applications such as bioimaging,[114] drug delivery,[115] cancer theranostics[116] and biosensing.[117] In all these applications, CNDs come in contact with biomolecules, interact with cells and are finally internalized. Studies of CNDs cellular uptake reveals that the uptake process can be affected by tailoring the surface charge *via* (post) synthetic methods.[85,88,118,119] This strategy increase the affinity of the nanoparticles for the specific target to bind, especially cell membranes. In addition, few examples of chiral CNDs have been employed for study of enantioselectivity in biological systems.[16,18,19] However, these studies are

mainly focused on the target applications and studies devoted to the understanding on how the chirality affects the bio-interaction of CNDs are missing.

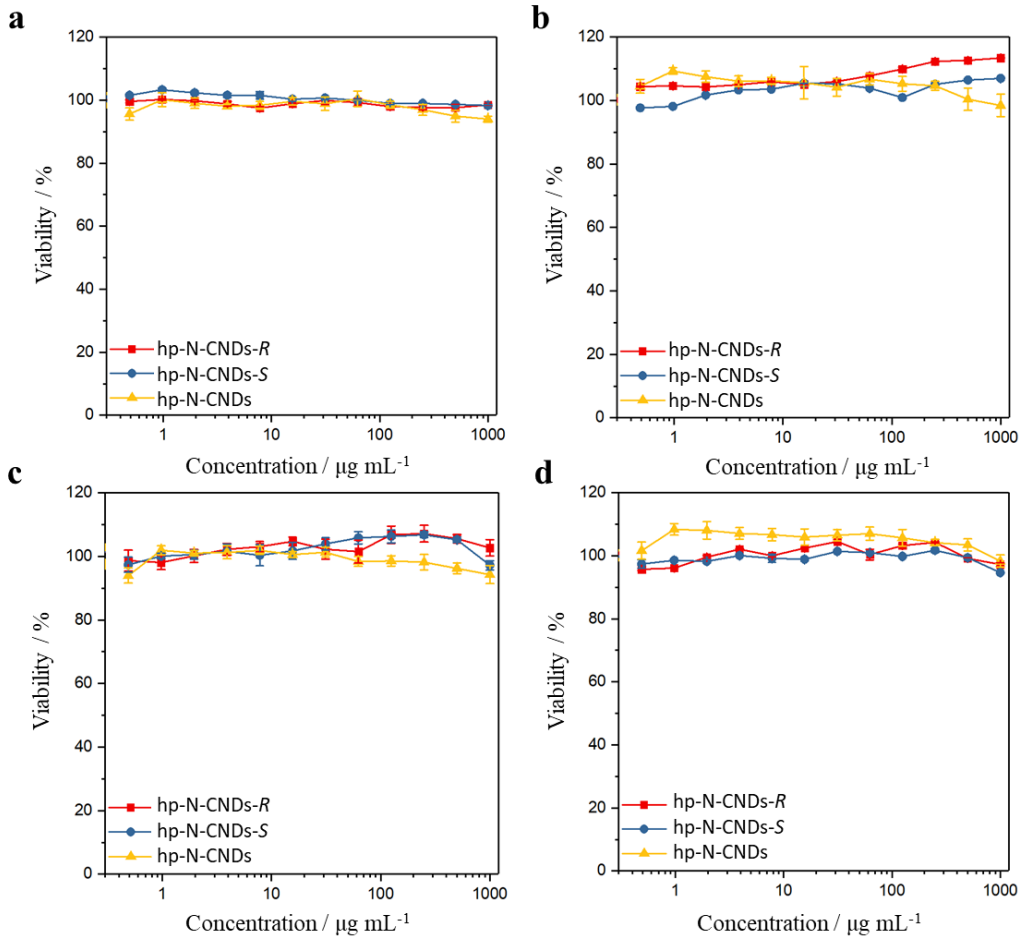

Figure 2.11 Resazurin assay test for cell viability of THP-1 cells exposed to hp-N-CNDs and hp-N-cCNDs: (**a**) 24 hours of incubation – RPMI with 10% of FBS; (**b**) 24 hours of incubation – RPMI with 0% of FBS; (**c**) 48 hours of incubation – RPMI with 10% of FBS; (**d**) 48 hours of incubation – RPMI with 0% of FBS. The cells were growth in RPMI 1640 medium (in presence or absence of 10% FBS) and then treated with CNDs (400 μg mL^{-1}). After the selected incubation times (24 or 48 hours), the cultures were washed with fresh medium to remove the dots not internalized and examined using a standard resazurin solution at a final concentration of 9% (v/v). The data is referred to cell viability percentage (fluorescence detection of resorufin as resazurin reduction product) against CNDs concentration. Each point is referred to the average of 3 measurements (triangle, circle or square) indicated with the relative standard deviation (error bar).

These studies could be helpful in pointing out how chirality could enhance or reduce the behavior of nanoparticles in a chiral (in this case biological) environment. In this context, we focused on our previously reported chiral hp-N-cCNDs[30] to explore their fate when introduced in an *in vitro* biological system and we compared the

cellular uptake of this achiral hp-N-CNDs[25] with the one of two chiral nanoparticles, at the same experimental conditions. We selected the cell line THP-1, an *in vitro* human model for nanoparticles cellular uptake.[56] This line consists in monocytes that are converted *in situ* in macrophages responsible of the uptake.[120] The nanoparticles were directly dissolved in the cell medium solution (Roswell Park Memorial Institute - RPMI 1640 Medium) and added to the culture. These experiments were performed using chiral (hp-N-CNDs-*R* and -*S*) and achiral (hp-N-CNDs) nanoparticles in presence and absence of fetal bovine serum (FBS), used to mimic the biological external environment and to promote the growth of the cell in the culture.[121] The first step of the study focused on the cell viability tests using the resazurin assay protocol.[122] Both hp-N-cCNDs showed no toxicity for exposure concentration up to 500 µg mL^{-1} opening at the possibility to perform the cell uptake tests (**Figure 2.11**).

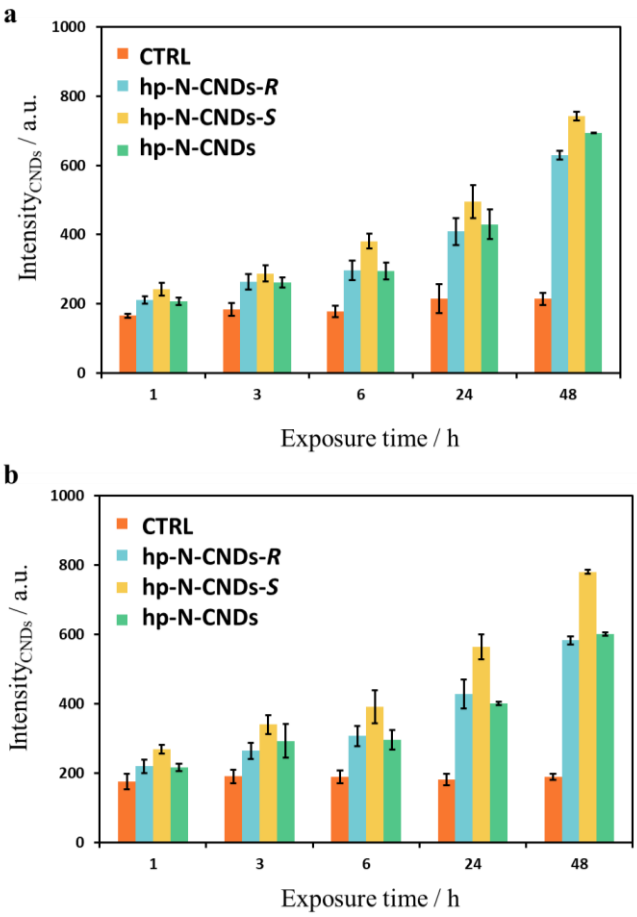

Figure 2.12 THP-1 (RPMI 1640 medium) cellular uptake of hp-N-CNDs and hp-N-cCNDs (400 µg mL^{-1}) as fluorescence intensity in function of the time of exposure *via* flow cytometry (excitation laser line 405 nm).

The cellular uptake was monitored through bioimaging of the fluorescence emission of the particles by using flow cytometry[123] (FC) and confocal laser scanning microscopy (CLSM).[124] FC results showed a substantial difference on the uptake kinetics of the two chiral hp-N-cCNDs at the highest exposure times (**Figure 2.12**). hp-N-CNDs-*S* showed a better uptake after 48 hours of exposure. The CLSM images confirm the statistical data obtained by FC (**Figures 2.13** and **2.14**).

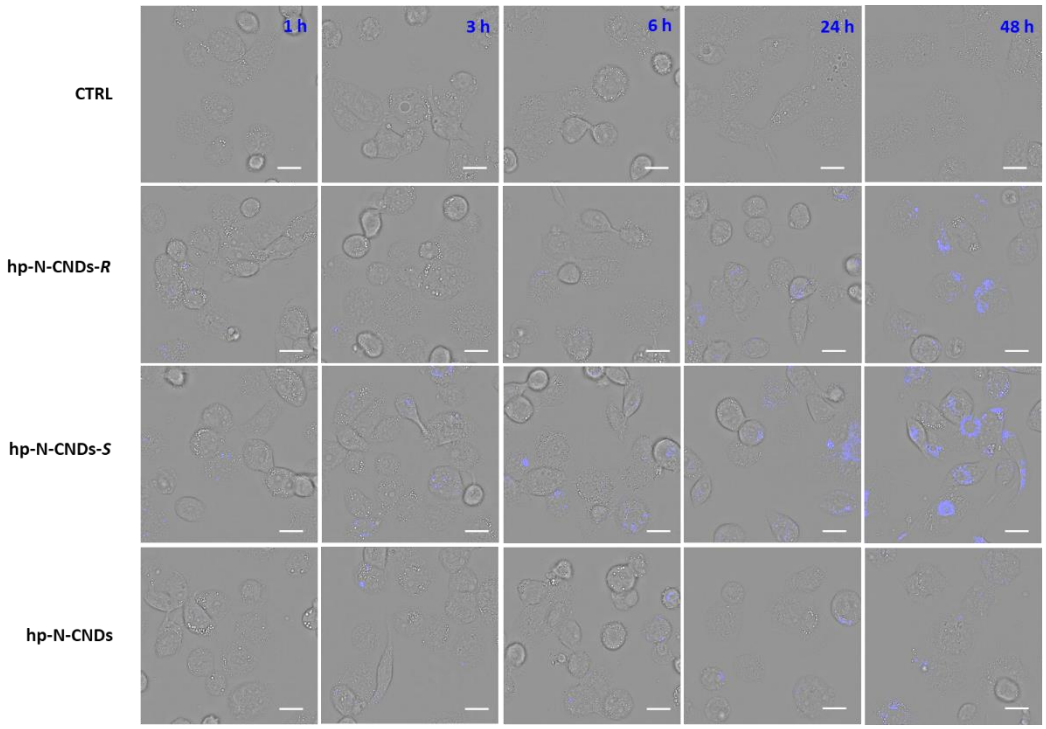

Figure 2.13 Cellular uptake of hp-N-CNDs and hp-N-cCNDs (400 μg mL^{-1}) in THP-1 macrophages using RPMI 1640 medium without FBS (scale bar 20 μm). The images were constructed as super imposition of the image obtained irradiating at 405 nm and the bright field image.

More specifically, for the tests without FBS a low internalization is generally registered at the first time points (1, 3 and 6 h) because during the first hour of exposure hp-N-CNDs-*S* are more internalized as compared to the -*R* (**Figure 2.13**). This difference is even more pronounced at higher time points. Moreover, in presence of FBS, the -*R* nanoparticles showed a lower internalization in CLSM, which is similar to the achiral dots (**Figure 2.14**). This difference is more pronounced at the shortest exposure times when the -*S* enantiomer begin to be better internalized after 1 h of exposure. Moreover, as compared to the test without FBS, the -*S* enantiomer maintains the same trend of higher uptake in respect to the -*R*.

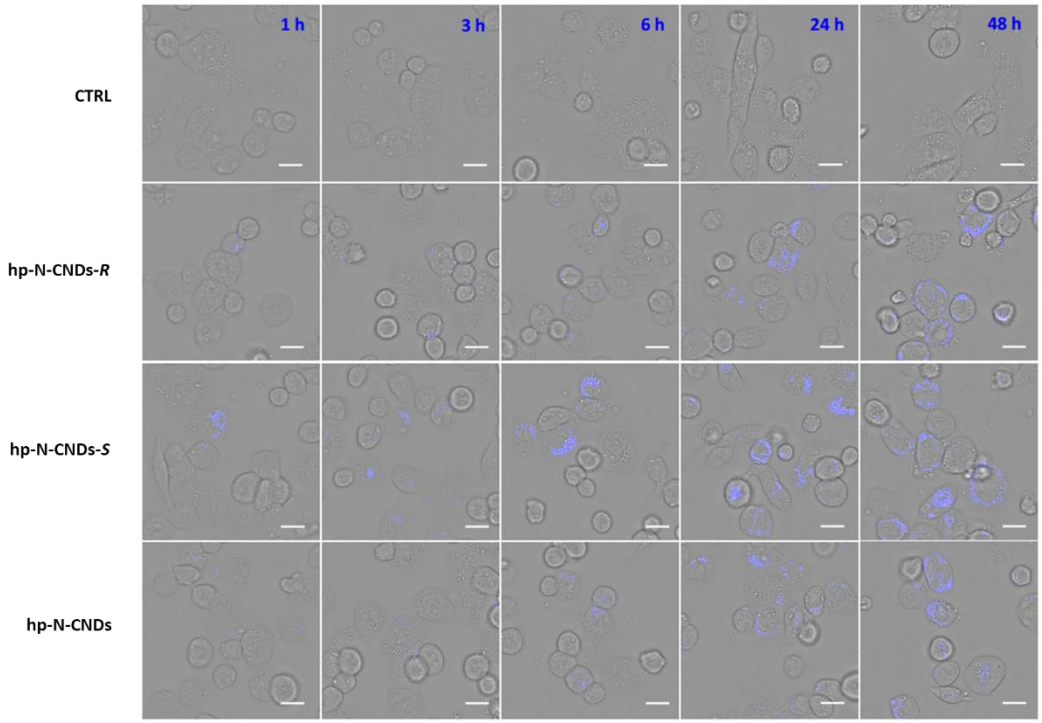

Figure 2.14 Cellular uptake of hp-N-CNDs and hp-N-cCNDs (400 μg mL^{-1}) in THP-1 macrophages using RPMI 1640 medium in presence of 10% FBS (scale bar 20 μm). The images were constructed as super imposition of the image obtained irradiating at 405 nm and the bright field image.

FBS is mainly composed of proteins and these are generally responsible for the agglomeration processes with nanoparticles.[64] These processes strongly affect the internalization and, in some cases, the protein/nanoparticle complex could better trespass the cytoplasmatic membrane in phagocytes.[125] This behavior could be ascribed to various factors such as the charge/chiral affinity, the curvature and the size of the nanoparticle. Such features influence the recognition of the extracellular material by the phagocyte receptors activating or blocking the process. If the interaction is strong and arises from high affinity, the protein could undergo changes of conformation. These changes result in unnatural conformations that strongly activate the phagocytosis during the opsonization. Human serum albumin (HSA) is the principal protein responsible of these interactions and forms the so known "protein corona" on the nanoparticle surface. The literature provide examples about the selectivity that HSA, in quality of chiral biomolecule, might have when it is interfaced to a chiral particle surface, but no studies on CNDs have been reported yet.[109,110,112] For these reasons, we studied the interactions between our chiral carbon dots and HSA. Therefore, we prepared the hp-N-cCNDs/HSA

complexes using size exclusion chromatography (SEC) as purification technique in order to separate the complex from the free nanoparticles. Then, the use of fluorescence correlation spectroscopy has been employed as useful technique to obtain information about the interactions present in the hp-N-cCNDs/HSA complexes.[126] In particular, by measuring the diffusion coefficients, we were able to get insights on the ratio and the magnitude of interaction between hp-N-cCNDs and HSA. The obtained results suggest that the two enantiomeric particles interact with different ratios of HSA (**Figure 2.15**). In particular, the hp-N-cCND-*S* enantiomer interacts with higher amounts of HSA. The higher shift of the fit of the autocorrelation function is typical of higher diffusion coefficients. These coefficients are related to higher hydrodynamic ratios due to the presence of bigger complexes as a result of the agglomeration with proteins.[126,127]

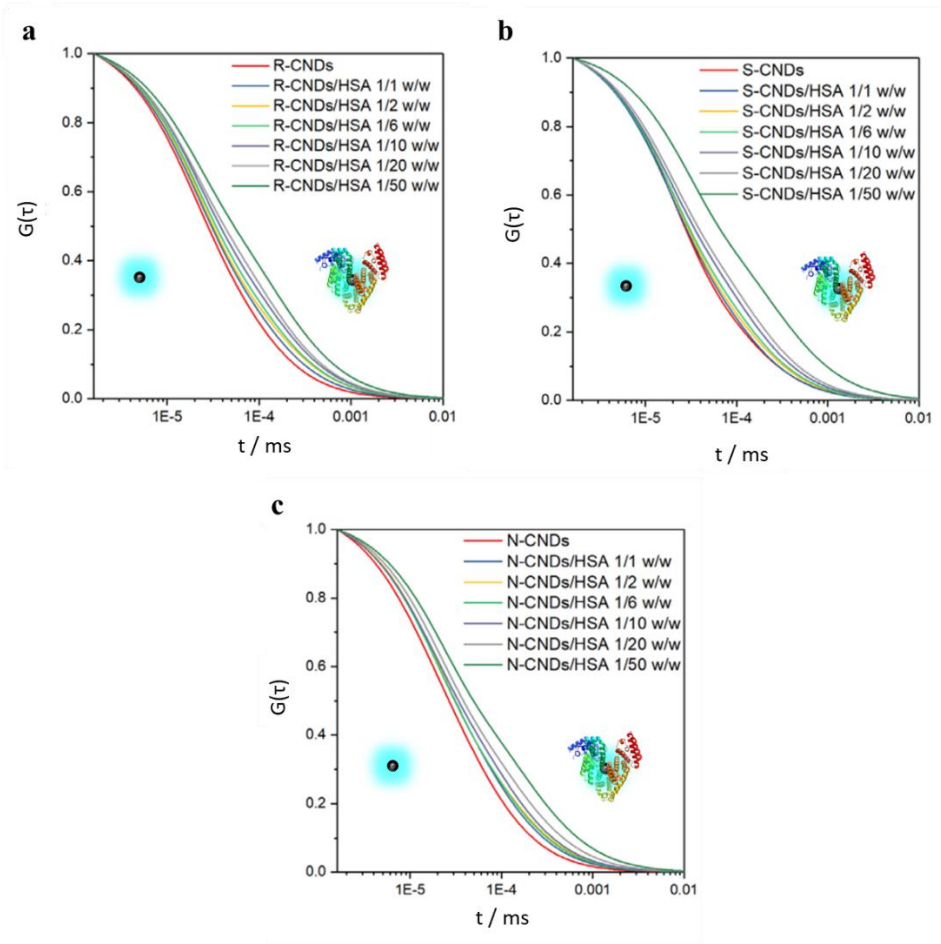

Figure 2.15 Autocorrelation function G(τ) of the fluorescence intensity of (**a**) hp-N-CNDs-*R*, (**b**) hp-N-CNDs-*S*, (**c**) hp-N-CNDs incubated with HSA at different concentrations. Excitation laser line: 488 nm. Each curve is the average of 100 repetitions.

We have also performed a screening on the cell uptake mechanism of these nanoparticles. These studies are based on the use of reference inhibitors, to understand which is the preferable uptake mechanism of the nanoparticle. We used nocodazole, bafilomycin A, amiloride and chlorpromazine hydrochloride that inhibit endocytosis, phagocytosis, macropinocytosis and clathrin-mediated endocytosis, respectively. The results show that, both in presence and absence of FBS, all the nanoparticles are internalized by phagocytosis (**Figure 2.16** and **2.17**).

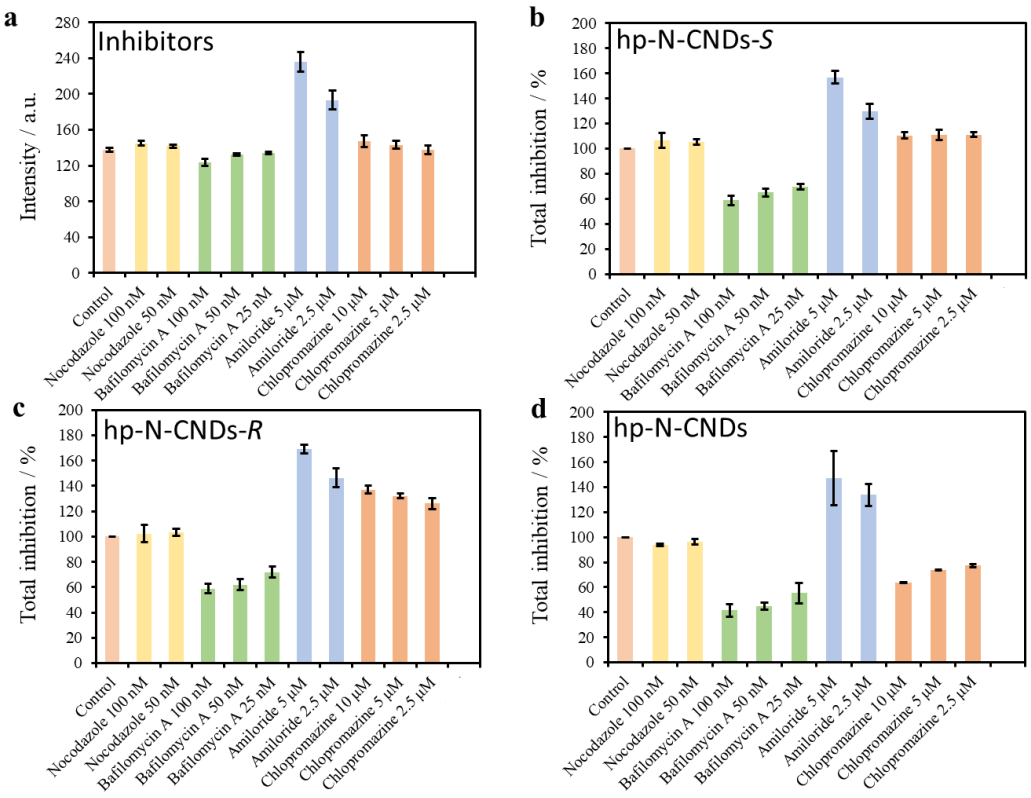

Figure 2.16 Uptake inhibition experiments at different concentration of selected inhibitors (**a**), in presence of hp-N-cCNDs (**b, c** - 400 µg mL^{-1}) and hp-N-CNDs (**d** - 400 µg mL^{-1}) in RPMI 1640 medium without FBS. All the cell samples were firstly incubated with the endocytic inhibitors for 7 hours. CNDs (**b**, **c**, **d**) were subsequently added and the measures were done after 6 hours of incubation.

This finding explains why, in presence of FBS, hp-N-cCNDs-*S* are more internalized at short exposure times in respect to the -*R* because it might be related to the higher affinity of the protein/nanoparticle complex, as discussed above. Moreover, the absence of FBS could explain why all the nanoparticles present a lower uptake at the first exposure time points. This behavior could be due to the

higher difficulty of the uptake of the free nanoparticles *via* phagocytosis because of a lower recognition ability by the receptors.

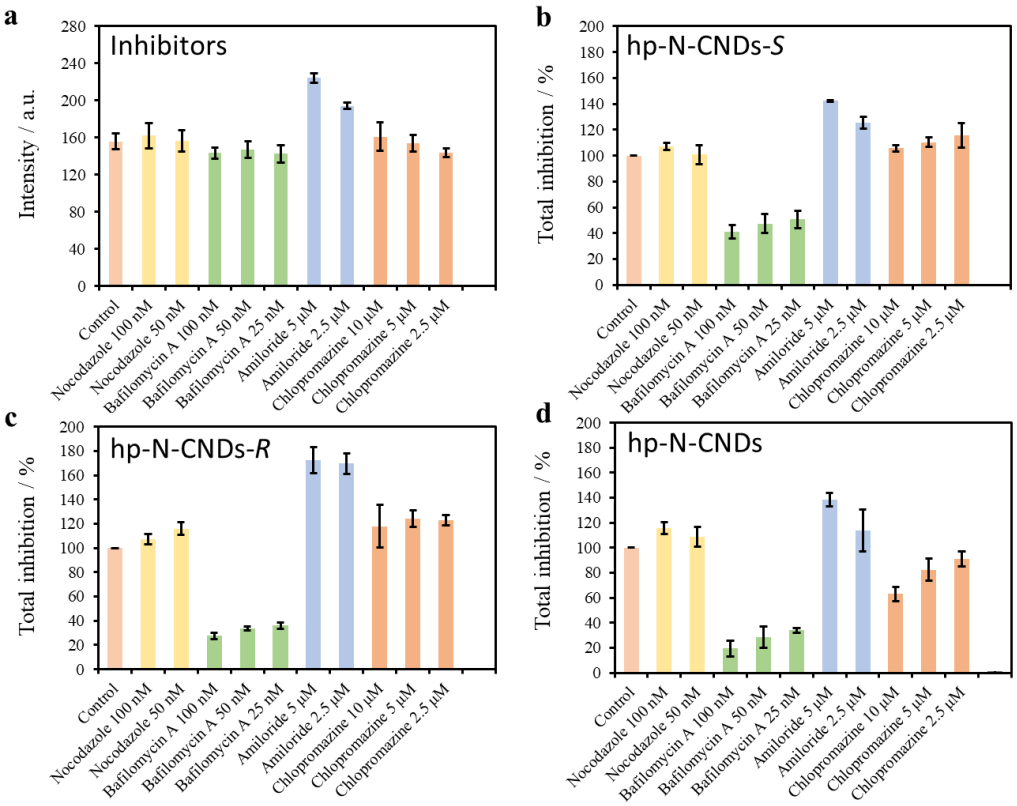

Figure 2.17 Uptake inhibition experiments at different concentration of selected inhibitors (**a**), in presence of hp-N-cCNDs (**b, c** - 400 µg mL^{-1}) and hp-N-CNDs (**d** - 400 µg mL-1) in RPMI 1640 medium with 10% FBS. All the cell samples were firstly incubated with the endocytic inhibitors for 7 hours. CNDs (**b**, **c**, **d**) were subsequently added and the measures were done after 6 hours of incubation.

2.2 Customizing chiral carbon nanodots by using naphthalene dianhydrides as precursors

2.2.1 Synthesis and purification

The introduction of chirality in carbon dots, as shown in **Section 2.1**, is of great relevance to design new chiral nanoparticles. The method that we proposed shows how making chiral nanoparticles in only one step synthetic approach.[30] This was possible by using precursors like (*R*,*R*)- or (*S*,*S*)-1,2-cyclohexanediamine that retain chirality at the working temperatures. In this context, the ability to produce particles with different photophysical properties, but still retain the chirality, is of great interest. As discussed in **Section 1.3** our group has recently shown how the chemistry of naphthalene diimides (NDI) could play an important role for the modification of the emissive properties of carbon nanodots.[27,128]

In this context, we used our protocol to tune the structural properties of CNDs using NDI as dopants but retaining the chirality. Indeed, we exploited the chemistry of naphthalene dianhydrides to modify the structure of chiral CNDs during the synthetic process. We focused on the use of 1,4,5,8-naphthalenetetracarboxylic acid-1,8:4,5-dianhydride (NDA) as dopant. The protocol consisted on a modified MW assisted hydrothermal process in which NDA was reacted directly with Arg and CHDA (**Figure 2.18**).

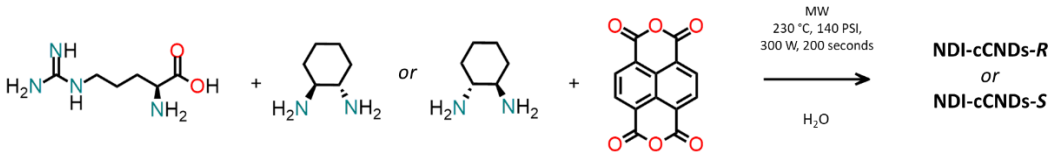

Figure 2.18 Synthetic scheme of hp-NDI-cCNDs.

After the synthesis the solution changed color from brown to dark brown indicating the successful carbonization. The reaction mixture was then microfiltered and purified using size exclusion chromatography, affording NDI-doped chiral CNDs (hp-NDI-CNDs-*R* and -*S*).

2.2.2 Characterization

The morphological and structural characterization was determined by AFM, FT-IR and XPS studies (**Figure 2.19 and Figure S2.13,14,15**).

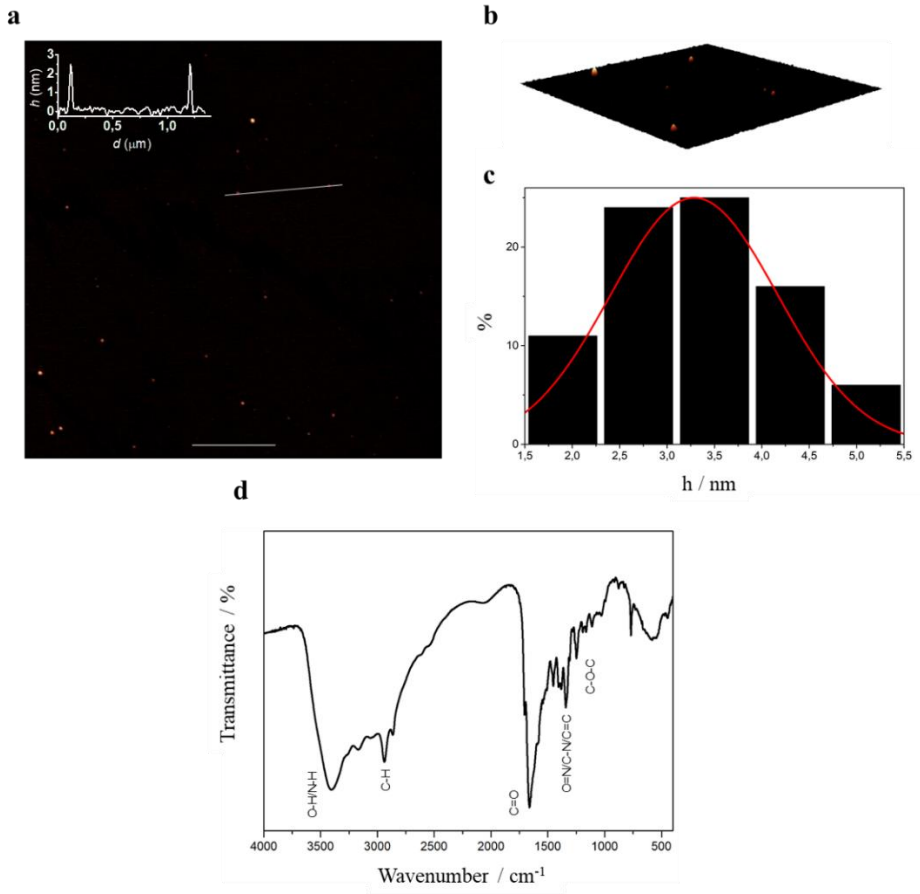

Figure 2.19 Morphological and structural characterization of hp-NDI-CNDs: (**a**) AFM image of hp-NDI-CNDs-*S* (5.0 × 5.0 μm), scale bar on the bottom (1 μm) and height profile along the dashed line (top left); (**b**) 3D close-up hp-NDI-CNDs-*R* AFM image (0.5 × 0.5 μm); (**c**) height sizes distribution histogram and superimposed Gaussian fit; (**d**) FT-IR spectrum (KBr) of hp-NDI-CNDs-*S*.

The AFM images indicated the formation of round shaped particles with an average size of 3.29 ± 0.88 nm, similarly to hp-NDI-CNDs (**Figure 2.19a,b,c** and **Figure S2.13**). FT-IR spectrum showed functional groups similar to the ones present in hp-NDI-CNDs (**Figure 2.19 d** and **Figure S2.14**). The intensity peaks at 1116, 1162 and 1196 cm^{-1} are representative of C-O-C bonds. Moreover, the signals at 1252, 1343 and 1382 cm^{-1} confirm the presence of C-O bonds. The absorption at 1453 cm^{-1} is indicative of C-N bond, while the shoulder at 1586 cm^{-1} suggests the presence of C=N/C=C bonds. The signals at 1661 and 1702 cm^{-1} indicate the

presence of C=O bonding and the peaks at 2857 and 2936 cm^{-1} are indicative of C-H stretching. Finally, the broad peaks at 3166 and 3402 cm^{-1} suggest the presence of O-H/N-H vibrations.

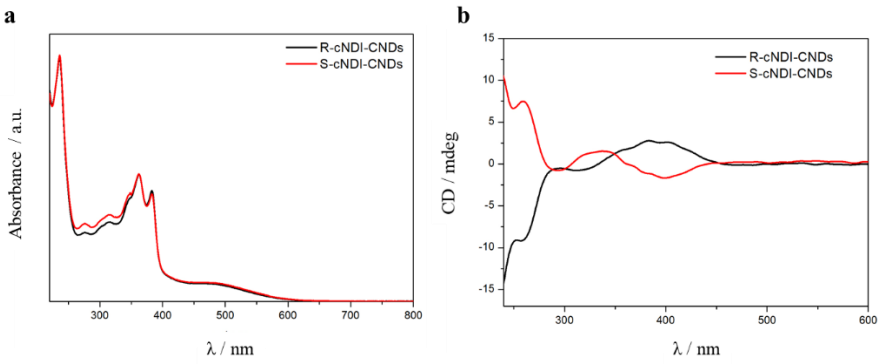

Figure 2.20 UV-Vis (**a**) and EDC (**b**) spectra of hp-NDI-CNDs-*R* (black line) and hp-NDI-CNDs-*S* (red line) registered in water.

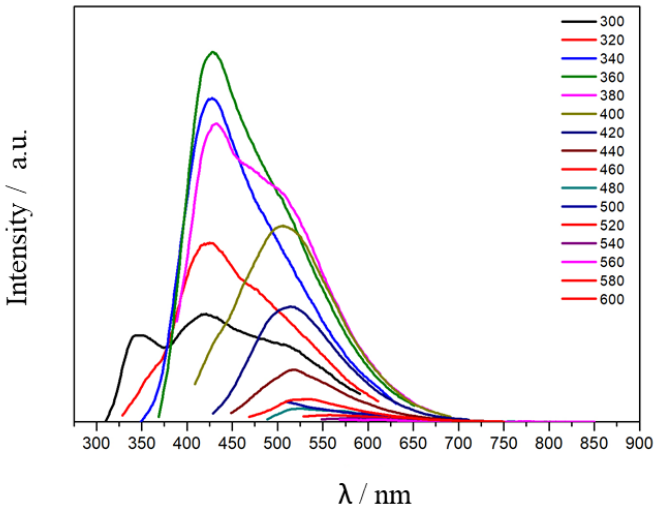

Figure 2.21 Fluorescence emission spectra of hp-NDI-CNDs-*S* at different excitation wavelengths (top right, from 300 nm to 600 nm) in water.

The optical properties were investigated by UV-Vis absorption and fluorescence emission spectroscopies. The two absorption maxima at 360 and 384 nm are typical of the NDI 0→0 and 1→0 vibronic bands related to the $S_0 \rightarrow S_1$ electronic transition.[129,130] The three absorption maxima at 236, 275, and 314 nm are typical of the π→π* and n→π*NDI and aromatic units present in the nanoparticle (**Figure 2.20a**). The successful conferring of chirality is observed by CD that showed four Cotton effects (260, 293, 327 and 385 nm) and mirror images between the two chiral

nanoparticles (**Figure 2.20b**). The first two bands could arise from the multiple excitation couplings between the chiral aromatic units, while the broader signals at 327 and 385 nm could be attributed to the $\pi \rightarrow \pi^*$ electronic transitions of the various NDI subunits composing the nanoparticle.

The fluorescence spectra exhibited a broad emission bands from 320 to 670 nm with a maximum peak at 430 nm (**Figure 2.21 and Figure S2.15**). The emission resulted excitation dependent (excitation from 300 to 600 nm) suggesting the presence of different emissive sites that is typical of CNDs.

2.3 Conclusions

This chapter report on the design, synthesis and characterization of chiral carbon nanodots. We demonstrate that the chirality is conferred, through a hydrothermal bottom-up microwave assisted synthesis, by using arginine and trans-cyclohexanediamine as precursors. The obtained carbon nanodots possess similar size, morphological and photophysical properties to the previously reported achiral CNDs (prepared using arginine and ethylenediamine). However, most importantly, they possess chirality that resulted in CNDs-S and CNDs-R. The chirality was investigated in their ground states and in the UV–Vis and IR regions. ECD spectroscopy show two mirror image profiles, also evidenced by their VCD spectra. Additionally, the origin of chirality is ascribed to the presence of numerous cyclohexanediamine moieties around the carbon-based amorphous core. These findings opened up to the application of this synthetic approach to introduce chirality in other carbon dots. Indeed, chiral CNDs were successfully obtained using different core precursors (citric acid) and using doping molecules (naphthalene dianhydrides) to tune their properties. The chirality was also successfully transferred from the chiral CNDs, through electrostatic interactions, to tetranionic porphyrins, inducing formation of chiral assemblies.

In the last part, we have studied the effects of chiral surfaces in CNDs are with cells and proteins. The cellular uptake studies on a phagocytic cell line revealed that the -*S* enantiomer of the nanoparticle is internalized more and faster compared to the -*R*. In addition, the cellular uptake studies in presence of PBS elucidated the possible role that the serum proteins has on the internalization by showing an enhanced uptake in the case of the -*S* when PBS is present as compared to when it is not and an inverted trend for the -*R* enantiomer. Moreover, a preliminary study on the CNDs/HSA interaction, obtained from FCS studies, indicated that the -*S* enantiomer is able to form bigger aggregates compared to the -*R* and the achiral reference. This latter evidence suggests that the chiral surface of the -*S* nanoparticles could be responsible of the higher affinity for the chiral protein. This phenomenon was previously reported in literature and could explain why the phagocytes favor the internalization of one enantiomer respect to the other because

the bigger size of the bio-conjugates are more prone to being internalized *via* phagocytosis.

2.4 Experimental section

2.4.1 Materials

All the reagents and solvents were bought from Sigma-Aldrich, TCI, VWR Int. and used as received. Dialysis tubes with molecular weight cut-off of 1 KDa were bought from Spectrum Labs. Ultrapure fresh water was obtained from a water purification system (>18MΩ·cm Milli-Q, Millipore). THP-1 cell lines were bought from ATCC®. Resazurin assay (AlamarBlue®), RPMI 1640 medium and FBS solutions were bought from Thermo Fisher.

2.4.2 Methods

All the hydrothermal processes were conducted on a CEM Discover-SP microwave synthesizer. Fourier-Transform Infrared (FT-IR) spectra were recorded on KBr pellet of the samples using a Perkin Elmer 2000 spectrometer. Atomic Force Microscopy (AFM) images were acquired using a Nanoscope IIIa microscope, VEECO Instruments. The AFM analyses were performed in tapping mode mounting a HQ:NSC19/ALBS probe (80kHz; 0.6 N/m) (MikroMasch). The AFM samples were prepared by drop casting the aqueous solution (concentration of few mg/mL) on a mica substrate. AFM-images were further analyzed in Gwyddion 2.35. The statistical analysis was performed on about one hundred nanoparticles and the average size was calculated from the size histogram with curve fit to the data using a Gaussian model. X-Ray Photoemission Spectroscopy (XPS) spectra were recorded on a SPECS Sage HR 100 spectrometer using a non-monochromatized Mg-Kα radiation of 1253.6 eV and 250 W, in an ultra-high vacuum chamber at pressure below 8×10^{-7} mbar. The XPS samples were prepared depositing an aqueous solution (ca. 3 mg/mL) of material on a gold thin film. The calibration was done using the 3d5/2 line of Ag. Survey and high- resolution spectra were collected with pass energy of 30 and 15 eV and 0.5 and 0.15 eV/step, respectively. CasaXPS 2.3.17 PR1.1 and Avantage (Thermo Fisher Scientific) software were used for data processing and fitting. Curve fittings were realized

using a Gaussian-Lorentzian peak shape after performing a Shirley background correction, to finally obtain the relative percentage of the chemical bonds of the analyzed sample.

UV-Vis spectra were recorded on a PerkinElmer Lambda 35 UV-Vis spectrophotometer. Fluorescence spectra were recorded on a Varian Cary Eclipse Fluorescence Spectrophotometer. Both UV-Vis and Fluorescence spectra were recorded at room temperature using 10 mm path-length cuvettes. The relative quantum yield measurements were performed using a quinine sulphate solution (0.10 M H_2SO_4) as reference (reported quantum yield 0.54).

Time-resolved fluorescence was measured by a duplicated tunable femtosecond (100 fs) Ti:Sa laser (Spectra Physics MaiTai DeepSee - Radiantis Inspire Blue), set at 350 nm, used for the excitation. The signal emitted at at 450 nm was selected through a monochromator (Oriel Cornerstone) with focal length of 280 mm and collected by a multichannel- plate photomultiplier (Hamamatzu R1645U-01, 100 ps rising-time). The electronic equipment necessary for pre-amplification, constant-fraction discrimination and laser pulse synchronization in the time-correlated-single-photon counting (TCSPC) method was realized with EG&G devices. By using nonlinear least-squares iterative reconvolution procedures a time resolution better than 50 ps was obtained. Fluorescence time decay curve was fitted according to the following multiexponential relation:

$$I(t) = I_0 \sum_i A_i \exp\left(-t/\tau_i\right)$$

in which *I(t)* is the fluorescence decay curve, I_0 is the intensity at time zero and A_i is the amplitude of the i^{th} component ($\Sigma_i A_i = 1$) with lifetime τ_i.

Differential fluorescence was recorded *via* fluorescence detection of circular dichroism. This was made exciting the sample with circularly polarized light generated by a JASCO J500A spectropolarimeter (with resolution of 8 nm).

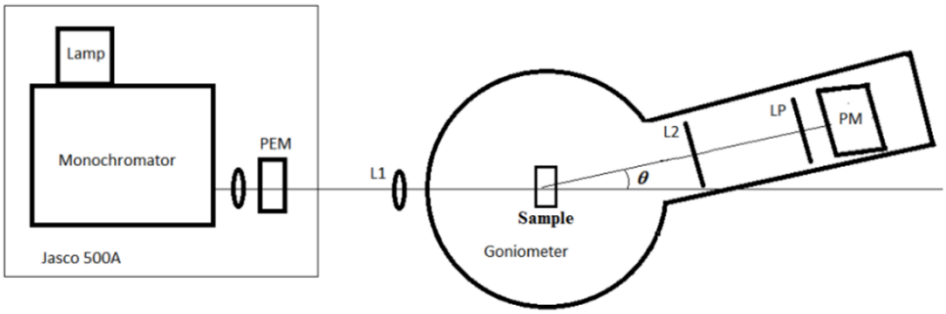

Figure 2.24 Scheme of the home-made experimental set-up for the fluorescence detected circular dichroism (FDCD) measurements.

The detection apparatus was modified as indicated in the scheme of **Figure 2.24**: the sample was contained in 4-windows quartz cuvette (length path of 1 cm); the circularly polarized light was focused on the cuvette, using a quartz lens (L1, focal length 150 mm), obtaining an irradiated volume of 2 mm wide; the exiting light was let passing through a glass lens (L2, focal length 50 mm) before the photomultiplier (PM, Hamamatzu R376); to eliminate the excitation light from the collected signal a long pass filter (LP, cut-off 465 nm, optical density higher than 3 below 425 nm and transmission of 90% above 500 nm) was placed before the photomultiplier; the detection optics were placed on a mobile goniometer to collect the emission at off the transmitted beam at different angles (the angle θ was set at 15° and at -15°, in order to avoid eventual artefacts arising from fluorescence polarization effects; the photomultiplier voltage was tuned between 650 and 850 V to maintain the current constant in all the investigated wavelength range; the pre-amplified signal as analyzed by a lock-in amplifier (Stanford SR510); due to the low signal-to-noise ratio, the lock-in integration time constant was set at 30 s and all the spectra reported are the average of five repeated measurements. The CNDs samples solutions were prepared at a concentration of 0.16 mg/mL (pH = 9). The baseline for the fluorescence detected CD was obtained using as reference sodium fluorescein aqueous solution (2×10^{-5} M).

Electronic circular dichroism spectra were recorded using Jasco J-810 at room temperature (quartz cuvette 1 cm path length): scanning rate 50 nm/min, data pitch 0.2 nm, D.I.T 2 s. Each CD spectrum resulted from an average of at least five scans.

Vibrational circular dichroism (VCD) spectra were acquired on a Bruker PMA 50 accessory coupled to a Tensor 27 Fourier transform infrared spectrometer. The experimental set-up consisted on a photoelastic modulator (Hinds PEM 90) set at 1/4 retardation for tuning the handedness of the circular polarized light; the demodulation was performed using a lock-in amplifier (SR830 DSP); an optical low-pass filter (< 1800 cm^{-1}) was placed in front of the photoelastic modulator to enhance the signal/noise ratio. The sample was prepared dissolving the CNDs in D_2O (ca. 5 mg in 50 mL). The spectra were finally recorded on a thin film of sample solution (thickness ca. 13 μm) sandwiched between two CaF_2 windows. The average of the measured VCD spectra of the two enantiomers served as the reference and was subtracted from the VCD spectra of pure enantiomers in order to eliminate artefacts.[131] This procedure automatically produces mirror image spectra. For both enantiomers 24000 scans at 4 cm^{-1} resolution were averaged. The simulation (DFT calculation) of VCD spectra started by constructing probable cyclohexanediamine fragments (information extracted from experimental data). Preliminary conformational searches of cyclohexanediamine fragments (neutral or protonated) were performed using semi-empirical level (PM3)[132] and the conformational geometries were then optimized using DFT (B3LYP/6-31G*)[133–135], using the Spartan program package.[136] The most stable conformers were then used as starting geometries for the optimization and frequency (=vcd) calculations (B3LYP/6-31G**), in water (PCM solvation)[137], using Gaussian software.[138] Finally, the selected fragments conformers were used for VCD calculations using the B3PW917,[139] hybrid functional and 6-31G** basis set,[140] in water. Vibrational frequencies were scaled by a factor of 0.95. IR and VCD spectra were constructed from calculated dipole and rotational strengths assuming Lorentzian band shape with a half-width at half-height = 5 cm^{-1}. Description of calculated vibrations was made from animations of the modes and spectra with GaussView 5.08.13.

Flow cytometry was performed on a BD LSRFORTESSA *via* direct injection of the cells solution using a 405 nm (violet laser) and detecting the emission at 450/50 nm (pacific blue). Confocal laser scanning microscopy images and fluorescence correlation spectroscopy measures were recorded on a Carl Zeiss CLSM 510 Meta.

Resazurin assay was determined treating the cells cultures with a concentration of 9% of resazurin and waiting an incubation period of 4 hours.[122] After this treatment the cell culture was washed with fresh RPMI medium and exposed to a RPMI solution of CNDs (400 μg mL^{-1}) for 24 or 48 hours. The cell cultures were then washed and analyzed by means of fluorescence emission of resorufin to calculate the viability assay as percentage referred to the control sample.

The FCS study of the carbon nanodots was carried out on a confocal light scanning microscope (LSM) Carl Zeiss 880 (Zeiss, Germany). HSA was mixed with a fixed concentration of the CNDs in phosphate buffered saline (PBS) solution (pH = 7.2). The solutions of HSA were varied in concentration from 0 μM to 500 μM prepared by sequential dilution of a concentrated stock solution. All samples were incubated for 15 minutes before the measurements. The samples were prepared by drop casting few microliters of CNDs solution in 35 mm petri dish with a glass bottom slide as cover (Cat.No: 81218-200, "ibidi", Germany). The measurements were collected for about 5 minutes and for each concentration three independent measurements were done. The correlation function was then calculated as previously reported.[126,127]

2.4.3 Synthesis of hp-N-cCNDs

Chiral CNDs were obtained *via* microwave irradiation of an aqueous solution of L-Arginine (Arg) and (R,R)-(-)-cyclohexanediamine or (S,S)-(+)-cyclohexanediamine (1:1 mol/mol). Typically, Arg (87.0 mg), (R,R)-(-)-cyclohexanediamine or (S,S)-(+)-cyclohexanediamine (57.0 mg) and Milli-Q water (100.0 μL) were heated at 240 °C, 70-110 psi and 200 W for 180 seconds. In the process of microwave heating, the color changed from yellow to dark brown as a result of formation of CNDs. The reaction mixture was then diluted with a few milliliters of water and the solution was filtered through a 0.1 μm microporous membrane separating a deep yellow solution that was dialyzed against pure water through a dialysis membrane for 2 days. The aqueous solution was then lyophilized giving a brownish solid (hp-N-CNDs-*R*: 20.5 mg; hp-N-CNDs-*S*: 22.0 mg).

2.4.4 Chiral Supramolecular Assemblies

CNDs stock solution was prepared by dissolving 1.9 mg in 2.5 mL of ultrapure water obtained from Elga Purelab Flex system by Veolia; the pH of the solution was 9. The porphyrin selected for our study is the tetranionic meso-tetrakis(4-sulfonatophenyl)porphyrin (H_2TSPP^{4-}). The stock solution of porphyrin was prepared by dissolving small amount of solid in ultrapure water at pH 7 in order to obtain concentration about 2×10^{-4} M, checked by spectrophotometer Jasco V-630 using $\varepsilon = 4.8 \times 10^{-5}$ M^{-1} cm^{-1} at $\lambda = 413$ nm. The sample solutions were achieved mixing CND solution and H_2TSPP^{4-} at pH = 6.5. After 30 minutes incubation, the pH was decreased to 2.5 in order to induce the formation of J-aggregates.

2.4.5 Synthesis of hp-NDI-cCNDs

A mixture of MilliQ water (130 μL), L-arginine (10.0 mg), NDA (15.1 mg) and (R,R)-(-)- cyclohexanediamine or (S,S)-(+)-cyclohexanediamine (13.0 mg) were heated at 230 °C, 140 PSI and 300 W for 200 seconds. After the thermal process the reaction turned is color to dark brown as result of formation of CNDs. The crude product was then diluted with few milliliters of MilliQ and the resulted solution (pH = 10.7) was acidified to pH 1.6 and filtered through a 0.1 μm microporous filter. The filtrate solution was then pH corrected at a value of 7.2 and filtered again through a 0.1 μm microporous filter. The obtained filtrate solution was then dried under vacuum. The solid residue was dissolved in few microliters of methanol and purified by size exclusion chromatography using a Sephadex LH-20 as stationary phase and methanol as mobile phase. The yellow product was then dried under vacuum, dissolved in water and lyophilized affording 12.7 mg of dark yellow solid.

2.4.6 Supporting figures

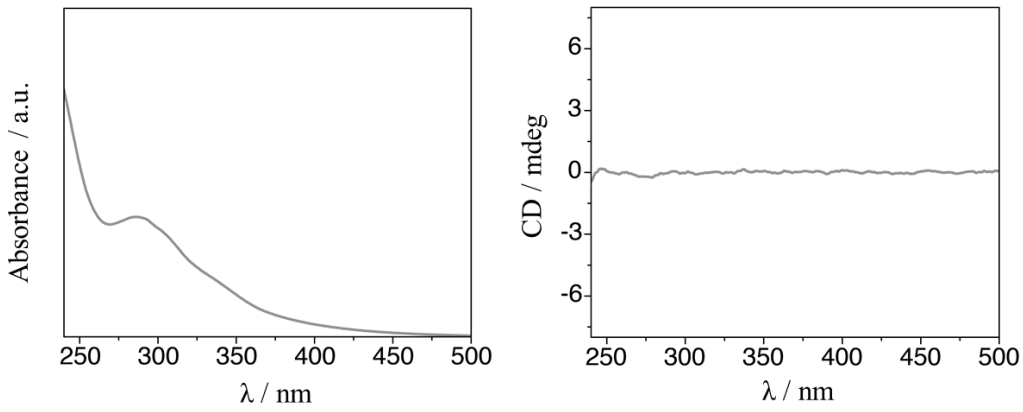

Figure S2.1 (Chiro)optical characterization in water (298 K) of hp-N-CNDs, obtained from Arg and EDA, *via* UV-Vis absorption (left) and ECD (right).

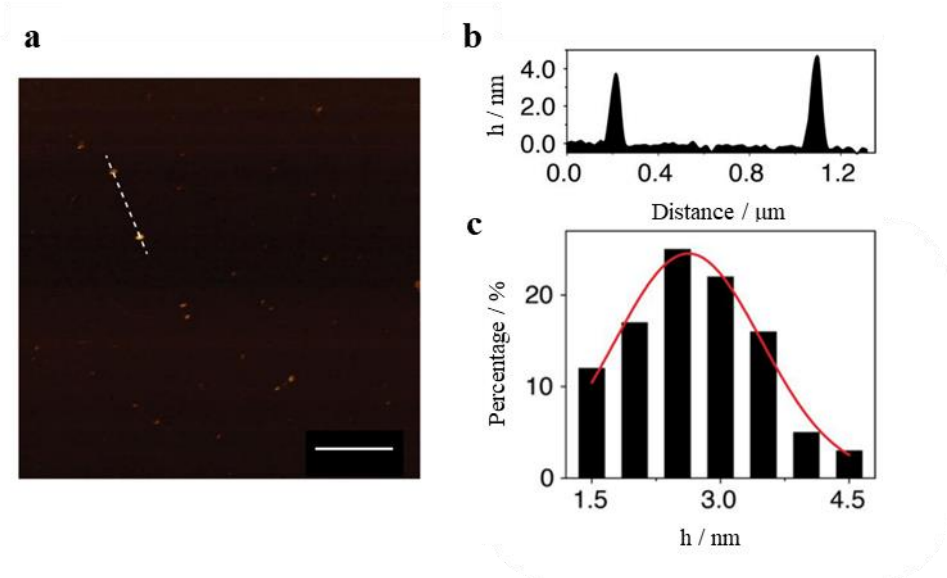

Figure S2.2 AFM analysis of hp-N-CNDs-*S*: (**a**) Tapping mode AFM (4.4 × 4.4 µm) from a drop-casted aqueous solution on a mica substrate (scale bar, 1 µm); (**b**) height profile along the dashed line; (**c**) size histogram with curve fit using a Gaussian model.

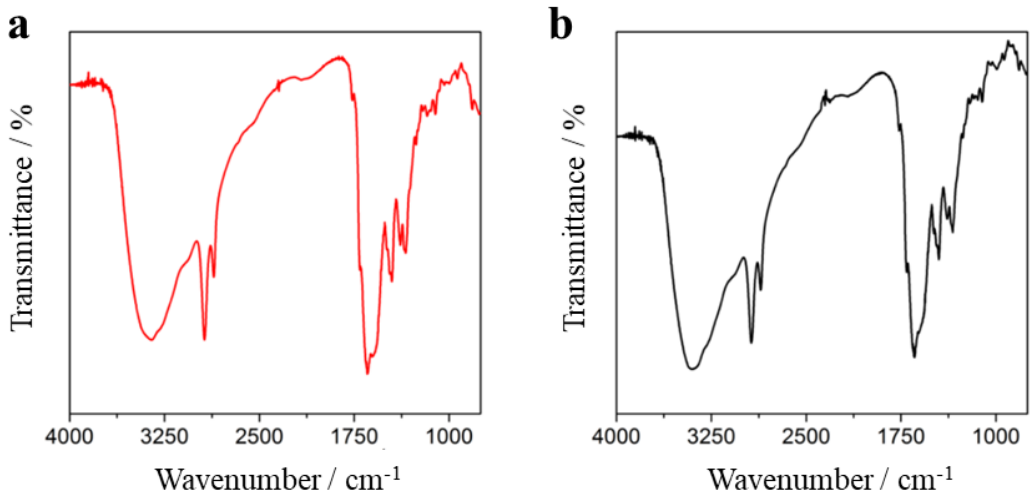

Figure S2.3 FT-IR spectra of hp-N-CNDs-*S* (**a**) and hp-N-CNDs-*R* (**b**).

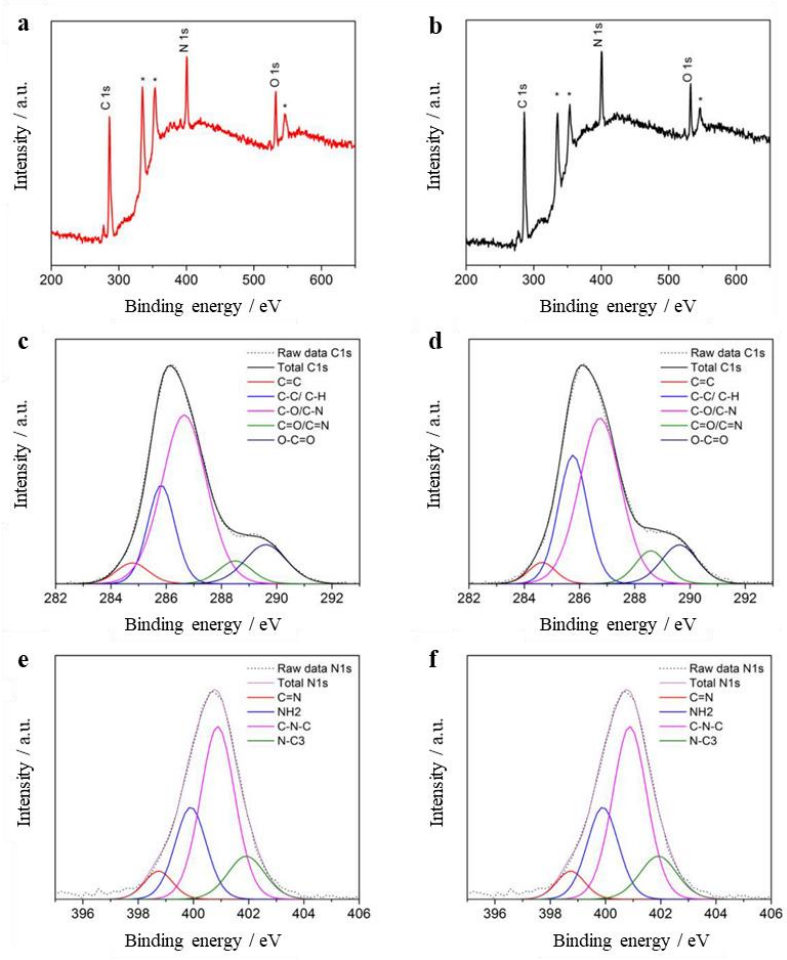

Figure S2.4 XPS analysis of hp-N-cCNDs: hp-N-CNDs-*S* (left) and hp-N-CNDs-*R* (right). (**a**,**b**) XPS survey showing the C1s, N1s and O1s (*from substrate Au4d3, Au4d5 and Au4p); (**c**,**d**) deconvoluted C1s spectra and (**e**,**f**) deconvoluted N1s spectra.

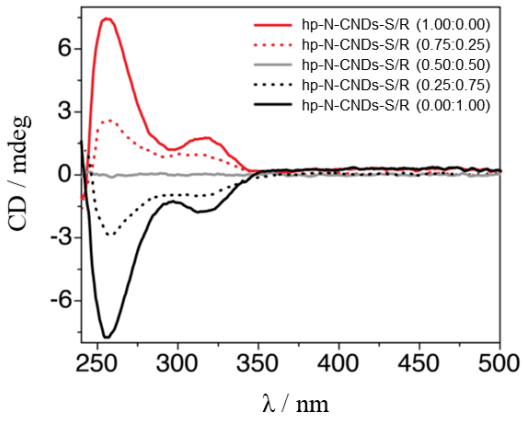

Figure S2.5 ECD spectra of hp-N-CNDs-*R*/*S* prepared by using arginine and different molar ratios of (*S*,*S*)- or (*R*,*R*)-CHDA: 1.00:0.00 (red line), 0.75:0.25 (red dashed line), 0.50:0.50 (gray line), 0.25:0.75 (black dashed line) and 0.00:1.00 (black line)**.**

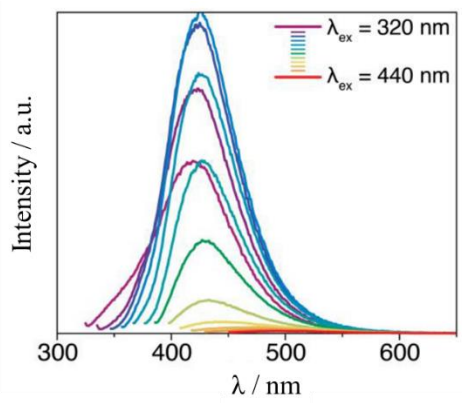

Figure S2.6 Fluorescence emission spectra of hp-N-CNDs-*S* in water at 298 K.

a

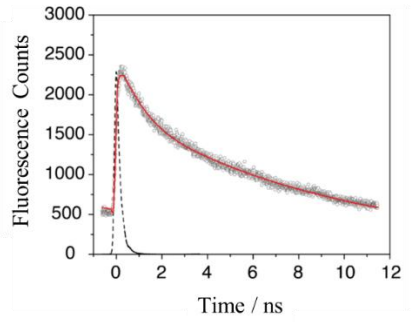

b

Sample	**A_1**	**$\tau_1 \pm 0.1$ (ns)**	**A_2**	**$\tau_2 \pm 0.1$ (ns)**	**τ_{ave} (ns)**
hp-N-CNDs-*S*	0.27	1.2	0.73	10.8	8.2
hp-N-CNDs-*R*	0.34	1.2	0.66	10.3	7.2

Figure S2.7 (**a**) Fluorescence time decay curve registered on an aqueous solution of hp-N-CNDs-*S* (black dashed line is instrument response) - analogous curve was measured for the hp-N-CNDs-*R* solution. (**b**) Fitting parameters of the fluorescence decay curves.

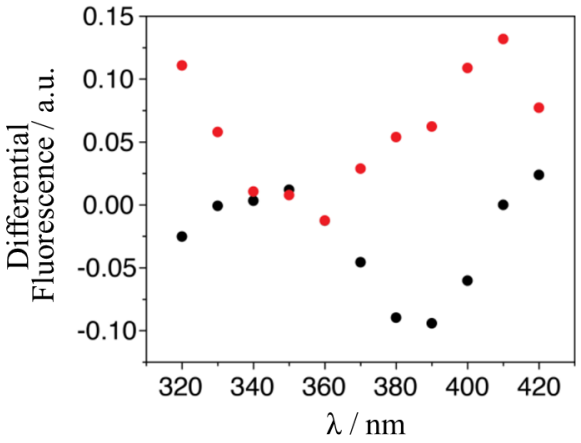

Figure S2.8 FDCD spectra of hp-N-CNDs-*S* and hp-N-CNDs-*R*: data collected above 465 nm at the angle θ = -15°, symmetric with respect to that reported in the main text.

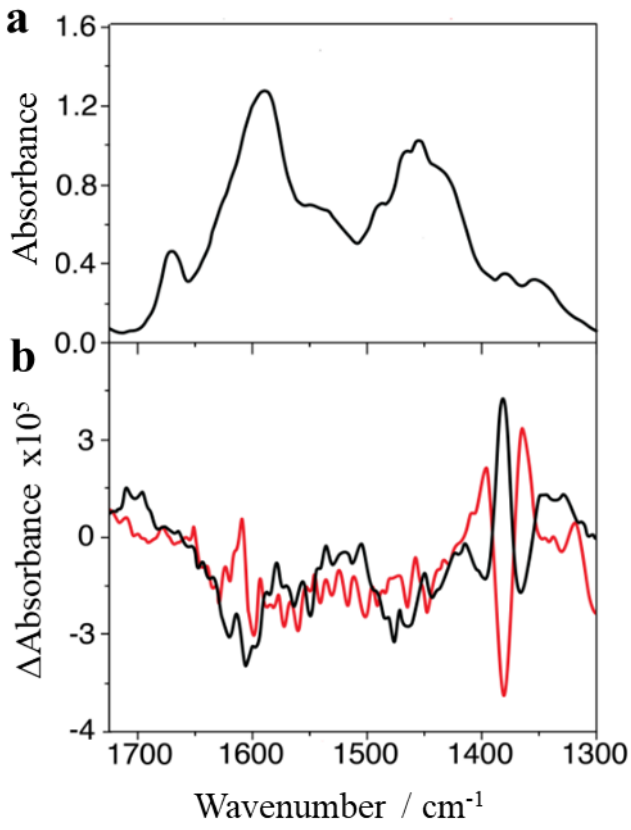

Figure S2.9 Experimental (**a**) IR and (**b**) VCD spectra for hp-N-CNDs-*R* (black trace) and hp-N-CNDs-*S* (red trace) referenced to D_2O. The spectra were then referenced to eliminate artefacts as described in **Section 2.4.2**.[131]

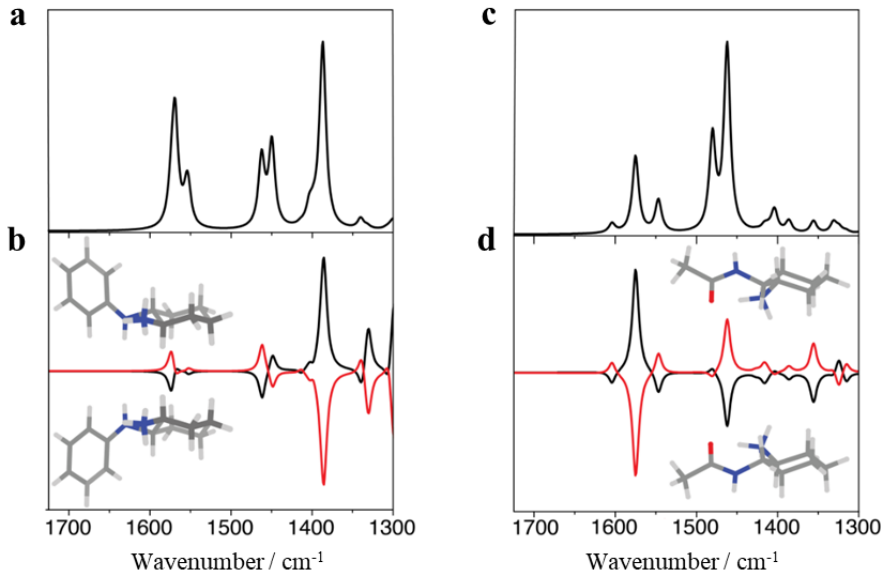

Figure S2.10 DFT calculated (**a**,**c**) IR and (**b**,**d**) VCD spectra for selected CHDA fragments, performed using the B3PW91 functional and a 6-31G** basis set, water PCM solvation.

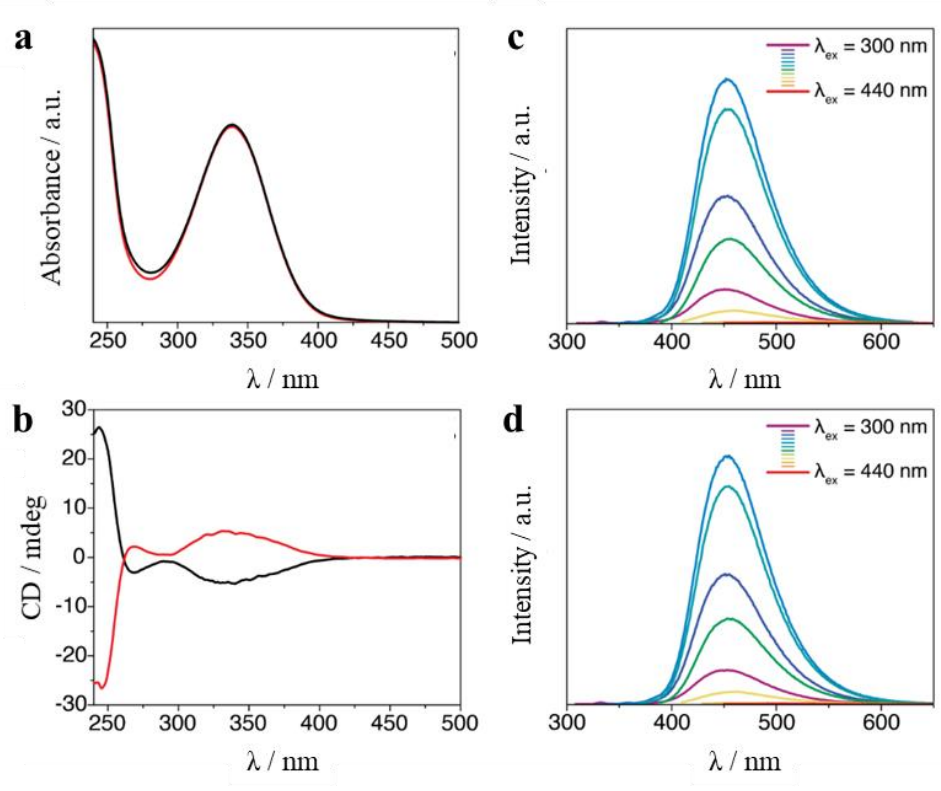

Figure S2.11 Photophysical and (chiro)optical characterization of hp-N-CitCNDs in water at 298 K: (**a**) UV-Vis spectra of hp-N-CitCNDs-*S* (red line) and hp-N-CitCNDs-*R* (black line); (**b**) ECD spectra of hp-N-CitCNDs-*S* (red line) and hp-N-CitCNDs-*R* (black line); (**c**,**d**) Fluorescence emission spectra of hp-N-CitCNDs-*R* and -*S*.

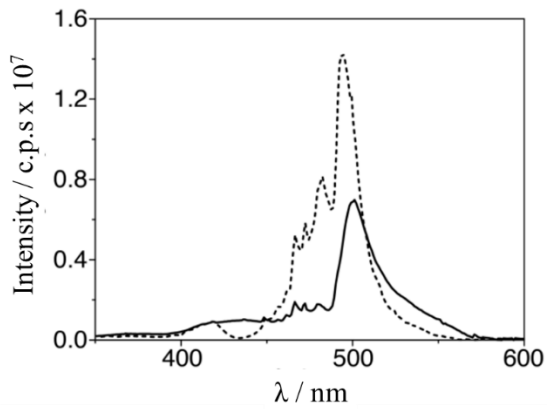

Figure S2.12 RLS spectra of a water solution of H_4TSPP^{2-} (6.0 μM) at pH 2.5 in the presence of hp-N-cCNDs (black line) and in the absence of hp-N-cCNDs (dashed line).

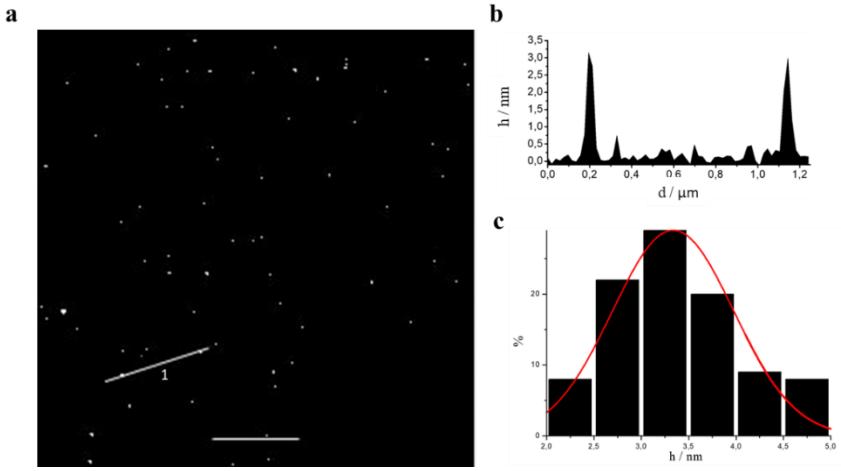

Figure S2.13 hp-NDI-CNDs-*R* AFM analysis: (**a**) AFM image of hp-NDI-CNDs-*R* (5.0 × 5.0 μm), scale bar on the bottom (1 μm); (**b**)height profile along the dashed line; (**c**) height sizes distribution histogram and superimposed Gaussian fit.

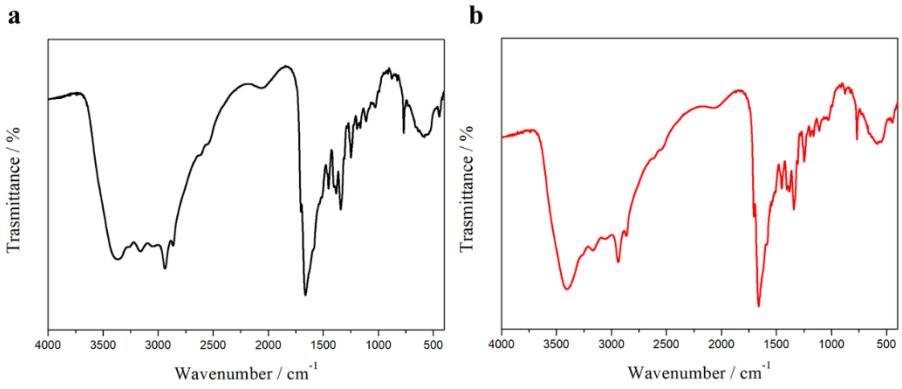

Figure S2.14 FT-IR spectra of (**a**) hp-NDI-CNDs-*R* and (**b**) hp-NDI-CNDs-*S*.

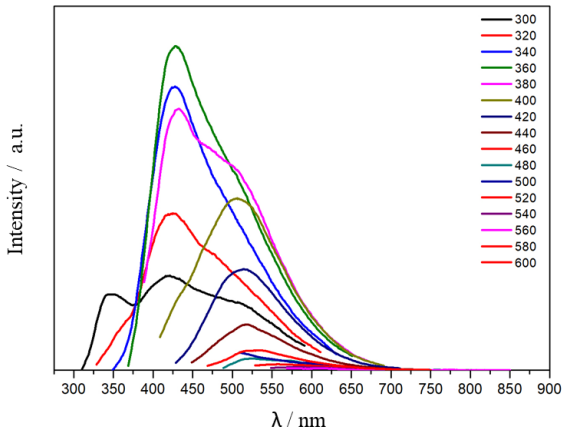

Figure S2.15 Fluorescence emission spectra of hp-NDI-CNDs-*R* at different excitation wavelengths (top right, from 300 nm to 600 nm) in water.

2.5 References

(1) Noguez, C.; Garzón, I. L. Optically Active Metal Nanoparticles. *Chem. Soc. Rev.* **2009**, *38* (3), 757.

(2) Schaaff, T. G.; Knight, G.; Shafigullin, M. N.; Borkman, R. F.; Whetten, R. L. Isolation and Selected Properties of a 10.4 KDa Gold:Glutathione Cluster Compound. *J. Phys. Chem. B* **1998**, *102* (52), 10643–10646.

(3) Gautier, C.; Bürgi, T. Chiral Gold Nanoparticles. *ChemPhysChem* **2009**, *10* (3), 483–492.

(4) Ben-Moshe, A.; Maoz, B. M.; Govorov, A. O.; Markovich, G. Chirality and Chiroptical Effects in Inorganic Nanocrystal Systems with Plasmon and Exciton Resonances. *Chem. Soc. Rev.* **2013**, *42* (16), 7028.

(5) Kumar, J.; Thomas, K. G.; Liz-Marzán, L. M. Nanoscale Chirality in Metal and Semiconductor Nanoparticles. *Chem. Commun.* **2016**, *52* (85), 12555–12569.

(6) Ma, W.; Xu, L.; De Moura, A. F.; Wu, X.; Kuang, H.; Xu, C.; Kotov, N. A. Chiral Inorganic Nanostructures. *Chem. Rev.* **2017**, *117* (12), 8041–8093.

(7) Durán Pachón, L.; Yosef, I.; Markus, T. Z.; Naaman, R.; Avnir, D.; Rothenberg, G. Chiral Imprinting of Palladium with Cinchona Alkaloids. *Nat. Chem.* **2009**, *1* (2), 160–164.

(8) Häkkinen, H. The Gold-Sulfur Interface at the Nanoscale. *Nat. Chem.* **2012**, *4* (6), 443–455.

(9) Ostovar Pour, S.; Rocks, L.; Faulds, K.; Graham, D.; Parchaňský, V.; Bouř, P.; Blanch, E. W. Through-Space Transfer of Chiral Information Mediated by a Plasmonic Nanomaterial. *Nat. Chem.* **2015**, *7* (7), 591–596.

(10) Farrag, M.; Tschurl, M.; Heiz, U. Chiral Gold and Silver Nanoclusters: Preparation, Size Selection, and Chiroptical Properties. *Chem. Mater.* **2013**, *25* (6), 862–870.

(11) Vázquez-Nakagawa, M.; Rodríguez-Pérez, L.; Herranz, M. A.; Martín, N. Chirality Transfer from Graphene Quantum Dots. *Chem. Commun.* **2016**, *52* (4), 665–668.

(12) Suzuki, N.; Wang, Y.; Elvati, P.; Qu, Z.-B.; Kim, K.; Jiang, S.; Baumeister, E.; Lee, J. J.; Yeom, B.; Bahng, J. H.; et al. Chiral Graphene Quantum Dots. *ACS Nano* **2016**, *10* (2), 1744–1755.

(13) Ostadhossein, F.; Vulugundam, G.; Misra, S. K.; Srivastava, I.; Pan, D. Chirality Inversion on the Carbon Dot Surface via Covalent Surface Conjugation of Cyclic α-Amino Acid Capping Agents. *Bioconjug. Chem.* **2018**, *29* (11), 3913–3922.

(14) Deka, M. J.; Chowdhury, D. Chiral Carbon Dots and Their Effect on the Optical Properties of Photosensitizers. *RSC Adv.* **2017**, *7* (84), 53057–53063.

(15) Hu, L.; Sun, Y.; Zhou, Y.; Bai, L.; Zhang, Y.; Han, M.; Huang, H.; Liu, Y.; Kang, Z. Nitrogen and Sulfur Co-Doped Chiral Carbon Quantum Dots with Independent Photoluminescence and Chirality. *Inorg. Chem. Front.* **2017**, *4* (6), 946–953.

(16) Zhang, M.; Hu, L.; Wang, H.; Song, Y.; Liu, Y.; Li, H.; Shao, M.; Huang, H.; Kang, Z. One-Step Hydrothermal Synthesis of Chiral Carbon Dots and Their Effects on Mung Bean Plant Growth. *Nanoscale* **2018**, *10* (26), 12734–12742.

(17) Hu, L.; Li, H.; Liu, C.; Song, Y.; Zhang, M.; Huang, H.; Liu, Y.; Kang, Z. Chiral Evolution of Carbon Dots and the Tuning of Laccase Activity. *Nanoscale* **2018**, *10*, 2333–2340.

(18) Li, F.; Li, Y.; Yang, X.; Han, X.; Jiao, Y.; Wei, T.; Yang, D.; Xu, H.; Nie, G.; Cellular, A.; et al. Highly Fluorescent Chiral N-S-Doped Carbon Dots from Cysteine: Affecting Cellular Energy Metabolism. *Angew. Chem. Int. Ed.* **2018**, *57* (9), 2377–2382.

(19) Arad, E.; Bhunia, S. K.; Jopp, J.; Kolusheva, S.; Rapaport, H.; Jelinek, R. Lysine-Derived Carbon Dots for Chiral Inhibition of Prion Peptide Fibril Assembly. *Adv. Ther.* **2018**, *1* (4), 1800006.

(20) Zhang, M.; Wang, H.; Wang, B.; Ma, Y.; Huang, H.; Liu, Y.; Shao, M.; Yao, B.; Kang, Z. Maltase Decorated by Chiral Carbon Dots with Inhibited Enzyme Activity for Glucose Level Control. *Small* **2019**, *1901512*, 1–7.

(21) Wei, Y.; Chen, L.; Wang, J.; Liu, X.; Yang, Y.; Yu, S. Investigation on the Chirality Mechanism of Chiral Carbon Quantum Dots Derived from Tryptophan. *RSC Adv.* **2019**, *9* (6), 3208–3214.

(22) Zhang, Y.; Hu, L.; Sun, Y.; Zhu, C.; Li, R.; Liu, N.; Huang, H.; Liu, Y.; Huang, C.; Kang, Z. One-Step Synthesis of Chiral Carbon Quantum Dots and Their Enantioselective Recognition. *RSC Adv.* **2016**, *6* (65), 59956–59960.

(23) Essner, J. B.; Kist, J. A.; Polo-Parada, L.; Baker, G. A. Artifacts and Errors Associated with the Ubiquitous Presence of Fluorescent Impurities in Carbon Nanodots. *Chem. Mater.* **2018**, *30*, 1878–1887.

(24) Verma Navneet C; Nandi, C. K. Paving the Path to the Future of Carbogenic Nanodots. *Nat. Commun.* **2019**, *10*, 2391.

(25) Arcudi, F.; Dordevic, L.; Prato, M.; Arcudi, F.; Dordevic, L.; Arcudi, F. Synthesis, Separation, and Characterization of Small and Highly Fluorescent Nitrogen-Doped Carbon Nanodots. *Angew. Chem. Int. Ed.* **2016**, *55* (6), 2107–2112.

(26) Arcudi, F.; Đorđević, L.; Prato, M. Design, Synthesis, and Functionalization Strategies of Tailored Carbon Nanodots. *Acc. Chem. Res.* **2019**, *52* (8), 2070–2079.

(27) Đorđević, L.; Arcudi, F.; Prato, M. Preparation, Functionalization and Characterization of Engineered Carbon Nanodots. *Nat. Protoc.* **2019**, *14* (10), In press.

(28) Bada, J. L. Racemization of Amino Acids. In *Chemistry and Biochemistry of the Amino Acids*; 1985.

(29) Bennani, Y. L.; Hanessian, S. Trans-1,2-Diaminocyclohexane Derivatives as Chiral Reagents, Scaffolds, and Ligands for Catalysis: Applications in Asymmetric Synthesis and Molecular Recognition. *Chem. Rev.* **1997**, *97* (8), 3161–3195.

(30) Đorđević, L.; Arcudi, F.; D'Urso, A.; Cacioppo, M.; Micali, N.; Bürgi, T.; Purrello, R.; Prato, M. Design Principles of Chiral Carbon Nanodots Help Convey Chirality from Molecular to Nanoscale Level. *Nat. Commun.* **2018**, *9* (1), 3442.

(31) *Electronic and Magnetic Properties of Chiral Molecules and Supramolecular Architectures*, 1st ed.; Naaman, R., Beratan, D. N., Waldeck, D., Eds.; Springer-Verlag Berlin Heidelberg, 2011.

(32) Cadranel, A.; Strauss, V.; Margraf, J. T.; Winterfeld, K. A.; Vogl, C.; Đorđević, L.; Arcudi, F.; Hoelzel, H.; Jux, N.; Prato, M.; et al. Screening Supramolecular Interactions between Carbon Nanodots and Porphyrins. *J. Am. Chem. Soc.* **2018**, *140* (3), 904–907.

(33) Prato, M.; Arcudi, F.; Strauss, V.; Cadranel, A.; Guldi, D. M.; Dordevic, L.; Dordević, L.; Cadranel, A.; Guldi, D. M.; Prato, M.; et al. Porphyrin Antennas on Carbon Nanodots: Excited State Energy and Electron Transduction. *Angew. Chem. Int. Ed.* **2017**, *56* (40), 12097–12101.

(34) Beletskaya, I.; Tyurin, V. S.; Tsivadze, A. Y.; Guilard, R.; Stern, C. Supramolecular Chemistry of Metalloporphyrins. *Chem. Rev.* **2009**, *109* (5), 1659–1713.

(35) Martínez-Díaz, M. V.; De La Torre, G.; Torres, T. Lighting Porphyrins and Phthalocyanines for Molecular Photovoltaics. *Chem. Commun.* **2010**, *46* (38), 7090–7108.

(36) Babu, S. S.; Bonifazi, D. Self-Organization of Polar Porphyrinoids. *Chempluschem* **2014**, *79* (7), 895–906.

(37) Li, L. L.; Diau, E. W. G. Porphyrin-Sensitized Solar Cells. *Chem. Soc. Rev.* **2013**, *42* (1), 291–304.

(38) Urbani, M.; Grätzel, M.; Nazeeruddin, M. K.; Torres, T. Meso-Substituted Porphyrins for Dye-Sensitized Solar Cells. *Chem. Rev.* **2014**, *114* (24), 12330–12396.

(39) Schick, G. A.; Schreiman, I. C.; Wagner, R. W.; Lindsey, J. S.; Bocian, D. F. Spectroscopic Characterization of Porphyrin Monolayer Assemblies. *J. Am. Chem. Soc.* **1989**, *111* (4), 1344–1350.

(40) Medforth, C. J.; Wang, Z.; Martin, K. E.; Song, Y.; Jacobsen, J. L.; Shelnutt, J. A. Self-Assembled Porphyrin Nanostructures. *Chem. Commun.* **2009**, *7345* (47), 7261–7277.

(41) Romeo, A.; Castriciano, M. A.; Occhiuto, I.; Zagami, R.; Pasternack, R. F.; Scolaro, L. M. Kinetic Control of Chirality in Porphyrin J-Aggregates. *J. Am. Chem. Soc.* **2014**, *136* (1), 40–43.

(42) D'Urso, A.; Fragalà, M. E.; Purrello, R. From Self-Assembly to Noncovalent Synthesis of Programmable Porphyrins' Arrays in Aqueous Solution. *Chem. Commun.* **2012**, *48* (66), 8165–8176.

(43) Ribó, J. M.; Crusats, J.; Farrera, J. A.; Valero, M. L. Aggregation in Water Solutions of

Tetrasodium Diprotonated Meso-Tetrakis(4-Sulfonatophenyl)Porphyrin. *J. Chem. Soc. Chem. Commun.* **1994**, *7* (6), 681–682.

(44) Maiti, N. C.; Ravikanth, M.; Mazumdar, S.; Periasamy, N. Fluorescence Dynamics of Noncovalently Linked Porphyrin Dimers and Aggregates. *J. Phys. Chem.* **1995**, *99* (47), 17192–17197.

(45) Akins, D. L.; Zhu, H. R.; Guo, C. Aggregation of Tetraaryl-Substituted Porphyrins in Homogeneous Solution. *J. Phys. Chem.* **1996**, *100* (13), 5420–5425.

(46) Koti, A. S. R.; Taneja, J.; Periasamy, N. Control of Coherence Length and Aggregate Size in the J-Aggregate of Porphyrin. *Chem. Phys. Lett.* **2003**, *375* (1–2), 171–176.

(47) Koti, A. S. R.; Periasamy, N. Self-Assembly of Template-Directed J-Aggregates of Porphyrin. *Chem. Mater.* **2003**, *15* (2), 369–371.

(48) Castriciano, M. A.; Romeo, A.; Villari, V.; Micali, N.; Scolaro, L. M. Structural Rearrangements in 5,10,15,20-Tetrakis(4-Sulfonatophenyl)Porphyrin J-Aggregates under Strongly Acidic Conditions. *J. Phys. Chem. B* **2003**, *107* (34), 8765–8771.

(49) Micali, N.; Villari, V.; Castriciano, M. A.; Romeo, A.; Scolaro, L. M. From Fractal to Nanorod Porphyrin J-Aggregates. Concentration-Induced Tuning of the Aggregate Size. *J. Phys. Chem. B* **2006**, *110* (16), 8289–8295.

(50) Castriciano, M. A.; Romeo, A.; Zagami, R.; Micali, N.; Scolaro, L. M. Kinetic Effects of Tartaric Acid on the Growth of Chiral J-Aggregates of Tetrakis(4-Sulfonatophenyl)Porphyrin. *Chem. Commun.* **2012**, *48* (40), 4872–4874.

(51) D'Urso, A.; Randazzo, R.; Faro, L. Lo; Purrello, R. Vortexes and Nanoscale Chirality. *Angew. Chem. Int. Ed.* **2010**, *49* (1), 108–112.

(52) Randazzo, R.; Mammana, A.; D'Urso, A.; Lauceri, R.; Purrello, R. Reversible "Chiral Memory" in Ruthenium Tris(Phenanthroline)- Anionic Porphyrin Complexes. *Angew. Chem. Int. Ed.* **2008**, *47* (51), 9879–9882.

(53) Kumar, V.; Sharma, N.; Maitra, S. S. In Vitro and in Vivo Toxicity Assessment of Nanoparticles. *Int. Nano Lett.* **2017**, *7* (4), 243–256.

(54) Feliu, N.; Docter, D.; Heine, M.; Del Pino, P.; Ashraf, S.; Kolosnjaj-Tabi, J.; Macchiarini, P.; Nielsen, P.; Alloyeau, D.; Gazeau, F.; et al. In Vivo Degeneration and the Fate of Inorganic Nanoparticles. *Chem. Soc. Rev.* **2016**, *45* (9), 2440–2457.

(55) Shang, L.; Yang, L.; Seiter, J.; Heinle, M.; Brenner-Weiss, G.; Gerthsen, D.; Nienhaus, G. U. Nanoparticles Interacting with Proteins and Cells: A Systematic Study of Protein Surface Charge Effects. *Adv. Mater. Interfaces* **2014**, *1* (2), 1–10.

(56) Behzadi, S.; Serpooshan, V.; Tao, W.; Hamaly, M. A.; Alkawareek, M. Y.; Dreaden, E. C.; Brown, D.; Alkilany, A. M.; Farokhzad, O. C.; Mahmoudi, M. Cellular Uptake of Nanoparticles: Journey inside the Cell. *Chem. Soc. Rev.* **2017**, *46* (14), 4218–4244.

(57) Foroozandeh, P.; Aziz, A. A. Insight into Cellular Uptake and Intracellular Trafficking of Nanoparticles. *Nanoscale Res. Lett.* **2018**, *13*.

(58) Phogat, N.; Kohl, M.; Uddin, I. *Interaction of Nanoparticles With Biomolecules, Protein, Enzymes, and Its Applications*; Elsevier Inc., 2018.

(59) Zeng, L.; Gao, J.; Liu, Y.; Gao, J.; Yao, L.; Yang, X.; Liu, X.; He, B.; Hu, L.; Shi, J.; et al. Role of Protein Corona in the Biological Effect of Nanomaterials: Investigating Methods. *Trends Anal. Chem.* **2019**.

(60) Yang, M.; Hoppmann, S.; Chen, L.; Cheng, Z. Human Serum Albumin Conjugated Biomolecules for Cancer Molecular Imaging. *Curr. Pharm. Des.* **2012**, *18* (8), 1023–1031.

(61) Elsadek, B.; Kratz, F. Impact of Albumin on Drug Delivery - New Applications on the Horizon. *J. Control. Release* **2012**, *157* (1), 4–28.

(62) Mariam, J.; Sivakami, S.; Dongre, P. M. Albumin Corona on Nanoparticles–a Strategic Approach in Drug Delivery. *Drug Deliv.* **2016**, *23* (8), 2668–2676.

(63) Zhu, D.; Yan, H.; Zhou, Z.; Tang, J.; Liu, X.; Hartmann, R.; Parak, W. J.; Feliu, N.; Shen, Y.; Yan, H.; et al. Detailed Investigation on How the Protein Corona Modulates the Physicochemical Properties and

Gene Delivery of Polyethylenimine (PEI) Polyplexes. *Biomater. Sci.* **2018**, *6* (7), 1800–1817.

(64) Treuel, L.; Docter, D.; Maskos, M.; Stauber, R. H. Protein Corona - from Molecular Adsorption to Physiological Complexity. *Beilstein J. Nanotechnol.* **2015**, *6* (1), 857–873.

(65) Kratz, F. Albumin as a Drug Carrier: Design of Prodrugs, Drug Conjugates and Nanoparticles. *J. Control. Release* **2008**, *132* (3), 171–183.

(66) Wojnarowska-Nowak, R.; Polit, J.; Zięba, A.; Stolyarchuk, I. D.; Nowak, S.; Romerowicz-Misielak, M.; Sheregii, E. M. Colloidal Quantum Dots Conjugated with Human Serum Albumin – Interactions and Bioimaging Properties. *Opto-electronics Rev.* **2017**, *25* (2), 137–147.

(67) Ke, P. C.; Lin, S.; Parak, W. J.; Davis, T. P.; Caruso, F. A Decade of the Protein Corona. *ACS Nano* **2017**, *11* (12), 11773–11776.

(68) Treuel, L.; Brandholt, S.; Maffre, P.; Wiegele, S.; Shang, L.; Nienhaus, G. U. Impact of Protein Modification on the Protein Corona on Nanoparticles and Nanoparticle-Cell Interactions. *ACS Nano* **2014**, *8* (1), 503–513.

(69) Docter, D.; Westmeier, D.; Markiewicz, M.; Stolte, S.; Knauer, S. K.; Stauber, R. H. The Nanoparticle Biomolecule Corona: Lessons Learned - Challenge Accepted? *Chem. Soc. Rev.* **2015**, *44* (17), 6094–6121.

(70) Li, Y.; Monteiro-Riviere, N. A. Mechanisms of Cell Uptake, Inflammatory Potential and Protein Corona Effects with Gold Nanoparticles. *Nanomedicine* **2016**, *11* (24), 3185–3203.

(71) Glancy, D.; Zhang, Y.; Wu, J. L. Y.; Ouyang, B.; Ohta, S.; Chan, W. C. W. Characterizing the Protein Corona of Sub-10 nm Nanoparticles. *J. Control. Release* **2019**.

(72) Moya, C.; Escudero, R.; Malaspina, D. C.; de la Mata, M.; Hernández-Saz, J.; Faraudo, J.; Roig, A. Insights into Preformed Human Serum Albumin Corona on Iron Oxide Nanoparticles: Structure, Effect of Particle Size, Impact on MRI Efficiency, and Metabolization. *ACS Appl. Bio Mater.* **2019**, *2* (7), 3084–3094.

(73) Walkey, C. D.; Olsen, J. B.; Guo, H.; Emili, A.; Chan, W. C. W. Nanoparticle Size and Surface Chemistry Determine Serum Protein Adsorption and Macrophage Uptake. *J. Am. Chem. Soc.* **2012**, *134* (4), 2139–2147.

(74) Jiang, Y.; Huo, S.; Mizuhara, T.; Das, R.; Lee, Y. W.; Hou, S.; Moyano, D. F.; Duncan, B.; Liang, X. J.; Rotello, V. M. The Interplay of Size and Surface Functionality on the Cellular Uptake of Sub-10 Nm Gold Nanoparticles. *ACS Nano* **2015**, *9* (10), 9986–9993.

(75) Mosquera, J.; García, I.; Liz-Marzán, L. M. Cellular Uptake of Nanoparticles versus Small Molecules: A Matter of Size. *Acc. Chem. Res.* **2018**, *51* (9), 2305–2313.

(76) Sahay, G.; Alakhova, D. Y.; Kabanov, A. V. Endocytosis of Nanomedicines. *J. Control. Release* **2010**, *145* (3), 182–195.

(77) Rivolta, I.; Panariti, A.; Lettiero, B.; Sesana, S.; Gasco, P.; Gasco, M. R.; Masserini, M.; Miserocchi, G. Cellular Uptake of Coumarin-6 as a Model Drug Loaded in Solid Lipid Nanoparticles. *J. Physiol. Pharmacol.* **2011**, *62* (1), 45–53.

(78) Doherty, G. J.; McMahon, H. T. Mechanisms of Endocytosis. *Annu. Rev. Biochem.* **2009**, *78* (1), 857–902.

(79) Lu, Y.; Low, P. S. Folate-Mediated Delivery of Macromolecular Anticancer Therapeutic Agents. *Adv. Drug Deliv. Rev.* **2002**, *54*, 675–693.

(80) Kelemen, L. E. The Role of Folate Receptor α in Cancer Development, Progression and Treatment: Cause, Consequence or Innocent Bystander? *Int. J. Cancer* **2006**, *119* (2), 243–250.

(81) Kuhn, D. A.; Vanhecke, D.; Michen, B.; Blank, F.; Gehr, P.; Petri-Fink, A.; Rothen-Rutishauser, B. Different Endocytotic Uptake Mechanisms for Nanoparticles in Epithelial Cells and Macrophages. *Beilstein J. Nanotechnol.* **2014**, *5* (1), 1625–1636.

(82) Kerr, M. C.; Teasdale, R. D. Defining Macropinocytosis. *Traffic* **2009**, *10* (4), 364–371.

(83) Jones, A. T. Macropinocytosis: Searching for an Endocytic Identity and Role in the Uptake of Cell Penetrating Peptides. *J. Cell. Mol. Med.* **2007**, *11* (4), 670–684.

(84) Kühn, S.; Lopez-Montero, N.; Chang, Y. Y.; Sartori-Rupp, A.; Enninga, J. Imaging Macropinosomes during Shigella Infections. *Methods* **2017**, *127*, 12–22.

(85) Cao, X.; Wang, J.; Deng, W.; Chen, J.; Wang, Y.; Zhou, J.; Du, P.; Xu, W.; Wang, Q. Q.; Wang, Q. Q.; et al. Photoluminescent Cationic Carbon Dots as Efficient Non-Viral Delivery of Plasmid SOX9 and Chondrogenesis of Fibroblasts. *Sci. Rep.* **2018**, *8* (1), 1–11.

(86) Wei, Y.; Jin, X.; Kong, T.; Zhang, W.; Zhu, B. The Endocytic Pathways of Carbon Dots in Human Adenoid Cystic Carcinoma Cells. *Cell Prolif.* **2019**, *52* (3), 1–7.

(87) Sun, Y.; Fan, L.; Shang, W.; Zhang, X.; Fan, Z.; Han, M.; Zhang, M. The Uptake Mechanism and Biocompatibility of Graphene Quantum Dots with Human Neural Stem Cells. *Nanoscale* **2014**, *6* (11), 5799–5806.

(88) Thoo, L.; Fahmi, M. Z.; Zulkipli, I. N.; Keasberry, N.; Idris, A. Interaction and Cellular Uptake of Surface-Modified Carbon Dot Nanoparticles by J774.1 Macrophages. *Cent. Eur. J. Immunol.* **2017**, *42* (3), 324–330.

(89) Yan, J.; Hou, S.; Yu, Y.; Qiao, Y.; Xiao, T.; Mei, Y.; Zhang, Z.; Wang, B.; Huang, C. C.; Lin, C. H.; et al. The Effect of Surface Charge on the Cytotoxicity and Uptake of Carbon Quantum Dots in Human Umbilical Cord Derived Mesenchymal Stem Cells. *Colloids Surfaces B Biointerfaces* **2018**, *171* (April), 241–249.

(90) Zhou, N.; Zhu, S.; Maharjan, S.; Hao, Z.; Song, Y.; Zhao, X.; Jiang, Y.; Yang, B.; Lu, L. Elucidating the Endocytosis, Intracellular Trafficking, and Exocytosis of Carbon Dots in Neural Cells. *RSC Adv.* **2014**, *4*, 62086.

(91) Marichal, L.; Giraudon--Colas, G.; Cousin, F.; Thill, A.; Labarre, J.; Boulard, Y.; Aude, J.-C.; Pin, S.; Renault, J. P. Protein–Nanoparticle Interactions: What Are the Protein–Corona Thickness and Organization? *Langmuir* **2019**.

(92) Stevenson, D.; Williams, G. A. The Biological Importance of Chirality and Methods Available to Determine Enantiomers. In *Chiral Separations*; Springer: Boston, MA, 1988.

(93) Crossley, R. The Relevance of Chirality to the Study of Biological Activity. *Tetrahedron* **1992**, *48* (38), 8155–8178.

(94) Brandt, J. R.; Salerno, F.; Fuchter, M. J. The Added Value of Small-Molecule Chirality in Technological Applications. *Nat. Rev. Chem.* **2017**, *1*, 0045.

(95) Calcaterra, A.; D'Acquarica, I. The Market of Chiral Drugs: Chiral Switches versus de Novo Enantiomerically Pure Compounds. *J. Pharm. Biomed. Anal.* **2018**, *147*, 323–340.

(96) Hanein, D.; Geiger, B.; Addadi, L. Differential Adhesion of Cells to Enantiomorphous Crystal Surfaces. *Science* **1994**, *263* (5152), 1413–1416.

(97) Hazen, R. M.; Sholl, D. S. Chiral Selection on Inorganic Crystalline Surfaces. *Nat. Mater.* **2003**, *2* (6), 367–374.

(98) Sun, T.; Han, D.; Rhemann, K.; Chi, L.; Fuchs, H. Stereospecific Interaction between Immune Cells and Chiral Surfaces. *J. Am. Chem. Soc.* **2007**, *129* (6), 1496–1497.

(99) Zhang, M.; Qing, G.; Sun, T. Chiral Biointerface Materials. *Chem. Soc. Rev.* **2012**, *41* (5), 1972–1984.

(100) Sun, T.; Qing, G.; Sua, B.; Jiang, L. Functional Biointerface Materials Inspired from Nature. *Chem. Soc. Rev.* **2011**, *40*, 2909–2921.

(101) El-Gindi, J.; Benson, K.; De Cola, L.; Galla, H. J.; Seda Kehr, N. Cell Adhesion Behavior on Enantiomerically Functionalized Zeolite L Monolayers. *Angew. Chem. Int. Ed.* **2012**, *51* (15), 3716–3720.

(102) Liu, G. F.; Zhang, D.; Feng, C. L. Control of Three-Dimensional Cell Adhesion by the Chirality of Nanofibers in Hydrogels. *Angew. Chem. Int. Ed.* **2014**, *53* (30), 7789–7793.

(103) Wang, Y.; Xu, J.; Wang, Y.; Chen, H. Emerging Chirality in Nanoscience. *Chem. Soc. Rev.* **2013**, *42* (7), 2930–2962.

(104) Li, Y.; Zhou, Y.; Wang, H. Y.; Perrett, S.; Zhao, Y.; Tang, Z.; Nie, G. Chirality of Glutathione Surface Coating Affects the Cytotoxicity of Quantum Dots. *Angew. Chem. Int. Ed.* **2011**, *50* (26), 5860–5864.

(105) Kehr, N. S.; Jose, J. Chirality-Dependent Cellular Uptake of Chiral Nanocarriers and Intracellular Delivery of Different Amounts of Guest Molecules. *Appl. Surf. Sci.* **2017**, *425*, 432–439.

(106) Martynenko, I. V.; Kuznetsova, V. A.; Litvinov, I. K.; Orlova, A. O.; Maslov, V. G.; Fedorov, A. V.; Dubavik, A.; Purcell-Milton, F.; Gun'ko, Y. K.; Baranov, A. V. Enantioselective Cellular Uptake of Chiral Semiconductor Nanocrystals. *Nanotechnology* **2016**, *27* (7).

(107) Palamà, I. E.; Di Maria, F.; Zangoli, M.; D'Amone, S.; Manfredi, G.; Barsotti, J.; Lanzani, G.; Ortolani, L.; Salatelli, E.; Gigli, G.; et al. Enantiopure Polythiophene Nanoparticles. Chirality Dependence of Cellular Uptake, Intracellular Distribution and Antimicrobial Activity. *RSC Adv.* **2019**, *9* (40), 23036–23044.

(108) Yuan, L.; Zhang, F.; Qi, X.; Yang, Y.; Yan, C.; Jiang, J.; Deng, J. Chiral Polymer Modified Nanoparticles Selectively Induce Autophagy of Cancer Cells for Tumor Ablation. *J. Nanobiotechnology* **2018**, *16* (1), 1–16.

(109) Deng, J.; Li, Z.; Yao, M.; Gao, C. Influence of Albumin Configuration by the Chiral Polymer-Grafted Gold Nanoparticles. *Langmuir* **2016**, *32* (22), 5608–5616.

(110) Sen, S.; Dasgupta, S.; DasGupta, S. Does Surface Chirality of Gold Nanoparticles Affect Fibrillation of HSA? *J. Phys. Chem. C* **2017**, *121* (34), 18935–18946.

(111) Deng, J.; Zheng, H.; Gao, C. Influence of Protein Adsorption on the Cellular Uptake of AuNPs Conjugated with Chiral Oligomers. *Mater. Chem. Front.* **2017**, *1* (3), 542–549.

(112) Wang, X.; Wang, M.; Lei, R.; Zhu, S. F.; Zhao, Y.; Chen, C. Chiral Surface of Nanoparticles Determines the Orientation of Adsorbed Transferrin and Its Interaction with Receptors. *ACS Nano* **2017**, *11* (5), 4606–4616.

(113) Jaleel, J. A.; Pramod, K. Artful and Multifaceted Applications of Carbon Dot in Biomedicine. *J. Control. Release* **2018**, *269* (November 2017), 302–321.

(114) Kasouni, A.; Chatzimitakos, T.; Stalikas, C. Bioimaging Applications of Carbon Nanodots: A Review. *C* **2019**, *5* (2), 19.

(115) Ostadhossein, F.; Pan, D. Functional Carbon Nanodots for Multiscale Imaging and Therapy. *Wiley Interdiscip. Rev. Nanomedicine Nanobiotechnology* **2017**, *9* (3), 1436.

(116) Du, J.; Xu, N.; Fan, J.; Sun, W.; Peng, X. Carbon Dots for In Vivo Bioimaging and Theranostics. *Small* **2019**, *15*, 1805087.

(117) Fong, J. F. Y.; Ng, Y. H.; Ng, S. M. Recent Advances in Carbon Dots for Bioanalysis and the Future Perspectives. *Carbon Nanomater. Bioimaging, Bioanal. Ther.* **2018**, 203–264.

(118) Yi, C.; Pan, Y.; Fang, Y. Surface Engineering of Carbon Nanodots (C-Dots) for Biomedical Applications. In *Novel Nanomaterials for Biomedical, Environmental and Energy Applications*; Elsevier Inc., 2019; pp 137–188.

(119) Jung, Y. K.; Shin, E.; Kim, B.-S. Cell Nucleus-Targeting Zwitterionic Carbon Dots. *Sci. Rep.* **2015**, *5*, 18807.

(120) Chanput, W.; Mes, J. J.; Wichers, H. J. THP-1 Cell Line: An in Vitro Cell Model for Immune Modulation Approach. *Int. Immunopharmacol.* **2014**, *23* (1), 37–45.

(121) Price, P. J.; Gregory, E. A. Relationship between in Vitro Growth Promotion and Biophysical and Biochemical Properties of the Serum Supplement. *In Vitro* **1982**, *18* (6), 576–584.

(122) Riss, T. L.; Moravec, R. A.; Niles, A. L.; Duellman, S.; Benink, H. A.; Worzella, T. J.; Minor, L. Cell Viability Assays. In *Assay Guidance Manual*; 2004.

(123) Ibuki, Y.; Toyooka, T. Nanoparticle Uptake Measured by Flow Cytometry. In *Nanotoxicity: Methods and Protocols, Methods in Molecular Biology*; 2012; Vol. 926, pp 157–166.

(124) Tantra, R.; Knight, A. Cellular Uptake and Intracellular Fate of Engineered Nanoparticles: A Review on the Application of Imaging Techniques. *Nanotoxicology* **2011**, *5* (3), 381–392.

(125) Gustafson, H. H.; Holt-Casper, D.; Grainger, D. W.; Ghandehari, H. Nanoparticle Uptake: The Phagocyte Problem Graphical Abstract HHS Public Access. *Nano Today* **2015**, *10* (4), 487–510.

(126) Maffre, P.; Brandholt, S.; Nienhaus, K.; Shang, L.; Parak, W. J.; Nienhaus, G. U. Effects of Surface

Functionalization on the Adsorption of Human Serum Albumin onto Nanoparticles - A Fluorescence Correlation Spectroscopy Study. *Beilstein J. Nanotechnol.* **2014**, *5* (1), 2036–2047.

(127) Maffre, P.; Nienhaus, K.; Amin, F.; Parak, W. J.; Nienhaus, G. U. Characterization of Protein Adsorption onto Fept Nanoparticles Using Dual-Focus Fluorescence Correlation Spectroscopy. *Beilstein J. Nanotechnol.* **2011**, *2* (1), 374–383.

(128) Arcudi, F.; Đorđević, L.; Prato, M.; Arcudi, F.; Dordevic, L. Rationally Designed Carbon NanoDots En Route to Pure White-Light Emission. *Angew. Chem. Int. Ed.* **2017**, *56* (15), 4170–4173.

(129) Wu, Y.; Krishna, S.; Nalluri, M.; Young, R. M.; Krzyaniak, M. D.; Margulies, E. A.; Stoddart, J. F.; Wasielewski, M. R. Charge and Spin Transport in an Organic Molecular Square. *Angew. Chem. Int. Ed.* **2015**, *54*, 11971–11977.

(130) Krishna, S.; Nalluri, M.; Liu, Z.; Wu, Y.; Hermann, K. R.; Samanta, A.; Kim, D. J.; Krzyaniak, M. D.; Wasielewski, M. R.; Stoddart, J. F. Chiral Redox-Active Isosceles Triangles. *J. Am. Chem. Soc.* **2016**, No. 138, 5968–5977.

(131) Laurence A. Nafie. *Vibrational Optical Activity: Principles and Applications*; John Wiley & Sons, Ltd, 2011.

(132) Stewart, J. J. P. Optimization of Parameters for Semiempirical Methods II. Applications. *J. Comput. Chem.* **1989**, *10* (2), 221–264.

(133) Becke, A. D. Density-Functional Exchange-Energy Approximation with Correct Asymptotic Behavior. *Phys. Rev. A* **1988**, *38* (6), 3098–3100.

(134) Lee, C.; Yang, W.; Parr, R. G. Development of the Colle-Salvetti Correlation-Energy Formula into a Functional of the Electron Density. *Phys. Rev. B* **1988**, *37* (2), 785–789.

(135) Becke, A. D. Density-Functional Thermochemistry. III. The Role of Exact Exchange. *J. Chem. Phys.* **1993**, *98* (7), 5648–5652.

(136) Spartan 14' Wavefunction, Inc., Irvine.

(137) Tomasi, J.; Mennucci, B.; Cammi, R. Quantum Mechanical Continuum Solvation Models. *Chem. Rev.* **2005**, *105* (8), 2999–3094.

(138) Frisch, M. J. et al. Gaussian 09, Revision D 0.1. 2009.

(139) Perdew, J.; Chevary, J.; Vosko, S.; Jackson, K.; Pederson, M.; Singh, D.; Fiolhais, C. Atoms, Molecules, Solids, and Surfaces: Applications of the Generalized Gradient Approximation for Exchange and Correlation. *Phys. Rev. B* **1992**, *46* (11), 6671–6687.

(140) Ditchfield, R.; Hehre, W. J.; Pople, J. A. Self-Consistent Molecular-Orbital Methods. IX. An Extended Gaussian-Type Basis for Molecular-Orbital Studies of Organic Molecules. *J. Chem. Phys.* **1971**, *54* (2), 724–728.

3 Fluorophore-doped CNDs

This chapter reports the design of fluorophore-doped CNDs for electrochemiluminescence (ECL) applications. As previously discussed in **Subsection 1.3.2**, the use of selected molecules in the reaction mixture allows the introduction of specific functionalities in the nanoparticle structure that results on the tuning of the luminescence and redox properties.

The first part of the chapter focuses on the synthesis and characterization of amino-passivated CNDs with green fluorescence emission by using difluoro-boron-dipyrromethene (BODIPY) as luminescent dopant (**Section 3.1**). Herein, a library of hp-BFN-CNDs (hereafter called BCNDs) by using two BODIPY isomers and modifying the surface functional groups through post-synthetic schemes is obtained.

In the second part, the electrochemiluminescence properties of the prepared BCNDs is discussed and the dependence of the ECL properties on the core/shell composition of the nanoparticles is investigated (**Subsection 3.1.3**). The study of the electrochemiluminescence properties is a result of a collaboration with *Prof. Francesco Paolucci*, *Dr. Giovanni Valenti* and *Dr. Alessandra Zanut* (University of Bologna).

3.1 CNDs doped with difluoro-boron-dipyrromethene (BODIPY) dyes

The majority of reported CDs show blue emission and the successful obtaining of nanoparticles with red-shifted fluorescence emission (and with high quantum yields) is still a challenge.[1] Obtaining multicolored CDs is pivotal to expand the efficient use of such nanoparticles in optoelectronic and bio-related applications. In the former applicative area, the tuning of emission has been investigated for uses in multi-emissive light emitting diodes or fluorescent sensors.[2] The latter involves the use of CDs in optical bioimaging and especially the NIR region offers minimized background autofluorescence and light scattering and improved light penetrating ability.[3] The tuning of the fluorescence emission could be achieved by: (1) optimization of the synthesis and purification parameters; (2) (heteroatom) doping; (3) the modification/passivation of the surface functional groups.[4] The lack in rationalization on the origin of fluorescence emission represents however the main difficulty in designing nanoparticles with the desired emissive properties and/or high fluorescence quantum yields.[5] This is strictly related to the variability of structures that could be obtained during the synthetic processes.[6] As discussed in **Subsection 1.3.2**, the introduction of specific emissive features in the dot structure can be attained by using properly selected fluorophores as precursors. This methodology is an useful way to tune the emissive properties of CDs and has been investigated in our group.[4,7,8]

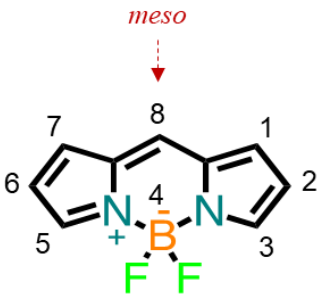

4,4′-difluoro-4-bora-3a,4a-diaza-s-indacene
BODIPY

Figure 3.1 Chemical structure of BODIPY dye.

This chapter describe the use of 4,4′-difluoro-4-bora-3a,4a-diaza-*s*-indacene dyes (BODIPY) as dopants for CNDs (**Figure 3.1**). BODIPYs are a class of dyes that present high extinction coefficients, narrow light absorption and emission bands with high fluorescence quantum efficiencies.[9] The fluorescence emission of BODIPYs can be conveniently tuned by structural modifications.[9–11] Thanks to these properties, BODIPY dyes are successfully used as fluorescent probes in biotechnology as valuable alternatives to the commonly used rhodamine, fluorescein, coumarin and Cy5 dyes.[12]

The main drawback of BODIPY dyes for their use in biotechnology is their poor solubility in water. Moreover the hydrophilic derivatives reported so far usually show a remarkable tendency to form non emissive aggregates and require tedious synthetic/purification pathways.[9] The most common way to confer hydrophilicity to BODIPY molecules is the modification of the aromatic skeleton with moieties such as oligo(ethylene glycol), N,N-bis(2-hydroxyethyl) amine, carbohydrates, nucleotides, or ionic hydrophilic groups such as carboxylic acid, sulfonic acid, or ammonium groups.[13–22] For example, a highly hydrophilic BODIPY derivative has been obtained by functionalizing the meso position with an oligo(ethylene glycol)methyl ether.[22] The reported fluorescence quantum yield is however low (4.2 %) compared to the hydrophobic dyes due to the aggregation-induced self-quenching. Therefore, to enhance the light emission efficiency, a further functionalization via substitution of fluorine atoms with ethynyl groups introduced steric hindrance and allow to reach a higher quantum yield of 35.7 % (**Figure 3.2**). The example described above shows the necessity of multi-step synthetic pathways and extensive purification means for the preparation of water soluble BODIPY dyes. Thus novel, efficient and simpler synthetic strategy to confer water solubility to this class of dyes is a topic of great importance for the prospective of the applications in biotechnology.

This work proposes a new solution to the problem of efficient BODIPY emission in water by the introduction of the dyes in CNDs via a simple one pot synthetic process. Indeed, the novel reported nanoparticles (BCNDs) show the optimal

photophysical features of the BODIPY in a water-soluble system avoiding self-aggregation induced quenching.

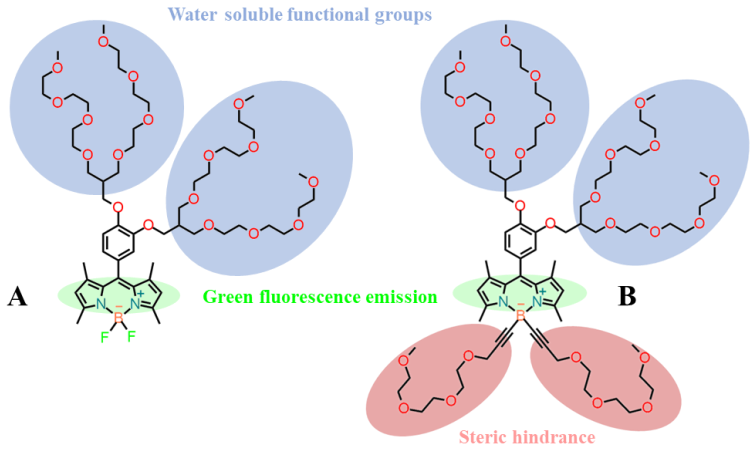

BODIPY dye	Solvent	λ_{excMAX} / nm	λ_{emMAX} / nm	QY / %
A	CH_2Cl_2	501	511	**68.0**
	PBS	499	510	**4.2**
B	CH_2Cl_2	499	508	**81.0**
	PBS	496	507	**35.7**

Figure 3.2 Top figure: chemical structures of the water soluble BODIPY derivatives bearing oligo(ethylene glycol)methyl ethers at the meso position (**A** and **B**) and ethynyl groups substituting the fluorine atoms (**B**). The ethynyl groups enable steric hindrance in aqueous solutions avoiding the formation of aggregates. Adapted from reference [22].

The first section describes the design, synthesis and purification of BCNDs (**Subsection 3.1.1**). The second section reports the structural, morphological and photophysical characterization of the prepared BCNDs (**Subsection3.1.2**). Since BODIPY molecules are known as active dyes in ECL, we finally investigated the electrochemiluminescence emission of BCNDs with tuned core/shell composition (**Subsection 3.1.1**) .[23]

3.1.1 Design, synthesis and purification

BODIPY-doped CNDs (BCNDs) were obtained by introducing a BODIPY dye to our Arg + EDA reaction mixture (discussed in **paragraph 1.3.2**):[8] 8-(4-carboxyphenyl)-1,3,7,9-tetramethyl-BODIPY (BODIPY-pCOOH) and 8-(2-

carboxyphenyl)-1,3,7,9-tetramethyl-BODIPY (BODIPY-oCOOH) were used as chromophore for the following reasons (**Figure 3.3**): *(i)* they can obtained via a one-pot synthesis adapting reported synthetic procedures (see **Section 3.2** for experimental details);[22,24] *(ii)* we envisaged that, in our hydrothermal conditions, the carboxylic moiety of the BODIPY would react with the amines of Arg and EDA thus facilitating the incorporation of the chromophore in the structure of the nanoparticle through their periphery giving us a fair amount of predictability in tuning the fluorescence emission of the nanoparticles *(iii)* the arylation at the meso position do not alter significantly the optical features, but the methyl groups in position 1,7 result in improved PL quantum yield since they prevent free rotation of the phenyl group and reduce loss of energy from the excited states via non-irradiative molecular motions;[9] *(iv)* the enhanced steric hindrance of the bulky *ortho*-substituent group on the meso-phenyl ring of BODIPY result in increased PLQY of the dye.[22,24]

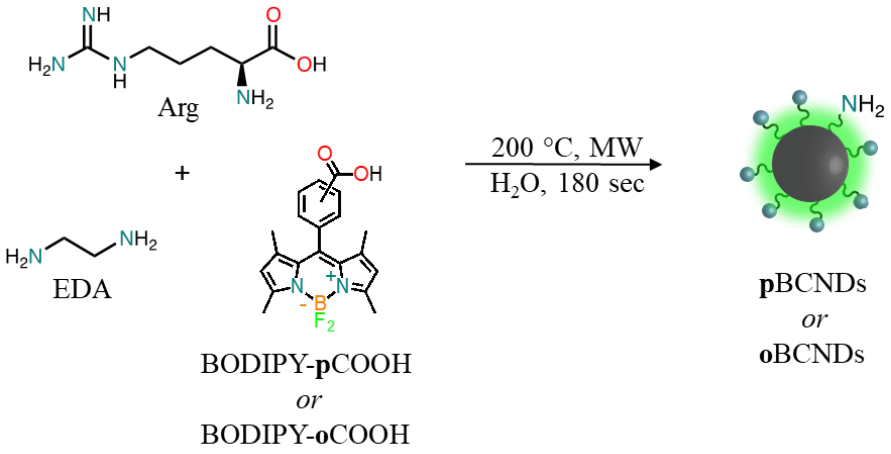

Figure 3.3 Synthetic scheme for the preparation of water soluble BODIPY-doped CNDs (BCNDs) with green fluorescence. Arg, EDA and either BODIPY-pCOOH or BODIPY-oCOOH are used as precursors for the MW-assisted synthesis of pBCNDs or oBCNDs.

BCNDs were prepared by using Arg and EDA with either BODIPY-pCOOH or BODIPY-oCOOH to obtain pBCNDs and oBCNDs, respectively. The synthesis consisted on a MW-assisted hydrothermal process and MW parameters and molar ratio of the three organic precursors were optimized to obtain the desired hydrophilicity and optical performances of the final material. Appropriate viscosity, temperature and MW power conditions ensure a uniform condensation, polymerization, aromatization and carbonization during the heating process.

BCNDs were obtained by employing the precursors Arg, EDA and BODIPY in a molar ratio of respectively 1:0.5:0.25 mol at 200 °C, 5 PSI, 200 W, for 180 seconds and using water as reaction medium (see **Section 3.2** for experimental details). Larger carbon particles were removed through microfiltration and the aqueous filtrate containing BCNDs was dialyzed against Milli-Q water. The aqueous solution is finally lyophilized to obtain BCNDs as dark red powdered material.

3.1.2 Characterization

Positive Kaiser tests of 845 μmol g^{-1} (pBCNDs) and 650 μmol g^{-1} (oBCNDs) indicate that BCNDs possess a surface rich in primary (or secondary) amino groups, similar to the undoped hp-N-CNDs.

pBCNDs and oBCNDs show very similar morphological, structural and photophysical (except for the PLQY, *vide infra*) features. The structure and the composition of BCNDs were determined by FT-IR and XPS spectroscopies and the morphological information were obtained by atomic force microscopy (AFM) (**Figure 3.4** and **Figure S3.1**).

The AFM analysis showed the round shape of the nanoparticles and sizes of 2.17 ± 0.64 nm for pBCNDs and 1.90 ± 0.72 for oBCNDs (**Figure 3.4a** and **Figure S3.1**). The FT-IR spectrum of BCNDs showed the presence of many surface functional groups, similar to hp-N-CNDs (**Figure 3.4d** and **Figure S3.1d**). Interestingly, the peak at 1683 cm^{-1} in FT-IR spectrum of the BODIPY-COOH precursor and indicative of the carboxylic acid moiety (**Figure S3.2**), disappeared in the BCNDs spectrum. The peak at 1669 and 1623 cm^{-1} are typical of the C=O stretching and the peak at 1342 cm^{-1} confirms the presence of C-O bond. The absorptions at 1178, 1155 and 1108 cm^{-1} are attributable to C-O-C bonds, while the broad peak at 3353 cm^{-1} displays the presence of O-H/N-H bonding. Indicative signal of B-N stretching is visible at 1385 cm^{-1} and the signal at 2945 cm^{-1} reveals the C-H stretching. The absorptions at 1545 and 1511 cm^{-1} are typical of C=N and C=C stretching, respectively, and the C-N bond is visible at 1470 and 1452 cm^{-1}.

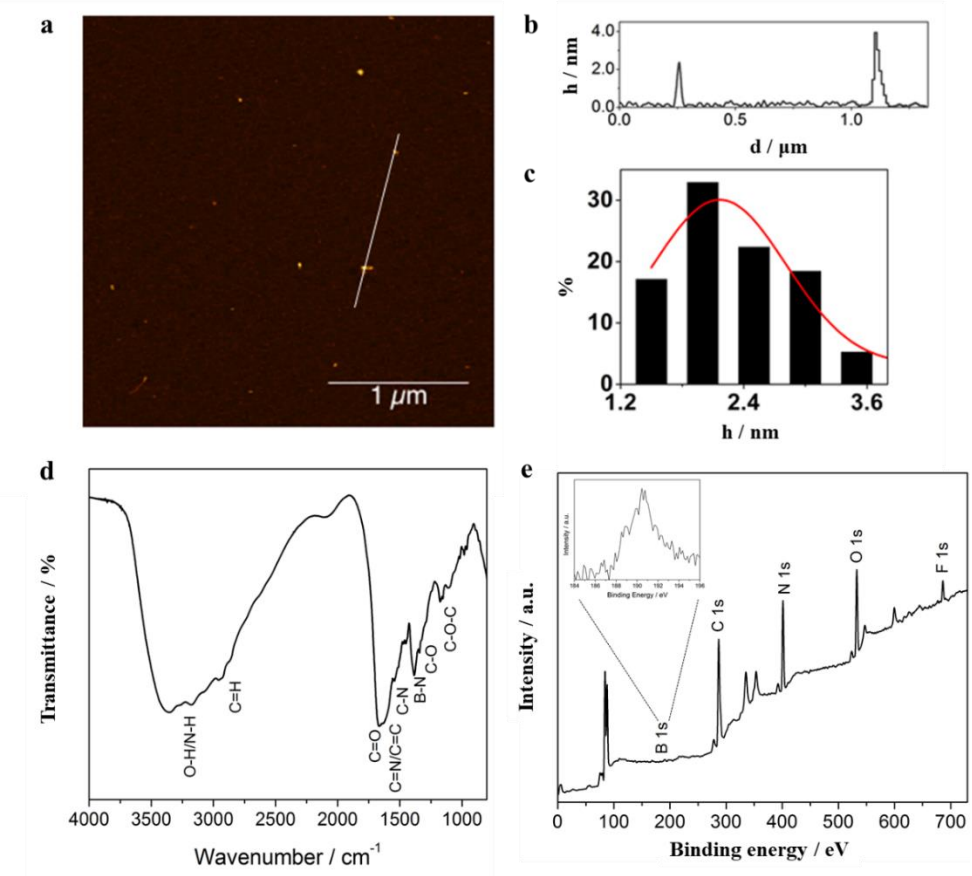

Figure 3.4 Structural and morphological characterization of pBCNDs: (**a**) tapping mode AFM image from a drop-cast aqueous solution of nanodots (scale bar 1 μm); (**b**) height profile along the dashed line in **a**; (**c**) sizes histogram with curve fit using a Gaussian model; (**d**) FT-IR spectrum (KBr); (**e**) XPS survey spectrum showing B1s, C1s, N1s, O1s and F1s.

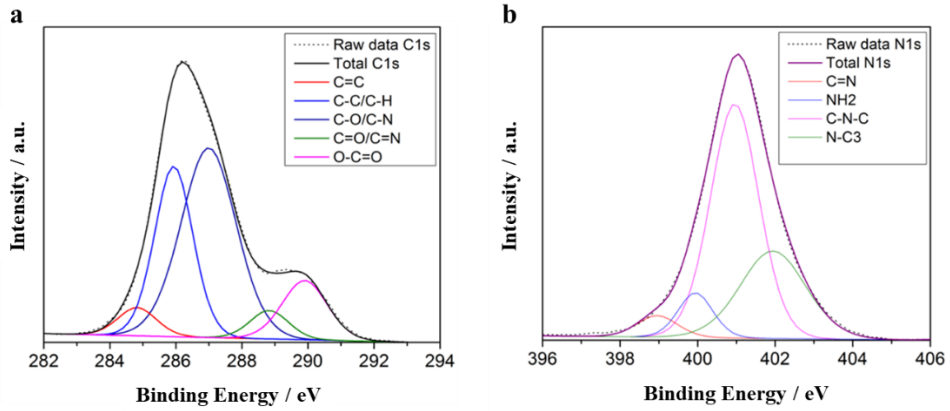

Figure 3.5 Deconvoluted C1s (**a**) and N1s (**b**) spectra of pBCNDs.

The surface components obtained from XPS analysis were in good agreement with the FT-IR results (**Figure 3.4e**). The full-scan XPS spectrum showed the presence

of carbon (C1s at 286.3 eV), nitrogen (N1s at 401.0 eV), oxygen (O1s at 532.3 eV), boron (B1s at 190.3 eV) and fluorine (F1s at 685.8 eV) and the atomic percentage of the five elements were as follow: 61.1, 22.4, 13.2, 1.2 and 2.1, respectively. The C and N configurations were examined by peak fitting analysis (**Figure 3.5a-b**). The C1s spectrum was deconvoluted into five components corresponding to C=C (284.8 eV, 5.0%), C-C/C-H (285.9 eV, 29.8%), C-O/C-N/C-Br (286.9 eV, 47.9%), C=O/C=N (288.8 eV, 5%) and O-C=O (289.9 eV, 12.3%) bonds. The N1s spectrum was deconvoluted into four peaks indicating C=N (398.9, 4.5%), NH_2 (399.9, 8.0%), C-N-C (400.9, 58.2%) and N-C_3 (401.9, 29.3%) bonds.

The photophysical properties of pBCNDs and oBCNDs were studied in water via absorption and fluorescence emission spectroscopies (**Figures 3.6-3.7** and **Figures S3.2-S3.3**).

The absorption spectrum of BCNDs showed the strong $S_0 \rightarrow S_1$ (π-π^*) transition at 496 nm and a weaker broad band around 350 nm attributed to the $S_0 \rightarrow S_2$ (π-π^*) related to the BODIPY. In addition, the absorption at *ca.* 300 nm could be ascribed to the π-π^* transition of the C=C units from the nanoparticle core.[25] As expected, the use of the BODIPY dye with carboxylic acid in *ortho* position on the meso-phenyl ring (BODIPY-oCOOH) does not affect the observed spectrum of oBCNDs as compared to pBCNDs, because it is typically related to the pyrrole substitution feature.

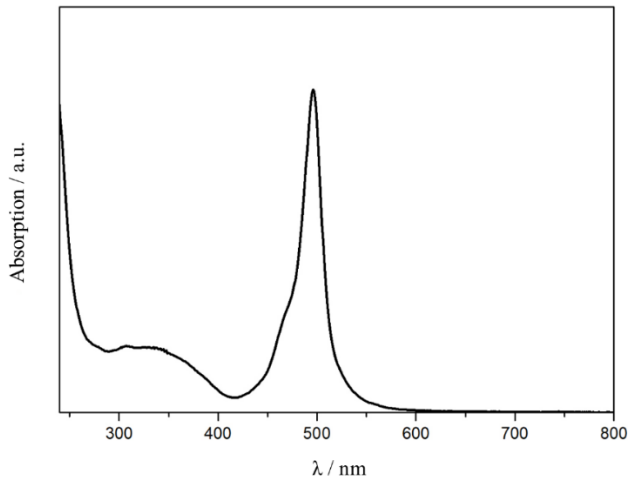

Figure 3.6 Absorption spectrum of pBCNDs in water.

The fluorescence emission spectrum of BCNDs shows the typical excitation wavelength-dependence phenomenon of CNDs resulting from the presence of different functional groups with different surface state levels that dominate the emission at characteristic excitation wavelenghts.[25] The fluorescence of these nanoparticles presents however a dual emission. In addition to the typical fluorescence peak in the blue region that shift from 352 to 470 nm when the excitation wavelength changes from 300 to 420 nm (similar to the hp-N-CNDs[25] previously reported), the use of BODIPY dopants in BCNDs results on the generation of a more intense peak centered at 507 nm that reaches the maximum intensity when exciting at 500 nm.

Fluorescence matrix scan experiments confirmed the BCNDs mainly green emission (**Figure 3.8)**. Fluorescence emission ranged from the blue-green to the green region upon excitation from 300 to 500 nm, showing CIE coordinates of x=0.17, y=0.39 exciting at 340 nm and x=0.15, y=0.69 exciting at 500 nm.

Finally, the measured fluorescence QY (PLQY) of pBCNDs and oBCNDs were 22% and 42%, showing that the increase of the PLQY of the BODIPY precursor through structural modification resulted on an advantageous strategy to enhance the emissive properties of the resulting nanoparticles.

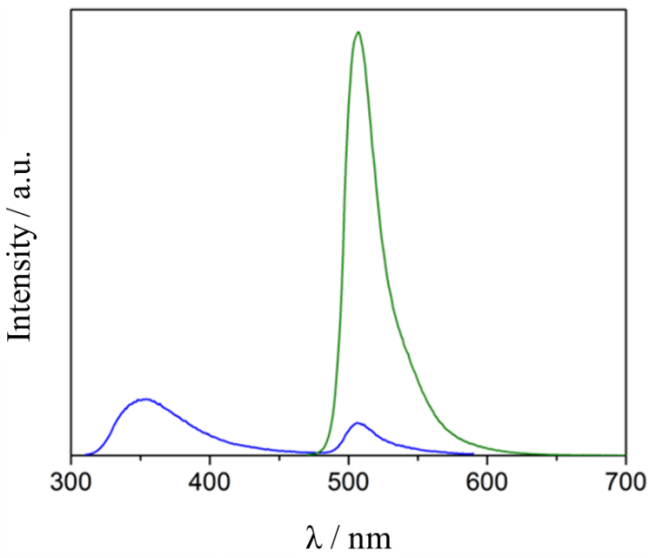

Figure 3.7 Fluorescence emission spectra of pBCNDs in water exciting at 300 nm (blue line) and 500 nm (green line).

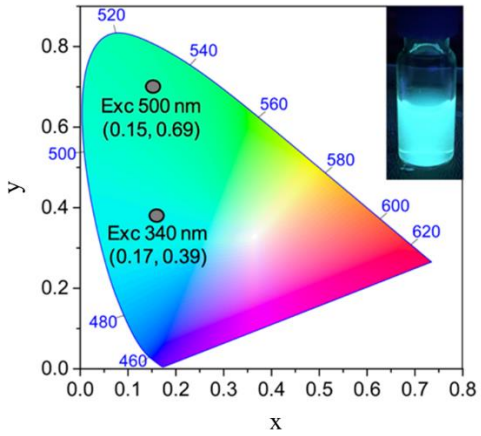

Figure 3.8 1931 CIE chromaticity diagram showing coordinates of BCNDs by exciting at 340 nm (x= 0.17, y= 0.39) and 500 nm (x= 0.15, y= 0.69).

3.1.3 Tuning core/shell composition of BCNDs and electrochemiluminescence studies

ECL is an electrochemically induced emission and since the excited species are produced with an electrochemical stimulus.

ECL techniques exploit the interesting combination of electrochemical and spectroscopic methods. As compared to other transduction techniques like photoluminescence (PL) and chemiluminescence (CL), ECL presents various advantages: (1) superior temporal and spatial control; (2) simple and efficient setup for rapid measurements using low volumes; (3) low background signal and high sensitivity due to the absence of a light excitation source.[26–29] All these features, together with robustness, versatility and low fabrication costs, offers unique characteristics in particular for (bio)sensor applications and make ECL the leading technique in clinical assays dealing with complex matrices.[30–32] Important companies, such as Roche© and Meso Scale Diagnostics©, developed and commercialized ECL-based assays for the detection of biological molecules that account for a market worth billions of dollars each year.

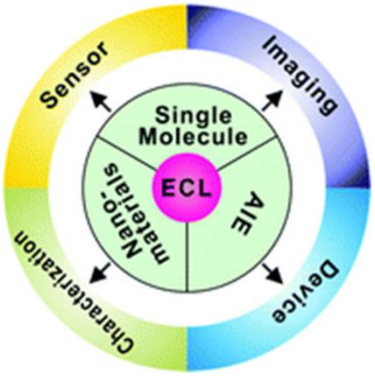

Figure 3.9 Scheme of the different ECL uses for specific materials and applications (AIE: aggregation induced emission). Adapted from reference [32].

ECL is an useful technique in the field of nanotechnology a lot of efforts are directed towards the study of the generation mechanisms of the ECL signal, as well as its amplification, from nanomaterials such as dye-doped silica nanoparticles, quantum and polymer dots and CDs.[33–36]

CDs showed interesting ECL processes that,[2] together with good chemical-physical stability, encourage the use of these nanoparticles as ECL emitters or co-reactant especially for (bio)sensor applications.[32,37,38]

Almost in the same period, Chi and Yang reported for the first time, in 2009, the use of hp-CQDs and hp-CNDs as ECL emitters.[39,40] Chi and coworkers demonstrate that hp-CQDs exhibit ECL emission under both anodic (+1.5 to 3.0 V) and cathodic (-1.0 to -3.0 V) applied potentials.[39] It was proposed an annihilation mechanism involving hp-CQDs$^{\bullet-}$ and hp-CQDs$^{\bullet+}$ and since the cathodic ECL emission was the most intense it was argued that the hp-CQDs$^{\bullet+}$ was the more stable. Also Yang and coworkers showed that hp-CNDs could also exhibit ECL via annihilation mechanism.[40] It was observed that the ECL intensity was higher at positive potentials suggesting that the reduced hp-CNDs$^{\bullet-}$ was in this case the most stable. ECL emission from CDs have been demonstrated also via co-reactant mechanism. For instance, Chi and coworkers studied how the ECL intensity could be affected by the co-reactant used and reported that SO_3^{2-} is a good co-reactant for hp-CQDs.[41]

The ECL efficiency of CDs could be enhanced through their chemical doping.[42] In this work hp-NS-GQDs, likely undoped hp-GQDs, have exhibited a low ECL efficiency. However, when mixed to $S_2O_8^{2-}$, as co-reactant, cathodic ECL (-1.5 - -2.5 V) of 32%, A 5.8-fold higher ECL emission from hp-NS-GQDs compared to the undoped hp-GQDs was reported and it was suggested that the increase hole acceptor behavior of the radical ion hp-NS-GQDs$^{\bullet-}$ respect to hp-GQDs$^{\bullet-}$ was responsible for the emission enhancement. In line with these studies, Xu and coworkers studied how the ECL is affected by the doping percentage.[43] They studied the ECL of a series of hp-N-CNDs with different nitrogen content. Higher ECL intensities were recorded for higher N doping (at negative potentials , from 0 to -1.5 V) using $S_2O_8^{2-}$ as co-reactant. The enhanced ECL was ascribed to the different electronic structure resulting from the different degree of doping, which resulted on the broadening of the band gap, the promotion of longer lifetimes of the excited states and finally the enhanced ECL emission.

There are few reports showing that the CDs surface functional groups affect the ECL emission.[42,44–46] In one work, the use of $NaBH_4$ to reduce the surface carboxylic groups on the surface of hp-CQDs has been reported as a successful way to enhance the ECL emission from the nanoparticles.[44] In another work, oxidized (treatment with H_2O_2) hp-CQDs are reported as better ECL emitters than the reduced (treatment with $NaBH_4$) hp-CQDs.[47]

In some reports, the ECL emission was reported to be red shifted respect to the PL emission.[42,46] This shift was attributed to the different energy separation of surface and core energy state in analogy to the inorganic (core/shell) QDs. However, a systematic investigation of the influence of core/shell nature of the carbon nanoparticles is missing, probably due to the elusive structure and its lack of fine control for targeted emission.

The majority of the works reported so far show therefore that CDs exhibit ECL in both annihilation/co-reactant mechanisms,[38,39,48,40–47] but the relationship between the nanoparticle structure/surface functional group and the electrogenerated emission has not been profoundly investigated.

In addition, it was showed the successful use of CDs as ECL co-reactants.[49–52] For instance, our group demonstrate the use of amino rich hp-N-CNDs as ECL co-reactants for the ECL emitter ruthenium(II) tris(2,2'-bipyridyl).[49] We also reported the enhancement of the ECL emission through the modification of the surface primary amino groups into tertiary amino groups, which is in agreement with previously reported molecular co-reactant,[53] showing therefore that the surface functional groups play an important role on the improvement of the ECL performances.

In the quest for novel systems with an ever-increasing sensitivity, able to emit across a palette of colors and to be easily modified for bioconjugation reaction, the work presented in this chapter focuses on the use of CNDs as ECL emitters and on the investigation of the effect of the shell and the core in the ECL mechanism. We have therefore studied the influence of *(i)* the introduction of the BODIPY dyes in the nanoparticle and *(ii)* the modification of the functional groups on the surface of the nanodots, through post-functionalization reaction, on the ECL emission properties.

Besides conferring various emissive properties to CNDs, as discussed in the previous paragraph, BODIPY dyes were chosen because of their known ECL activity.[54–59] The stability of BODIPY radical ions is higher when the positions of the core (**Figure 3.1**) are substituted or protected by steric hindrance. ECL of BODIPYs is usually produced by a typical annihilation mechanism. The absence of substituents, especially in positions 2 and 6 results in unstable radical ions ($BODIPY^{\bullet -}$ or $BODIPY^{\bullet +}$) that undergo dimerization with usually low ECL intensities.[60,61] We thus envisage that the incorporation of the dye in the nanoparticle structure might mitigate these ECL quenching effects.

The ECL spectra of the pBCNDs samples (pBCNDs bearing primary amino groups on their surface, methylated mpBCNDs and propionylated ppBCNDs tertiary amines, see **Section 3.3** for synthesis details) showed a red shift of the peak maximum wavelength (*ca.* 640 nm) compared to the photoluminescence peak (*ca.* 420 nm) (**Figure 3.10**). This observation supports the hypothesis that ECL is mainly

governed by the emissive states arising from the surface functional groups. This behavior was investigated by Ding and co-workers studying the ECL of silicon nanocrystals (NCs).[62] In this work, the PL is proved to depend by the excitation energy that exceeds the absorption of the edge states. This phenomenon is responsible of the different PL and ECL energies in silicon nanocrystals resulting complex to understand. Moreover, the NC polydispersity was highly controlled and the effect of the nanoparticle size, which can affect the photoluminescence emission, was excluded.[62–64]

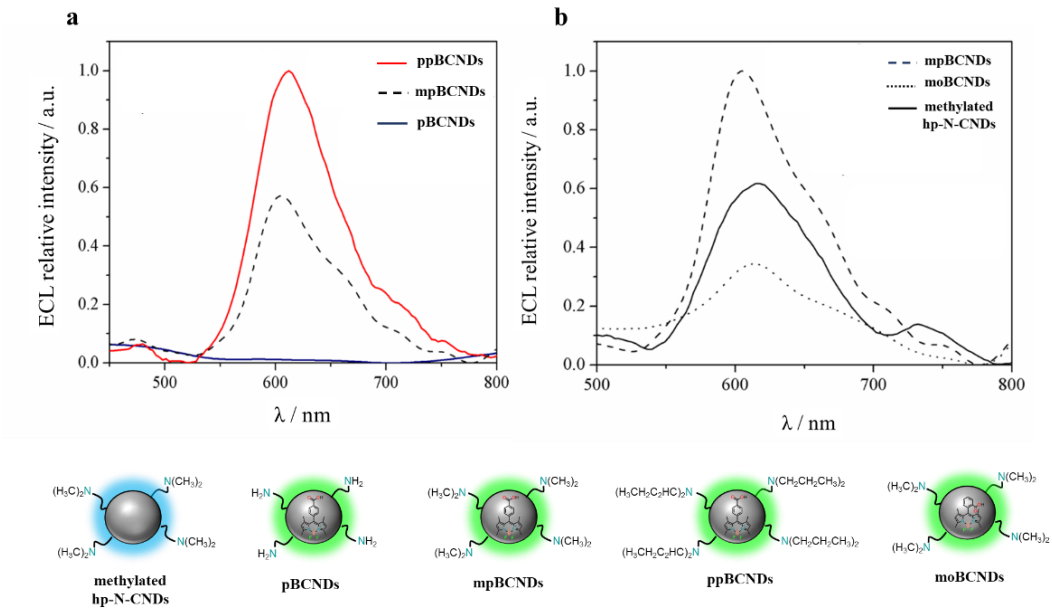

Figure 3.10 (**a**) ECL emission (glassy carbon electrode potential referred to Ag/AgCl at room temperature with platinum wire as counter electrode) of 1 mg mL^{-1} pBCND with primary amines on the surface (blue line), 1 mg mL^{-1} pBCND methylated (mpBCNDs, dashed black line) and 1 mg mL^{-1} pBCND with propionyl surface group (ppBCNDs, red line). Tri-*n*-propylamine (TPrA) is used as co-reactant at a concentration of 180 mM in phosphate buffer 0.2 M. (**b**) ECL emission (glassy carbon electrode potential referred to Ag/AgCl at room temperature with platinum wire as counter electrode) of 1 mg mL^{-1} of mpBCNDs (dashed black line), 1 mg mL^{-1} of moBCND (dotted black line) and 1 mg mL^{-1} methylated hp-N-CNDs not doped with BODIPY in the core (black line). TPrA is used as co-reactant at a concentration of 180 mM in phosphate buffer 0.2 M. Bottom images: schemes of the structures of the five nanoparticles analyzed.

The energy difference observed for PL and ECL indicates therefore a difference in the emission states of BCNDs. While PL mainly occurs through excitation and emission from the core, the ECL process is influenced by the superficial states (the shell) (**Figure 3.10**). The observed red shift underlines that the excitation states are

different and the energy separation in surface states, responsible of the ECL emission, is smaller compared to the band gap of the core, which is related to the PL emission.[39]

Notably, the ECL spectra recorded for the three pBCNDs with different surface functionalities, using the same concentration and experimental conditions, show similar peak wavelengths but different ECL maximum intensities (**Figure 3.10a**). Therefore the modification of the superficial states of the nanoparticles through post-functionalization reactions is a powerful tool in order to improve the ECL efficiency. The ppBCNDs show the highest ECL intensity followed by mpBCNDs, while pBCNDs bearing primary amines do not present any ECL emission. This result is in accordance with our previous studies in which the modification of primary amine into tertiary amines on the dot surface results in enhanced ECL performances.[49]

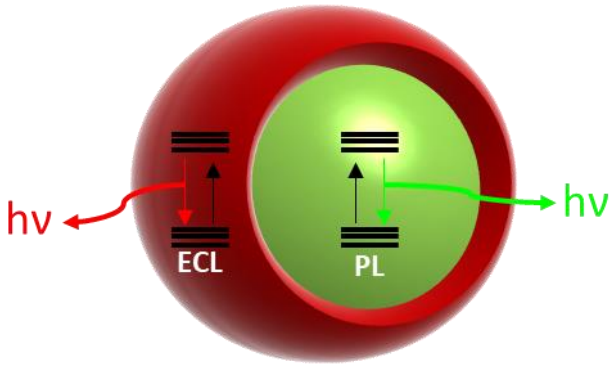

Figure 3.11 Scheme of the core-shell structure of BCNDs bearing BODIPY-pCOOH or BODIPY-oCOOH in the core (green) and methylated, propylated or primary amino groups on the surface (red).

The data presented above suggest that the BODIPY dye is incorporated in the core of the nanoparticle. Therefore we studied BCNDs prepared by using different BODIPY (pBCNDs and oBCNDs) or in their absence (hp-N-CNDs) in order to unravel the effect of the core composition on the ECL response (**Figure 3.9b**). For this purpose, we evaluate the ECL response of nanodots possessing the same shell, *i.e.* methyl as surface functional groups. The mpBCNDs show the higher ECL intensity respect to the moBCNDs that result on a partially quenched emission controlled by the surface methylated amino groups (**Figure 3.10b**). In fact, the methylated hp-N-CNDs without BODIPY in the core present a lower ECL emission

compared to the mpBCNDs but higher intensity than the observed with the moBCNDs. These results confirmed that the structural properties of the BODIPY dye also affect the ECL emission wavelength and efficiency, but with a different trend as compared to the PL emission, because PL and ECL are originated by different emissive states of the nanoparticles.

3.2 Conclusions

This chapter reports the design, synthesis and characterization of CNDs doped with BODIPY dyes (BCNDs) showing the versatility of a multicomponent hydrothermal synthesis for preparing materials with predictable optical properties.

Experimental evidences suggest that the BODIPY has been successfully incorporated in the nanodots through a carboxylic moiety meso-phenyl ring of the dye that likely reacts with the amines of Arg and EDA The BCNDs are highly water soluble, possess amino groups on the surface that are amenable for further functionalization and present the typical green fluorescence emission of the BODIPY. We have also showed that the PLQY of the dye affect the PLQY of the resulting nanoparticles demonstrating that the structural modification of the BODIPY precursor lead to nanodots with enhanced fluorescence emission.

The rational brought forward in this work could be extended for preparing multicolored CNDs by using different BODIPY precursors.

In the quest for novel ECL emitters, able to emit across a palette of colors and to be easily modified for bioconjugation reaction, we studied the ECL properties of the prepared materials. BCNDs showed a good ECL emission that can be mainly modulated through post-synthetic surface modification and thus suggesting that the dye is likely incorporated in the core of the nanodots.

3.3 Experimental section

3.3.1 Materials and methods

L-Arginine was bought from Fluorochem (>98%). Ethylendiamine (>99,5%), Benzyl bromide (98%), N,N-Diisopropylethylamine (99.5%), Boron trifluoride diethyl etherate (>99%) and Paraformaldehyde (Sigma Aldrich, 95%) were bought from Sigma-Aldrich. Terephthalaldehydic acid (>98%), 2,4-Dimethylpyrrole (>98%) and Sodium cyanoborohydride (>95%) were bought from TCI chemicals. 2-Carboxybenzaldehyde (99%) and 2,3-Dichloro-5,6-dicyano-p-benzoquinone (98%) were bought from Acros Organics. The formalin aqueous solution (37% w/v) was prepared according to a reference protocol.[65]

Kaiser test kit was purchased from Sigma-Aldrich. Dialysis tubes with molecular weight cutoff 0.5-1KDa were bought from Spectrum Labs. A Millipore water purification system (>18Milli-Q, Millipore) was used to produce ultrapure fresh water for all the experiments.

The microwave syntheses were performed on a CEM Discover-SP microwave reactor.

UV-vis absorption spectra were recorded on a Varian Cary 5000 UV–vis-NIR spectrometer. Fluorescence emission spectra were recorded using a Varian Cary Eclipse fluorescence spectrophotometer. All the measures were performed using 10 mm path-length quartz cuvettes.

Fourier-Transform Infrared Spectroscopy spectra (KBr) were recorded using a Perkin Elmer 2000 spectrometer.

Atomic force microscopy (AFM) images were recorded on a Nanoscope IIIa VEECO Instruments microscope. AFM analyses were performed using a HQ:NSC19/ALBS probe (80kHz; 0.6 N/m) (MikroMasch) from drop cast of samples in an aqueous solution (concentration of few mg/mL) on a mica substrate. The AFM-images were examined using Gwyddion 2.50 as AFM-image analysis software.

^{1}H and ^{13}C nuclear magnetic resonance (NMR) spectra were measured using a Varian Inova at 500 MHz.

3.3.2 Multistep synthesis of BODIPY-pCOOH

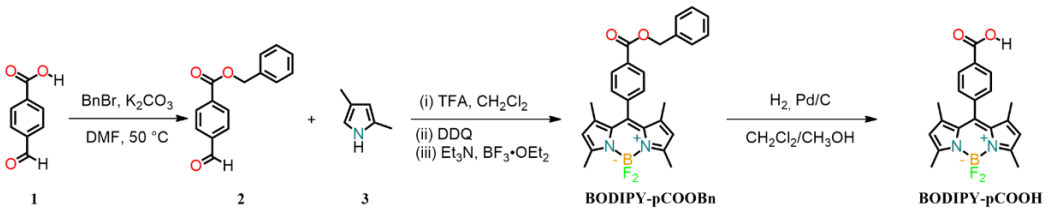

Figure 3.12 Scheme of the multistep synthesis of BODIPY-pCOOH.

3.3.2.1 Synthesis of benzyl 4-formylbenzoate (2)

To a solution of 4-formylbenzoic acid (**1**, 2.20 g, 14.65 mmol) in anhydrous DMF (15 mL) was added K_2CO_3 (2.02 g, 14.65 mmol) and the mixture was stirred for 30 min at 50 °C, under argon. Then, benzyl bromide (BnBr, 1.58 mL, 13.32 mmol) was added dropwise and the mixture was stirred for 3 h at 50 °C, under argon. The mixture was diluted with H_2O and Et_2O, the organic phase was washed with sat. aq. K_2CO_3 (2 ×), brine and H_2O. The organic phase was dried (Na_2SO_4) and concentrated under reduced pressure. The residue is a transparent oil that solidifies on standing. Product was obtained as white solid (3.09 g, 97 % yield). **M.p.**: 37.1°C. **^{1}H-NMR** (500 MHz, $CDCl_3$): δ 10.10 (s, 1H), 8.23 (d, J = 8.4 Hz, 2H), 7.99 – 7.92 (m, 2H), 7.48 – 7.44 (m, 2H), 7.43 – 7.35 (m, 3H), 5.40 (s, 2H). **^{13}C-NMR** (126 MHz, $CDCl_3$): δ 191.81, 165.60, 139.42, 135.74, 135.31, 130.52, 129.73, 128.91, 128.72, 128.56, 67.54. Characterization in accordance with literature.[66]

3.3.2.2 Synthesis of BODIPY-pCOOBn

In a 0.5 L round-bottomed flask, a solution of benzyl 4-formylbenzoate (**2**, 2.40 g, 9.99 mmol) and 2,4-dimethylpyrrole (**3**, 2.06 mL, 19.97 mmol) in CH_2Cl_2 (0.25 L) was prepared and stirred for 20 min at r.t., under argon. Then, trifluoroacetic acid

(catalytic, one drop) was added and the mixture was stirred overnight, under dark and argon. Then, a solution of 2,3-dichloro-5,6-dicyano-1,4-benzoquinone (2.27 g, 10.00 mmol) in CH_2Cl_2 (0.10 L) was added and the mixture was stirred for 1.5 h. Then was added Et_3N (30.0 mL, 215.3 mmol), followed by slow addition of $BF_3{\cdot}OEt_2$ (30.0 mL, 243.1 mmol) and the mixture was left stirring for 2 h. To the mixture was diluted with H2O and the organic phase was washed with H_2O (2 ×), 1 M aq. HCl solution (5 ×) and brine. The organic phase was dried (Na_2SO_4) and concentrated under reduced pressure. The mixture was purified by two consecutive column chromatography (SiO_2, 40-63 µm, Pet.Et./CH_2Cl_2 9:1 → 6:4) to obtain pure product as bright orange solid (1.10 g, 24 % yield). **M.p.**: 133.1 °C. **^{1}H-NMR** (500 MHz, $CDCl_3$): δ 8.21 (d, J = 8.3 Hz, 2H), 7.52 – 7.48 (m, 1H), 7.45 – 7.35 (m, 2H), 5.99 (s, 1H), 5.40 (s, 1H), 2.56 (s, J = 6.8 Hz, 3H), 1.35 (s, J = 11.8 Hz, 3H). **^{13}C-NMR** (126 MHz, $CDCl_3$): δ 166.02, 156.23, 143.10, 140.40, 140.19, 135.90, 131.13, 131.00, 130.70, 128.91, 128.71, 128.70, 128.63, 121.69, 67.38, 14.84, 14.78. ^{19}F-NMR (376 MHz, $CDCl_3$): δ -146.20, -146.29, -146.38, -146.46. **FT-IR** (KBr): cm^{-1} 1724, 1681, 1544, 1508, 1472, 1405, 1307, 1272, 1194, 1153, 1085, 978, 737. ES (MS +): 459.3 (M + H+), C27H25BF2N2O2 requires 458.3. Characterization in accordance with literature.[67]

3.3.2.3 Synthesis of BODIPY-pCOOH

A solution of **BODIPY-COOBn** (1.00 g, 2.17 mmol) in CH_2Cl_2/CH_3OH (0.35 L, 1:1 v/v) was degassed with argon for 30 min. Then, Pd/C (10%, 100 mg) was added, while flushing argon. The flask was then filled with H_2 (by 3 cycles of evacuating under vacuum and purging with H_2) and the mixture was left stirring at r.t. for 4 h. The mixture was then filtered over a 0.1 µm Teflon membrane, the membrane was washed with CH_2Cl_2/CH_3OH (1:1 v/v) and the filtrate was concentrated under reduced pressure. Product was obtained as red solid (0.80 g, quantitative yield). **M.p.** > 250 °C. **^{1}H-NMR** (500 MHz, DMSO-d_6): δ 13.28 (bs, 1H), 8.10 (d, J = 8.3 Hz, 2H), 7.53 (d, J = 8.3 Hz, 2H), 6.20 (s, 2H), 2.46 (s, 6H), 1.33 (s, 6H). **^{13}C-NMR** (126 MHz, DMSO-d_6): δ 166.86, 155.24, 142.63, 140.81, 138.30, 130.26, 130.13, 128.35, 121.58, 14.24, 14.06. 19F NMR (376 MHz, DMSO-d_6): δ -143.52, -143.61, -143.69, -143.78. **FT-IR** (KBr): cm^{-1} 1683, 1610, 1549, 1516, 1471, 1412, 1314,

1291, 1199, 1157, 1124, 1091, 1048, 973, 739. ES (MS -): 367.0 (M - H+), C20H19BF2N2O2 requires 368.18. Characterization in accordance with literature.[58]

3.3.3 Multistep synthesis of BODIPY-oCOOH

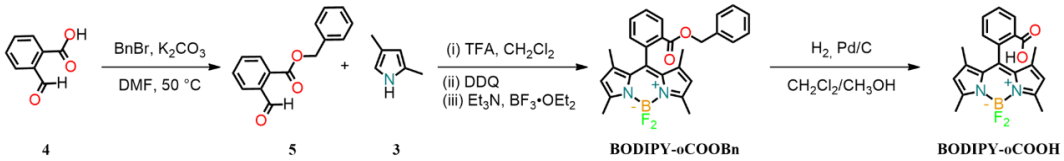

Figure 3.13 Scheme of the multistep synthesis of BODIPY-oCOOH.

3.3.3.1 Synthesis of benzyl 2-formylbenzoate (5)

Benzyl bromide (BnBr, 1.50 mL, 12.63 mmol) was added dropwise to a solution of 2-formylbenzoic acid (**4**, 2,00 g, 13.32 mmol) and K_2CO_3 (2.09 g, 15.12 mmol) in anhydrous DMF (15 mL) at 45°C, under argon. The resulting mixture was left stirring at these conditions for three hours and then quenched with Et_2O, washed with sat. aq. $NaHCO_3$ (2 ×), brine and H_2O. The organic layer was dried (Na_2SO_4) and concentrated under reduced pressure. Product was obtained as yellow oil (3.06 g, 95 % yield). **^{1}H-NMR** (500 MHz, $CDCl_3$): δ 10.64 (s, 1H), 8.03 – 7.98 (m, 1H), 7.98 – 7.92 (m, 1H), 7.65 (m, 2H), 7.41 (m, 5H), 5.43 (s, 2H). **^{13}C-NMR** (126 MHz, $CDCl_3$): δ 192.05, 191.99, 166.10, 137.11, 135.28, 132.93, 132.45, 132.00, 130.43, 128.74, 128.61, 128.47, 67.67. **FT-IR** (KBr): cm^{-1} 1713, 1596, 1576, 1497, 1453, 1377, 1265, 1194, 1128, 1072, 912, 830, 798, 749, 696, 640.

3.3.3.2 Synthesis of BODIPY-oCOOBn

Trifluoroacetic acid (**TFA**, catalytic, 1 drop) was added to a solution of 2-formylbenzoate (**5**, 1.21 g, 5.04 mmol) and 2,4-dimethylpyrrole (**3**, 1.12 mL, 10.86 mmol) in CH_2Cl_2 (200 mL) under argon. The resulting solution was left stirring under argon for 9 h in dark at room temperature. Then 2,3-dichloro-5,6-dicyano-1,4-benzoquinone (1.13 g, 4.98 mmol) was added and the mixture was left stirring for 1.5 h. Et_3N (9.6 mL, 68.88 mmol) was then added, followed by dropwise

addition of $BF_3{\cdot}OEt_2$ (10.4 mL, 84.27 mmol). The resulting mixture was left stirring overnight, washed with $NaHCO_3$ 0.1 M (2 ×) and brine. The organic phase was dried (Na_2SO_4) and concentrated under reduced pressure. The resulting mixture was eluted by gravity through a pad of silica using CH_2Cl_2 as eluent. Then the eluate was dried under reduced pressure and purified by two consecutive column chromatography (SiO_2, 40-63 µm, Pet. Et./CH_2Cl_2 9:1 → 3:1) obtaining pure product as orange solid (0.49 g, 22% yield). **M.p.**: 48.4 °C. **^{1}H-NMR** (500 MHz, $CDCl_3$): δ 8.12 (dd, J = 7.9, 1.2 Hz, 1H), 7.65 (td, J = 7.5, 1.4 Hz, 1H), 7.57 (td, J = 7.7, 1.3 Hz, 1H), 7.33 (dd, J = 7.6, 1.3 Hz, 1H), 7.25 (dd, J = 4.9, 1.7 Hz, 3H), 7.14 (dd, J = 6.4, 3.3 Hz, 2H), 5.89 (s, 2H), 5.14 (s, 2H), 2.56 (s, 5H), 1.28 (s, 6H). **^{13}C-NMR** (126 MHz, $CDCl_3$): δ 165.99, 155.01, 142.10, 141.14, 135.63, 135.09, 132.93, 131.17, 131.03, 130.53, 129.66, 129.48, 129.20, 128.55, 128.32, 121.15, 120.96, 67.47, 14.67, 14.03. **FT-IR** (KBr): cm^{-1} 1720, 1632, 1547, 1508, 1472, 1409, 1383, 1368, 1308, 1285, 1257, 1195, 1155, 1121, 1084, 1048, 979, 734, 696, 477. **ES** (MS +): 459.2 (M + H+), C27H25BF2N2O2 requires 458.3.

3.3.3.3 Synthesis of BODIPY-oCOOH

BODIPY-oCOOBn (0.40 g, 872,77 µmol) was dissolved in CH_2Cl_2/CH3OH (0.12 L, 5:1 v/v) and the resulting solution was degassed with argon for 30 min. Then this solution was treated with Pd/C (10%, 78 mg) while flushing argon. The flask was then filled with H_2 (first 15 minutes the gas was left bubbling into the solution) and left stirring for 1 h at room temperature. The final mixture was then filtered through a 0.1 µm Teflon membrane, the membrane was washed with CH_2Cl_2/CH_3OH (1:1 v/v) and the filtrate was concentrated under reduced pressure. Product was obtained as red solid (0.32 g, quantitative yield). **M.p.** > 250 °C. **^{1}H-NMR** (500 MHz, acetone): δ 11.45 (s, 1H), 8.19 (d, J = 7.9 Hz, 1H), 7.84 (t, J = 7.6 Hz, 1H), 7.74 (t, J = 7.7 Hz, 1H), 7.47 (d, J = 7.6 Hz, 1H), 6.08 (s, 2H), 2.50 (s, 6H), 1.38 (s, 6H). **^{13}C-NMR** (126 MHz, acetone): δ 166.10, 154.38, 142.63, 141.99, 135.83, 133.15, 131.20, 130.93, 130.82, 130.76, 129.66, 129.53, 120.78, 13.63, 13.26. **FT-IR** (KBr): cm^{-1} 1727, 1540, 1508, 1469, 1405, 1370, 1300, 1251, 1226, 1197, 1158, 1135, 1102, 1082, 981, 933, 823, 799, 775, 734, 688, 649, 579, 513, 477. **ES** (MS +): 369.2 (M + H+), C20H19BF2N2O2 requires 368.18.

3.3.4 Synthesis of pBCNDs

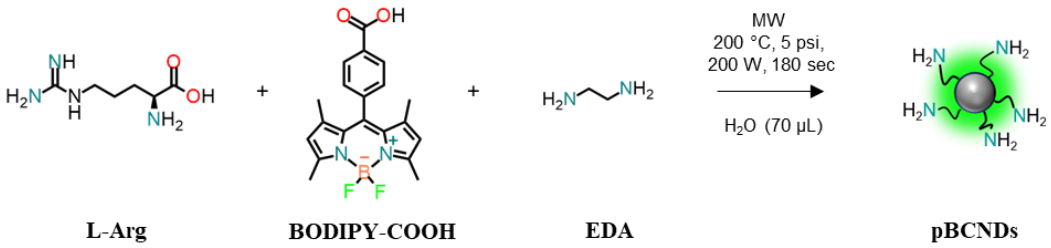

Figure 3.14 Scheme of the pBCNDs synthesis.

A solution of L-arginine (40.0 mg, 230 µmol), BODIPY-COOH (22.0 mg, 59.8 µmol) and ethylendiamine (8 µL, 115 µmol) in MilliQ water (70 µL) was heated by microwave at 200°C, 5 psi, 200 W for 180 seconds. After the heating process mixture colour changed from yellow to red as result of formation of CNDs. The reaction mixture was then diluted with few millilitres of water and filtered through a 0.1 µm microporous membrane. The solution was pH corrected to pH 7.2 and filtered once again through a 0.1 µm microporous membrane. The obtained deep orange filtrate solution was then dialyzed against pure water through a dialysis membrane (molecular weight cutoff 0.5-1 KDa) for 1 day. The purified solution was then lyophilized obtaining a red solid (20.0 mg, Kaiser Test 900 $\mu mol_{NH2}/g$).

3.3.5 Synthesis of mpBCNDs

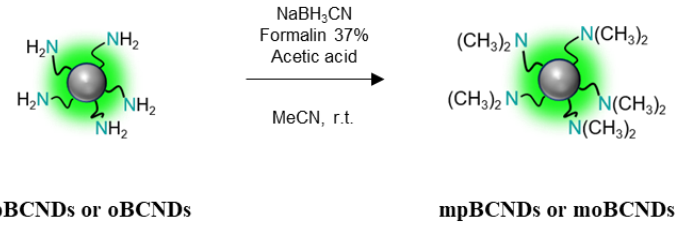

Figure 3.15 General scheme of the methylated BCNDs synthesis (**mpBCNDs** or **moBCNDs**).

$NaBH_3CN$ (33 mg) was added to a solution of **pBCNDs** (18 mg), formalin (37% solution in water, 1.50 mL) in MeCN (1.50 mL). Then acetic acid (77 µL) was added and the resulting solution was left stirring for 3 h at room temperature. The resulting mixture was dried under vacuum obtaining a red solid. This residue was dissolved in MeOH and purified by size exclusion chromatography (Sephadex LH-

20), dried under vacuum and lyophilized from water obtaining a red solid (19.6 mg, Kaiser Test 70 $\mu mol_{NH2}/g$).

3.3.6 Synthesis of oBCNDs

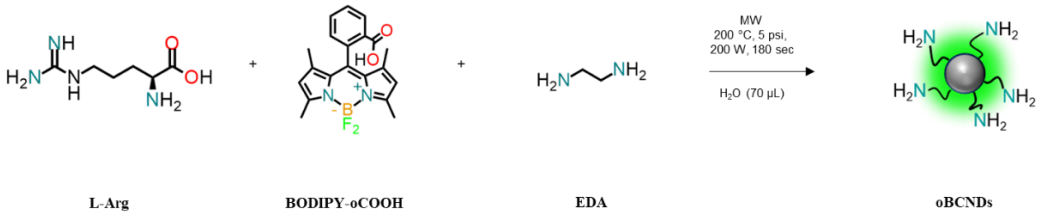

Figure 3.16 Scheme of the oBCNDs synthesis.

oBCNDs were synthetized using the same procedure and stoichiometric ratios used for of **pBCNDs**. The resulting product was obtained as red solid (21.0 mg, Kaiser Test 650 $\mu mol_{NH2}/g$).

3.3.7 Synthesis of moBCNDs

A solution of $NaBH_3CN$ (22 mg), **oBCNDs** (18 mg), formalin (37% aqueous solution, 1 mL) and acetic acid (51 µL) in MeCN (1 mL) was left stirring for 3 h at room temperature. The resulting mixture was dried under vacuum obtaining a red solid. This residue was dissolved in MeOH and purified by size exclusion chromatography (Sephadex LH-20), dried under vacuum and lyophilized from water obtaining a red solid (18.9 mg, Kaiser Test 20 $\mu mol_{NH2}/g$).

3.3.8 Synthesis of ppBCNDs

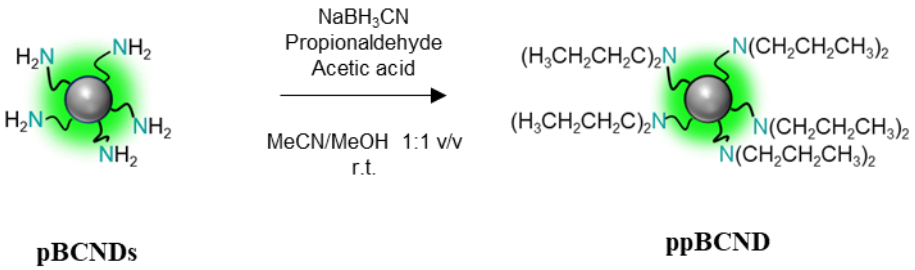

Figure 3.17 Scheme of the ppBCNDs synthesis.

Similarly to mpBCNDs synthesis, a solution of $NaBH_3CN$ (33 mg), pBCNDs (20 mg), propionaldehyde (0.55 mL) and acetic acid (77 µL) in a MeCN/MeOH (1:1 v/v, 3 mL) was left stirring for 1 day at room temperature. The resulting mixture was dried under vacuum obtaining a red solid. This residue was dissolved in MeOH and purified by size exclusion chromatography (Sephadex LH-20), dried under vacuum and lyophilized from water obtaining a red solid (22.0 mg, Kaiser Test 60 $\mu mol_{NH_2}/g$).

3.3.9 Supporting figures

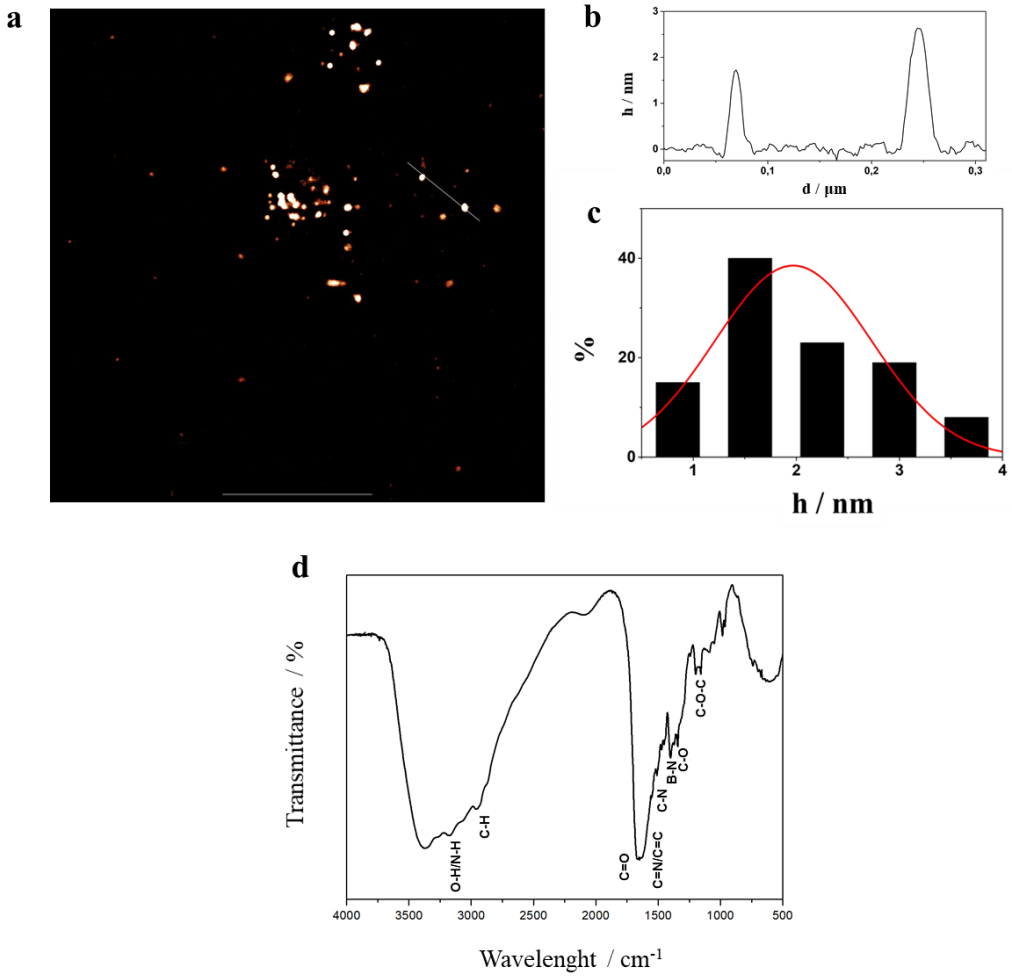

Figure S3.1 Morphological and structural analysis of oBCNDs: (**a**) tapping mode AFM image, on the bottom right the white scale bar (500 nm); (**b**) height profile along the dashed line in **a**; (**c**) height sizes distribution histogram and superimposed Gaussian fit; (**d**) FT-IR spectrum (KBr).

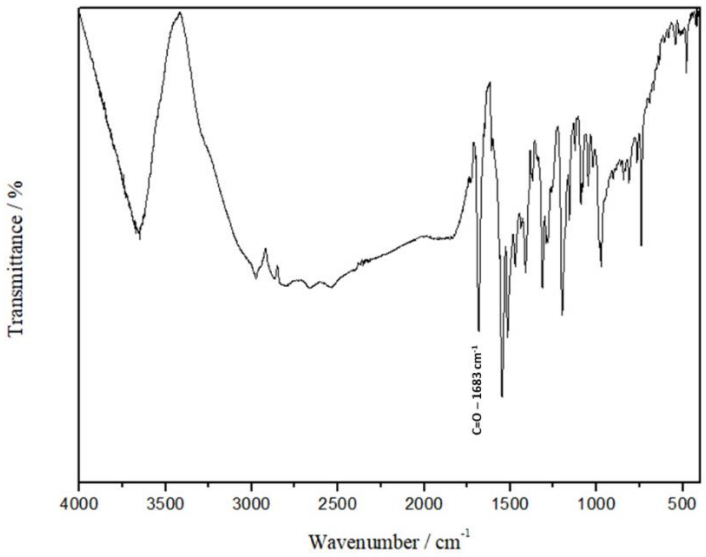

Figure S3.2 FT-IR spectrum (KBr) of BODIPY-pCOOH.

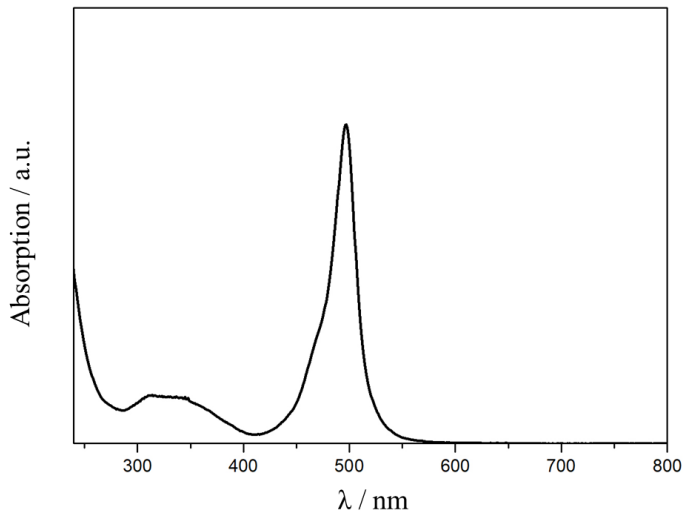

Figure S3.3 UV-vis absorption spectrum of oBCNDs in water.

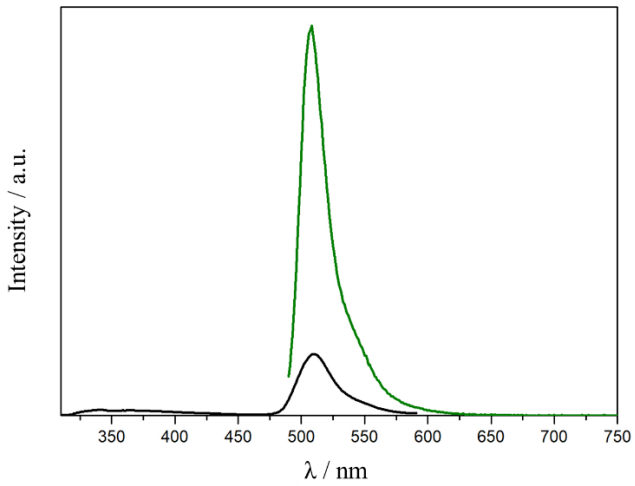

Figure S3.4 Fluorescence emission spectra of oBCNDs in water exciting at 300 nm (black line) and 480 nm (green line).

3.4 References

(1) Liu, M. L.; Chen, B. Bin; Li, C. M.; Huang, C. Z. Carbon Dots: Synthesis, Formation Mechanism, Fluorescence Origin and Sensing Applications. *Green Chem.* **2019**, *21* (3), 449–471.

(2) Tian, X.-T.; Yin, X.-B. Carbon Dots, Unconventional Preparation Strategies, and Applications Beyond Photoluminescence. *Small* **2019**, *1901803*, 1901803.

(3) Jaleel, J. A.; Pramod, K. Artful and Multifaceted Applications of Carbon Dot in Biomedicine. *J. Control. Release* **2018**, *269* (November 2017), 302–321.

(4) Yan, F.; Sun, Z.; Zhang, H.; Sun, X.; Jiang, Y.; Bai, Z. The Fluorescence Mechanism of Carbon Dots, and Methods for Tuning Their Emission Color: A Review. *Microchim. Acta* **2019**, *186* (8).

(5) Yuan, F.; Li, S.; Fan, Z.; Meng, X.; Fan, L.; Yang, S. Shining Carbon Dots: Synthesis and Biomedical and Optoelectronic Applications. *Nano Today* **2016**, *11* (5), 565–586.

(6) Yao, B.; Huang, H.; Liu, Y.; Kang, Z. Carbon Dots: A Small Conundrum. *Trends Chem.* **2019**, *1* (2), 235–246.

(7) Arcudi, F.; Đorđević, L.; Prato, M.; Arcudi, F.; Dordevic, L. Rationally Designed Carbon NanoDots En Route to Pure White-Light Emission. *Angew. Chem. Int. Ed.* **2017**, *56* (15), 4170–4173.

(8) Đorđević, L.; Arcudi, F.; Prato, M. Preparation, Functionalization and Characterization of Engineered Carbon Nanodots. *Nat. Protoc.* **2019**, *14* (10), 2931-2953.

(9) Loudet, A.; Burgess, K. BODIPY Dyes and Their Derivatives: Syntheses and Spectroscopic Properties. *Chem. Rev.* **2007**, *107* (11), 4891–4932.

(10) Ulrich, G.; Ziessel, R.; Harriman, A. The Chemistry of Fluorescent Bodipy Dyes: Versatility Unsurpassed. *Angew. Chem. Int. Ed.* **2008**, *47* (7), 1184–1201.

(11) Lu, H.; MacK, J.; Yang, Y.; Shen, Z. Structural Modification Strategies for the Rational Design of Red/NIR Region BODIPYs. *Chem. Soc. Rev.* **2014**, *43* (13), 4778–4823.

(12) Kowada, T.; Maeda, H.; Kikuchi, K.; Maeda, H. BODIPY-Based Probes for the Fluorescence Imaging of Biomolecules in Living Cells. *Chem. Soc. Rev.* **2015**, *44* (14), 4953–4972.

(13) Vo-Hoang, Y.; Micouin, L.; Ronet, C.; Gachelin, G.; Bonin, M. Total Enantioselective Synthesis and In Vivo Biological Evaluation of a Novel Fluorescent BODIPY α-Galactosylceramide. *ChemBioChem* **2003**, *4* (1), 27–33.

(14) Gießler, K.; Griesser, H.; Göhringer, D.; Sabirov, T.; Richert, C. Synthesis of 3'-BODIPY-Labeled Active Esters of Nucleotides and a Chemical Primer Extension Assay on Beads. *Eur. J. Org. Chem.* **2010,** *19*, 3611-3620.

(15) Dilek, Ö.; Bane, S. L. Synthesis, Spectroscopic Properties and Protein Labeling of Water Soluble 3,5-Disubstituted Boron Dipyrromethenes. *Bioorg. Med. Chem. Lett.* **2009**, *19* (24), 6911–6913.

(16) Dodani, S. C.; He, Q.; Chang, C. J. A Turn-On Fluorescent Sensor for Detecting Nickel in Living Cells. *J. Am. Chem. Soc.* **2009**, *131* (50), 18020–18021.

(17) Niu, S.-L.; Ulrich, G.; Retailleau, P.; Harrowfield, J.; Ziessel, R. New Insights into the Solubilization of Bodipy Dyes. *Tetrahedron Lett.* **2009**, *50* (27), 3840–3844.

(18) Niu, S. L.; Ulrich, G.; Ziessel, R.; Kiss, A.; Renard, P.-Y.; Romieu, A. Water-Soluble BODIPY Derivatives. *Org. Lett.* **2009**, *11* (10), 2049–2052.

(19) Li, L.; Han, J.; Nguyen, B.; Burgess, K. Syntheses and Spectral Properties of Functionalized, Water-Soluble BODIPY Derivatives. *J. Org. Chem.* **2008**, *73* (5), 1963–1970.

(20) Atilgan, S.; Ozdemir, T.; Akkaya, E. U. A Sensitive and Selective Ratiometric near IR Fluorescent Probe for Zinc Ions Based on the Distyryl-Bodipy Fluorophore. *Org. Lett.* **2008**, *10* (18), 4065–4067.

(21) Jiao, L.; Li, J.; Zhang, S.; Wei, C.; Hao, E.; Vicente, M. G. H. A Selective Fluorescent Sensor for Imaging Cu2+ in Living Cells. *New J. Chem.* **2009**, *33* (9), 1888.

(22) Zhu, S.; Zhang, J.; Vegesna, G.; Luo, F. T.; Green, S. A.; Liu, H. Highly Water-Soluble Neutral BODIPY Dyes with Controllable Fluorescence Quantum Yields. *Org. Lett.* **2011**, *13* (3), 438–441.

(23) Hesari, M.; Lu, J.; Wang, S.; Ding, Z. Efficient Electrochemiluminescence of a Boron-Dipyrromethene (BODIPY) Dye. *Chem. Commun.* **2015**, *51* (6), 1081–1084.

(24) Wang, D.; Fan, J.; Gao, X.; Wang, B.; Sun, S.; Peng, X. Carboxyl BODIPY Dyes from Bicarboxylic Anhydrides: One-Pot Preparation, Spectral Properties, Photostability, and Biolabeling. *J. Org. Chem.* **2009**, *74* (20), 7675–7683.

(25) Arcudi, F.; Đorđević, L.; Prato, M. Synthesis, Separation, and Characterization of Small and Highly Fluorescent Nitrogen-Doped Carbon NanoDots. *Angew. Chem. Int. Ed.* **2016**, *55* (6), 2107–2112.

(26) Miao, W. Electrogenerated Chemiluminescence and Its Biorelated Applications. *Chem. Rev.* **2008**, *108* (7), 2506–2553.

(27) Richter, M. M. Electrochemiluminescence (ECL). *Chem. Rev.* **2004**, *106(6)*, 3003-3036.

(28) Hesari, M.; Ding, Z. Review-Electrogenerated Chemiluminescence: Light Years Ahead. *J. Electrochem. Soc.* **2016**, *163* (4), H3116–H3131.

(29) Pravda, M.; Guilbault, G. G.; Fahnrich, K. A. Recent Applications of Electrogenerated Chemiluminescence in Chemical Analysis. *Talanta* **2001**, *54*, 531–559.

(30) Huo, X.-L.; Lu, H.-J.; Xu, J.-J.; Zhou, H.; Chena, H.-Y. Recent Andvances of Ratiometric Electrochemiluminescence Biosensors. *J. Mater. Chem. B* **2019**, *7*, 6469–6475.

(31) Miao, W.; Choi, J.-P.; Bard, A. J. Electrogenerated Chemiluminescence 69: The Tris(2,2'-Bipyridine)Ruthenium(II), (Ru(Bpy) 3 2+)/Tri- n -Propylamine (TPrA) System RevisitedA New Route Involving TPrA •+ Cation Radicals. *J. Am. Chem. Soc.* **2002**, *124* (48), 14478–14485.

(32) Zhang, Z.; Du, P.; Pu, G.; Wei, L.; Wu, Y.; Guo, J.; Lu, X. Utilization and Prospects of Electrochemiluminescence for Characterization, Sensing, Imaging and Devices. *Mater. Chem. Front.* **2019**, *3* (11), 2246–2257.

(33) Valenti, G.; Rampazzo, E.; Bonacchi, S.; Petrizza, L.; Marcaccio, M.; Montalti, M.; Prodi, L.; Paolucci, F. Variable Doping Induces Mechanism Swapping in Electrogenerated Chemiluminescence of Ru(Bpy) 3 2+ Core–Shell Silica Nanoparticles. *J. Am. Chem. Soc.* **2016**, *138* (49), 15935–15942.

(34) Valenti, G.; Rampazzo, E.; Kesarkar, S.; Genovese, D.; Fiorani, A.; Zanut, A.; Palomba, F.; Marcaccio, M.; Paolucci, F.; Prodi, L. Electrogenerated Chemiluminescence from Metal Complexes-Based Nanoparticles for Highly Sensitive Sensors Applications. *Coord. Chem. Rev.* **2018**, *367*, 65–81.

(35) Kesarkar, S.; Rampazzo, E.; Zanut, A.; Palomba, F.; Marcaccio, M.; Valenti, G.; Prodi, L.; Paolucci, F. Dye-Doped Nanomaterials: Strategic Design and Role in Electrochemiluminescence. *Curr. Opin. Electrochem.* **2018**, *7*, 130–137.

(36) Zhu, S.; Song, Y.; Zhao, X.; Shao, J.; Zhang, J.; Yang, B. The Photoluminescence Mechanism in Carbon Dots (Graphene Quantum Dots , Carbon Nanodots , and Polymer Dots): Current State and Future Perspective. *Nano Res.* **2015**, *8* (2), 355–381.

(37) Fiorani, A.; Merino, J. P.; Zanut, A.; Criado, A.; Prato, M.; Paolucci, F. Advanced Carbon Nanomaterials for Electrochemiluminescent Biosensor Applications. *Curr. Opin. Electrochem.* **2019**, *16*, 66–74.

(38) Chen, Y.; Cao, Y.; Ma, C.; Zhu, J.-J. Carbon-Based Dots for Electrochemiluminescence Sensing. *Mater. Chem. Front.* **2020,** *4(2)*, 369-385.

(39) Zheng, L.; Chi, Y.; Dong, Y.; Lin, J.; Wang, B. Electrochemiluminescence of Water-Soluble Carbon Nanocrystals Released Electrochemically from Graphite. *J. Am. Chem. Soc.* **2009**, *131* (13), 4564–4565.

(40) Zhu, H.; Wang, X.; Li, Y.; Wang, Z.; Yang, F.; Yang, X. Microwave Synthesis of Fluorescent Carbon Nanoparticles with Electrochemiluminescence Properties. *Chem. Commun.* **2009**, 34, 5118–5120.

(41) Dong, Y.; Chen, C.; Lin, J.; Zhou, N.; Chi, Y.; Chen, G. Electrochemiluminescence Emission from

Carbon Quantum Dot-Sulfite Coreactant System. *Carbon* **2013**, *56*, 12–17.

(42) Zhang, R.; Adsetts, J. R.; Nie, Y.; Sun, X.; Ding, Z. Electrochemiluminescence of Nitrogen- and Sulfur-Doped Graphene Quantum Dots. *Carbon* **2018**, *129*, 45–53.

(43) Wang, X. X.; Zhang, M.; Huo, X. X.; Zhao, W.; Kang, B.; Xu, J. J.; Chen, H. H. Modulating the Electronic Structure of a Semiconductor to Optimize Its Electrochemiluminescence Performance. *Nanoscale Adv.* **2019**, *1* (5), 1965–1969.

(44) Wang, M.; Sun, R.; Wang, Q.; Chen, L.; Hou, L.; Chi, Y.; Lu, C. H.; Fu, F.; Dong, Y. Effects of C-Related Dangling Bonds and Functional Groups on the Fluorescent and Electrochemiluminescent Properties of Carbon-Based Dots. *Chem.: Eur. J.* **2018**, *24* (17), 4250–4254.

(45) Li, L. L.; Ji, J.; Fei, R.; Wang, C. Z.; Lu, Q.; Zhang, J. R.; Jiang, L. P.; Zhu, J. J. A Facile Microwave Avenue to Electrochemiluminescent Two-Color Graphene Quantum Dots. *Adv. Funct. Mater.* **2012**, *22* (14), 2971–2979.

(46) Zhou, J.; Booker, C.; Li, R.; Sun, X.; Sham, T. K.; Ding, Z. Electrochemistry and Electrochemiluminescence Study of Blue Luminescent Carbon Nanocrystals. *Chem. Phys. Lett.* **2010**, *493* (4–6), 296–298.

(47) Qin, Y.; Liu, N.; Li, H.; Sun, Y.; Hu, L.; Zhao, S.; Han, D.; Liu, Y.; Kang, Z.; Niu, L. Oxygen Containing Functional Groups Dominate the Electrochemiluminescence of Pristine Carbon Dots. *J. Phys. Chem. C* **2017**, *121* (49), 27546–27554.

(48) Long, Y. M.; Bao, L.; Peng, Y.; Zhang, Z. L.; Pang, D. W. Self-Co-Reactant and Ion-Annihilation Electrogenerated Chemiluminescence of Carbon Nanodots. *Carbon* **2018**, *129*, 168–174.

(49) Carrara, S.; Arcudi, F.; Prato, M.; Cola, L. De; De Cola, L. Amine-Rich Nitrogen-Doped Carbon NanoDots as Platform for Self-Enhancing Electrochemiluminescence. *Angew. Chem. Int. Ed.* **2017**, 4757–4761.

(50) Long, Y.-M.; Bao, L.; Zhao, J.-Y.; Zhang, Z.-L.; Pang, D.-W. Revealing Carbon Nanodots As Coreactants of the Anodic Electrochemiluminescence of Ru(Bpy) 3 2+. *Anal. Chem.* **2014**, *86* (15), 7224–7228.

(51) Li, L.; Yu, B.; Zhang, X.; You, T. A Novel Electrochemiluminescence Sensor Based on Ru(Bpy)3 2+/N-Doped Carbon Nanodots System for the Detection of Bisphenol A. *Anal. Chim. Acta* **2015**, *895*, 104–111.

(52) Xu, Z.; Yu, J.; Liu, G. Fabrication of Carbon Quantum Dots and Their Application for Efficient Detecting Ru(Bpy)32+ in the Solution. *Sensors Actuators B Chem.* **2013**, *181*, 209–214.

(53) Downey, T. M.; Nieman, T. A. Chemiluminescence Detection Using Regenerate Tris(2, 2'-Bipyridyl)Ruthenium(II) Immobilized in Nafion. *Anal. Chem.* **1992**, *64* (3), 261–268.

(54) L. Thompson, B.; Heiden, Z. Redox Chemistry of BODIPY Dyes. In *BODIPY Dyes - A Privilege Molecular Scaffold with Tunable Properties*; Bañuelos-Prieto, J., Llano, R. S., Eds.; IntechOpen, 2019.

(55) Ishimatsu, R.; Shintaku, H.; Adachi, C.; Nakano, K.; Imato, T. Electrogenerated Chemiluminescence of a BODIPY Derivative with Extended Conjugation. *ChemistrySelect* **2017**, *2* (32), 10531–10536.

(56) Hesari, M.; Swanick, K. N.; Lu, J. S.; Whyte, R.; Wang, S.; Ding, Z. Highly Efficient Dual-Color Electrochemiluminescence from BODIPY-Capped PbS Nanocrystals. *J. Am. Chem. Soc.* **2015**, *137* (35), 11266–11269.

(57) Qi, H.; Teesdale, J. J.; Pupillo, R. C.; Rosenthal, J.; Bard, A. J. Synthesis, Electrochemistry and Electrogenerated Chemiluminesce of Two BODIPY-Appended Bipyridine Homologues. *J. Am. Chem. Soc.* **2013**, *135* (36), 13558–13566.

(58) Nepomnyashchii, A. B.; Pistner, A. J.; Bard, A. J.; Rosenthal, J. Synthesis, Photophysics, Electrochemistry and Electrogenerated Chemiluminescence of PEG-Modified BODIPY Dyes in Organic and Aqueous Solutions. *J. Phys. Chem. C* **2013**, *117* (11), 5599–5609.

(59) Nepomnyashchii, A. B.; Bard, A. J. Electrochemistry and Electrogenerated Chemiluminescence of BODIPY Dyes. *Acc. Chem. Res.* **2012**, *45* (11), 1844–1853.

(60) Nepomnyashchii, A. B.; Bröring, M.; Ahrens, J.; Bard, A. J. Synthesis, Photophysical,

Electrochemical, and Electrogenerated Chemiluminescence Studies. Multiple Sequential Electron Transfers in BODIPY Monomers, Dimers, Trimers, and Polymer. *J. Am. Chem. Soc.* **2011**, *133* (22), 8633–8645.

(61) Nepomnyashchii, A. B.; Br, M.; Ahrens, J.; Bard, A. J. Chemiluminescence Studies . Multiple Sequential Electron Transfers in BODIPY Monomers , Dimers , Trimers , and Polymer. *J. Am. Chem. Soc.* **2011**, No. Scheme 2, 8633–8645.

(62) Ding, Z.; Quinn, B. M.; Haram, S. K.; Pell, L. E.; Korgel, B. A.; Bard, A. J. Electrochemistry and Electrogenerated Chemiluminescence from Silicon Nanocrystal Quantum Dots. *Science* **2002**, *296* (5571), 1293–1297.

(63) Bao, L.; Liu, C.; Zhang, Z. L.; Pang, D. W. Photoluminescence-Tunable Carbon Nanodots: Surface-State Energy-Gap Tuning. *Adv. Mater.* **2015**, *27* (10), 1663–1667.

(64) Sun, Y.; Zhou, B.; Lin, Y.; Wang, W.; Fernando, K. A. S.; Pathak, P.; Meziani, M. J.; Harruff, B. A.; Wang, X.; Wang, H.; et al. Quantum-Sized Carbon Dots for Bright and Colorful Photoluminescence. *J. Am. Chem. Soc.* **2006**, *128*, 7756–7757.

(65) Formaldehyde (37%, w/V). *Cold Spring Harb. Protoc.* **2008**.

(66) Riches, A. G.; Cablewski, T.; Glattauer, V.; Thissen, H.; Meagher, L. Scalable Synthesis of an Integrin-Binding Peptide Mimetic for Biomedical Applications. *Tetrahedron* **2012**, *68* (46), 9448–9455.

(67) Iwaki, S. S. . S.; Hokamura, K. K. .; Ogawa, M. . M.; Takehara, Y. . Y.; Muramatsu, Y. Y. .; Yamane, T. T. . T.; Hirabayashi, K. K. .; Morimoto, Y. Y. . Y.; Hagisawa, K. K. .; Nakahara, K. K. . K.; et al. A Design Strategy for Small Molecule-Based Targeted MRI Contrast Agents: Their Application for Detection of Atherosclerotic Plaques. *Org. Biomol. Chem.* **2014**, *12* (43), 8611–8618.

4 Carbon Nanodots-based hybrid materials

This chapter reports the use of CNDs as building block for the synthesis of covalent hybrid materials by exploiting the CNDs surface functional groups (as discussed in **Subsection 1.3.3**). This is done by reacting the CNDs surface functional groups with functional molecules forming covalent conjugates.

Depending on the specific application, the hybrids could be designed by choosing the molecular partner. In this chapter, we focused on covalent hybrids for the preparation of electron donor/acceptor nano-systems. Indeed, CNDs were coupled to phthalocyanines. We investigate the photophysics of the hybrid and unraveled the role that CND play in symmetry-breaking charge breaking/transfer between the phthalocyanine chromophores. This part of the work has been developed in collaboration with the group of *Prof. Dirk Guldi* at the Friedrich-Alexander University of Erlangen-Nürnberg. Additionally, the results of this project have been used for the preparation of the manuscript “Symmetry-breaking charge transfer chromophore interactions supported by carbon nanodots”.

4.1 Covalent donor-acceptor nanohybrids with phthalocyanines

CNDs have been continuously used in energy-related applications thanks to their unique semiconductor behavior and light absorption/emission ability.[1,2] In particular, applications such as photovoltaics, light emitting diodes and photocatalysis have been explored ever since Sun et al reported the photoinduced electron donor/acceptor properties of these nanoparticles.[3] In these intense areas of research, CNDs were found to be suitable building blocks for supramolecular and covalent photoactive nanohybrids.[4–9] The coupling with molecules, or nanomaterials, has shown the ability of CNDs to enhance the activity of certain photocatalysts and light harvesting materials. This has been related to the activity of these nanoparticles that works as good electron transfers, not only under photoirradiation, but also when interfaced (covalently or not covalently) to electron donor or acceptor systems.[7,10] However, there are still few works that analyze in-depth the behavior of this class of carbon dots in photoinduced charge transfer processes. Besides photophysical analysis with common techniques such as absorption and emission spectroscopies, these studies are generally supported by the use of femtosecond transient absorption spectroscopy (fsTAS) for the evaluation electron transfer process and the study of non-emissive excited states.[11–14] This spectroscopic technique, also called “pump-probe” spectroscopy, is able to examine non-emissive excited state species that could be detected in timescales that range from femtosecond to second. The excited state is produced via irradiation with a short laser pulse, “pump”, followed by a second laser pulse that “probe” the absorption variations during the time.

CNDs as electron acceptor systems have been investigated with these techniques in covalent hybrids with electron donating molecules such as porphyrins and tetrathiafulvalene.[15–18] Our group has investigated the use of hp-N-CNDs,[19] obtained from Arg and EDA, for the photoinduced electron transfer interaction with a tetraarylporphyrin.[15] The covalent nanoconjugate synthetized showed a broader absorption and a quenching of the fluorescence emission respect to the reference

materials. The further fsTAS analysis revealed that the system exhibited a photoactive behavior producing, immediately after visible-light excitation, a charge separation forming a one-electron oxidized form of porphyrin and a one-electron reduced form of hp-N-CND. Martin, Guldi and coworkers reported a similar performance of hp-N-CNDs, synthetized from citric acid and urea, discussing the photoinduced charge transfer in a covalent hybrid with tetrathiafulvalene (TTF).[16] Here the photophysical studies on the system revealed no changes of the absorption properties of the coupled TTF respect to the reference material. However, the fsTAS study revealed a disabling of the excited state of TTF, after irradiation, with an emission quenching of about 90%. Further analysis accounted this result to a photoinduced electron transfer from TTF to hp-N-CNDs. The charge transfer produced a reduced hp-N-CNDs$^{\bullet-}$ and an oxidized TTF$^{\bullet+}$ that, in a timescale of picoseconds, undergo through non-radiative charge recombination.

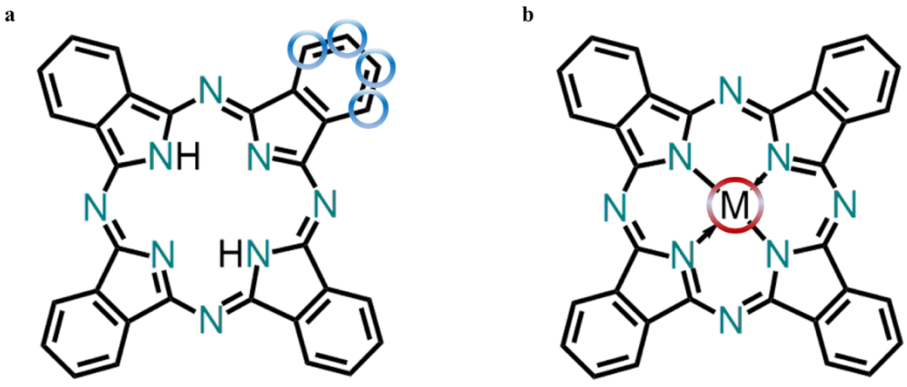

Figure 4.1 Chemical structures of phthalocyanine (**a**) and metal phthalocyanine (**b**). The blue and red circles indicate the peripheral and axial positions, respectively, that could be functionalized.

CNDs resulted also good electron donors when coupled to well-known electron acceptors like SWCNTs and perylenediimides (PDI).[20,21] Guldi and coworkers reported a non-covalent hybrid composed of hp-N-CNDs and SWCNTs. The interaction between the two hybrid components was electrostatic, interfacing negatively charged hp-N-CNDs and SWCNTs covered with a positively charged polymer. The hybrid was produced via titration of the surface modified SWCNTs with hp-N-CNDs and monitored by absorption and emission spectroscopies. The titration showed a red shift both on the absorption and emission of SWCNTs suggesting a charge transfer process. Moreover, an emission quenching of the two

components in the hybrid and further fsTAS experiments confirmed a charge separation that consisted on the electron transfer from hp-N-CNDs to SWCNTs.

The discussed properties of electron transfer system made CNDs good candidates for producing electron transfer bridges in different photoactive materials such as dye sensitized solar cells (DSSCs),[22] gold nanoclusters[23] and metal dichalcogenides.[24] In this panorama phthalocyanines (Pcs), synthetic analogues of porphyrins, have shown interesting physicochemical properties for applications in photoactive devices.[25] Phthalocyanine is an aromatic macrocycle composed of four isoindole units that form a conjugated electronic system composed of 18 π-electrons (**Figure 4.1**). These are delocalized on the aromatic structure and are responsible for the unique photophysical properties. In particular, these molecules present an intense absorption into all the visible spectrum (with a maximum extinction coefficient near 700 nm), rich redox chemistry and versatility of these molecules, in terms of chemical modification. Metal coordination, associated with the deprotonation of pyrrolic nitrogen atoms, together with introduction of functional groups at the peripheral or axial positions, are two common ways to chemically modify the Pcs structure. This results in fine-tuning of the electronic and, therefore, optical properties of these molecule. Additional beneficial properties, such as high thermal and photochemical stabilities, have made Pcs quite appealing tools for the synthesis of robust electron donor acceptor systems (D-A). In particular, a large variety of works have been reported Pcs as photoactive tools in D-A dyads, triads and more complex ensembles, in presence of nanocarbon systems.[26,27] In this context, Pcs have shown good matching behavior as electron donor or light antenna when coupled covalently or non-covalently with carbon nanotubes and fullerenes.

Compared to other carbon nanoforms, CNDs and Pcs D-A systems have been investigated to a lesser degree and have been limited to their supramolecular assembly.[28–30] In these cases the interaction is established by electrostatic interactions between the surface charges of the two partners at different ratios. Exploring the properties of a covalent Pcs-CND system is so far not investigated and it is of great relevance to understand how the two members interact when coupled by chemical bond. For this system we selected our hp-N-CNDs[19] (here after called NCNDs discussed in the **Chapter 1**), synthetized from Arg and EDA, and a

zinc phthalocyanine bearing a carboxylate handle (**Figure 4.2**). In the next subsections we will discuss the synthesis, purification and characterization of such nano-conjugates. Subsequently, we will analyze the D-A properties of these systems by means of steady-state and pump-probe transient absorption spectroscopies.

4.1.1 Synthesis and purification

By using an easy EDC coupling protocol,[19] NCNDs were coupled to Pcs. In particular we focused on a zinc carboxyphthalocyanine (ZnPc, **Figure 4.2**) bearing a carboxy group linked directly to the phthalocyanine ring.

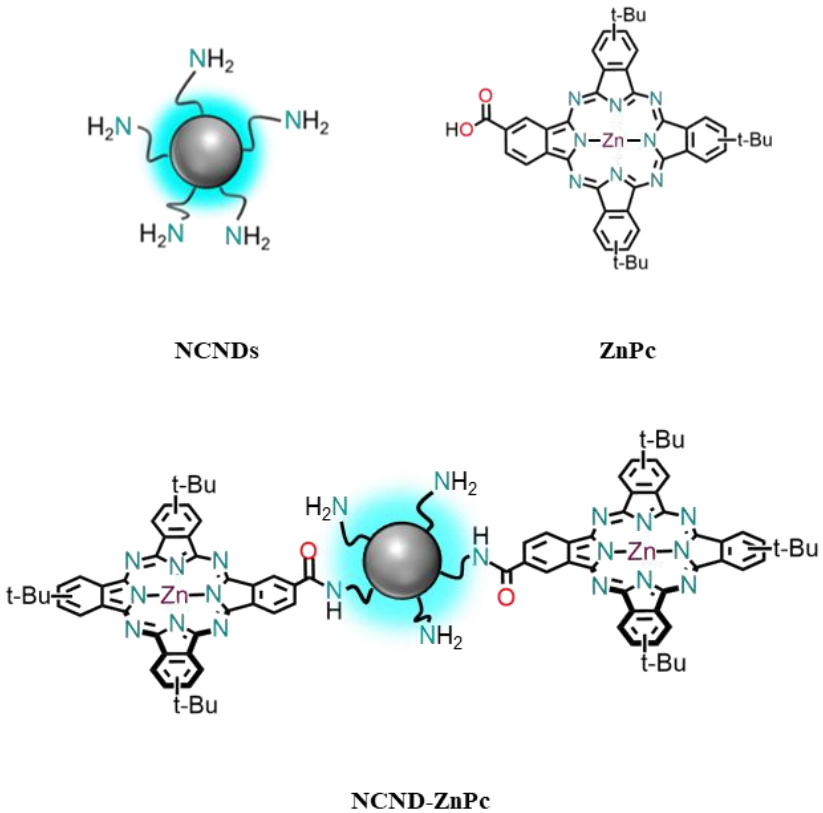

Figure 4.2 Structures of NCNDs reference (top left) and ZnPc reference (top right) as well as NCND-ZnPc nanoconjugate.

ZnPc is a good photosensitizer presenting a high incident photon-to-current conversion efficiency of 80% at 690 nm and a recorded efficiency of 3.52%.[31] Being a good NIR-adsorbing electron donor we reasoned that its electronic

properties could interact with the electron acceptor behavior of our CNDs. We expected that the primary amino groups of the NCNDs surface could react with the carboxylic acid of ZnPc to obtain amide bonds. After the reaction, the DMF was removed under reduced pressure and the crude solid mixture was purified by SEC using MeOH as mobile phase. The nanoconjugate, named NCND-ZnPc, was then obtained as blue solid after a freeze-drying process. This material showed a good solubility in organic polar solvents, especially when compared to ZnPc, a resulted quite stable in solution for days (**Figure S4.1)**.

4.1.2 Characterization

The successful synthesis of the NCND-ZnPc conjugate was firstly confirmed by a Kaiser test that revealed a decrease of free amino groups on NCND (from 1350 to 100 μmol g^{-1}). The product was additionally characterized by FT-IR (KBr) spectroscopy and compared with the two precursors (**Figure S4.2**).[19,31] NCND-ZnPc shows a carbonyl C=O and N-H bending signals at 1637 cm^{-1} and 1565 cm^{-1} typical of amide bonds. The successful amide coupling is also suggested by the disappearance of the carboxylic acid carbonyl of Pcs at 1716 cm^{-1}. The typical signatures of ZnPc, in the covalent hybrid, are also visible by its diagnostic signals of C-H stretching at 2850, 2928 and 2961 cm^{-1} and the C-H bending at 1380 cm^{-1}. Finally, morphological information about this nanoconjugate was provided by AFM. A size distribution of 4.19 ± 1.11 nm indicated the presence of larger objects when compared to the starting NCNDs (**Figure S4.3)**.[19]

In the following subsection we are going to discuss the photophysical properties of NCND-ZnPc by means of steady-state and pump-probe transient absorption spectroscopies, which revealed symmetry-breaking charge separation and recombination dynamics.

4.1.3 Studies of the electron donor/acceptor properties

The D-A properties of the NCND-ZnPc were firstly analyzed by comparison with the two precursors, NCND and ZnPc, using the steady-state absorption and fluorescence spectroscopies (**Figure 4.3**).

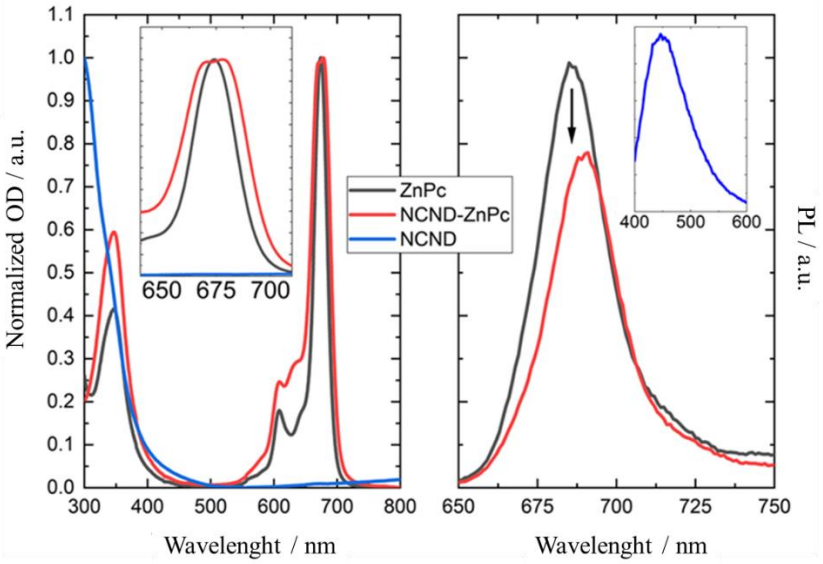

Figure 4.3 Left: Absorption spectra of the NCND reference, the ZnPc reference, and the NCND-ZnPc nanoconjugate in methanol at room temperature. Inset: Zoom into the Q-band absorption. Right: Fluorescence spectra of the ZnPc reference and the NCND-ZnPc nanoconjugate with matching absorbance at the 387 nm excitation wavelength in methanol and at room temperature. Inset: NCND fluorescence upon 387 nm excitation in methanol and at room temperature.

The absorption spectrum of ZnPc shows the typical Q-band absorption at 674 nm and a weaker Soret-band at 346 nm. The NCNDs showed their typical absorption spectrum with a broad signal that tails to the visible. Compared to the two precursors, NCND-ZnPc conjugate presents a different absorption. In particular the Q band results split in two maxima at 678 and 670 nm of similar intensity. This phenomenon is known as Davydov splitting[32] and it is associated to the electronic communication of two or more ZnPc units that are close to each other.[33,34] In addition the NCND-ZnPc was studied at the excited-state and, again, was compared to the precursors (**Figure 4.3**). To excite ZnPc an excitation wavelength of 387 nm (3.2 eV) was used and the samples were adjusted to obtain the same optical density. ZnPc shows a strong fluorescence emission at 686 nm with a quantum yield of 0.15. In the nanoconjugate NCND-ZnPc a quenching of emission of 22% is registered, together with a 4 nm red-shift to 690 nm. Using an excitation wavelength of 675

nm (1.84 eV), an analogous red shift is seen, with a lower fluorescence quenching of 9% (**Figure S4.4**). These findings suggest that NCND and ZnPc present electron transfer when excited.

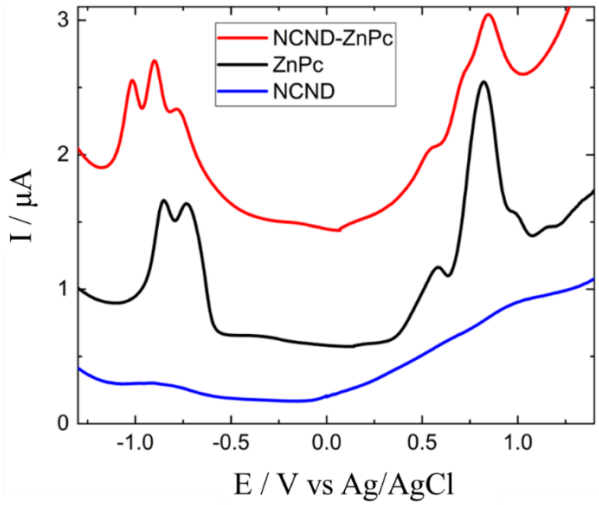

Figure 4.4 Electrochemistry of NCND (blue profile), ZnPc (black profile), and the NCND-ZnPc (red profile) conjugate in methanol at room temperature.

This aspect was better investigated by electrochemical means (**Figure 4.4**) on the conjugate and its precursors. The NCND reference presents weak and broad signals that are not easy to distinguish. Compared to these, ZnPc shows oxidations at +0.59 and +0.82 V vs. Ag/AgCl, and reductions at -0.73 and -0.85 V. Respect to this, NCND-ZnPc showed three (rather than two) oxidations and reductions, respectively at +0.55, +0.72, +0.84 V and -0.78, -0.90, -1.01 V. This result strongly suggests that, when conjugated, ZnPc centered orbitals are split because of the ground-state electronic interactions, facilitated by NCND, with other ZnPc. For this reason, a symmetry-breaking charge transfer state is expected at around 1.33 eV above the ground state.

To better understand the excited state dynamics responsible of the ZnPc fluorescence quenching, fsTAS experiments were performed. These were done for the conjugate and the ZnPc as reference, exciting at 387 nm in methanol at room temperature. The ZnPc reference (**Figure S4.5**) showed positive transients at 485, 590, 630 and 808 nm next to a negative signal at 674 nm. These features persist until the nanosecond timescale, after which a positive transient at 480 nm and negative ones at 609 and 674 nm appear. The global analysis suggests a three-

species kinetic model with two exponentially decaying species at time constants of 7 ps and 2.2 ns together with infinitely-lived species. These two decays are ascribed to an internal conversion $S_1 \leftarrow S_2$ and an intersystem crossing $T \leftarrow S_1$. The triplet (T) excited states resulted much longer-lived respect to the resolution of these experiments which in turn helps to rationalize their infinitively-lived nature.[35] Similar results were obtained when the ZnPc was excited at 675 nm (**Figure S4.6**). The excitation lead to a hot-S1 population that decay in 1.6 ps to afford S_1. Then, the intersystem crossing $T \leftarrow S_1$ takes 2.9 ns, preceding the decay in the ground state that comes in a microsecond time scale.

Compared to ZnPc, NCND-ZnPc shows very different excited state dynamics. Exciting at 387 nm two minima are seen at 633 nm and 670 nm (**Figure 4.5**).

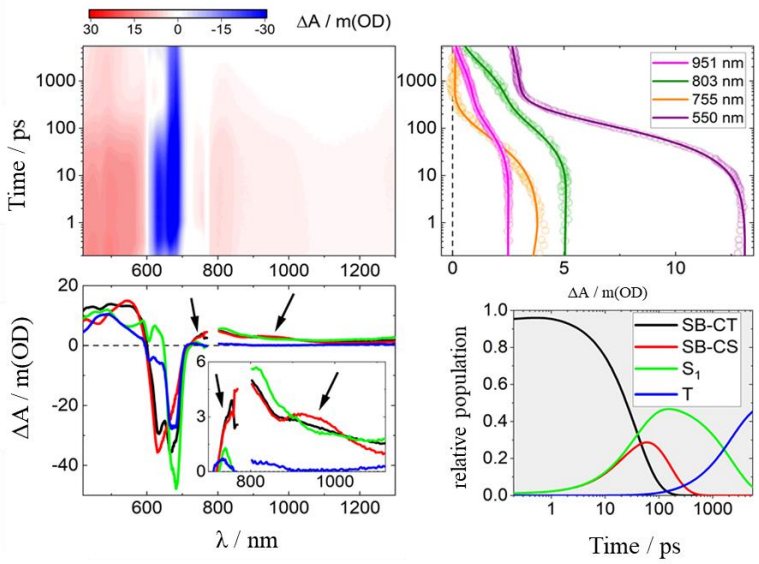

Figure 4.5 Top left: Differential absorption 3D map obtained upon fsTAS on NCND-ZnPc in methanol at room temperature upon 387 nm excitation. Top right: Time absorption profiles and corresponding fittings at 951 (magenta), 803 (dark green), 755 (orange) and 550 (purple) nm. Bottom left: Species associated differential spectra of the SB-CT (black), SB-CS (red), S1 (green) and T (blue) excited states. Bottom right: concentration evolution over time.

These signals are accompanied by positive transients at 547 and 750 nm, which, importantly, were not seen in the ZnPc reference. Moreover these findings suggest the typical fingerprint absorption of the one-electron oxidized ZnPc.[36] In contrast, on the nanosecond timescale, the transient absorption spectra resemble those observed for the ZnPc reference. The kinetic model that comes from this data results

in three exponentially decaying species and a fourth one, which is persistent on the timescale of these experiments. Moreover, taking also into account the result of fluorescence spectroscopy, a parallel target model was necessary to fit the transient absorption measurements. This model considers two parallel cascades. One of the two cascades, responsible of the fluorescence, includes the same singlet excited state. This intersystem crosses in 2.2 ns to its corresponding microsecond-lived triplet excited state that was seen in the ZnPc reference (**Figure 4.6**). The second cascade is related to the fluorescence quenching and it is characterized by two excited states with distinct transients at 547, 750, and 925 nm. Notably, the maxima at 547 and 750 nm match the ones responsible to the observed formation of one-electron oxidized ZnPc.[36] Compared to these, NCNDs are characterized by a rather broad and featureless band, which extends all across the visible range of the solar spectrum. Moreover, the one-electron reduced ZnPc show a 1000 nm maximum that resembles the one recorded for the nanoconjugate. This global information suggests a system formed at least by a NCND particle that bounds two ZnPc. Here a symmetry-breaking charge transfer/separation occurs by an oxidation of one ZnPc on one side and a reduction of another ZnPc in the other side. Thus, these two species could be assigned in one case to symmetry-breaking charge transfer $ZnPc^{\delta-}$-$ZnPc^{\delta+}$ state (SB-CT) which is populated directly upon light absorption. In the other case the system could involve the symmetry-braking charge separated $ZnPc^{-}$-$ZnPc^{+}$ state (SB-CS) that is formed in 37 ps and reinstates the ground state via charge recombination in 108 ps (**Figure 4.6**). When excited at 675 nm, the excited state dynamics of NCND-ZnPc are quite similar (**Figure S4.6**). More specifically, although the SB-CS state evolves from a hot-S1 state in 11 ps, the charge recombination takes 101 ps and matches the results obtained exciting at 387 nm (**Figure 4.6**). To further compare these states, **Figure S4.7** shows the differential spectra of the NCND-ZnPc generated species upon 387 and 675 nm.

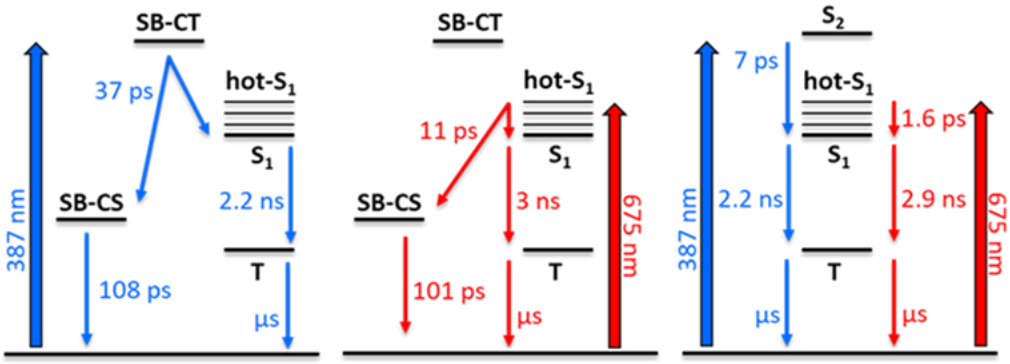

Figure 4.6 Target models employed to fit fsTAS data. Left: NCND-ZnPc under 387 nm excitation. Center: NCND-ZnPc under 675 nm excitation. Right: ZnPc under 387 and 675 nm excitation.

4.2 Conclusions

In this Chapter, zinc phthalocyanines were conjugated to NCNDs, in order to study the photophysics of the resulting donor-acceptor nanosystem. Carbodiimide coupling protocol, between ZnPc carboxylate derivative and NCNDs amino groups, was successfully applied and the corresponding nanohybrid was purified (by size exclusion chromatography) and its structural and morphological features characterized.

An in-depth study of the photophysical properties of the nanohybrid of the nanohybrid was then performed. From comparative absorption studies emerges that, under excitation, ZnPcs found on the CNDs surface are able to communicate by electron transfer. This phenomenon is visible in the typical phthalocyanine Q-band splitting better known as Davydov splitting. This result is confirmed by the electrochemical and the pump probe spectroscopies studies. In the former study the hybrid shows triple oxidation and reduction respect to the double oxidation and reduction pattern observed in the free ZnPc suggesting a symmetry-breaking charge transfer/separation. The latter study confirmed this phenomenon indicating the photoinduced oxidation of a Pcs and the contemporary reduction of another Pcs that could be visualized in charge transfer ($ZnPc^{\delta-}$-$ZnPc^{\delta+}$) or separation ($ZnPc^{-}$-$ZnPc^{+}$) under excitation.

This phenomenon arises from the redox behavior of phthalocyanines that electronically communicates through CNDs. The study reveals that CNDs act as optimal building blocks for the preparation of donor-acceptor covalent hybrids with more than two units bonded together. CNDs show to be versatile and interesting charge carriers for optoelectronic nanoconjugates thanks to the remarkable semiconductor properties. These results inspire on the use of these nanoparticles for electron transfer systems interesting for uses in sensors and photovoltaics.

4.3 Experimental section

4.3.1 Materials

NCNDs were synthetized as previously reported.[19] Ultrapure water was obtained by a MilliQ™ water purification system (water resistivity of 18.2 MΩ at 25 °C). All the solvent and reagents (reagent grade) were bought from Sigma-Aldrich and used without further purification.

ZnPc was synthetized by using 4-*tert*-butylphthalonitrile (32703-80-3, Sigma 423122-1G) and 1,2-dicyano-4-(methoxycarbonyl)benzene as precursors. 1,2-Dicyano-4-(methoxycarbonyl)benzene was prepared by two steps: (1) bromination with Br_2 in H_2SO_4 (0 °C) of methyl 4-bromobenzoate (619-42-1, Sigma 407593-10G), followed by (2) double cyanation (CuCN in DMSO, 150 °C under Ar), using published procedures.[37,38] The two phthalonitrile precursors were reacted together, using literature procedures ($ZnCl_2$ and 1,5-diazabiciclo(5.4.0)undec-7-ene, in *n*-pentanol at 145 °C for 24 h), to obtain the tri-*tert*-butyl ester Zinc phthalocyanine mono ester. The ester was deprotected to acid using literature procedure.[15] The final characterization of the acid phthalocyanine was in accordance to literature procedure.[31]

4.3.2 Methods

Thin layer chromatography was performed on pre-coated aluminum sheets with 0.20 mm Machevery-Nagel Alugram SIL G/UV254. Column chromatography was made using Merck silica gel 60 Å (particle size 40-63 μm). Size exclusion chromatography (SEC) was carried out using Sephadex™ LH-20 as stationary phase and methanol as mobile phase. Fourier-transform infrared spectra (KBr) were recorded on a Perkin Elmer 2000 spectrometer. Atomic force microscopy (AFM) images were recorded using a Nanoscope IIIa, VEECO Instruments. As a general procedure to perform AFM analyses, tapping mode with a HQ:NSC19/ALBS probe (80kHz; 0.6 N/m) (MikroMasch) from drop cast of samples in a methanolic, or aqueous, solution (concentration of few mg/mL) on a mica substrate was

performed. The obtained AFM-images were analyzed in Gwyddion 2.35. ^{1}H and ^{13}C NMR spectra were measured using a Varian Inova spectrometer at 500 and 125 MHz, respectively. Chemical shifts are reported in parts per million (ppm) and are referenced to the residual solvent peak. Mass spectrometry Electrospray Ionization (ESI, 5600 eV) mass analysis was performed on a Perkin-Elmer API1. Melting points (m.p.) were measured on a Büchi SMP-20 in open capillary tubes.

4.3.3 Synthesis of NCND-ZnPc

In a two necked round bottom flask, ZnPc (12.4 mg, 15.8 µmol) was dissolved in anhydrous DMF (4.0 mL) under Ar, followed by addition of EDC·HCl (6.1 mg, 31.6 µmol) and NHS (3.6 mg, 31.6 µmol). The whole mixture was left stirring under Ar atmosphere at r.t. for 30 minutes. NCNDs (8.0 mg) were subsequently added as solids, under Argon, and the reaction was left stirring at the same conditions for 18 hours. Then the solvent was removed under reduced pressure. The blue residue was dissolved in methanol and purified by SEC. The methanolic fractions were collected and dried under vacuum, then dissolved in water and lyophilized affording 15.43 mg of a blue solid.

4.3.4 Supporting figures

Figure S4.1 Photograph of a methanolic solution of NCND-ZnPc in daylight (left) and under UV light (365 nm) illumination (right).

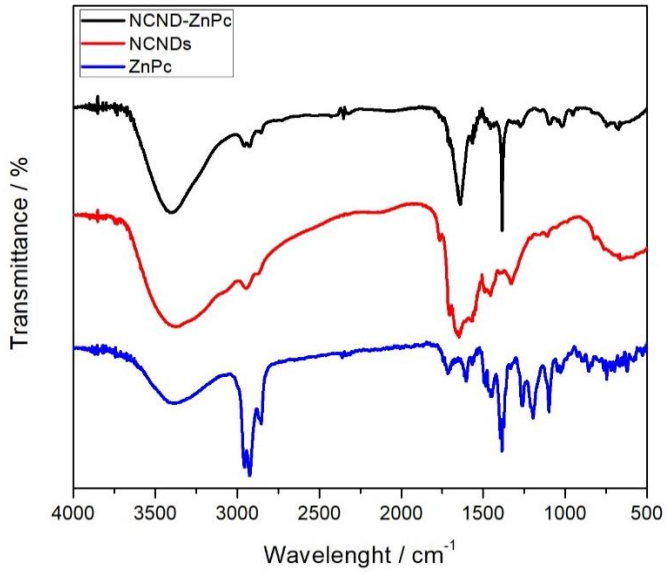

Figure S4.2 FT-IR spectra of NCND-ZnPc (black), NCNDs (red) and ZnPc (blue).

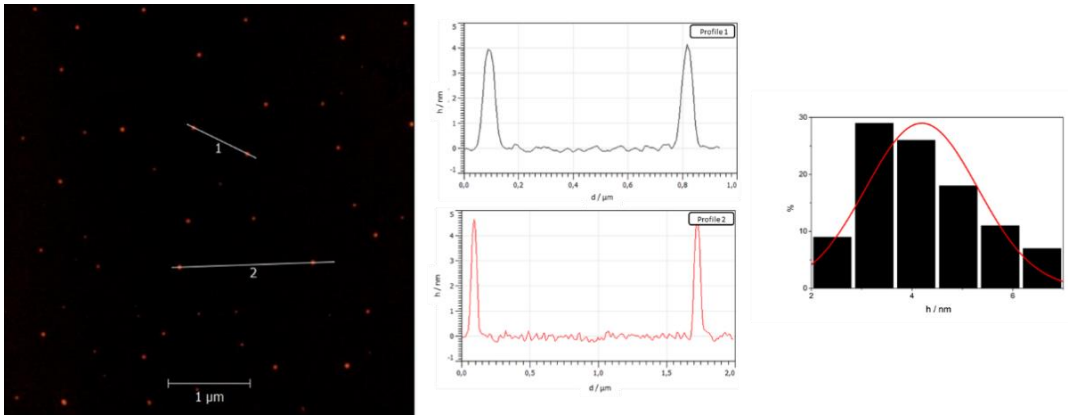

Figure S4.3 2D tapping mode AFM images (5.0 × 5.0 µm) from drop-cast NCND-ZnPcs methanolic solutions on mica substrates (left); height profile along the dashed line (center); height sizes distribution histogram and superimposed Gaussian fit (right).

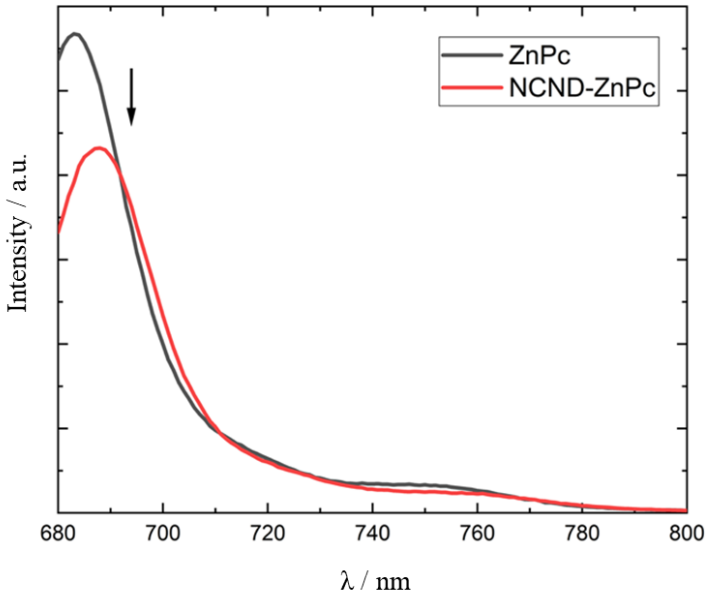

Figure S4.4 Emission spectra of matching absorbance solutions of ZnPc and NCND-ZnPc under 675 nm excitation in methanol at room temperature.

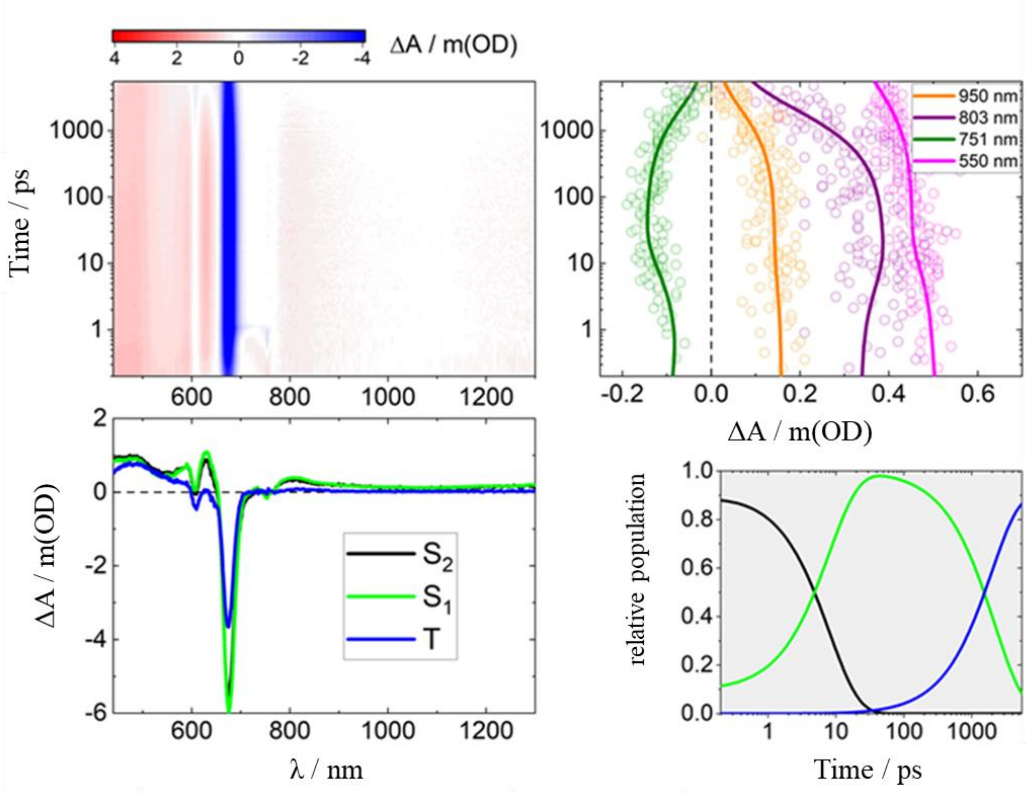

Figure S4.5 Top left: Differential absorption 3D map obtained upon fsTAS on ZnPc in methanol at room temperature upon 387 nm excitation. Top right: Time absorption profiles and corresponding fittings at 950 (orange), 803 (purple), 751 (dark green) and 550 (magenta) nm. Bottom left: Species associated differential spectra of the S2 (black), S1 (green) and T (blue) excited states. Bottom right: concentration evolution over time.

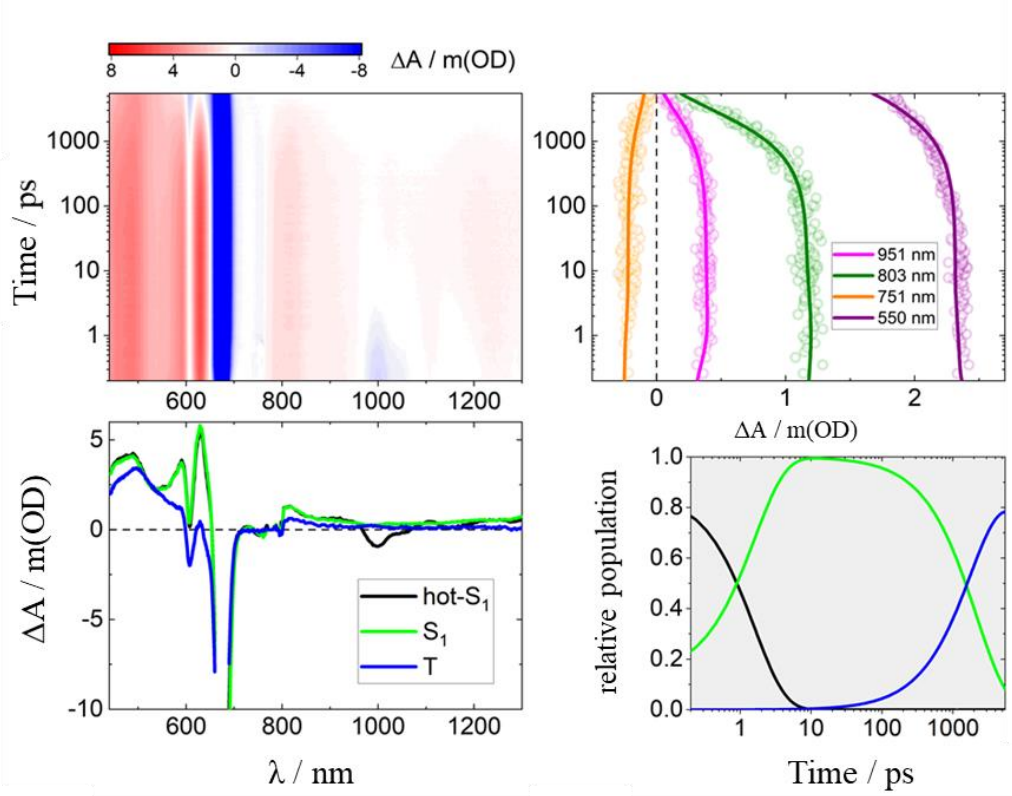

Figure S4.6 Top left: Differential absorption 3D map obtained upon fsTAS on ZnPc in methanol at room temperature upon 675 nm excitation. Top right: Time absorption profiles and corresponding fittings at 951 (magenta), 803 (dark green), 751 (orange) and 550 (purple) nm. Bottom left: Species associated differential spectra of the hot-S1 (black), S1 (green) and T (blue) excited states. Bottom right: concentration evolution over time.

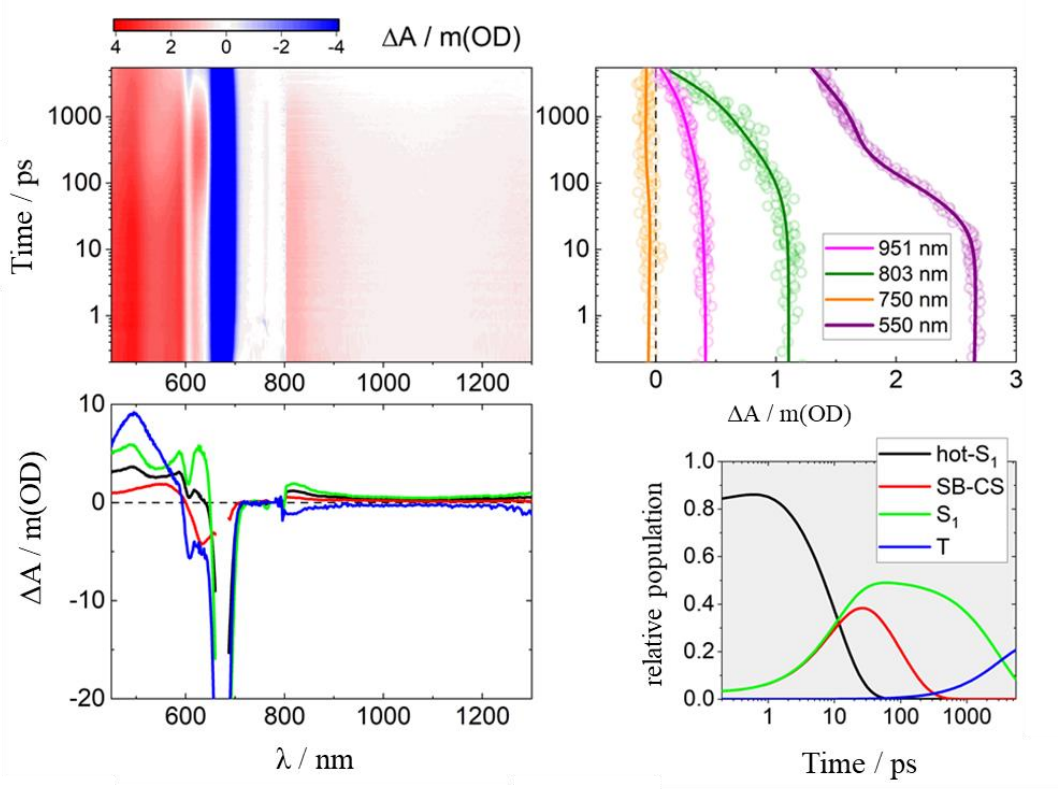

Figure S4.7 Top left: Differential absorption 3D map obtained upon fsTAS on NCND-ZnPc in methanol at room temperature upon 675 nm excitation. Top right: Time absorption profiles and corresponding fittings at 951 (magenta), 803 (dark green), 750 (orange) and 550 (purple) nm. Bottom left: Species associated differential spectra of the hot-S1 (black), SB-CS (red), S1 (green) and T (blue) excited states. Bottom right: concentration evolution over time.

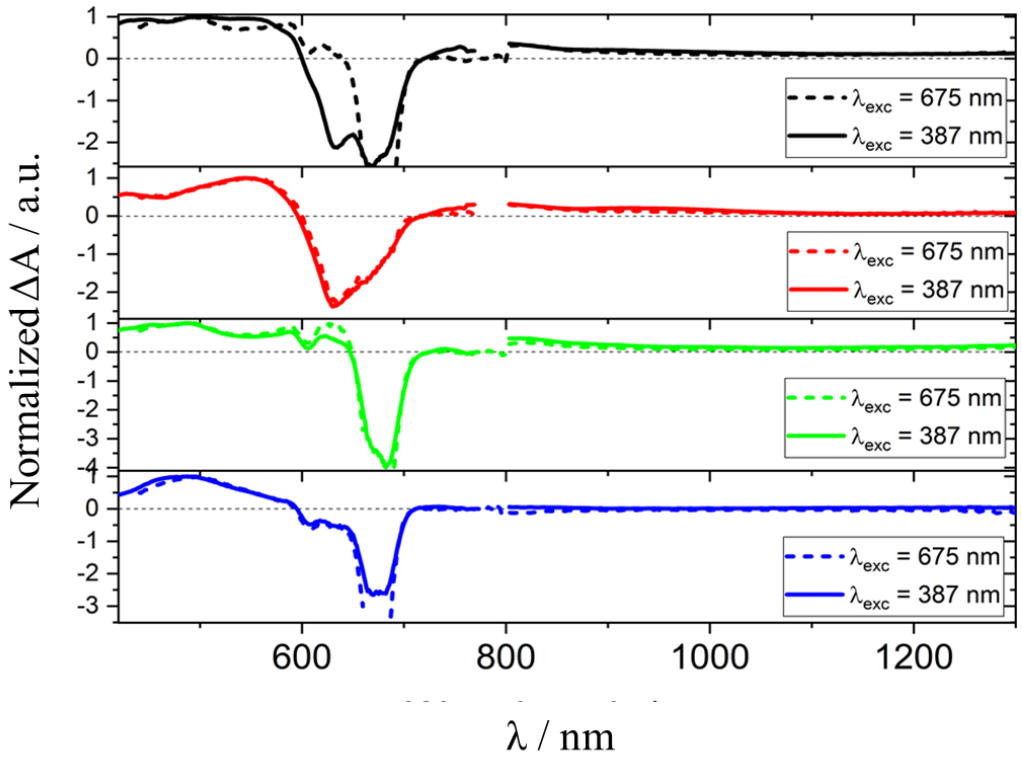

Figure S4.8 Species associated differential spectra for NCND-ZnPc in methanol at room temperature under 387 (solid curves) and 675 (dashed curves) nm excitation. From top to bottom: SB-CT / hot-S1 (black), SB-CS (red), S1 (green), T (blue).

4.4 References

(1) Hutton, G. A. M. M.; Martindale, B. C. M. M.; Reisner, E. Carbon Dots as Photosensitisers for Solar-Driven Catalysis. *Chem. Soc. Rev.* **2017**, *46* (20), 6111–6123.

(2) Hu, C.; Li, M.; Qiu, J.; Sun, Y. P. Design and Fabrication of Carbon Dots for Energy Conversion and Storage. *Chem. Soc. Rev.* **2019**, *48* (8), 2315–2337.

(3) Wang, X.; Cao, L.; Lu, F.; Meziani, M. J.; Li, H.; Qi, G.; Zhou, B.; Harruff, B. A.; Kermarrec, F.; Sun, Y. P. Photoinduced Electron Transfers with Carbon Dots. *Chem. Commun.* **2009**, No. 25, 3774–3776.

(4) Yao, B.; Huang, H.; Liu, Y.; Kang, Z. Carbon Dots: A Small Conundrum. *Trends Chem.* **2019**, *1* (2), 235–246.

(5) Tian, X.-T.; Yin, X.-B. Carbon Dots, Unconventional Preparation Strategies, and Applications Beyond Photoluminescence. *Small* **2019**, *1901803*, 1901803.

(6) Arcudi, F.; Đorđević, L.; Prato, M. Design, Synthesis, and Functionalization Strategies of Tailored Carbon Nanodots. *Acc. Chem. Res.* **2019**, *52* (8), 2070–2079.

(7) Cadranel, A.; Margraf, J. T.; Strauss, V.; Clark, T.; Guldi, D. M. Carbon Nanodots for Charge-Transfer Processes. *Acc. Chem. Res.* **2019**, *52* (4), 955–963.

(8) Kang, Z.; Lee, S. T. Carbon Dots: Advances in Nanocarbon Applications. *Nanoscale* **2019**, *11* (41), 19214–19224.

(9) Xia, C.; Zhu, S.; Feng, T.; Yang, M.; Yang, B. Evolution and Synthesis of Carbon Dots : From Carbon Dots to Carbonized Polymer Dots. *Adv. Sci.* **2019**, *1901316*.

(10) Srivastava, I.; Khamo, J. S.; Pandit, S.; Fathi, P.; Huang, X.; Cao, A.; Haasch, R. T.; Nie, S.; Zhang, K.; Pan, D. Influence of Electron Acceptor and Electron Donor on the Photophysical Properties of Carbon Dots: A Comparative Investigation at the Bulk-State and Single-Particle Level. *Adv. Funct. Mater.* **2019**, *1902466*, 1–14.

(11) Willkomm, J.; Orchard, K. L.; Reynal, A.; Pastor, E.; Durrant, J. R.; Reisner, E. Dye-Sensitised Semiconductors Modified with Molecular Catalysts for Light-Driven H2 Production. *Chem. Soc. Rev.* **2016**, *45* (1), 9–23.

(12) Berera, R.; van Grondelle, R.; Kennis, J. T. M. Ultrafast Transient Absorption Spectroscopy: Principles and Application to Photosynthetic Systems. *Photosynth. Res.* **2009**, *101* (2–3), 105–118.

(13) Kwon, W.; Do, S.; Kim, J.-H.; Seok Jeong, M.; Rhee, S.-W. Control of Photoluminescence of Carbon Nanodots via Surface Functionalization Using Para-Substituted Anilines. *Sci. Rep.* **2015**, *5* (1), 12604.

(14) Sciortino, A.; Gazzetto, M.; Soriano, M. L.; Cannas, M.; Cárdenas, S.; Cannizzo, A.; Messina, F. Ultrafast Spectroscopic Investigation on Fluorescent Carbon Nanodots: The Role of Passivation. *Phys. Chem. Chem. Phys.* **2019**, *21* (30), 16459–16467.

(15) Prato, M.; Arcudi, F.; Strauss, V.; Cadranel, A.; Guldi, D. M.; Dordevic, L.; Dordević, L.; Cadranel, A.; Guldi, D. M.; Prato, M.; et al. Porphyrin Antennas on Carbon Nanodots: Excited State Energy and Electron Transduction. *Angew. Chem. Int. Ed.* **2017**, *56* (40), 12097–12101.

(16) Ferrer-Ruiz, A.; Scharl, T.; Haines, P.; Rodríguez-Pérez, L.; Cadranel, A.; Herranz, M. Á.; Guldi, D. M.; Martín, N. Exploring Tetrathiafulvalene–Carbon Nanodot Conjugates in Charge Transfer Reactions. *Angew. Chem. Int. Ed.* **2018**, *57* (4), 1001–1005.

(17) Cadranel, A.; Strauss, V.; Margraf, J. T.; Winterfeld, K. A.; Vogl, C.; Đorđević, L.; Arcudi, F.; Hoelzel, H.; Jux, N.; Prato, M.; et al. Screening Supramolecular Interactions between Carbon Nanodots and Porphyrins. *J. Am. Chem. Soc.* **2018**, *140* (3), 904–907.

(18) Scharl, T.; Cadranel, A.; Haines, P.; Strauss, V.; Bernhardt, S.; Vela, S.; Atienza, C.; Gröhn, F.; Martín, N.; Guldi, D. M. Fine-Tuning the Assemblies of Carbon Nanodots and Porphyrins. *Chem. Commun.* **2018**, *54* (82), 11642–11644.

(19) Arcudi, F.; Đorđević, L.; Prato, M. Synthesis, Separation, and Characterization of Small and Highly Fluorescent Nitrogen-Doped Carbon NanoDots. *Angew. Chem. Int. Ed.* **2016**, *55* (6), 2107–2112.

(20) Strauss, V.; Margraf, J. T.; Clark, T.; Guldi, D. M. A Carbon–Carbon Hybrid – Immobilizing Carbon Nanodots onto Carbon Nanotubes. *Chem. Sci.* **2015**, *6*, 6878–6885.

(21) Strauss, V.; Margraf, J. T.; Dolle, C.; Butz, B.; Nacken, T. J.; Walter, J.; Bauer, W.; Peukert, W.; Spiecker, E.; Clark, T.; et al. Carbon Nanodots: Toward a Comprehensive Understanding of Their Photoluminescence. *J. Am. Chem. Soc.* **2014**, *136* (49), 17308–17316.

(22) Margraf, J. T.; Lodermeyer, F.; Strauss, V.; Haines, P.; Walter, J.; Peukert, W.; Costa, R. D.; Clark, T.; Guldi, D. M. Using Carbon Nanodots as Inexpensive and Environmentally Friendly Sensitizers in Mesoscopic Solar Cells. *Nanoscale Horizons* **2016**, *1* (3), 220–226.

(23) Hasenöhrl, D.; Saha, A.; Strauss, V.; Wibmer, L.; Klein, S.; Guldi, D. M.; Hirsch, A. Bulbous Gold-Carbon Nanodot Hybrid Nanoclusters for Cancer Therapy. *J. Mater. Chem. B* **2017**, *5*, 8591–8599.

(24) Vallan, L.; Canton-Vitoria, R.; Gobeze, H. B.; Jang, Y.; Arenal, R.; Benito, A. M.; Maser, W. K.; D'Souza, F.; Tagmatarchis, N. Interfacing Transition Metal Dichalcogenides with Carbon Nanodots for Managing Photoinduced Energy and Charge-Transfer Processes. *J. Am. Chem. Soc.* **2018**, *140* (41), 13488–13496.

(25) De La Torre, G.; Claessens, C. G.; Torres, T. Phthalocyanines: Old Dyes, New Materials. Putting Color in Nanotechnology. *Chem. Commun.* **2007**, No. 20, 2000–2015.

(26) Bottari, G.; De La Torre, G.; Guldi, D. M.; Torres, T. Covalent and Noncovalent Phthalocyanine - Carbon Nanostructure Systems: Synthesis, Photoinduced Electron Transfer, and Application to Molecular Photovoltaics. *Chem. Rev.* **2010**, *110* (11), 6768–6816.

(27) Bottari, G.; Suanzes, J. A.; Trukhina, O.; Torres, T. Phthalocyanine-Carbon Nanostructure Materials Assembled through Supramolecular Interactions. *J. Phys. Chem. Lett.* **2011**, *2* (8), 905–913.

(28) Barman, M. K.; Jana, B.; Bhattacharyya, S.; Patra, A. Photophysical Properties of Doped Carbon Dots (N, P, and B) and Their Influence on Electron/Hole Transfer in Carbon Dots-Nickel (II) Phthalocyanine Conjugates. *J. Phys. Chem. C* **2014**, *118* (34), 20034–20041.

(29) Hu, S.; Tian, R.; Dong, Y.; Yang, J.; Liu, J.; Cao, S. Preparation and Optical Properties of Phthalocyanine-Carbon Dot Blends. *RSC Adv.* **2013**, *3* (44), 21447–21452.

(30) Mao, L.; Wang, X.; Guo, Y.; Yao, L.; Xue, X.; Wang, H. X.; Xiong, C.; Wen, W.; Zhang, X.; Wang, S. A Synergistic Approach to Enhance the Photoelectrochemical Performance of Carbon Dots for Molecular Imprinting Sensors. *Nanoscale* **2019**, *11* (16), 7885–7892.

(31) Cid, J. J.; Yum, J. H.; Jang, S. R.; Nazeeruddin, M. K.; Martínez-Ferrero, E.; Palomares, E.; Ko, J.; Grätzel, M.; Torres, T. Molecular Cosensitization for Efficient Panchromatic Dye-Sensitized Solar Cells. *Angew. Chem. Int. Ed.* **2007**, *46* (44), 8358–8362.

(32) Davydov, A. S. The Theory of Molecular Excitons. *Uspekhi Fiz. Nauk* **1964**, *82* (3–4), 145–178.

(33) Piet, J. J.; Taylor, P. N.; Wegewijs, B. R.; Anderson, H. L.; Osuka, A.; Warman, J. M. Photoexcitations of Covalently Bridged Zinc Porphyrin Oligomers: Frenkel versus Wannier−Mott Type Excitons. *J. Phys. Chem. B* **2002**, *105* (1), 97–104.

(34) Martin, M. M.; Lungerich, D.; Haines, P.; Hampel, F.; Jux, N. Electronic Communication across Porphyrin Hexabenzocoronene Isomers. *Angew. Chem. Int. Ed.* **2019**, *0033*, 8932–8937.

(35) Wibmer, L.; Lourenço, L. M. O.; Roth, A.; Katsukis, G.; Neves, M. G. P. M. S.; Cavaleiro, J. A. S.; Tomé, J. P. C.; Torres, T.; Guldi, D. M. Decorating Graphene Nanosheets with Electron Accepting Pyridyl-Phthalocyanines. *Nanoscale* **2015**, *7* (13), 5674–5682.

(36) Kadish, K. M.; Smith, K. M.; Guilard, R. *Handbook of Porphyrin Science - Volume 9*; World Scientific: Singapore, 2010.

(37) Dieing, R.; Schmid, G.; Witke, E.; Feucht, C.; Dre??en, M.; Pohmer, J.; Hanack, M. Soluble Substituted μ-Oxo(Phthalocyaninato)Iron(III) Dimers. *Chem. Ber.* **1995**, *128* (6), 589–598.

(38) Tilley, J. W.; Clader, J. W.; Zawoiski, S. S.; Wirkus, M.; LeMahieu, R. A.; O'Donnell, M.; Crowley, H.; Welton, A. F. Biphenylcarboxamide Derivatives as Antagonists of Platelet-Activating Factor. *J. Med. Chem.* **1989**, *32* (8), 1814–1820.